

**Silicon-based Micro Fuel Cell Membrane Electrode Assembly for  
Energy Supply of Portable Electronic Devices and  
High Throughput Material Characterization**

Von der Fakultät für Ingenieurwissenschaften, Abteilung Maschinenbau und  
Verfahrenstechnik der  
Universität Duisburg-Essen

zur Erlangung des akademischen Grades

eines

Doktors der Ingenieurwissenschaften

Dr.-Ing.

genehmigte Dissertation

von

Benedikt Funke  
aus  
Attendorn

Gutachter: Prof. Dr. rer. nat. Angelika Heinzel  
Prof. Dr.-Ing. Joachim Burghartz

Tag der mündlichen Prüfung: 09.05.2019

# DuEPublico

Duisburg-Essen Publications online

UNIVERSITÄT  
DUISBURG  
ESSEN

*Offen im Denken*

ub | universitäts  
bibliothek

Diese Dissertation wird über DuEPublico, dem Dokumenten- und Publikationsserver der Universität Duisburg-Essen, zur Verfügung gestellt und liegt auch als Print-Version vor.

**DOI:** 10.17185/duepublico/70156

**URN:** urn:nbn:de:hbz:464-20190625-144955-7

Alle Rechte vorbehalten.

*"Edison's electric light did not come about from the  
continuous improvement of the candle."*

Oren Harari





## Vorwort

Die vorliegende Arbeit zum Thema „Silizium-basierte Mikro-Membran-Elektroden-Einheiten“ wurde im Zuge meiner Tätigkeit als wissenschaftlicher Mitarbeiter am Zentrum für BrennstoffzellenTechnik GmbH, Duisburg, verfasst.

Mein besonderer Dank gilt Professor Dr. Angelika Heinzl, die diese Arbeit ermöglicht und mich während der gesamten Zeit mit wertvollen Ratschlägen, kritischen Anmerkungen und ihrem breiten Erfahrungsschatz auf dem Gebiet der Mikrobrennstoffzellen unterstützt hat. Ebenso möchte ich Professor Dr. Joachim Burghartz für die Übernahme des Ko-Referats danken.

Mein großer Dank gilt darüber hinaus den Kollegen der Abteilung „Mikrosysteme und Strömungsmechanik“, insbesondere den beiden Abteilungsleitern Jens Wartmann und Georg Dura. Dr. Ivan Radev möchte ich danken für große Unterstützung bei der Interpretation von Messergebnissen der zyklischen Voltammetrie und elektrochemischen Impedanzspektroskopie sowie der Hilfe bei der Erstellung von Ersatzschaltbildern mittels ZPlot®. Dr. Susanne Palecki möchte ich für die Hilfe bei der Aufnahme zahlreicher REM-Bilder danken.

Ich möchte mich zudem herzlich bei den technischen Mitarbeitern des ZBT bedanken. Dies beinhaltet insbesondere Jürgen Galka, der bei der Realisierung des Dip Coaters unverzichtbar war. Zudem wäre ohne Ralf Thelen, der durch zahlreiche Fräsarbeiten an der Mikrofräse viele Messaufbauten realisierte, die Arbeit nicht möglich gewesen. Auch bei Sabrina Fricke, die eine unerlässliche Hilfe bei der Herstellung von gesprühten Katalysatorschichten war, möchte ich mich bedanken. Ich bedanke mich beim gesamten Team des ZBT für kollegiale Atmosphäre, die stete Unterstützung und die denkwürdigen Firmenfeiern.

Ein großes Dankeschön möchte ich auch dem Institut für Mikroelektronik Stuttgart (IMS CHIPS) für die Bereitstellung der Mikromembranen aussprechen, insbesondere Herrn Dr. Florian Letzkus, der während der gesamten Zeit eine große Hilfe bei der Betrachtung sämtlicher Fragestellungen im Bereich der Siliziumtechnologie war. Für die Vermessung der Mikro-Membran-Elektroden-Einheiten mittels EC-AFM möchte ich mich ganz herzlich bei Prof. Dr. Renate Hiesgen und ihrem Team an der Hochschule Esslingen bedanken.

Nicht vergessen möchte ich auch alle studentischen Hilfskräfte, Bachelor- und Masterarbeiter, die durch ihren engagierten Einsatz und die zahllosen Stunden im Labor zum Erfolg dieser Arbeit beigetragen haben.

Schließlich möchte ich mich bei Andrea für ihr Verständnis und ihre uneingeschränkte Unterstützung bedanken.

## Zusammenfassung

Portable Elektronikgeräte wie Smartphones, Tablet PC's oder Wearables sind in unserer Gesellschaft nicht mehr wegzudenken. Die stetige Erweiterung mit neuen Funktionen wie GPS oder Bluetooth führt zu starken Leistungszuwächsen der Geräte einerseits, jedoch auch zu einem deutlich erhöhten Energieverbrauch andererseits. Die Entwicklung neuer Batterietechnologien mit höherer Energiedichte konnte hierbei nicht Schritt halten, so dass die durchschnittliche Nutzungsdauer zwischen Ladezyklen deutlich gesunken ist. Die Entwicklung alternativer Technologien ist daher von großer Bedeutung für den zukünftigen Erfolg portabler, vernetzter Elektronikgeräte, insbesondere im Umfeld des Internets der Dinge.

Mikrobrennstoffzellen stellen eine interessante Variante zur Erzielung höherer Energiedichten dar. Jedoch müssen Ansätze erarbeitet werden, um die Miniaturisierung voranzutreiben. Daher werden in dieser Arbeit die Grundlagen zur Herstellung einer siliziumbasierten Membran-Elektroden-Einheit geschaffen, um mit Hilfe der Halbleitertechnologie extrem miniaturisierte, jedoch für Massenfertigung geeignete Mikrobrennstoffzellen realisieren zu können. Dies beinhaltet zum einen die Erarbeitung eines Konzeptes zur Herstellung ultradünner, mikrostrukturierter Membranen, die als mechanische Grundlage der Membran-Elektroden-Einheit dienen sowie die Entwicklung eines Verfahrens zur Integration eines Protonen leitenden Ionomers in die Mikrostruktur der Membranen. Zum anderen werden verschiedene Elektrodenkonfigurationen hergestellt und untersucht. Dabei kommen neben verbreiteten Verfahren wie der Aufnahme von Polarisationskurven und elektrochemischer Impedanzspektroskopie auch spezialisierte Messmethoden wie die elektrochemische Rasterkraftmikroskopie zum Einsatz, mit deren Hilfe die Protonenleitfähigkeit entlang der einzelnen Mikrokanäle der Protonenleitmembran bestimmt werden kann.

Im letzten Abschnitt der Arbeit wird untersucht, inwieweit sich das Konzept der siliziumbasierten Membran-Elektroden-Einheiten im Bereich der Hochdurchsatzmethoden zur Materialentwicklung einsetzen lässt. Dazu wird ein Versuchsaufbau realisiert, bei dem verschieden aufgebaute Membran-Elektroden-Einheiten in einer speziell angefertigten Versuchskammer unter definierten Bedingungen eine Brennstoffzellenreaktion durchlaufen und die entstehende Reaktionswärme mittels emissionskorrigierter Infrarot-Thermographie untersucht wird. Durch Nutzung des neuartigen, ultradünnen Aufbaus der Mikro Membran-Elektroden-Einheiten kann auf der einen Seite eine große Anzahl verschiedener Elektrodenkonfigurationen hergestellt werden. Auf der anderen Seite lässt sich durch die geringe Dicke der Membranen die Reaktionswärme mit hoher Genauigkeit den einzelnen Elektrodenkonfigurationen zuweisen. Dies ermöglicht Rückschlüsse auf die Leistungsfähigkeit der Elektroden.

## Abstract

Portable electronic devices like smartphones, tablet PC's or wearables have become an essential part of everyday life. Continuous integration of more features like GPS or Bluetooth has led to significant technical improvements and convenience, but also to increased energy requirements. However, the development of new battery technologies with higher energy density is lacking behind which results in lower usage duration between single recharge cycles. Hence, the identification of alternative technologies is crucial for future success of portable, connected devices, especially in the field of the internet of things.

The development of innovative micro fuel cells may be an interesting approach to reach the goal of high energy capacity with minimal volumetric requirements. For this, it is mandatory to find solutions for miniaturization of the fuel cell. In this thesis, essential concepts for fabrication of silicon-based micro electrode membrane assemblies are developed with a focus on applicability of mass fabrication. On the one hand, this includes the design of a concept to manufacture ultra-thin, microstructured membranes which serve as mechanical basis for the membrane electrode assemblies as well as development of a process to integrate a proton conducting ionomer into the microstructure of the membrane. On the other hand, different electrode configurations were realized and characterized in detail. This includes the use of established methods like measurement of polarization curves and the use of electrochemical impedance spectroscopy, but also the application of specialized characterization methods, namely electrochemical atomic force microscopy which makes it possible to validate the proton conductivity of single micro channels of the proton conducting membrane.

The last part of the thesis investigates the potential of silicon-based micro membrane electrode assemblies to be used in high throughput material research. An experimental setup was designed, manufactured and assembled which allows initiating a fuel cell reaction under defined ambient conditions on a number of different electrode configurations. The electrodes are characterized regarding their heat of reaction with the help of emissivity corrected infrared spectroscopy. Because of the utilization of semiconductor processes, it is possible to manufacture a large quantity of varying electrode configurations. At the same time, the ultra-thin design of the micro membrane electrode assemblies makes it possible to allocate the origin of the heat of reaction precisely. This allows to evaluate different electrodes in parallel and to draw conclusion regarding the effectivity of the fuel cell reaction.

## Table of contents

Zusammenfassung.....	vi
Abstract .....	vii
Nomenclature.....	x
List of figures .....	xv
List of tables .....	xix
1 Motivation.....	1
2 Fundamentals of polymer electrolyte membrane fuel cells .....	4
2.1 Electrochemical fundamentals.....	5
2.2 Overpotentials in fuel cells.....	7
2.3 Components of membrane electrode assemblies .....	10
2.3.1 Polymer membrane.....	10
2.3.2 Catalyst layer .....	12
2.3.3 Current collector.....	17
3 Bringing fuel cells to low power and portable applications .....	18
3.1 Concepts for micro membrane electrode assemblies.....	18
3.2 Sputtered catalyst layers and current collectors for micro fuel cell applications.....	24
3.3 Integration of $\mu$ MEAs into micro fuel cell systems .....	27
4 Characterization methods.....	30
4.1 Cyclic voltammetry.....	30
4.2 Polarization curves .....	31
4.2.1 Test package and experimental setup.....	32
4.3 Electrochemical Impedance Spectroscopy.....	34
4.4 Electrochemical atomic force microscopy (EC-AFM) .....	39
4.5 Kelvin probe resistance measurements .....	40
5 Concept of a micro membrane electrode assembly .....	41
5.1 Design.....	41
5.2 Fabrication process .....	43

5.3	Integration of polymer electrolyte .....	46
5.3.1	Identification of suitable electrolyte dispersion.....	46
5.3.2	Dip Coating process for integration of electrolyte .....	49
6	Characterization of MEMS-based $\mu$ MEAs .....	53
6.1	Sputter coated bifunctional Cr-/Pt-layer.....	54
6.1.1	Evaluation of the sputter parameters for optimized electrode performance .....	54
6.1.2	Fuel Cell operation .....	58
6.2	Additional spray coated, porous catalyst layer .....	64
6.3	Evaluation of the $\mu$ MEA via EC-AFM .....	67
6.4	Electrically conductive catalyst layer.....	73
6.4.1	Percolation theory.....	74
6.4.2	Enhancing electrical conductivity of the catalyst layer with Carbon Nano Tubes .....	76
6.4.3	Characterization of electrically conductive catalyst layers in $\mu$ MEAs .....	82
6.4.4	Electrodeposition of Pt inside the catalyst layer.....	83
6.5	Summarizing considerations on MEMS-based $\mu$ MEAs.....	89
7	Combining micro fuel cells with high throughput methods for catalyst development .....	91
7.1	Combinatorial methods in materials development .....	91
7.2	Infrared thermography for high-throughput screening .....	92
7.2.1	Physical principles of IR-thermography.....	93
7.2.2	IR-thermography for characterization of catalysts and fuel cells .....	95
7.3	Micro fuel cells as basis for high throughput screening.....	96
7.3.1	Design of a reaction chamber for micro fuel cell libraries .....	98
7.4	Validation of IR-thermography by characterization of conventional MEAs.....	100
7.5	Characterization of $\mu$ MEA through IR-thermography.....	104
7.6	Characterization of Pt/Cu alloy micro fuel cell library .....	107
8	Summary and outlook .....	115
	References.....	118

## Nomenclature

### List of abbreviations

μMEA	Micro Membrane Electrode Assembly
A3PE	Amyloid Peptide
AFM	Atomic Force Microscope
APU	Auxiliary Power Unit
CB	Carbon Black
CCGDL	Coated Gas Diffusion Layer
CCM	Catalyst Coated Membrane
CENIDE	Centre for Nanointegration Duisburg-Essen
CHP	Combined Heat and Power
CNT	Carbon Nano Tube
CVD	Chemical Vapor Deposition
DC	Direct Current
DMAC	Dimethylacetamide
DMFC	Direct Methanol Fuel Cell
DRIE	Deep Reactive Ion Etching
EC-AFM	Electrochemical Atomic Force Microscopy
ECAS	Electrochemical Active Surface
ecIRT	emissivity corrected Infrared Thermography
GDL	Gas Diffusion Layer
GNS	Graphene Nano Sheets
GPS	Global Positioning System
HF	Hydrofluoric Acid
HTS	High Throughput Screening
ICP	Inductively Coupled Plasma
IMS Chips	Institute for Microelectronics Stuttgart
IoT	Internet of Things
IR	Infrared

KOH	Potassium Hydroxide
LC-AFM	Local Conductivity Atomic Force Microscopy
MEA	Membrane Electrode Assembly
MEMS	Micro Electro-Mechanical System
MFC	Mass Flow Controller
MFP	Mean Free Path
MPP	Maximum Power Point
MPTMS	3-Mercaptopropyltrimethoxysilane
MWCNT	Multi Walled Carbon Nano Tube
OCV	Open Circuit Voltage
OEM	Original Equipment Manufacturer
ORR	Oxygen Reduction Reaction
PEMFC	Polymer Electrolyte Membrane Fuel Cell
PFSA	Perfluorosulfonic Acid
PTFE	Polytetrafluoroethylene
PVD	Physical Vapor Deposition
RF	Radio Frequency
RFa	Roughness Factor
ROI	Region of Interest
SDC	Scanning Droplet Cell
SECM	Scanning electrochemical microscope
SEM	Scanning Electron Microscope
Si <sub>3</sub> N <sub>4</sub>	Silicon Nitride
SiO <sub>2</sub>	Silicon Dioxide
SOI	Silicon on Insulator
SWCNT	Single Walled Carbon Nano Tube
USB	Universal Serial Bus

## List of symbols

Name	Unit	Description
$\Delta G$	[kJ/mol]	Gibbs free energy
$\Delta H_f$	[kJ/mol]	Enthalpy of formation
$\Delta U$	[V]	Sum of overpotentials in fuel cell
$\Delta U_o$	[U]	Change in open circuit voltage
$\Delta U_a$	[V]	Activation losses
$\Delta U_c$	[V]	Concentration losses
$\Delta U_p$	[V]	Polarization losses
$\Delta U_\Omega$	[V]	Ohmic losses
$\mu_f$		Fuel utilization
$A$	[V]	Constant in activation losses
$A_{geom.}$	[m <sup>2</sup> ]	Geometric area
$c$		Fluid specific constant
$c$	[m/s]	Speed of light
$C_A$		Adsorption coefficient
$c_i$	[mol/m <sup>3</sup> ]	Inorganic molar concentration
$C_R$		Reflection coefficient
$C_T$		Transmission coefficient
$D_{Pt}$	[kg/A s]	Deposition rate of platinum
$e$		Euler constant
$E$	[m <sup>3</sup> /s]	Evaporation rate
$ECAS$	[m <sup>2</sup> ]	Electrochemically active surface
$F$	[C/mol]	Faraday-constant
$g$	[m/s <sup>2</sup> ]	Acceleration of gravity
$h$	[m <sup>2</sup> kg/s]	Planck's constant
$h_L$	[m]	Layer thickness
$i$	[A/m <sup>2</sup> ]	Current density
$I$	[A]	Current
$i_o$	[A/m <sup>2</sup> ]	Exchange current density
$i_o'$	[A/m <sup>2</sup> ]	Current density dominated by oxygen diffusion
$i_c$	[A/m <sup>2</sup> ]	Current density summarizing mass transport
$I_D$	[A]	Deposition current
$i_n$	[A/m <sup>2</sup> ]	Current density resulting from parasitic short circuits



<b>Name</b>	<b>Unit</b>	<b>Description</b>
$i_{ref}$	$[A/m^2]$	Reference current density in catalyst layer
$k_B$	$\frac{m^2 kg}{s K}$	Boltzmann constant
$L$	$[m]$	Width
$l_{ref}$	$[m]$	Reference thickness in catalyst layer
$m$	$[V]$	Empirical constant to determine concentration losses (basis)
$M_b$		Emittance
$m_i$	$[kg]$	Mass of fuel that reacts inside fuel cell
$M_i$	$[kg/mol]$	Molar mass
$m_{Pt}$	$[kg]$	Mass of platinum
$m_r$	$[kg]$	Mass of fuel pushed into fuel cell
$n$		Number of electrons involved in electrochemical reaction
$n$	$[m^2/A]$	Empirical constant to determine concentration losses (exponent)
$\eta$	$[Pa s]$	Viscosity
$N_A$	$\left[ \frac{kg m^2}{s^2 mol K} \right]$	Avogadro constant
$\eta_{max}$		Efficiency
$P$	$[W]$	Power
$p_{H_2}$	$[Pa]$	Partial pressure hydrogen
$p_{H_2O}$	$[Pa]$	Partial pressure water vapor
$p_{O_2}$	$[Pa]$	Partial pressure oxygen
$P_r$	$[W]$	Radiation power
$Q_H$	$[C]$	Charge
$r$	$[\Omega m]$	Resistivity
$R$	$[\Omega]$	Resistance
$RFa$		Roughness factor
$T$	$[K]$	Temperature
$t$	$[s]$	Time
$T$	$[K]$	Temperature
$U$	$[V]$	Cell voltage
$u$	$[m/s]$	Coating velocity
$\alpha$		Charge transfer coefficient
$\alpha_i$		Volume fraction
$\gamma_{LV}$	$[N/m]$	Surface tension

<b>Name</b>	<b>Unit</b>	<b>Description</b>
$\varepsilon$		Emissivity
$\lambda$		Stoichiometry
$\lambda_R$	[m]	Wavelength of radiation
$\rho$	[kg/m <sup>3</sup> ]	Density
$\rho_{el}$	[ $\Omega$ m]	Specific electrical resistance
$\sigma$	[W/m]	Stefan Boltzmann constant
$\sigma'$	[S/m]	Proton conductivity
$\Phi$	[W/m <sup>2</sup> ]	Heat flow
$\varphi$	[SLM/A]	Specific volumetric flow
$\Phi_A$	[W/m <sup>2</sup> ]	Adsorbed heat flow
$\varphi_{mol}$	$\left[\frac{mol}{A \cdot s}\right]$	Molar flow
$\Phi_R$	[W/m <sup>2</sup> ]	Reflected heat flow
$\Phi_T$	[W/m <sup>2</sup> ]	Transmitted heat flow
$\varphi$		Emissivity

## List of figures

Figure 1: Development of connected devices in the near future	1
Figure 2: Energy requirements vs. battery size and battery energy density	2
Figure 3: Comparison of energy densities	2
Figure 4: JAQ™ Hybrid micro fuel cell recharging device by myFC	3
Figure 5: FCgen®-micro fuel cell stack by Ballard systems for recreational and portable applications.	3
Figure 6: Principle structure of a membrane electrode assembly (MEA)	5
Figure 7: Typical polarization curve of a PEMFC with different overpotentials depending on applied current	7
Figure 8: Chemical structure and different conduction mechanisms in PFSA polymer	11
Figure 9: Basic principle of using catalysts by decreasing the activation energy	13
Figure 10: Exchange current density vs. binding energy of hydrogen to metal	14
Figure 11: Basic drawing of the catalyst layer	15
Figure 12: Choice of optimal catalyst layer thickness depending on current density	16
Figure 13: Basic sketch of a micro MEA with silicon electrodes and integrated PEM sheet	19
Figure 14: Silicon micro MEA based on a free-standing, micro porous membrane	19
Figure 15: Silicon micro MEA based on a free-standing membrane with uniform array of micro channels	19
Figure 16: Principle drawing of ionomer integration into micro channels	22
Figure 17: SEM-image of Ionomer filled micro channels	22
Figure 18: Zone diagram of layer morphology depending on substrate temperature and Argon pressure	25
Figure 19: SEM-image of sputtered Pt catalyst layer on PFSA (Nafion®) substrate with varying thickness	26
Figure 20: SEM-images of Pt catalyst layers that show the influence of Argon sputter pressure	27
Figure 21: Sketch of vertical fuel cell stack and planar fuel cell stack	28
Figure 22: Comparison of mass and volume specific energy density for different hydrogen carriers	29
Figure 23: Cyclic voltammogram of Pt	30
Figure 24: Technical drawing of the final test package	33
Figure 25: Cross-sectional view of the final test package	33
Figure 26: Basic drawing of the test setup	34
Figure 27: Equivalent circuit for interpretation of AC impedance measurements	36
Figure 28: Nyquist plot of equivalent circuit described in Figure 27	36
Figure 29: Equivalent circuit of a membrane-electrode-assembly	37
Figure 30: Resulting Nyquist plot of EIS measurement in membrane electrode assemblies	37
Figure 31: Principle drawing of the measurement setup for electrochemical atomic force microscopy	39
Figure 32: Principle of ratiometric measurement of an Ohmic resistance $R_s$	41
Figure 33: Principle of Kelvin resistance measurements of an Ohmic resistance $R_s$	41
Figure 34: Basic drawing of the new $\mu$ MEA concept	42
Figure 35: Sputter deposition of catalyst layer/current collector	42
Figure 36: Fabrication process of the micro membrane	43
Figure 37: Back side of the substrate after defining the membrane areas inside the $Si_3N_4$	44

Figure 38: Front side of the substrate after structuring of the micro channels _____	44
Figure 39: SEM image of the double SOI wafer etched anisotropically down to the buried SiO <sub>2</sub> layer _____	45
Figure 40: SEM image of isotropically etched of SiO <sub>2</sub> layer for creating undercut structure _____	45
Figure 41: SEM image of resulting micro channels with buried undercut structure _____	46
Figure 42: Image of a 10x20 mm <sup>2</sup> micro membrane with 5 mm solid edge _____	46
Figure 43: Fumion® FLA on membrane surface _____	47
Figure 44: Fumion® FLNA on membrane surface _____	47
Figure 45: Fumion® FLN on membrane surface _____	47
Figure 46: Water on membrane surface as reference measurement _____	47
Figure 47: SEM image of PFSA polymer integrated into micro membrane by drop coating process _____	48
Figure 48: Sketch of the principle emergence of the coffee-ring effect _____	48
Figure 49: PFSA dispersion (Fumion® FLNA) dried in a vacuum chamber _____	48
Figure 50: PFSA dispersion (Fumion® FLNA) dried on a hotplate at 50°C _____	48
Figure 51: Principle drawing of the dip-coating process for a porous membrane _____	49
Figure 52: Photo of a membrane where the PFSA was integrated by dip-coating process _____	49
Figure 53: Photo of the final dip coater which was designed and assembled at ZBT _____	51
Figure 54: Film thickness as a function of withdrawal speed for two different PFSA dispersions _____	53
Figure 55: Sketch of the measurement setup for characterization of the sputter deposited Pt-layers _____	55
Figure 56: SEM image of a Pt-layer sputter coated at $4.3 \times 10^{-3}$ mbar _____	55
Figure 57: SEM image of a Pt-layer sputter coated at $1.9 \times 10^{-1}$ mbar _____	55
Figure 58: Cyclic voltammograms of 6 layers with 3 varying sputter pressures and layer thickness of 50 nm _____	56
Figure 59: Cyclic voltammograms of 6 layers with 3 varying thicknesses, deposited at $1.9 \times 10^{-1}$ mbar _____	57
Figure 60: Polarization curve of a $\mu$ MEA that was fabricated by drop coating _____	59
Figure 61: Polarization curve of a $\mu$ MEA that was fabricated by dip coating _____	60
Figure 62: EIS spectra and simulated fits of dip-coated $\mu$ MEA at different current densities _____	62
Figure 63: SEM-image of the $\mu$ MEA with porous catalyst layer _____	64
Figure 64: Effect of adding a porous catalyst layer onto the surfaces of the $\mu$ MEA _____	65
Figure 65: EIS spectra and simulated fits of a $\mu$ MEA with a spray coated catalyst layer _____	66
Figure 66: Sketch of prepared sample for EC-AFM _____	68
Figure 67: AFM image of surface topography of $\mu$ MEA (source: Esslingen University of Applied Science) _____	69
Figure 68: Measured proton current of $\mu$ MEA on area with no spray coated additional catalyst layer _____	69
Figure 69: Geometrical information of silicon membrane front side _____	69
Figure 70: Corresponding measurements of proton current on surface of $\mu$ MEA _____	69
Figure 71: AFM measurement result of topography on a single micro channel _____	70
Figure 72: Combined EC-AFM measurement result of topography and proton current on a micro channel _____	70
Figure 73: AFM measurement result of topography on membrane surface with relatively low residual layer thickness _____	71
Figure 74: Measurement result of proton current on membrane surface with relatively low residual layer thickness _____	71

Figure 75: Combined EC-AFM image showing topography and proton current of $\mu$ MEA _____	71
Figure 76: Combined EC-AFM image of topography and proton current of a single micro channel _____	71
Figure 77: EC-AFM image of proton current on surface of $\mu$ MEA with significant residual layer _____	72
Figure 78: Combined EC-AFM image of topography and proton current on surface of $\mu$ MEA with significant residual layer _____	72
Figure 79: Theoretical pathway of an electron at the anode of a conventional MEA using an electronically highly conductive gas diffusion layer _____	74
Figure 80: Theoretical pathway of an electron at the anode of a silicon-based $\mu$ MEA _____	74
Figure 81: Schematic influence of filler particles in catalyst layers on electric conductivity _____	76
Figure 82: Fabrication process of catalyst layers with CNT add-ins _____	77
Figure 83: Microscopy images of the catalyst samples with 15 spray coated single layers each and varying amounts of CNT at 20-fold magnification _____	78
Figure 84: SEM-image of spray coated catalyst layer (10,000 fold magnification) with 10 wt% CNT exhibiting a thickness of 6.5 $\mu$ m (according to 10 single coating steps) _____	79
Figure 85: Detailed view of catalyst layer at 50,000 fold magnification _____	79
Figure 86: Specific electrical resistivity in $\Omega$ cm correlating to CNT content _____	80
Figure 87: Cyclic voltammogram of catalyst layers without CNT and with 15 wt% CNT _____	82
Figure 88: Polarization curves of two different $\mu$ MEAs with different CNT loading _____	83
Figure 89: Sketch of principle setup for galvanic deposition of Pt on catalyst layer and photo of the actual deposition setup _____	84
Figure 90: SEM image of the catalyst layer after galvanic deposition of Pt _____	86
Figure 91: EDX measurement of the catalyst layer showing the distribution of the deposited Pt _____	86
Figure 92: Detailed image of the catalyst layer near surface at 50,000 fold magnification _____	86
Figure 93: Photo of a $\mu$ MEA after galvanic deposition of Pt for 840 s at 30 mA _____	86
Figure 94: Electrochemical performance of the $\mu$ MEA with electrodeposited Pt compared to bare catalyst layer with CNTs only _____	87
Figure 95: Electrochemical characterization of operating $\mu$ MEA with electrodeposited Pt through EIS and corresponding simulation fits _____	88
Figure 96: Process flow of a high-throughput catalyst optimization from validation to commercialization _____	92
Figure 97: Distribution of heat flow in an arbitrary body _____	93
Figure 98: Emittance vs. wavelength for different temperatures calculated with the help of Planck's law _____	94
Figure 99: Heat dissipation of two different fuel cells at a constant current density $I_m$ _____	96
Figure 100: Heat dissipation of two different fuel cells at a constant potential $U_m$ _____	96
Figure 101: Principle setup of high throughput screening based on micro fuel cells _____	98
Figure 102: Schematic illustration of the reaction chamber _____	98
Figure 103: Photo of the final test setup _____	99
Figure 104: Photo of the thin metal grid for current collection (a), the MEA (b) and the two components integrated into the measurement chamber _____	101
Figure 105: Typical image of the IR-camera while the MEA is operating _____	101

Figure 106: Polarization curve of the conventional MEA for 76°C and 90 % RH	102
Figure 107: IR image of the reaction chamber with condensated water on the ZnSe window	102
Figure 108: Polarization curves of the MEA at 81°C for different levels of humidification	103
Figure 109: Polarization curves of the MEA with 75 ml/min humidification process (1 h) for 2 different temperatures	103
Figure 110: Increase in temperature of the MEA depending on the applied current density for different levels of humidification according to polarization curves shown in Figure 108	103
Figure 111: Relative increase in temperature of the MEA depending on the applied current density for different operating temperatures of the chamber according to polarization curves shown in Figure 109	103
Figure 112: Increase in temperature of the MEA depending on the applied potential for different levels of humidification according to polarization curves shown in Figure 108.	103
Figure 113: Increase in temperature of the MEA depending on the applied potential for different temperatures of the chamber according to polarization curves shown in Figure 109	103
Figure 114: Photo of the $\mu$ MEA inserted into the measurement chamber	105
Figure 115: IR image of the inserted $\mu$ MEA	105
Figure 116: IR image of the measurement chamber including the observation points and the ROI	106
Figure 117: Absolute temperature averaged over ROI over time	106
Figure 118: Relative change in temperature of the observation points depending on the applied current	107
Figure 119: Relative change in temperature of the observation points depending on the applied current including the subtraction of the relative temperature increase of the flange (reference point J)	107
Figure 120: Schematic illustration of the fabrication process for porous alloy catalyst layer	107
Figure 121: Result of EDX measurement of materials library	108
Figure 122: Result of EDX thickness measurements of the materials library	108
Figure 123: Illustration of the SDC as used for electrochemical characterization of the materials library	109
Figure 124: Results of the 1 <sup>st</sup> CV scan of each sample of the materials library	110
Figure 125: Results of the 200 <sup>th</sup> CV scan of each sample of the materials library	110
Figure 126: Diagram showing only the results of the CV scans with stable Pt signal	111
Figure 127: Position of the samples on the materials library	111
Figure 128: Result of EDX measurement of the micro fuel cell library	112
Figure 129: Photo of the final micro fuel cell library (left) and integration of the library into the measurement chamber (right)	112
Figure 130: Polarization curve of the micro fuel cell library	113
Figure 131: Absolute temperature of the micro fuel cell library over time	113
Figure 132: Relative changes in temperature of the single micro fuel cells	114

## List of tables

Table 1: Overview of achieved performance for silicon-based micro membrane electrode assemblies _____	24
Table 2: Overview of PFSA dispersions tested for applicability in silicon-based micro MEA _____	47
Table 3: Overview of applied sputter conditions for deposition of Cr-/Pt-layer _____	54
Table 4: Overview of the resulting roughness factors and ECAS depending on layer thickness and sputter pressure. _____	58
Table 5: Parameters of the equivalent circuits in ZView for each result of the EIS measurement _____	63
Table 6: Composition of the spray coated catalyst layer _____	64
Table 7: Parameters of the equivalent circuits in ZView for each result of the EIS measurements: a constant model containing anode and cathode equivalent circuit can be applied _____	67
Table 8: Composition of manufactured catalyst layers with varying amount of CNT _____	77
Table 9: Overview of specific electrical resistivity of 10 sample which were fabricated identically _____	81
Table 10: Parameters of the equivalent circuits in ZView for each result of the EIS measurements: a second CPE is added to take polarization of the cathode at low frequencies into consideration _____	89





# 1 Motivation

In modern society consumer electronics have become of tremendous importance. Especially portable devices have found their way into everyday life. A reason for this development can be found in the occurrence of the internet which gave people the possibility to connect with each other around the world. Along with that a strong need for portable internet devices arose. Smartphones, tablet PCs, wearables and mobile audio speakers are all part of the Internet of Things (IoT) which enables society to take advantage of staying connected, even if people are not at home. Figure 1 shows the development of different internet devices today and in the near future. It is estimated that there will be 28 billion connected devices by 2022.

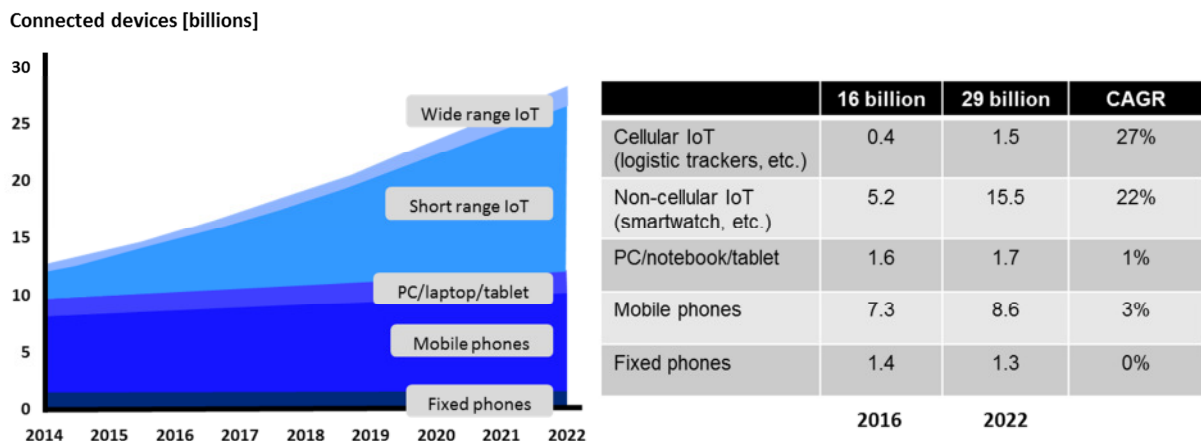


**Figure 1: Development of connected devices in the near future; connected devices will reach a quantity of 28 billion in 2021 with remarkable compound annual growth rates (CAGR) [according to Ericsson mobility report 2017]**

One major drawback for mass market applications of mobile electronic devices can be found in their energy supply. Customers expect one week of normal use before battery has to be recharged. But as the number of functions and with it the energy consumption has continuously increased, battery capacity has almost stagnated (cf. Figure 2). The integration of HD-displays, cameras, audio boxes, sensors, WiFi connection or GPS modules allow innovative mobile applications but are energy intensive and decrease the time of use dramatically [1] [2].

Moreover, the customer requirement for miniaturized and light devices limits the possibility to increase the size of the battery and by that the total capacity. Hence, new technologies with higher energy densities and faster recharging capabilities have to be developed.

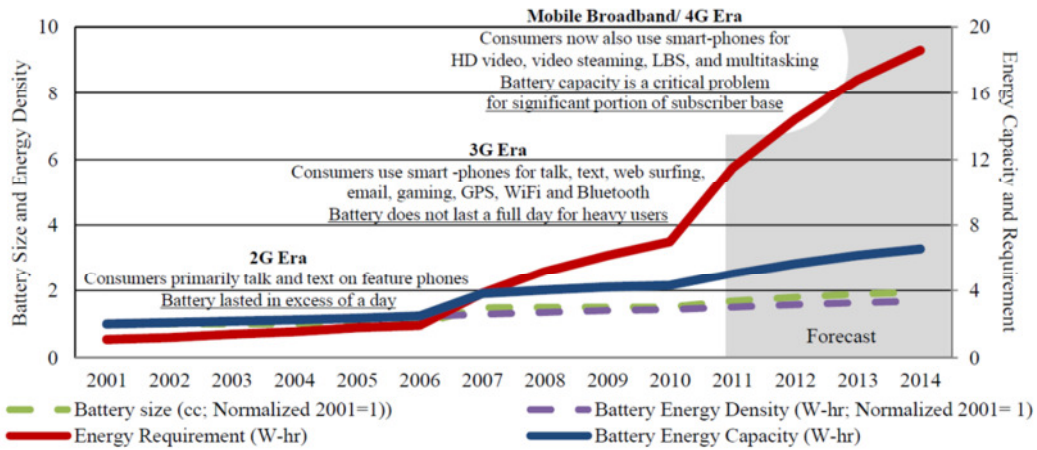


Figure 2: Energy requirements vs. battery size and battery energy density; the introduction of new technologies leads to gap between energy requirements and supply [2].

Besides supercapacitors and energy harvesting devices, micro fuel cells are promising candidates to fulfil the requirements mentioned above. Figure 3 gives information about the energy densities of different technologies in comparison to fuel cells. While higher energy densities lead to longer usage times improved power densities enable better accelerations for high power applications. It becomes obvious that fuel cells – depending on the hydrogen carrier that is used – offer energy densities that are at least two times higher than conventional lithium ion batteries. The option to use hydrogen stored in carbon hydrides, like methanol or ethanol, which are liquid at room temperature and can be handled easily makes it possible to recharge the devices fast by replacing the cartridge. Alternatively, the hydrogen may be stored in metal hydrides that can be recharged fast. Their independence from electrical outlets is another advantage, especially for outdoor applications [3] [4] [5].

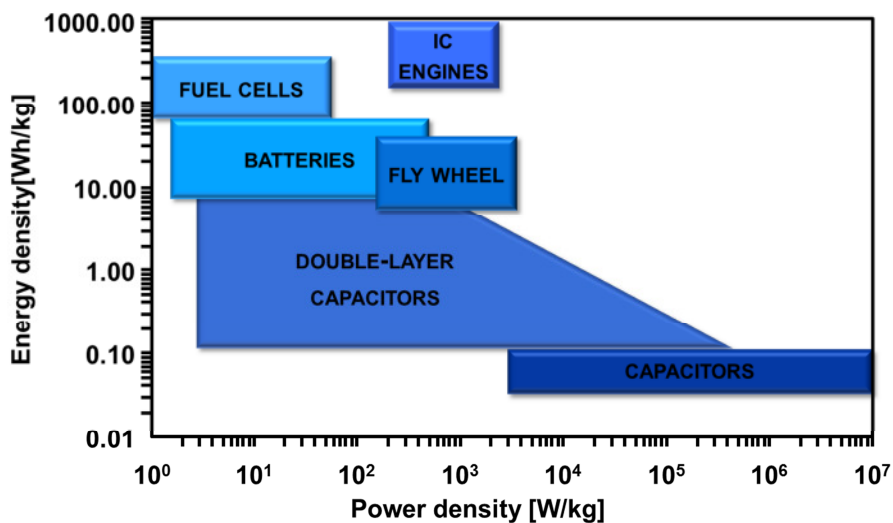


Figure 3: Comparison of energy densities; fuel cells offer high energy density at low to moderate power densities (according to [4] and [5]).

With those benefits in mind it is not surprising that the first products based on micro fuel cells have been introduced to the market. The main target market of these products is recharging devices [6]. Figure 4 and Figure 5 show two examples for such devices. Manufacturers like myFC have developed end user products while Ballard Power Systems is offering a micro fuel cell stack for original equipment manufacturers (OEM). Usually, the electronic devices that need to be recharged can be connected via USB ports (cf. Figure 4).



Figure 4: JAQ™ Hybrid micro fuel cell recharging device by myFC [[www.myfcpower.com](http://www.myfcpower.com)].



Figure 5: FCgen®-micro fuel cell stack by Ballard systems for recreational and portable applications.

Looking at the micro fuel cell stack in Figure 5, it is obvious that conventional fuel cell stack designs are not suitable for direct integration into consumer electronics like smartphones, because of their thickness and the complex assembly that does not correlate with modern mass production in consumer electronics. Hence, it would be more desirable to develop solutions of micro fuel cells that can be integrated into portable devices without drawbacks regarding thickness or assembly time and costs.

Smartphones are the most important portable device today. People can use them to communicate, to get information from the internet, to find their way or to take photos. A common design element of these devices is that they need to be as flat as possible. This is because users usually carry smartphones in their pockets and do not want to be bothered by the device, on the one hand. On the other hand, the size of the screen needs to be big enough for convenient viewing. So, developing flat devices can be an important sales argument for the manufacturers. For the development of applicable micro fuel cells this means that their thickness needs to be minimized as well.

Therefore, advances in miniaturization have to be achieved. This can be realized by the application of microsystem technologies. New fuel cell concepts that transfer the components of conventional fuel cells into microsystem components as well as innovative materials and fabrication methods have to be identified. Hence, the purpose of this thesis is to develop a micro membrane electrode assembly

( $\mu$ MEA) that is small in size, has a high power density and can be fabricated by mass production technologies of semiconductor industry. Therefore, widely established semiconductor processes will be used in order to replace conventional fuel cell components like the ionomer membrane and the gas diffusion layer.

Moreover, the potential for applying micro fuel cells in high throughput screening will be evaluated within this thesis as micro fuel cell offer advantages according to temperature control, parallelization and material consumption. Thus, combining micro fuel cells and emissivity corrected infrared thermography for the characterization of fuel cell libraries is the second goal that is addressed with this thesis.

## 2 Fundamentals of polymer electrolyte membrane fuel cells

The first proof of the working principle of a fuel cell was achieved by Sir William Grove in 1839, when he successfully showed in an experimental setup that bringing hydrogen and oxygen in contact with a platinum wire which is placed in an acid electrolyte creates a small current [7]. After that it took more than a hundred years before fuel cells attracted interest again with their first application within the Apollo project in the 1960's.

Today, fuel cells are at the barrier of commercial launch in several applications: vehicles like cars, buses or fork lifters, combined heat and power (CHP) and auxiliary power units (APU) have already been operated with fuel cells for energy conversion. The reason for targeting these applications is that fuel cells combine the high volumetric energy density of chemical fuels with a high conversion efficiency of up to 90 % if the generated heat is used as well.

Along with the rapid technological progress in microsystem technology throughout the 1990's, also portable and micro fuel cells have gained interest for their use as back-up power or as a potential replacement of conventional batteries.

This chapter gives an overview about the fundamentals of fuel cells with a focus on Polymer Electrolyte Membrane Fuel Cells (PEMFC) and the specific characteristics of micro fuel cells.

PEMFCs are low temperature fuel cells that can operate at 20°C – 80°C. This makes them interesting for mobile applications, e. g. in automotive industry or as portable recharger. They use a solid acid polymer as electrolyte which is proton conductive but electrically insulating and impermeable for gases. At the anode side hydrogen serves as fuel and energy carrier while oxygen is utilized at the cathode side. The hydrogen may be produced by industrial cracking, by electrolysis or originate from a reforming process whereas oxygen contained within the ambient air may be used. Figure 6 shows

the basic structure of a conventional membrane electrode assembly (MEA), which consists of the solid membrane, a porous catalyst layer and a porous carbon cloth. This cloth acts as current collector as well as for gas distribution which is why it is also referred to as gas diffusion layer (GDL).

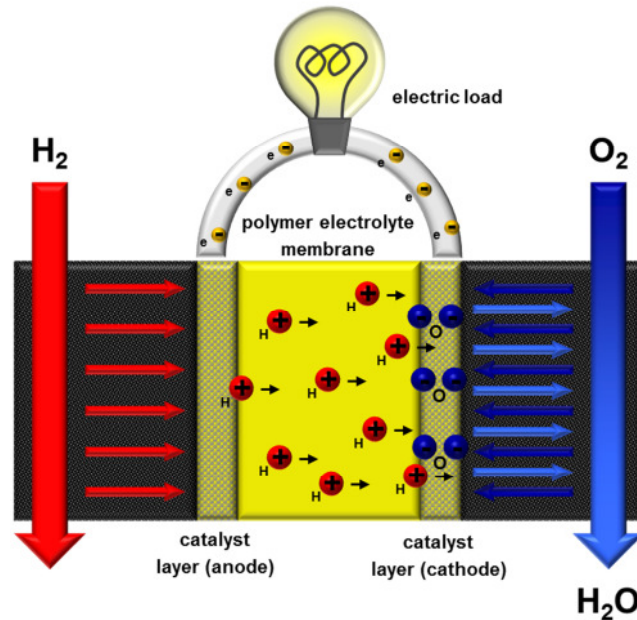


Figure 6: Principle structure of a membrane electrode assembly (MEA); main components are anode, cathode and electrolyte membrane.

## 2.1 Electrochemical fundamentals

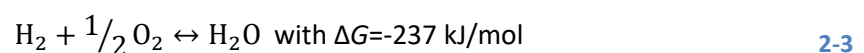
As mentioned above, PEMFCs belong to the group of acid electrolyte fuel cells. This means that hydrogen is oxidized at the catalyst of the anode:



At the catalyst of the cathode oxygen is reduced and reacts with the incoming electrons to form O<sup>2-</sup> ions. These react with the incoming protons to water in an exothermal reaction:



While the protons (H<sup>+</sup>) migrate through the electrolyte from the anode to the cathode, the electrons move through an external electrical circuit where they can be used in an electrical load. As a sum the overall reaction of a PEMFC is:



$\Delta G$  is called the Gibbs free energy change, which is directly related to the change of the open circuit voltage  $\Delta U_0$  of the fuel cell:

$$\Delta G = -nF\Delta U_0 \quad 2-4$$

As  $n$  is the number of electrons involved in the reaction and  $F$  refers to the Faraday-constant ( $F = 96487 \text{ C/mol}$ ) the reversible open circuit voltage (OCV) of a  $\text{H}_2/\text{O}_2$  fuel cell operating at standard conditions ( $25^\circ\text{C}$ ,  $0.1 \text{ MPa}$ ) may be calculated:

$$\Delta U_0 = \frac{\Delta G}{-nF} = 1,23 \text{ V} \quad 2-5$$

In order to be able to make a scientific statement about the efficiency of a PEM fuel cell one has to discuss the term “efficiency” first. A common way is to define the so-called “thermodynamic efficiency” as the relation between the electrical energy produced per mole of fuel and the enthalpy of formation  $\Delta H_f$ , which describes the amount of energy released in case the fuel would be burnt. The necessary values have been determined in experiments and can be taken from literature. In fuel cells the electrical energy equals to the Gibbs free energy change  $\Delta G$ . For hydrogen  $\Delta H_f$  equals  $-285.84 \text{ kJ/mol}$ . This also includes the energy that is released when the product water is precipitated back to the liquid phase. Hence, the thermodynamic efficiency  $\eta_{max}$  of a PEMFC can be calculated as following:

$$\eta_{max} = \frac{\Delta G}{\Delta H_f} \cdot 100 \% \quad 2-6$$

The values of  $\Delta G$  and with that those of the OCV as well as the thermodynamic efficiency vary with the operating temperature. For a PEMFC working at  $25^\circ\text{C}$   $\eta_{max}$  is  $83 \%$ . However, increasing the temperature leads to a loss in thermodynamic efficiency. In practice, these losses will not be observed due to the fact that overpotentials which occur throughout operation are usually minimized at higher temperatures (cf. chapter 2.2) [8]. Hence, overall efficiency will increase with increasing temperature although thermodynamic efficiency is reduced.

Not only the temperature but also the partial pressures of the fuel and product gases influence the Gibbs free energy change by changing the chemical activity. This correlation can be summarized with the help of the Nernst equation which gives information about the cell voltage  $U$  depending on the partial pressures:

$$U = U_0 + \frac{RT}{nF} \ln \left( \frac{p_{\text{H}_2} p_{\text{O}_2}^{1/2}}{p_{\text{H}_2\text{O}}} \right) \quad 2-7$$

When hydrogen and oxygen are converted to water vapor their partial pressures decline which results in a reduction of the cell voltage. In case only pure hydrogen and oxygen are used, the partial pressures correlate to the total pressures.

In contrast to that the percentage of fuel gas that is utilized at the electrodes should be as high as possible. This is defined as the so-called fuel utilization coefficient  $\mu_f$ :

$$\mu_f = \frac{m_r}{m_i} \quad 2-8$$

The terms  $m_r$  and  $m_i$  represent the mass of fuel that enters the fuel cell on the one hand and the mass of fuel which reacts inside the fuel cell, on the other hand.

For optimal operation the partial pressures of the fuel gases and the fuel utilization coefficient have to be taken into consideration and balanced carefully [8]. In micro fuel cells this might not be possible in many applications as atmospheric pressures need to be used at the electrodes due to application constraints.

## 2.2 Overpotentials in fuel cells

The Nernst equation describes the characteristics of the cell voltage under reversible conditions. However, several energy losses occur during fuel cell operation. Some energy is transformed into heat and does not contribute to the electrical performance anymore. Such an irreversibility of energy loss is called overpotential. Hence, it is essential to consider the overpotentials inside fuel cells for the development of  $\mu$ MEAs and to minimize them in order to achieve an optimized electrical performance and high efficiency.

Figure 7 illustrates the effects of different kinds of overpotentials depending on the current density applied to the fuel cell. The total loss  $\Delta U$  can be defined as a sum of the individual overpotentials:

$$\Delta U = \Delta U_p + \Delta U_a + \Delta U_\Omega + \Delta U_c \quad 2-9$$

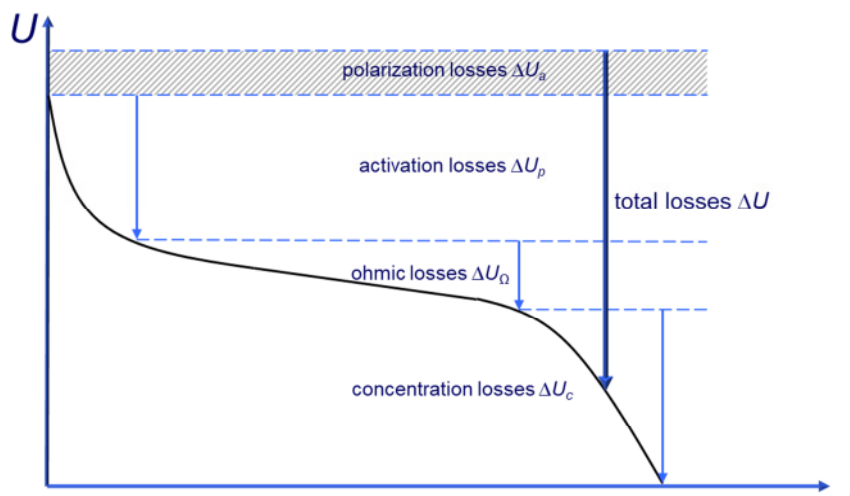


Figure 7: Typical polarization curve of a PEMFC with different overpotentials depending on applied current

Four major losses can be identified:

- Activation losses  $\Delta U_a$
- Polarization losses  $\Delta U_p$
- Ohmic losses  $\Delta U_\Omega$
- Concentration losses  $\Delta U_c$

**Activation losses** originate from the reaction kinetics on the surface of the electrodes. They can be described with the help of the Tafel equation:

$$\Delta U_a = A \ln\left(\frac{i}{i_0}\right) \text{ with } i > i_0 \quad 2-10$$

It can be shown that the constant  $A$  is defined as:

$$A = \frac{N_A T}{2\alpha F} \text{ with } 0 < \alpha < 1 \quad 2-11$$

with  $\alpha$  being the so-called charge transfer coefficient which describes the rate of an electrochemical reaction going through its transition state at the boundary between electrode and electrolyte. It can take values between 0 and 1, depending on the reaction and the electrode material. In case of  $\alpha = 0$  the reaction is dominated by the reactants whereas in case of  $\alpha = 1$  the reaction kinetics are shifted to the product. In hydrogen electrodes,  $\alpha$  usually exhibits a value of 0.5 [8]. The constant  $A$  increases with slower reactions which means that a rise in temperature should result in slowing down the reaction. This is not the case as the so-called exchange current density  $i_0$  is far more dominant. It describes the amount of electrons that are exchanged between electrolyte and electrode at zero net current ( $I=0$  A) as the reaction at the electrodes represents a dynamic equilibrium of the reactants and the products. Its value increases at higher temperatures and by that accelerates the reaction.

For anode and cathode  $i_0$  differs significantly. The reaction at the cathode is up to  $10^5$  times slower for low temperature fuel cells like PEMFCs. Hence, the activation losses at the cathode are dominant for the overall reaction. However, it is essential to maximize  $i_0$  which can be realized by certain methods: Besides an increase in temperature the choice of the electrode material and its specific surface (porosity) play important roles (cf. chapter 2.3.2). Having the Nernst-equation in mind, it is also advantageous to increase the concentration (the partial pressure) of the oxygen and the total pressure inside the fuel cell because the accessibility of the reactants to the electrodes is facilitated.

**Polarization losses** occur from fuel crossover of hydrogen molecules to the cathode and parasitic electrical short circuits that generate internal currents even at OCV. These internal currents are also called mixed potentials and cause severe drops of the cell voltage at low current densities. This effect



can be described by adding a term  $i_n$  to the Tafel equation which describes the current density resulting from these internal short circuits:

$$\Delta U_a + \Delta U_p = A \ln \left( \frac{i + i_n}{i_0} \right) \quad 2-12$$

It is obvious that  $i_n$  is dominant only at small current densities and only for small values of  $i_0$ . Hence, polarization losses are more relevant for low temperature fuel cells.

**Ohmic losses** are the sum of all internal electrical and ionic resistances within the electrodes and the electrolyte that hinder the electrons and protons on their way from the anode to the cathode. Considering Ohm's law these overpotentials can be characterized by a linear proportion:

$$\Delta U_\Omega = ir \quad 2-13$$

with  $i$  being the current density and  $r$  being the specific resistance of the fuel cell. As most electric conductors of the MEA like the GDL are highly conductive the main contribution of  $r$  originates from the electrolyte. This leads to the conclusion that thinner electrolyte membranes exhibit better performance due to lower Ohmic losses. For conventional MEAs this is a challenging task as the membrane also acts as support for the electrodes and electrical short circuits as well as gas crossover need to be avoided.

At high current densities **concentration losses** arise. They originate from mass transport phenomena at the electrodes. The high current densities result in high conversion rates of the reactants which lead to a limited transport of fresh reactants to and evacuation of products from the electrodes. Especially for air-fueled PEMFCs this becomes a crucial challenge as nitrogen – which is not used within the reaction – also blocks the transport of oxygen and product water.

Research on concentration losses showed that they cannot be described properly by physical models, for example the Nernst-equation [8]. A quite common way to deal with this dilemma is to use an empirical approach:

$$\Delta U_c = me^{(ni)} \quad 2-14$$

The constants  $m$  and  $n$  need to be determined by experimental validation of each fuel cell.

Reconsidering equation 2-9 the overall voltage drop can be described as the sum of all overpotentials depending on the current density:

$$\Delta U = A \ln \left( \frac{i + i_n}{i_0} \right) + ir + me^{(ni)} \quad 2-15$$

Accordingly, the cell voltage  $U$  of a PEMFC is determined as:

$$U = U_0 - \Delta U = 1,23 \text{ V} - A \ln\left(\frac{i + i_n}{i_0}\right) - ir - me^{(ni)} \quad 2-16$$

Equation 2-16 describes the mathematical dependence of the cell voltage on the applied current density which leads to the behavior shown in Figure 7: At low current densities the cell voltage shows a logarithmic behavior whereas at moderate current densities the cell voltage drops linearly and at high current densities the voltage drop accelerates exponentially.

## 2.3 Components of membrane electrode assemblies

A MEA consists of three main components which are responsible for ionization of the reactants, transport of the protons and removal, respectively input, of the generated electrons. These components are the proton conducting **polymer membrane** and the porous **catalyst layer** including the **current collector**. At spots where these components congregate with the reaction gases the electrochemical reaction can take place. That is why those spots are called triple phase boundaries. It becomes clear that a maximization of the amount of triple phase boundaries is essential for a good fuel cell performance. Hence, the following paragraphs will discuss the design of MEA components regarding the occurrence of triple phase boundaries.

### 2.3.1 Polymer membrane

The proton conducting polymer membrane of PEMFCs is often described by the term “solid acid” or “ionomer” which refers to functionalized ends of the polymer chains that enable proton conductivity.

The most commonly used material for proton conducting membranes are perfluorosulfonated random copolymers with a tetrafluoroethylene backbone and perfluoroalkyl ether side chains terminated by sulfonic acid groups. These perfluorosulfonic acids (PFSA) were invented by DuPont in the 1960s and marketed under the registered trademark Nafion®. Since then, PFSA has proven to be the best available electrolyte material for PEMFCs.

For synthesis perfluoroalkyl ether side chains are integrated into a polytetrafluorethylen (PTFE) matrix which has high chemical resistance and exhibits strong hydrophobic behavior. After that, the polymer is “sulfonated” which means that  $(\text{SO}_3^-)$  - end groups are added to the side chains. Figure 8 shows a possible configuration of the chemical structure. Depending on the length of the polymer chains different properties regarding proton conductivity and mechanical behavior of the PFSA can be obtained. The ionic ends result in the formation of hydrophilic pores where water is absorbed.

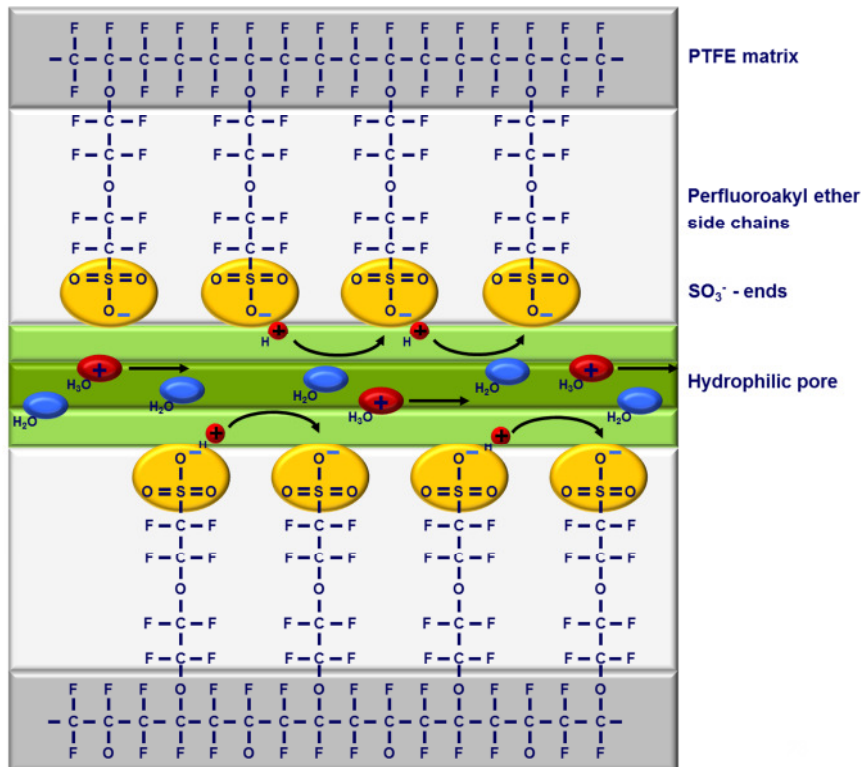


Figure 8: Chemical structure and different conduction mechanisms in PFSA polymer; proton conduction takes place in hydrophilic pores.

This hydration of the PFSA is essential for proton conductivity as through these pores the protons can reach from the anode to the cathode by two major mechanisms of conduction:

- i) Grotthuss mechanism
- ii) En masse diffusion (vehicle mechanism)

Both mechanisms are driven by the electric field between the electrodes and described with the help of the Nernst equation.

The **Grotthuss mechanism** was developed by Theodor Grotthuss (1785-1822) and describes the diffusion of an excess proton through a solvent. In polymer electrolyte membranes this mechanism can be found at the surface of the hydrophilic pores as well as in the adsorbed bulk water that is present inside the pores. At the surface of the pores the protons diffuse along the hydrophilic ( $\text{SO}_3^-$ ) - end groups of the side chains. Due to the high electrostatic bonds of the ( $\text{SO}_3^-$ ) - end groups and the low volumetric fraction where it takes place this mechanism plays a minor role in proton conduction. Accordingly, an excess proton might be "hopping" from one water molecule to another, forming a structural diffusion pathway through the membrane. Temporary  $\text{H}_3\text{O}^+$ , respectively  $\text{H}_5\text{O}_2^+$  and  $\text{H}_9\text{O}_3^+$  ions are generated, passing on a proton to neighboring water molecules. As this mechanism takes place in the bulk water volume of the hydrated pores it is the major driving force in proton conduction and is much faster than en masse diffusion.

**En masse diffusion** differs from the Grotthuss mechanism in that way that  $\text{H}_3\text{O}^+$  ions diffuse all the way through the pore without breaking O-H bonds and exchanging excess protons between water molecules. This is why it is also called the vehicle mechanism [9] [10] [11] [12].

Now, it also becomes evident why it is crucial to operate PEMFCs with PFSA membranes at temperatures below  $100^\circ\text{C}$  as there is an essential need for liquid water to enable proton conduction. The absorption of water into the hydrophilic pores also results in significant swelling of the polymer [12]. In chapter 3.1 it will be explained in detail, why these two effects can be quite challenging regarding the development of a silicon-based micro MEA.

### 2.3.2 Catalyst layer

Another important part of a MEA is the catalyst layer. On the surface of the catalyst material the electrochemical reaction of the fuel cell gases takes place. Typically, the whole catalyst layer consists of a compound made from ionomer and catalytically active, metallic nanoparticles embedded into electrical conductive support materials. Using porous support materials and coating methods like ultrasonic spray coating, high specific surface and porosity are achieved. The effectiveness of the catalyst layer regarding conversion rate determines the overall effectiveness of the fuel cell reaction in a major way, especially at the cathode (cf. chapter 2.2). Hence, the optimization of the catalyst layer should address the following issues:

1. Maximization of the electrochemical active surface (ECAS)
2. Fast transport of protons from catalyst material to ionomer membrane with minor losses
3. Efficient transport of the reactants from and to the catalyst
4. Low electric resistances for effective current collection

In order to achieve these four goals the electrochemical processes that happen at the catalyst particles have to be considered.

In general, the use of a solid catalyst within the gaseous electrochemical reaction decreases the activation energy. The basic mechanism of this so-called heterogeneous catalysis is chemisorption which means that the atoms at the metal surface adsorb a reactant and generate chemical bonds. After that, a chemical reaction takes place and the reactant desorbs again. The peak values of the activation energies used in this reaction, including the formation of at least one intermediate, are smaller compared to the same reaction without the use of catalysts (cf. Figure 9). The kinetics of those reactions strongly depend on the potential energy barrier which correlates to the emerging adsorption enthalpy. This is why especially transition metals are suitable as catalyst materials. They exhibit an incomplete filling of electrons within the d-orbitals and an accordingly low ionization enthalpy [13] [14].

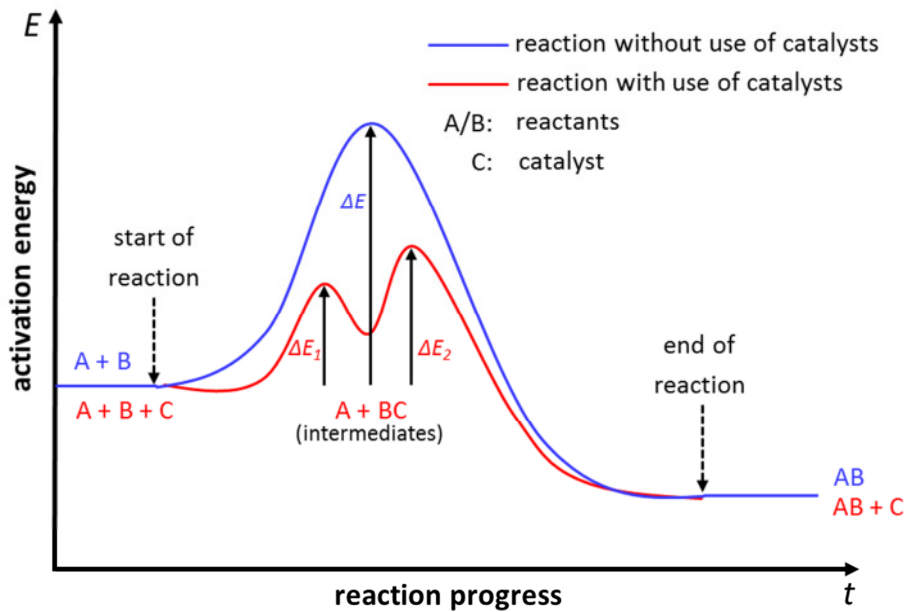


Figure 9: Basic principle of using catalysts by decreasing the activation energy; the formation of intermediates leads to lower activation energy peaks which results in higher possibility of the chemical reaction to happen.

An example for such a transition metal is Platinum (Pt) which is the dominating catalyst material in PEMFCs today. The reason for that can be found by comparing the binding energies of hydrogen for different transition metals with each other: If the binding energy is too strong, the desorption processes are too slow for an effective reaction. In case of the oxygen reduction reaction (ORR) taking place at the cathode this means that the catalyst is oxidized but the following reduction step that is necessary to release oxygen ions and to form  $H_2O$  is hindered. However, if the binding energy is too low, the electron transfer within the reaction cannot take place as the reactant desorbs too quickly. Again this will decrease the effectiveness of the ORR because oxygen atoms at the surface of the catalyst will desorb and form  $O_2$  molecules before they can be reduced to  $H_2O$ .

The correlation between the binding energy and the activity of certain metals can be described by the so-called volcano plot which is shown in Figure 10. By drawing the exchange current density  $i_0$  vs. the binding energy  $E_{M-H}$  it becomes obvious why Pt is the standard catalyst material in PEMFCs. Its specific binding energy represents an optimum, leading to a maximum of the exchange current density within the fuel cell reaction. Compared to metals like silver (Ag) or gold (Au), the binding energy is stronger, so that protons can still be adsorbed by the metal. In comparison to metals like titan (Ti) the binding energy is weaker, so that the reactants can still be desorbed by their reacting agents [15].

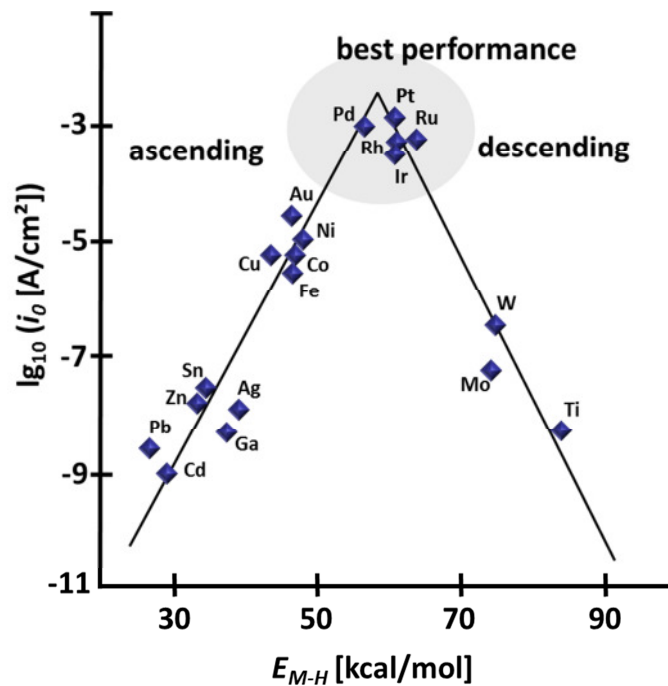


Figure 10: Exchange current density vs. binding energy of hydrogen to metal (according to [15])

With the use of Pt based catalysts the question of costs arises. Throughout the last years, new developments in catalyst research have led to a constant increase in effectiveness of the used Pt which resulted in Pt-loadings as low as  $0.15 \text{ mg}_{\text{Pt}}/\text{cm}^2$  and caused a constant decrease of fuel cell costs down to  $2.300 \text{ \$/kW}$  [16].

As mentioned before, the catalyst layer not only consists of pure catalyst materials. In order to achieve best performance, additional components have to be added. Therefore, PFSA ionomer as well as carbon grains are intermixed with catalyst nanoparticles (cf. Figure 11). This way, efficient proton transfer from the catalyst to the membrane and effective electron conduction to the current collector are realized. Depending on the fabrication process and possible additional components a porous structure can be obtained to provide high specific surface area and porosity resulting in optimized mass transport and minimized reaction limitations (cf. chapter 2.2) [17] [18].

Regarding MEA fabrication it can be distinguished between catalyst coated membranes (CCM) and catalyst coated gas diffusion layers (CCGDL) which depends on whether the catalyst layer is coated onto the polymer electrolyte membrane or onto the carbon cloth of the current collector. The decision where the catalyst layer is deposited has to be evaluated according to the application [17]. For fabrication, different methods can be used, e. g. direct coating, a decal transfer or a spray coating technique [18] [19]. One of the challenges in the development of the catalyst layer is the proper choice of the content of the ionomer and the carbon grains. Best results found in literature suggest an amount of 25 – 35 wt-% of PFSA polymer and a volume ratio PFSA/carbon grains = 1. This way, a

sufficient proton and electron conducting behavior as well as adequate porosity for gas supply was achieved [20] [21] [22] [23].

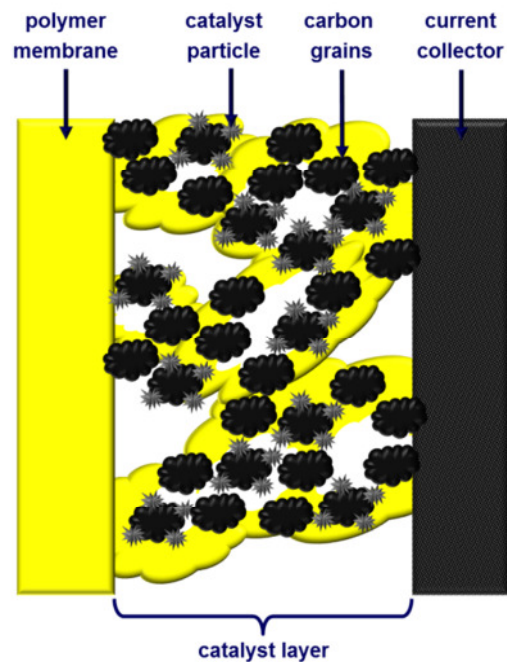


**Figure 11: Basic drawing of the catalyst layer; main components are the catalyst nanoparticles (grey), the catalyst support (black) and the ionomer (yellow). Typical amounts of PFSA ionomer are 25 – 35 wt-% while the volume ratio PFSA/carbon grains is usually 1.**

Another important aspect that needs to be addressed is the thickness of the catalyst layer. A suitable choice of the thickness is crucial to reach optimized catalyst utilization. The thicker the layer the higher the flow resistance will be inside the porous structure and the harder it gets to supply the catalyst with reactants near the membrane. Thus, the catalyst utilization will decrease which will increase the costs of the MEA. In contrast to that a thin catalyst layer will result in a poor performance of the fuel cell as the porous structure is well supplied with gases but the result will be a weak current density due to an insufficient availability of reaction sites. All in all, the effects depending on the layer thickness can be subdivided into three regions [14]:

- The kinetic region.
- The intermediate region.
- The oxygen depletion region.

The kinetic region which appears in thin catalyst layers is reflected by the activation overvoltage that has been mentioned in chapter 2.2 and that can be characterized with the help of the Tafel equation. When the layer thickness is increased the intermediate region will be reached where activation losses and mass transport losses occur but the catalyst utilization is still high. Over a relative wide range of thicknesses no loss in performance will be detected because the mass transfer losses will be



compensated by the increasing number of three phase boundaries. In this region the so-called doubled Tafel equation can be used:

$$\Delta U_a = 2A \ln\left(\frac{i}{i_0'}\right) \quad 2-17$$

In this case,  $i_0'$  is a characteristic current density that is dominated by the oxygen diffusion constant. A further increase in layer thickness will induce the oxygen depletion region where the utilization of the catalyst will become worse, mainly due to mass transport losses and increased resistances in proton and electron transfer. This is why the doubled Tafel equation has to be expanded to [14]:

$$\Delta U_a \approx 2A \ln\left(\frac{i}{i_c}\right) + \frac{i}{\sigma'} \quad 2-18$$

The constant  $i_c$  is a current density that summarizes all effects relating to mass transport losses while  $\sigma'$  represents the proton conductivity which depends on the length of the conductive pathway of the protons. Eikerling *et al.* define a “phase diagram” for optimal catalyst layer thickness  $l$  depending on the current density  $i$  with respect to a certain reference thickness  $l_{ref}$  and reference current density  $i_{ref}$  (cf. Figure 12). In their example, the reference catalyst layer has a thickness of  $l_{ref} = 10 \mu\text{m}$  while the reference current density is set to  $i_{ref} = 1 \text{ A/cm}^2$ . According to their findings, an electrode with a thickness of  $l = 10 \mu\text{m}$  ( $l/l_{ref} = 1$ ) will show best catalyst utilization in the range of  $i/i_{ref} = 0.5$  to  $i/i_{ref} = 1$  which correlates to current densities of  $0.5 \text{ A/cm}^2$  to  $1 \text{ A/cm}^2$ . These values

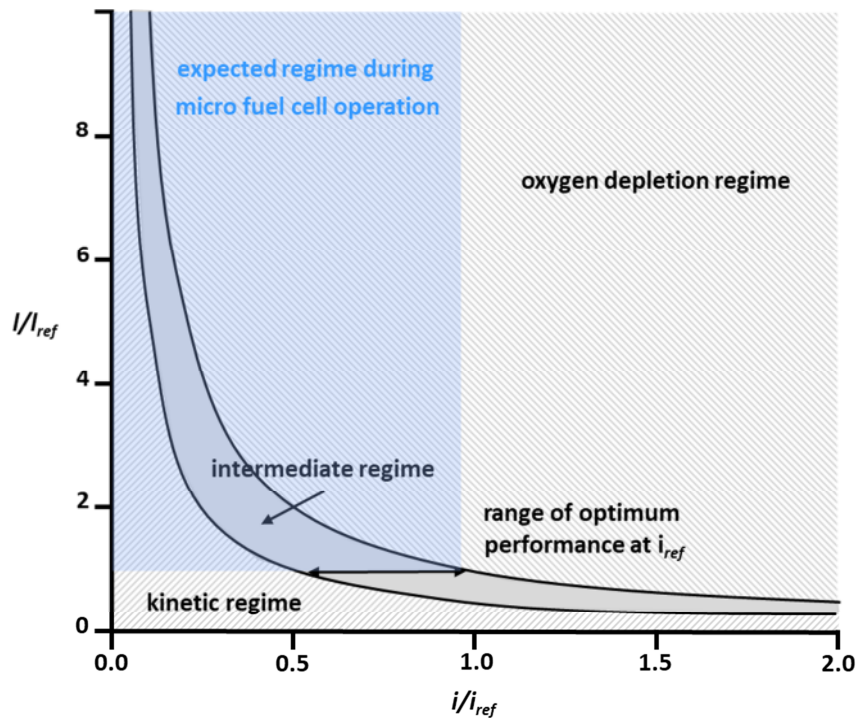


Figure 12: Choice of optimal catalyst layer thickness depending on current density; the reference values are  $i_{ref} = 1 \text{ A/cm}^2$  and  $l_{ref} = 10 \mu\text{m}$  (according to [14]).



agree with other results found in literature [23] [24]. Looking at Figure 12, it becomes clear that for  $i/i_{ref} < 1$ , the ratio of  $l/l_{ref}$  needs to increase ( $l/l_{ref} > 1$ ) which means that fuel cells operated at lower current densities should have thicker catalyst layers. Taking into account the low expected operating temperatures and presumably missing humidification, it is likely that a silicon-based micro fuel cell will operate at low current densities ( $i/i_{ref} \ll 1$ ). Thus, the catalyst layer for such a micro fuel cell should be rather thick ( $> 10 \mu\text{m}$ ) in order to achieve best catalyst utilization.

### 2.3.3 Current collector

In conventional fuel cells the transport of electrons from the anode catalyst layer to the external electrical circuit and from the external electrical circuit to the cathode catalyst layer is realized by a carbon paper which is either woven into a carbon cloth or hot-pressed to form a mat of carbon fibres. This way, it is possible to provide an effective current collection while the porous structure of the carbon paper will lead to homogenous gas distribution along the electrodes. This is why the current collector is also called gas diffusion layer (GDL). The GDL can be designed in different thicknesses (usually 100 – 250  $\mu\text{m}$ ), porosities and with integrated coatings (e.g. PTFE coating for hydrophobic behavior), depending on the application [25]. Hence, the GDL at the anode differs from the GDL at the cathode as there are different challenges to be managed, e. g. related to water management or distribution of the different fuels and reaction products. Of course, the right choice of the GDL parameters has a significant effect on cell performance.

The intrinsic electric resistance of a GDL is negligible [26] because of the high specific conductivity of carbon. More important are the contact resistances between the GDL and its adjacent components [27]. As most conventional fuel cell stacks are assembled based on mechanical compression the contact resistance between the GDL and the catalyst layer on the one side and the bipolar plate on the other side is minimized by squeezing the GDL and generating a certain pressure.

Another major aspect of the GDL is related to water transport. Liquid water that evolves from the chemical reaction blocks the pores of the GDL, cools down the active surface and inhibits the gas supply. This aspect mainly applies to the cathode where product water needs to be transported away from the electrode. Hence, most GDLs are coated with hydrophobic materials such as PTFE in order to transport all water to the gas flow channels of the bipolar plate by capillary forces [28].

The different features of a GDL described above are important aspects when designing a fuel cell. However, as carbon paper shows brittle behavior, has inaccurate geometric tolerances and needs to be compressed for minimizing the contact resistances the integration into micro membrane electrode assemblies can be expected to be inadequate. So, the silicon-based  $\mu\text{MEA}$  developed in

this thesis will not make use of carbon cloth respectively a GDL and current collection, water transport and allocation of the reaction gases will need to be addressed in a different way.

### 3 Bringing fuel cells to low power and portable applications

Throughout the 90's and early 2000's, the emerging market for portable electronics like notebooks and mobile phones evoked the question of power supply for those new applications. Fuel cells exhibit good efficiency, fast recharging and – depending on the way of storing the hydrogen – high energy density. This led to first attempts to develop fuel cells that were able to recharge or even supply electronic devices with low power needs. They mainly used concepts that were based on conventional fuel cell systems like the use of carbon paper, metallic or compound bipolar plates and conventional assembly technologies like screwing [29].

With ongoing advances made in microsystem technology, especially in microelectromechanical systems (MEMS), new fabrication technologies as well as materials and with that innovative micro fuel cells concepts were developed. Silicon which is widely used in semiconductor and sensor industry was proved to be a promising material in micro fuels cells.

#### 3.1 Concepts for micro membrane electrode assemblies

The task for researchers and engineers in micro fuel cell development is to transfer the basic components of fuel cells that were described above to microsystem devices. In case of a PEM-based micro MEA three main concepts can be identified:

- Silicon electrodes with a conventional polymer electrolyte membrane in-between.
- Micro porous silicon membranes with functionalized surface.
- Macro porous silicon membranes with integrated polymer electrolyte.

Figure 13, Figure 14 and Figure 15 give an impression about the basic idea of these concepts. The first one uses a polymer membrane which is integrated between two silicon electrodes that carry the catalyst layer and the current collector. In contrast to that the other two concepts are based on free-standing silicon membranes that are etched into a bulk substrate. They differ in the way the porosity of the membrane is realized which is needed for integration of the electrolyte. This can either be done by anodization of the silicon which leads to a microporous membrane with pores in the nanometer range or by semiconductor processes like lithography and anisotropic deep reactive ion etching resulting in a uniform array of micro channels where the electrolyte can be integrated. As each concept exhibits certain characteristics, the individual (dis-)advantages have to be discussed in detail.

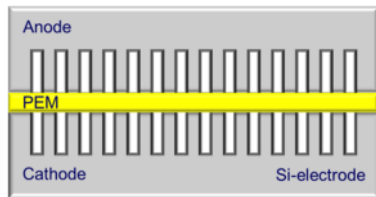


**Figure 13: Basic sketch of a micro MEA with silicon electrodes and integrated PEM sheet.**

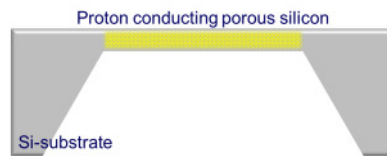


**Figure 14: Silicon micro MEA based on a free-standing, micro porous membrane.**



**Figure 15: Silicon micro MEA based on a free-standing membrane with uniform array of micro channels.**

Figure 13 illustrates an approach of two silicon electrodes with an integrated PEM sheet. It becomes clear that this concept is quite similar to the principle of a conventional fuel cell. Thus, it was identified to be the earliest attempt in research [30]. By applying semiconductor fabrication processes like lithography and deep reactive ion etching (DRIE) flow fields are inserted into silicon substrates. These flow fields can be realized with geometries in the range of  $\mu\text{m}$  and superior precision compared to conventional manufacturing processes like milling. After that, a deposition process for coating the specific electrodes with a metal film, e. g. by sputter deposition, can provide an electric conductivity resulting in a micro bipolar plate with small pattern size and precise tolerances [31]. This way, electrodes with active oxygen supply or self-breathing micro fuel cells with passive oxygen supply have been realized. For those, a conventional MEA with carbon GDL and catalyst coated membrane was integrated between the micro bipolar plates. Due to the brittle mechanic behavior of the silicon, an appropriate way to assemble those micro fuel cells may be adhesive bonding [32] [33].

Instead of fabricating silicon based micro bipolar plates only, the approach of utilizing silicon can be extended in several ways. First, the silicon structures can also be used as catalyst support when a catalyst coating is deposited onto the surface of the substrate. In this case, micro structures with high specific surface, e. g. silicon nanograss or microporous silicon are advantageous as they feature a large chemical active surface. On top of these silicon micro structures, a thin layer of catalyst is deposited, giving the same specific surface as the underlying silicon substrate [34] [35]. An alternative option might also be realized by using electroplating of Pt as a catalyst layer. By optimization of the process parameters, the Pt deposition leads to fibrous, porous structures that result in high specific surface area [36].

The polymer membrane itself and its specific surface area can be improved by using Nano Imprint Lithography. An impregnation of certain convex micro patterns into the polymer leads to an increase of the specific surface. Those patterns may be pins, cavities, lines or dots. Maximizing the aspect ratio of the structure and improving the degree of miniaturization increases the specific surface area, so that more active reaction sites are realized [37].

In contrast to that, Kouassi *et al.* present a way to substitute the GDL by using microporous silicon which is capable of supplying the PEM with fuel and – at the same time – is being used as mechanic support for the MEA [38].

Besides the use of silicon as substrate material it is also possible to deploy metals like stainless steel, as Weinmüller *et al.* and Hahn *et al.* presented in their work. The ductile characteristic of thin metal foils result in easier assembly and lower costs [39] [40].

The concept of micro patterned electrodes with a PEM sheet in-between offers a large specific surface area and benefits from the knowledge and experience of conventional fuel cell technology which leads to good results in power density up to  $450 \text{ mW/cm}^2$  [35]. On the other side, the concept requires to have three individual components (two micro bipolar plates and one MEA, respectively, two electrodes and one polymer membrane) which have to be fabricated independently. This causes high costs, difficult assembly and relatively large dimensions, especially regarding the thickness of the device. However, microsystem technology opens the possibility to combine different components and functions on one substrate, e. g. the proton conducting membrane, the catalyst layer and the current collector. This is what is intended with the other two concepts which will be described in detail in the following section.

Both are based on free-standing membranes that serve as a mechanical support for the MEA components. These membranes are usually realized by thinning a silicon substrate with the help of anisotropic etching processes such as deep reactive ion etching or wet etching, e. g. in diluted potassium hydroxide (KOH). As solid silicon does not exhibit any proton conductivity a proton conducting pathway between the backside and the front side has to be realized. Therefore the silicon membrane has to be permeable, either by making it porous or by fabricating regular patterns of micro channels.

Porous silicon can be achieved by anodization. The principle of this process is based on two half cells separated by a single crystalline silicon substrate that is subject to anodization. Inside the half cells a hydrofluoric acid (HF)/ethanol solution serves as electrolyte. The electrodes are made of precious metals, e. g. Pt, in order to prevent corrosion. By applying a DC current, corrosion of the single crystalline silicon starts at the anode progressing through the thickness of the silicon due to divalent and trivalent reaction with the HF. Varying HF concentration and current densities lead to different pore sizes and porosities [41] [42] [43] [44] [45] [46]. For micro fuel cell applications pore sizes of less than 10 nm were achieved [47].

Pichonat *et al.* have shown that porous silicon membranes with a thickness of  $40 \mu\text{m}$  can reach high proton conductivities by either filling the pores with PFSA or by grafting the pores' internal surface

with silane molecules bearing acid functions. The second method appears to be advantageous because it does not need any organic components. However, it requires the smallest pore sizes in order to avoid gas crossover through the pores. Filling the pores with PFSA resulted in power densities of 20 mW/cm<sup>2</sup> whereas 17 mW/cm<sup>2</sup> could be achieved by grafting the pores [47].

Moggadham *et al.* present a way to functionalize the pore walls of a 24 μm thick micro porous silicon membrane by first assembling 3-mercaptopropyltrimethoxysilane (MPTMS; SH-(CH<sub>2</sub>)<sub>3</sub>-Si-(OCH<sub>3</sub>)<sub>3</sub>) molecules on the modified surface of the pores and then oxidizing the membrane surface at moderate temperatures (300°C) in order to decrease the pore size down to 1 nm. This leads to a stable water meniscus inside the pores, even at 10% relative humidity. By applying a conventional catalyst layer onto the porous membrane and a Cr-/Au-layer at the edge of the device, a fully functioning MEA could be realized that exhibited up to 331 mW/cm<sup>2</sup> [41].

It can be summarized that micro porous silicon is a promising method to fabricate micro MEAs as high power densities can be achieved and the membranes are capable to be integrated into mass production technologies. But it has to be considered that coating the membrane with a catalyst layer or a current collector which is manufactured by MEMS compatible processes seems to be very challenging because standard thin film coating technologies like sputter deposition would close the pores. Thus, conventional porous catalyst layers need to be employed, e. g. by spray coating.

The third way of designing a μMEA is to use a free-standing membrane with a regular micro pattern. The micro pattern consists of round or rectangular channels with a certain diameter. These channels are filled with a proton conducting electrolyte, e. g. PFSA. The front side and back side of the membrane can be coated with thin films for current collection or as catalyst layer.

Nagayama *et al.* studied the influence of the micro pattern on cell performance. They used a silicon substrate that was patterned by anodic etching with rectangular channels of different lateral lengths (5 – 15 μm) and varying channel pitches (3 – 10 μm). The substrate was thinned down to 125 μm by mechanical polishing and the channels were filled with a PFSA-polymer (Nafion®). The method of electrolyte integration was not mentioned. After that, a GDL was hot-pressed onto the surface and the resulting MEA was characterized. They found that power density increased with smaller and more densely packed surface structures. The best results could be achieved with a channel size of 5 μm and a pitch of 3 μm (165.7 mW/cm<sup>2</sup>, Pt loading not mentioned). Moreover, a denser pattern led to a reduction of the activation overpotential which was explained by an increase of available triple phase boundaries [48]. Due to the complex way of fabrication, the low level of integration and the fact that the membrane could easily be replaced by a conventional polymer membrane this attempt

does not seem to be suitable for the use in micro fuel cell systems. However, for the design of a silicon-based micro fuel cell a small pitch seems to be a critical parameter that should be minimized.

Larsen *et al.* used a patterned silicon membrane for the application in direct methanol fuel cells (DMFC) [50]. The micro pattern consisted of homogeneously distributed holes with a diameter of 20  $\mu\text{m}$  and two different pitches of 100  $\mu\text{m}$  and 30  $\mu\text{m}$ . Current collection was realized by a thin TiW-sublayer (10 nm) and an Au-layer (100 nm) deposited by sputter deposition onto each surface of the silicon membrane. The group identified ionomer integration as a critical step in fabrication of micro MEAs. Especially the low ionomer content in common polymer dispersion of less than 20 wt% was seen to be an issue due to the formation of voids throughout drying and thus leading to partially filled membranes. Hence, they developed a method based on an evaporation process under low pressure conditions of  $\sim 300$  mbar (cf. Figure 16). With the help of this method, completely filled micro channels could be obtained (cf. Figure 17). Long process times of 2 hours and a residual polymer layer on top of the surface of the membrane with a thickness of 5  $\mu\text{m}$  are serious disadvantages of this method. In this case, the residual layer isolates the spray coated catalyst layer ( $2 \text{ mg}_{\text{Pt}}/\text{cm}^2$ ) from the current collector. It was also noted that sputter deposition of the current collector will result in metal deposition at the side walls of the micro channels. The result would be electric short circuits, if the membrane is fabricated with a thickness of less than 100  $\mu\text{m}$  which correlates to an aspect ratio of 5 (membrane thickness vs. diameter of the micro channels). Hence, thinner proton conducting membranes are not possible for this attempt and lead to increased Ohmic resistances of the  $\mu\text{MEA}$ . Power densities reached peak values of  $2.5 \text{ mW}/\text{cm}^2$  [49] [51]. Nevertheless, two important results were obtained from their research. First, polymer integration must be designed very carefully as it is mandatory to avoid leakages between anode and cathode.

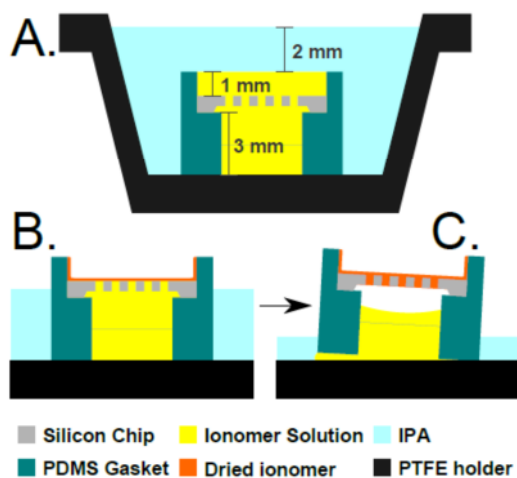


Figure 16: Principle drawing of ionomer integration into micro channels [49]

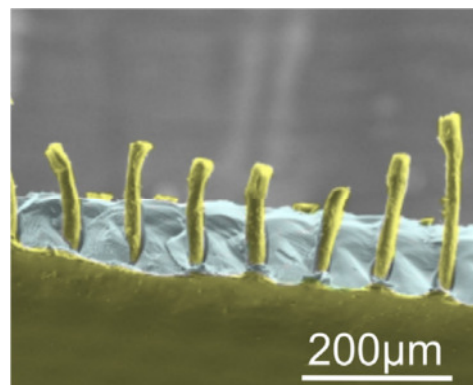


Figure 17: SEM-image of Ionomer filled micro channels [50]

Second, a minimization of thickness of the silicon membrane – and thereby a decrease of the aspect ratio of the micro channels – may lead to electrical short circuits if a metal current collectors is deposited by sputter deposition.

Moghaddam *et al.* as well as Zhu *et al.* tried to overcome this issue by first coating the membrane with a Cr-/Au-layer and then etching the micro channels. The fabricated micro MEAs reached power densities up to 237 mW/cm<sup>2</sup> although it has to be considered that 20 mg<sub>Pt</sub>/cm<sup>2</sup> were used as catalyst loading which is remarkably high [52] [53]. So, in terms of performance of the MEA this seems to be a proper way. But it has to be stated that etching of precious metals like Au and Pt is hard to achieve, because the high chemical stability of these metals lead to slow etching rates during wet with hardly any selectivity of the etch medium. For dry etching the most widely utilized method is sputter etching. This leads to deposition of the etched metal at the side walls of the etching masks. These residuals are called fences. They make further processing very challenging, especially bonding of the device. This is why patterning of precious metal is almost not used in industrial applications and not suitable for mass production [54] [55] [56] [57] [58].

Bretthauer *et al.* developed a micro fuel cell based on alkaline polymer electrolytes in order to be able to use AB<sub>5</sub> metal hydrides as hydrogen storage medium. They integrated the electrolyte, the electrodes and the AB<sub>5</sub> metal hydride into a silicon cavity which was protected by a gas permeable PTFE membrane at the air breathing cathode and with a lid on the anode. La<sub>0.6</sub>Ca<sub>0.4</sub>CoO<sub>3</sub> served as cathode material which was integrated into a patterned Nickel metal sheet. The alkaline nature of the electrolyte made it necessary to protect the silicon cavity with a Si<sub>3</sub>N<sub>4</sub> layer in order to prevent dissolution of the silicon substrate. As ion conductivity in alkaline electrolytes is significantly lower than in acidic electrolytes the resulting power densities were as low as 0.66 mW/cm<sup>2</sup>. Besides that, the group identified the spray coated electrode to be a crucial factor in effectiveness [59]. It has to be stated that this attempt differs significantly from the previous mentioned developments as alkaline fuel cell materials were used and no microstructured silicon membrane was needed. However, the low power density originating from the low level of material development makes this type of fuel cell far from being ready for industrial applications.

Table 1 sums up different works on  $\mu$ MEAs, their concept and the achieved power densities:

Membrane technology	Fuel gases	Open circuit voltage (OCV) [V]	Power density [mW/cm <sup>2</sup> ]	Reference
Filling by PFSA	H <sub>2</sub> /air	0.8	20	[47]
Sulphuric acid loaded membrane	H <sub>2</sub> /air	0.97	12.75	[60]
Pore surface grafting by silane molecules	H <sub>2</sub> /air	0.47	17	[47]
Acid loaded membrane	formic acid+sulphuric acid/air	0.65	94	[61]
Filling by PFSA	methanol/air	0.3	2.5	[50] [49]
Filling by PFSA	H <sub>2</sub> /air	0.98	237	[52]
Filling by A3PE (alkaline)	H <sub>2</sub> /air	0.8	0.7	[59]
Filling by PFSA	H <sub>2</sub> /air	0.8	165.7	[48]

**Table 1: Overview of achieved performance for silicon-based micro membrane electrode assemblies**

It becomes clear that achieved power densities vary in a wide range as the concepts and fabrication methods differ significantly. Though there might be some attempts where high power densities of more than 100 mW/cm<sup>2</sup> were reached, these results are often realized by using high amounts of Pt catalyst whereas average power densities are found to be significantly less than 100 mW/cm<sup>2</sup>.

### 3.2 Sputtered catalyst layers and current collectors for micro fuel cell applications

With ongoing progress in microsystem technology, physical vapor deposition (PVD) respectively sputter deposition technology gained interest in fuel cell development, especially for fabrication of highly effective catalyst layers. PVD describes a method to coat a substrate at temperatures below the melting point ( $T_m$ ) of the coating material by striking out atoms from a target through bombardment by ionized gas molecules from Argon (Ar) plasma. This enables the deposition of thin-metal films onto a vast amount of possible substrates, e. g. polymers, metals or semiconductors like silicon.

For sputter deposition of metals Thornton *et al.* developed a physical model that describes the influence of certain sputter parameters on the morphology of the final layer (cf. Figure 18). It was found that morphology strongly depends on sputter power, temperature and chamber pressure. Due to poor surface diffusion as well as little energetic bombardment at low temperatures ( $T/T_m < 0.3$ ) and high Ar pressures porous coatings with fibrous, columnar grains occur (zone 1). At higher



temperatures ( $T/T_m > 0.8$ ) the surface diffusion of the metal atoms increases rapidly so that Ar pressure gets negligible and the layer consists of homogeneously distributed grains similar to cast metals (zone 3). The dependency of the morphology on Ar pressure results from scattering processes between the coating metals and the gas molecules. This leads to varying impact directions and shadowing effects [62] [63] [64] [65]. Hence, for development of a sputter coated catalyst layer in micro fuel cells the parameters of the sputter deposition process should be chosen according to zone 1. This ensures optimal Pt utilization as a porous structure will lead to high specific surface and thereby to high effectivity.

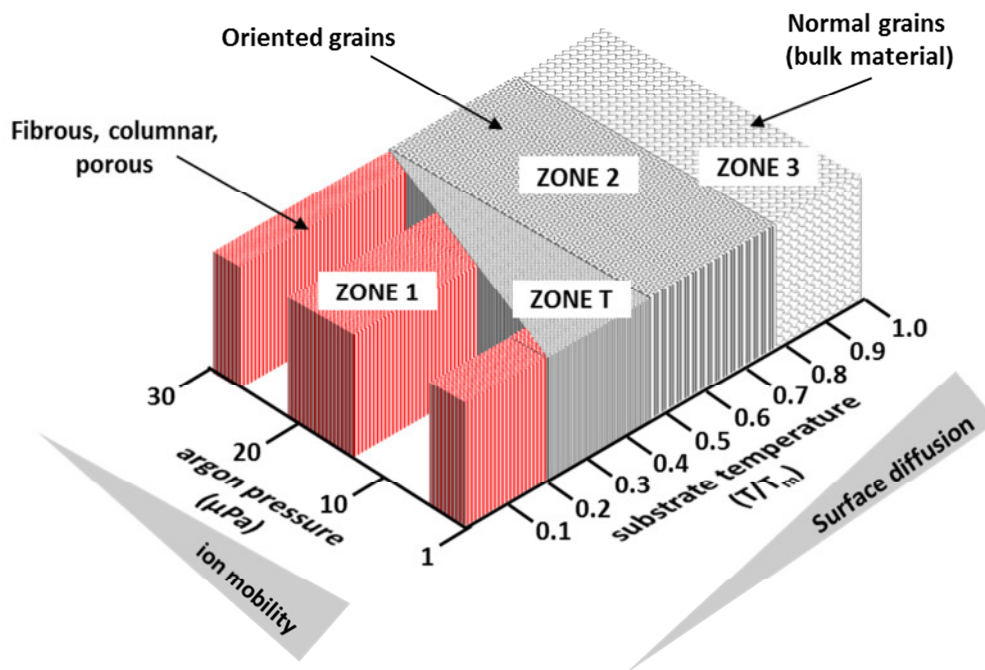
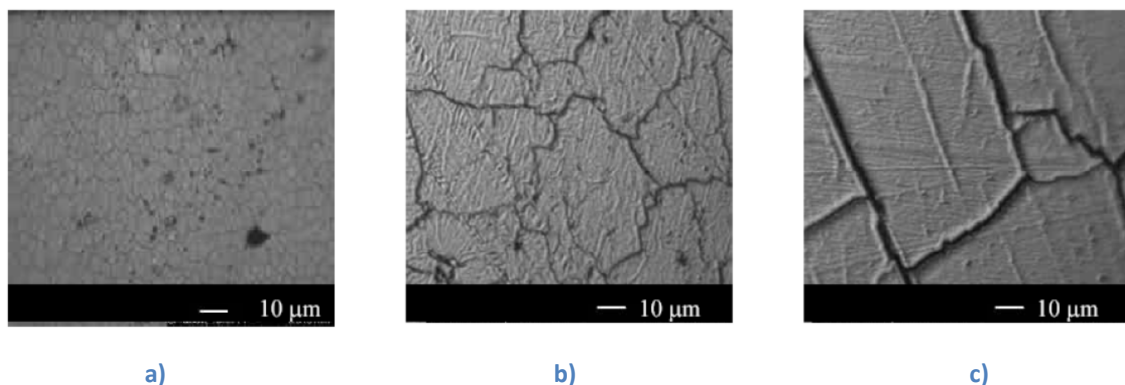


Figure 18: Zone diagram of layer morphology depending on substrate temperature and Argon pressure (developed and validated by Thornton); zone 1 is marked red as porous structures are highly desirable for effective catalyst layers in micro fuel cells (according to [63]).

Because of the possibility to influence surface morphology in a wide range, researchers have examined the influence of sputter deposited catalyst layers on fuel cell performance. Thin layers as well as metal cluster have been fabricated onto ionomer membranes or gas diffusion layers [66] [67] [68]. The focus of research was to find optimized parameters (sputter pressure, substrate temperature, sputter power etc.) of the deposition process but also to investigate the dependence of the ECAS on the layer thickness and the substrate roughness.

O'Hayre *et al.* found that optimal layer thickness for sputter deposited catalyst layers on PFSA membranes can be determined due to changing film morphology. Thin Pt layers with thicknesses between 10 nm and 100 nm were coated onto ionomer membranes in order to serve as catalyst layer. At the transition between ionomer and Pt metal the triple phase boundary can occur. According to their findings thinner films exhibit a higher number of cracks because of the high

intrinsic stress of sputtered Pt coatings. These cracks increase the specific surface significantly and result in a more effective Pt utilization as the triple phase boundary is multiplied. With increasing film thickness these cracks disappear and the Pt utilization decreases as only the Pt atoms at the surface can participate to the electrochemical reaction. In Figure 19, SEM images of the different stages for varying Pt layer thickness are shown [69]. Moreover, a surface roughened by SiC abrasion leads to an increase of the specific surface even at thicker films. The researchers already mention the potential for sputter deposited catalyst layers in micro fuel cell applications [70]. Instead of roughening the polymer surface by SiC abrasion, plasma treatment may also be used as demonstrated by Haug *et al.* [66].



**Figure 19: SEM-image of sputtered Pt catalyst layer on PFSA (Nafion®) substrate with varying thickness: a) 15 nm; b) 30 nm; c) 100 nm [69]; Thinner layers obtain more cracks that lead to an increase of the specific Pt surface.**

Slavcheva *et al.* worked on the development of sputter coated catalyst layers for silicon-based micro fuel cells that are solely fabricated by semiconductor processes. Their results show that layer morphology and electrochemical performance can be influenced by sputter pressure, dc power and film thickness which is in good match with the Thornton model. High sputter pressures and dc powers lead to porous Pt layers that show high catalytic activity (cf. Figure 20). In contrast to O'Hayre the sputter deposition of Pt on Si does not have an optimal layer thickness. Instead, thicker layers lead to higher specific surfaces and hence, to better catalytic activity. As best result, an ECAS that is 93.63 times higher compared to the geometric surface of the electrode could be obtained. Thus, sputter deposition of Pt catalyst layers is a promising technique for the development of micro fuel cells based on semiconductor fabrication methods [71].

For current collection in micro fuel cells sputter deposited metal thin films can be applied, too. Due to the limited adhesion of precious metals like Au and Pt on silicon surfaces an adhesion layer, usually made of Cr or Ti, has to be applied. The thicknesses found in literature vary between 100 nm [50] and 200 nm [53]. This seems to be sufficient for achieving a good electrical conduction.

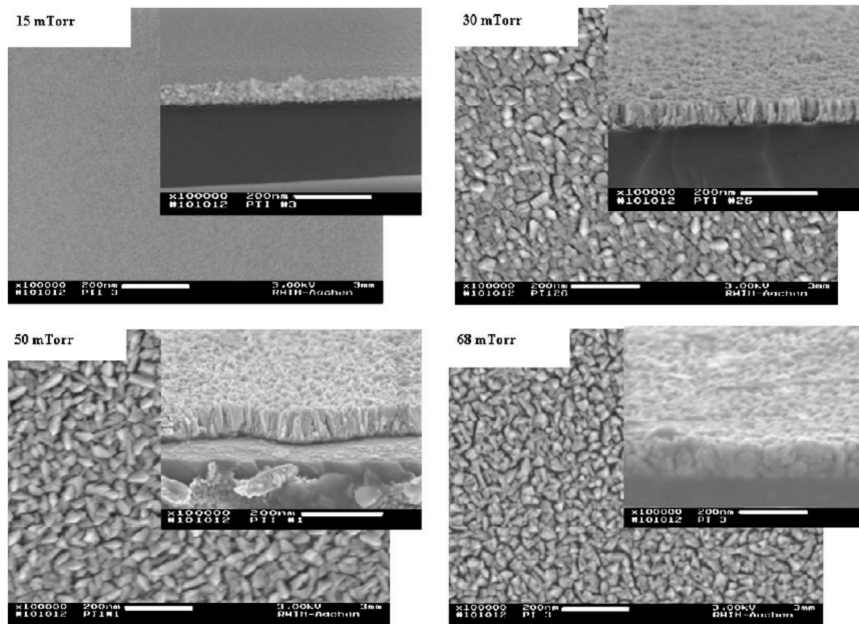


Figure 20: SEM-images of Pt catalyst layers that show the influence of Argon sputter pressure [71]; the large images show the top view while the inset show a cross section of the sample.

### 3.3 Integration of $\mu$ MEAs into micro fuel cell systems

Besides the development of a  $\mu$ MEA with high effectiveness and low volume fraction the integration into a fuel cell system represents a major challenge for establishing micro fuel cells inside portable applications. The use of microsystem technology is not only limited to the  $\mu$ MEA but also to all aspects of the periphery which includes components like hermetic package, electrical connectivity and control, fuel supply and  $H_2$  storage.

One important aspect is the design of the electrical connections. Single  $\mu$ MEAs are electrically connected in series to create a stack. A fuel cell stack is necessary to gain higher voltage levels in order to power the application of interest, e. g. a smartphone which is powered at 3.5 V. Due to the need of creating devices of minimized thickness, micro fuel cell systems are usually designed as so-called self-breathing planar stacks. In contrast to vertical fuel cell stacks, where the serial connection is realized by stacking the electrically conductive bipolar plates, planar fuel cells are placed next to each other (cf. Figure 21). This way, all single fuel cells are in-plane and the overall thickness of the fuel cell stack is defined by the thickness of the single cell. When there is no active oxygen supply, e. g. by a fan, but just the oxygen from the ambient air which reaches the cathode by convection and diffusion the fuel cell is defined as self-breathing. This offers the advantage that no gas supplying periphery at the cathode is needed. Hence, thinner fuel cells with more simple architecture can be realized. However, oxygen supply to the cathode catalyst is limited by convection and diffusion rates which results in limited power densities compared to active oxygen supply in vertical fuel cell stacks.

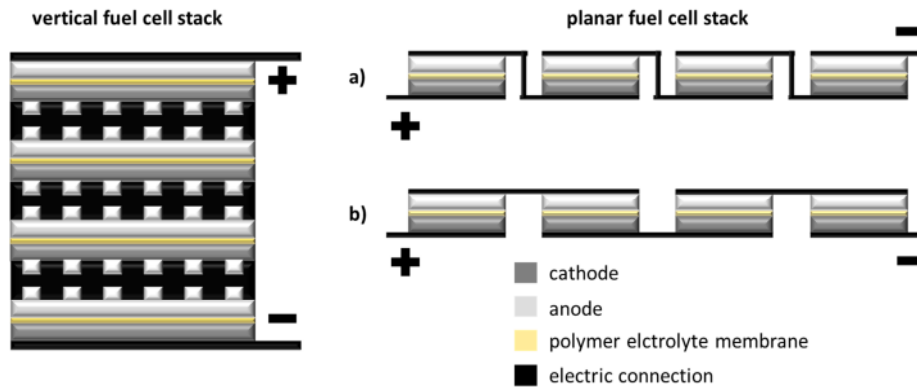


Figure 21: Sketch of vertical fuel cell stack and planar fuel cell stack; in planar fuel cell stacks electrical connection of the single cells is more challenging but total height of the stack can be reduced to the height of one fuel cell: a) each fuel cell anode is connected to the cathode of a neighboring fuel cell, b) two fuel cell anodes are connected in parallel and each pair is connected in series to another pair. This way, there is no need to build a vertical electrical connection.

Furthermore, the question of H<sub>2</sub> storage determines the periphery in a major way, for example if liquid or gaseous fuels are used. As pressure tanks with compressed H<sub>2</sub> gas are not compatible with microsystem technology alternative fuel storage principles have to be applied. Solid and liquid hydrides seem to be the most promising for micro PEM fuel cells. Figure 22 gives information about the energy densities (weight and volume specific) of different fuels. Metal hydrides, chemical hydrides and liquid carbon hydrides offer high energy densities at low volume fractions. It can be observed that liquid carbon hydrides exhibit the lowest mass density which results in lightweight hydrogen storage. On the other hand, they also exhibit the lowest mass specific energy density. Compared to that, chemical hydrides and metal hydrides are able to carry more hydrogen in terms of volume specific energy density. As absolute volume in portable devices is small, weight is of minor importance in these applications. Hence, the high volumetric energy density of hydrides seems to be advantageous. Especially metal hydrides might be a suitable hydrogen storage solution as some materials allow hydrogen storage at room temperature and affordable pressure levels.

The question of the most sufficient H<sub>2</sub> storage for micro fuel cells remains unanswered and strongly depends on the intended application which is also reflected by different attempts found in literature.

Frank *et al.* worked on micro fuel cell systems using Palladium based hydrogen storage. For this, a thin Pd layer was coated onto a silicon substrate by electroplating. Combining the storage device with a self-breathing PEM fuel cell and a micro electrolyzer for hydrogen production, 200 cycles of charge and discharge could be achieved [72].

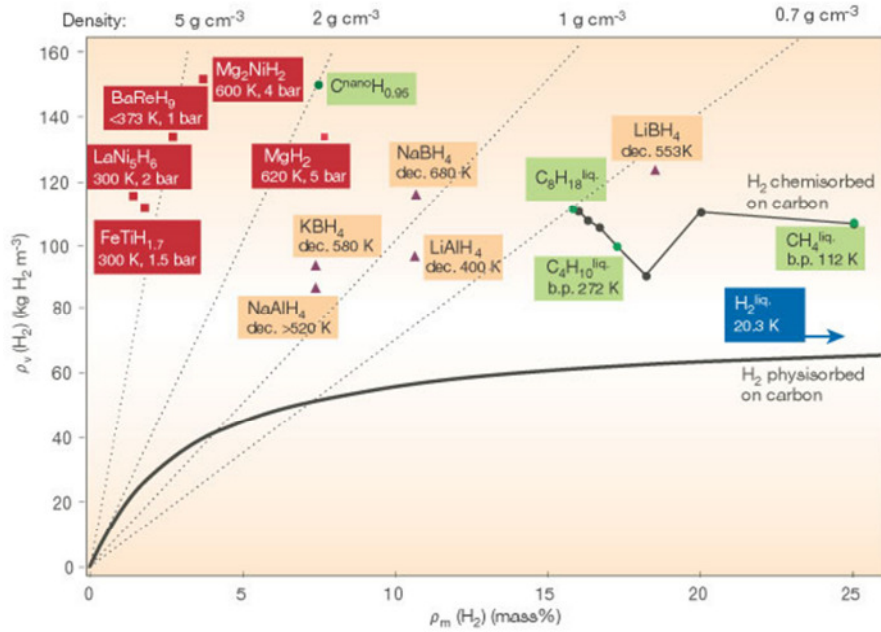


Figure 22: Comparison of mass and volume specific energy density for different hydrogen carriers [73]; As available volume in portable devices is rather small, mass specific energy density is of lower importance; metal hydrides might be a possible storage system for portable applications as they offer high volumetric energy density at low storage pressures and may be recharged

Further developments of that approach were reported by Balakrishnan *et al.*, who realized a system including a Pd/polymer composite which was filled into a silicon cavity. By using Pd flakes with high specific surface the storage capacity could be improved in comparison to former thin Pd layers. The storage device could be loaded with hydrogen by placing it into a pressurized hydrogen atmosphere. Achieved power density of the whole system was 2.1 mW/cm<sup>2</sup> [74]. Moghaddam *et al.* used metal hydrides based on LiAlH<sub>4</sub> for H<sub>2</sub> storage. The final device had a total volume of 9  $\mu$ L and worked on the principle of passive fuel delivery systems. Hydrogen was released through a chemical reaction of the hydride with water vapor giving 254 Wh/l for a time of 32 hours [53].

In contrast to that Hur *et al.* developed a fuel cell system running on methanol. In conventional fuel cell systems, this kind of hydrogen supply requires a separate pumping system that needs a power supply. By applying microsystem technology, no moving components were needed in this case. Anode and cathode were supplied by self-pumping mechanisms utilizing capillary effects. Two cartridges connected to the electrodes enabled easy recharge and made the fuel cell independent from ambient conditions [75].

To sum up this section, it can be stated that whole fuel cell systems can be fabricated by using microsystem technology. It was proved that those micro fuel cells have sufficient volumetric energy density and are capable of working independently without external pumps. Major challenges can be identified in optimizing the power density and lifetime.

## 4 Characterization methods

In this chapter the different characterization methods to analyze the developed  $\mu$ MEA are discussed. Methods for determination of catalytic activity, electrical and proton conductivity as well as electrochemical performance and molecular characteristics have been used.

### 4.1 Cyclic voltammetry

Cyclic voltammetry is a powerful method to characterize electrochemical reactions. By applying a changing electric potential to a test electrode the current answer can be used to gain information about the instantaneous electrochemical reactions. The test electrode is integrated into a three electrode setup in an acid electrolyte, measuring the current between test electrode and counter electrode relative to a reference electrode. Usually, a linearly changing potential between an upper and lower potential limit is applied with constant sweep rate. This way, additional aspects like corrosion, degradation and other time depending effects can be studied [76] [77] [78].

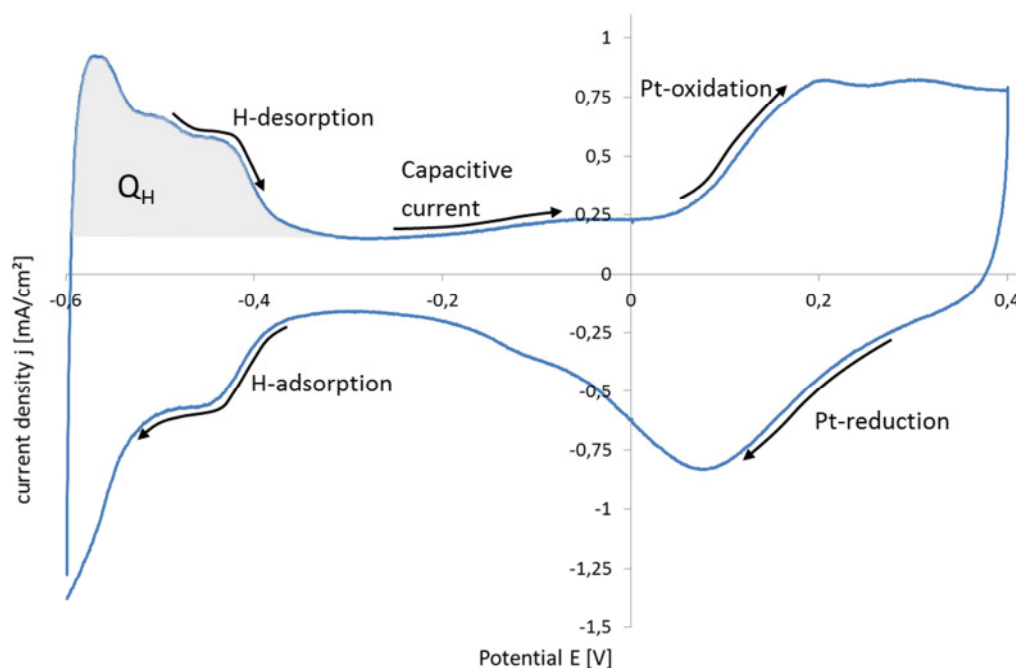


**Figure 23:** Cyclic voltammogram of Pt in 0.1 M  $\text{HClO}_4$  electrolyte with  $\text{Hg}/\text{Hg}_2\text{SO}_4$  in saturated  $\text{K}_2\text{SO}_4$  reference electrode at a scan rate of 20 mV/sec and 0 rpm.

For Pt catalysts cyclic voltammetry can be used to observe adsorption and desorption effects as well as oxidation and reduction reactions on the metal surface. Presuming there are no parasitic species present in the electrolyte of the measurement setup, a characteristic diagram forms (cf. Figure 23) [79].

With the reference electrode used for gaining the diagram in Figure 23, the electrochemical behavior of the Pt electrode can be described as follows: At low potentials between -0.6 V and

0.35 V and with positive sweeping rate hydrogen desorption takes place. This results in characteristic peaks of the current answer. Between -0.3 V and 0.05 V the current drops to almost 0 A. Here, the resuming capacitive current originates from the electric double layer at the surface of the Pt. With increasing potentials larger than 0.05 V Pt-OH and Pt-O is formed at the working electrode giving a significant rise of the current answer. When the direction of the potential sweep is turned to a negative rate, the Pt is reduced again. With decreasing potential below -0.3 V hydrogen is adsorbed again resulting in an increasing negative current.

It is possible to calculate the ECAS from the hydrogen adsorption respectively the desorption peak [80]. The total amount of charge  $Q_H$  is determined by integration of the current  $I$  within the potential range  $\Delta E$  where hydrogen is desorbed/adsorbed and subtraction of the capacitive current from the double layer (cf. Figure 23):

$$Q_H = \int_{\Delta E} dQ(E) = \int_{\Delta E} I dt = \frac{1}{v} \int_{\Delta E} I dE \quad 4-1$$

The term  $v$  represents the sweeping rate in mV/s.

If one assumes that one H-atom is adsorbed at one Pt-atom the ECAS results directly from the charge. Measurements with ideally flat electrodes exhibit a charge of  $210 \mu\text{C}/\text{cm}^2$ . Biegler *et al.* determined empirically that between 0.08 V and 0.35 V RHE 77 % of the metal surface is covered with hydrogen [81]. Taking this into account, the ECAS and with that a roughness factor RFa can be calculated:

$$ECAS = \frac{Q_H}{210 \frac{\mu\text{C}}{\text{cm}^2} 0.77} \quad 4-2$$

$$Rfa = \frac{ECAS}{A_{geom.}} \quad 4-3$$

with  $A_{geom.}$  being the geometric area of the electrode [81].

## 4.2 Polarization curves

In chapter 2.2 the structure of a polarization curve was already discussed in terms of overpotentials decreasing the reversible voltage.

Polarization curves are helpful to display the different regions of overpotentials depending on the current density. A steady-state polarization curve may be received either by defining a current density and measuring the resulting constant potential or by defining a potential and measuring the



resulting current density. As it takes some time in the range of minutes to achieve a steady-state for every measuring point, the recording of polarization curves is time consuming. By calculating the power density, direct information about the performance of the fuel cell can be obtained. Polarization curves are useful in order to gain information about changes in operation parameters like volume flow of the supply gases, temperature, humidity or pressure. With this method, it is not possible to identify and differentiate between individual reasons that cause a change in cell performance, for example a performance drop due to drying or flooding of the membrane [79].

An essential parameter of polarization curves is the so-called stoichiometry  $\lambda$ . It is defined as the ratio between the reaction gases pumped through the gas channels and the gas molecules that are actually needed at a specific point of operation (current density). The stoichiometry can be calculated by taking into account the moles that are needed to maintain the reaction of a single cell at a certain current:

$$\varphi_{mol} = \frac{1}{nF} \quad [\varphi_{mol} = \frac{mol}{A \cdot s}] \quad 4-4$$

with  $n = 2$  being the number of electrons used in the reaction and  $F$  representing the Faraday constant ( $F = 96485.3 \text{ As/mol}$ ). From the number of moles needed the specific volumetric flow in standards litres per minutes and ampere (SLM/A) can be calculated by applying the ideal gas law under standard conditions (273.15 K, 101325 Pa):

$$\varphi = \varphi_{mol} \cdot V_{mol} \cdot 60s/min \quad [\varphi = \frac{SLM}{A}] \quad 4-5$$

For hydrogen fuel cells this leads to  $\varphi_{H_2} = 7.0 \times 10^{-3} \text{ SLM/A H}_2$  for the anode and  $\varphi_{O_2} = 3.5 \times 10^{-3} \text{ SLM/A O}_2$  for the cathode. As most fuel cells are fed with air instead of pure oxygen, this has to be taken into account for the calculation of the cathode gas flow ( $\varphi_{air} = 16.6 \times 10^{-3} \text{ SLM/A}$ ). These numbers represent the ideal gas supply that would be necessary to maintain a certain current of a single cell ( $\lambda=1$ ). In reality, the applied stoichiometries are higher in order to minimize mass transport overpotentials. However, the stoichiometry should be kept as low as possible so that fuel utilization is maximized and drying of the polymer membrane is avoided [82] [83] [84].

#### 4.2.1 Test package and experimental setup

For characterization of the electrochemical performance of the  $\mu$ MEA a test setup was designed. With the help of this test package it is possible to measure polarization curves at different gas flows and to conduct further electrochemical measurements.



The most important specifications are:

- hermetic impermeability
- good/homogeneous electrical contact
- minimized intrinsic electrical resistances
- easy integration of the  $\mu$ MEA-sample
- homogeneous gas flow

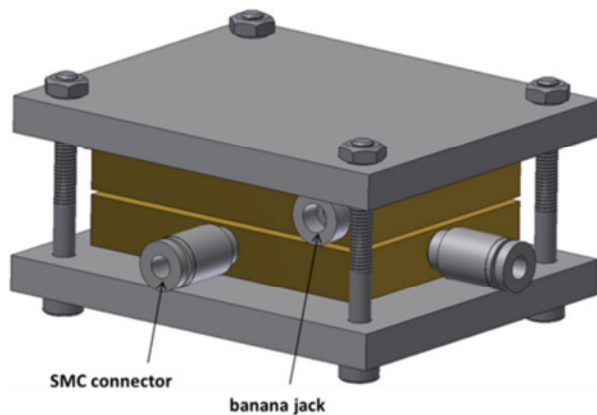


**Figure 24: Technical drawing of the final test package; the  $\mu$ MEA is placed between two gold-coated metal plates; SMC connectors are used for gas supply and banana jacks for electrical connection.**

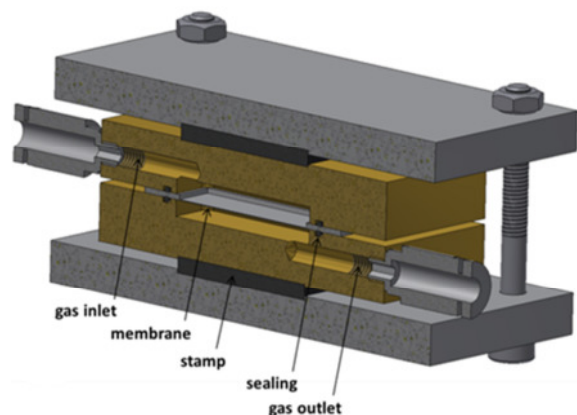


**Figure 25: Cross-sectional view of the final test package; the plastic stamps protect the  $\mu$ MEA from transverse forces and electrical short circuits by the screws; the sealing is made of an electrically conductive material (silicone impregnated with nickel) to improve current collection on the  $\mu$ MEA.**

Figure 24 and Figure 25 show drawings of the test package. The  $\mu$ MEA is integrated between two stainless steel plates that have cavities for gas supply and were electroplated with a chromium/gold layer to minimize electrical resistances. Due to the small amount of gases needed and the small electrochemically active area, the cavities were designed without flow fields. The  $\mu$ MEA is standing freely between the cavities and no GDL is used for current collection. Hence, current collection from the electrochemical active area to the package has to be integrated into the  $\mu$ MEA itself.

The sealing was realized by a notch in each plate that was filled with an electrically conductive rubber seal (silicone impregnated with nickel) by micro dispensing in order to obtain a good electrical contact between  $\mu$ MEA and stainless steel plate. The rubber seal was delivered by Germania Elektronik, Germany.

For applying an electrical load, a Keithley source meter was used. The electric connection from the test setup to the source meter was realized by micro banana jacks that were screwed into the plates. The overall intrinsic resistance of the test setup and its cables without  $\mu$ MEA was 167 m $\Omega$  at 20°C. For gas flow connection SMC connectors were used at the anode as well as on the cathode side for

gas inlet and gas outlet. This way, the test setup could easily be integrated into an existing test stand which is already equipped with SMC standard connectors. As hermetic impermeability is of great importance and a silicon-based  $\mu$ MEA is sensitive to inhomogeneous mechanical loads, the assembly of the test package is essential. Hence, two steel plates which are assembled by four metal fasteners served as end plates. For electrical insulation between the end plates and the test setup a polymer stamp of  $10 \times 20 \text{ mm}^2$  was placed in the centre of the test setup. This way the mechanical load of the end plates is induced into the centre of the test setup which leads to a homogeneous pressure distribution across the  $\mu$ MEA.

After that, the test package was integrated into an existing test stand. A diagram of the basic test configuration can be seen in Figure 26. Gas flows are controlled by mass flow controllers (MFC) which can be varied between 2 ml/min and 50 ml/min for  $\text{H}_2$  supply and between 4 ml/min and 200 ml/min for air supply. MFCs and source meter are controlled via a LabView based software. There was no temperature control and no humidity control added. All experiments were done at room temperature ( $20^\circ\text{C}$ ) within the temperature tolerance of the lab and without humidification. This way, the experiments correlate to the intended application in portable devices.

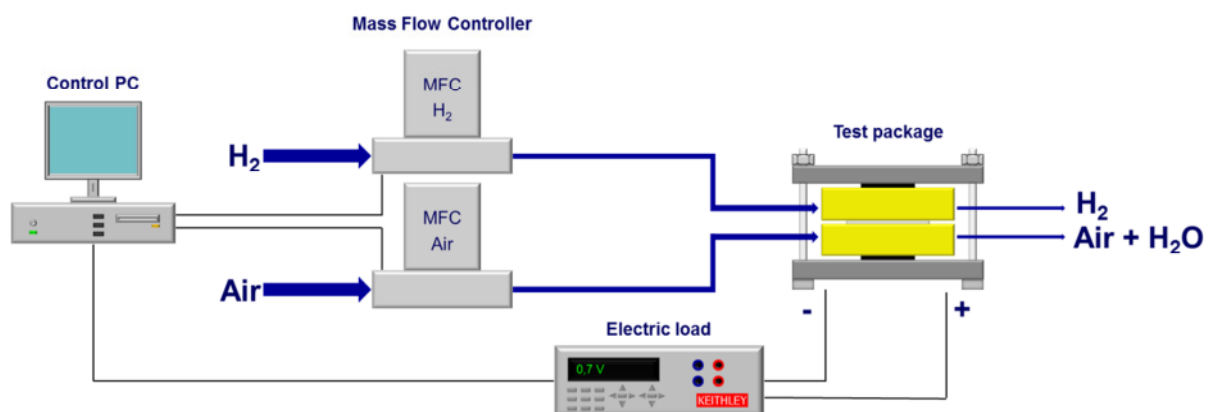


Figure 26: Basic drawing of the test setup

### 4.3 Electrochemical Impedance Spectroscopy

Electrochemical Impedance Spectroscopy (EIS) is an important tool for analyzing fuel cells and its components. It describes the characterization of a system's complex alternating-current resistance within a specified frequency range. By applying an alternating potential respectively a current with defined frequency and detecting the electrical answer of the system, the complex impedance is determined. With variation of the frequency impedance spectra can be generated. For electrochemical devices this is of great interest, especially for the characterization of fuel cells and

their electrodes as it gives information about Ohmic resistances, proton conductivity and the reaction kinetics of the specific system.

For calculation of the impedance with the help of a potentiostatic characterization, an alternating potential is applied to the electrochemical system:

$$U(t) = U_0 e^{-i\omega t} \quad 4-6$$

Then, the resulting current answer is:

$$I(t) = I_0 e^{-i(\omega t - \phi)} \quad 4-7$$

The current exhibits a characteristic phase shift  $\phi$  which leads to the impedance  $Z$ :

$$Z = \frac{U}{I} = \frac{U_0}{I_0} e^{i\phi} = |Z| e^{i\phi} \quad 4-8$$

This corresponds to:

$$Z = \text{Re}(Z) + i \cdot \text{Im}(Z) \quad 4-9$$

As current answer and impedance depend on the applied frequency, it is necessary to measure a wide band of frequencies in order to receive as much information as possible. Practically, the frequency range is limited by the influence of inductive reactances (e. g. cables) at high frequencies  $> 1$  MHz and by the time dependent stability at low frequencies  $< 1$  Hz.

The resulting impedance spectra can be interpreted with the help of equivalent circuit diagrams that represent the specific components inside the fuel cell. Those equivalent circuits consist of Ohmic resistances, capacitances and inductances. This way, a visual illustration of the possible characteristics can be created. However, it has to be considered that there are also impedance elements that cannot be represented by standard electronic circuit elements.

In the equivalent circuit of a basic electrochemical system, all inner resistances are represented by an Ohmic resistor  $R_i$ . This includes the resistance of the electrolyte as well as all components with an Ohmic behavior like current conducting and connecting components (cables, etc.). The charge transfer inside an electrochemical electrode shows Ohmic behavior as well, so another resistance  $R_{ct}$  is added to the equivalent circuit. Between electrode and electrolyte forms an electric double layer which consists of the electrons at the specific electrode and the ions that have the opposite charging. It can be described with the help of a capacitor. However, an ideal capacitor would not reproduce the real behavior inside the fuel cell correctly. Reasons for that may be found in inhomogeneity of the charge distribution inside the electrode as well as the morphology of the porous surface [85] [86]. That is, why an empirical element, called constant phase element  $Z_{CPE}$ , needs to be introduced. This element behaves like a capacitor, except that the phase angle  $\varphi$  is not  $-\pi/2$ , but  $0 \leq \varphi \leq -\pi/2$ . It

can be described by two parameters  $CPE-n$  and  $CPE-Q$ .  $CPE-n$  quantifies the distortion of the phase with  $0 \leq CPE-n \leq 1$ . At  $CPE-n = 1$   $Z_{CPE}$  becomes a true capacitor exhibiting the capacitance  $CPE-Q$ . Because of this,  $CPE-Q$  is called a pseudo capacitance.

Figure 27 shows the resulting equivalent circuit of the electrochemical system. When the frequency response is constructed with the real part of impedance drawn on the x-axis and the imaginary part of the impedance drawn on the y-axis, the result is called Nyquist diagram. Figure 28 shows the Nyquist diagram derived from the equivalent circuit shown in Figure 27 [87] [88]. It consists of an arc which is shifted along  $Re(Z)$  according to  $R_i$ . Depending on  $CPE-n$ , the arc is distorted while at  $CPE-n = 1$  being a perfect semicircle.

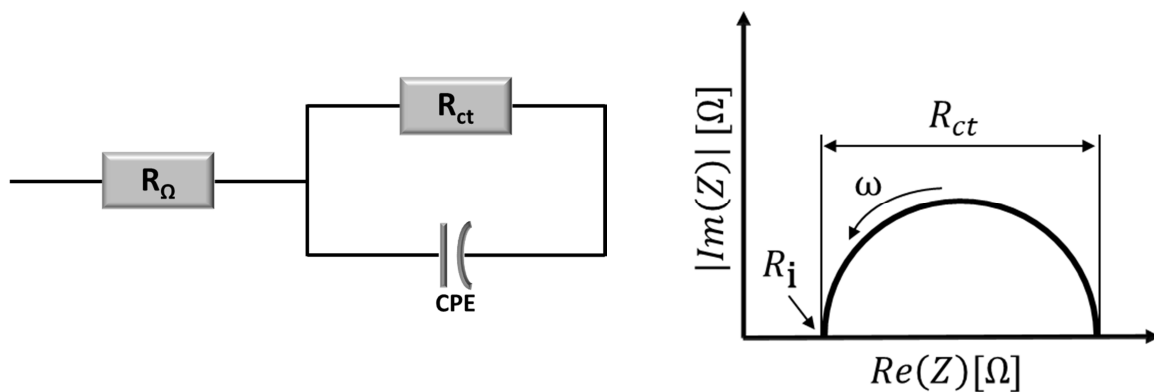


**Figure 27: Equivalent circuit for interpretation of AC impedance measurements for characterization of proton conductivity in proton conducting materials** **Figure 28: Nyquist plot of equivalent circuit described in Figure 27**

In order to generate the equivalent circuit of an operating fuel cell the system described above has to be expanded. A second electrode is added to the equivalent circuit in order to be able to distinguish between anode and cathode. Their individual charge transfer resistances are represented by  $R_A$  and  $R_C$ .

The polymer electrolyte membrane together with all other conducting components like current collector, GDL, bipolar plate and adjacent cables are summarized to an Ohmic resistance  $R_Ω$  which marks the minimal impedance and thereby the starting point of the Nyquist diagram at high frequencies (cf. Figure 29).

The diffusion of the species inside the electrodes is another important impedance element. It is described by the so-called Warburg impedance  $Z_W$ . As diffusion is a comparably slow process, the value of  $Z_W$  strongly depends on the applied frequency. At high frequencies, the diffusing reactants are not able to migrate long distances in direction of the electric field, leading to low impedances.

With decreasing frequencies, the pathway length of the reactants increases and the impedance increases accordingly. This behavior can be described by the so-called infinite Warburg impedance:

$$Z_W(\omega) = Y_0 \sqrt{j\omega} \quad 4-10$$

with  $Y_0$  being the Warburg coefficient which depends on the diffusion coefficients of the diffusing species, the surface area of the electrode and the number of electrons involved in the reaction. As infinite diffusion layers do not exist in reality, a Finite Length Warburg impedance is defined as:

$$Z_W = Y_0 \sqrt{j\omega} \tanh\left(\delta \sqrt{\frac{j\omega}{D}}\right) \quad 4-11$$

with  $\delta$  being the Nernst diffusion layer thickness and  $D$  being the average of the diffusion coefficients of the diffusing species.

At higher frequencies the diffusion length of the reaction species influenced by the electric field of the measurement is small compared to the diffusion layer thickness of the electrode. Hence, the resulting Nyquist diagram exhibits a diagonal line with a 45° slope, equally to the behavior of an infinite Warburg element. When the measurement frequency is reduced further or when the diffusion layer thickness is small, the diffusion length of the species becomes relevant and the resulting Nyquist plot merges into a semicircle. In order to describe different results more accurately, the Finite Length Warburg impedance is expanded to a Generalized Finite Warburg impedance which is defined as:

$$Z_W = Y_0 (j\omega)^P \tanh\left(\delta \left(\frac{j\omega}{D}\right)^P\right) \quad 4-12$$

In this case, the square root is exchanged by a continuously varying exponent  $P$ .

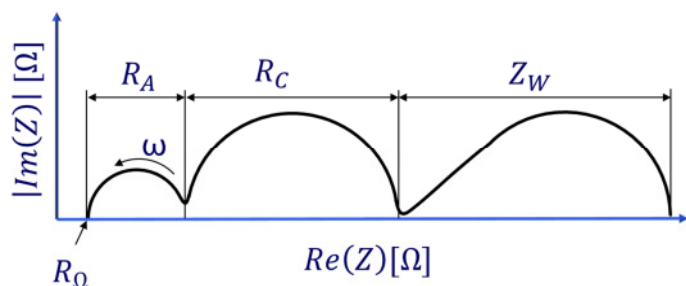
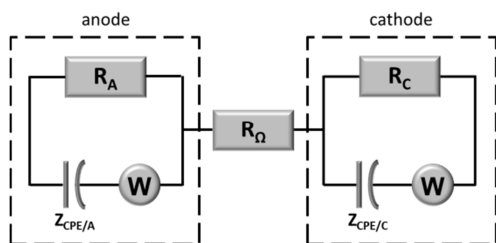


Figure 29: Equivalent circuit of a membrane-electrode-assembly

Figure 30: Resulting Nyquist plot of EIS measurement in membrane electrode assemblies

However, there is no conventional electrical component which describes such a behavior and could be inserted into an equivalent electric circuit. As the diffusion of the species is interlinked to the

charge transfer, these two elements are connected in series. Figure 29 shows the final equivalent circuit of a typical fuel cell.

Figure 30 illustrates an idealized measurement result of a Nyquist plot. It has to be considered that the impedances of the anode are significantly smaller compared to the cathode because the reaction kinetics are much faster. Hence, the performance of the cathode is the limiting factor inside fuel cells and of great interest when aspects for optimization are identified with the help of EIS measurements. This also means that the impedance of the anode is hardly detectable within a real Nyquist diagram. For best results, it has to be ensured that the applied potential of the spectroscopy measurement has only minimal influence on the system itself, e. g. that no oxidation takes place at the electrodes. This is realized by using small amplitudes below 100 mV. It is also possible to apply an alternating current and measure the potential of the system. This is called a galvanostatic measurement.

For interpretation of EIS spectra it is important to know the correlations of fuel cell parameters and their influence on the measurement result. In literature, the effects of materials, components and operating conditions have been discussed intensively. As mentioned above, the starting point of the Nyquist diagram at high frequencies marks the Ohmic resistances of the fuel cell summing up all electric components. However, the electric parts are usually constant throughout operation, so a change in  $R_o$  can be correlated to a change of the electrolyte membrane. This will be recognized by a shift of the Nyquist diagram along  $Re(Z)$  and may originate from a variation in proton conductivity. Typical reasons for this are changes in the humidity of the membrane, aging or poisoning [89].

In real experiments, the high frequency arc caused by the charge transfer and the electric double layer at the anode is of minor importance. Most results show a dominating arc originating from the reaction kinetics of the oxygen reduction at the cathode. This high frequency arc strongly depends on the applied current density. At high potentials but low current densities inside the fuel cell the resulting reaction kinetics at the electrode are relatively slow which leads to a high resistance for the charge transfer. Hence, a large diameter of the arc in the Nyquist diagram is measured. Changing specific design or operation parameters of the fuel cell like optimized internal resistances and better humidification will increase the current density at the same potential. This results in acceleration of the oxygen reduction reaction and pushes the reaction rate. Thereby, the charge transfer resistance is decreased and smaller diameters of the arc are observed [79] [90] [91] [92].

The low frequency arc of the Nyquist diagram is caused by the diffusion, respectively the mass transfer, of the reaction species at the electrodes. Hence, it is a measure for the accessibility of the 3 phase boundaries inside the catalyst layer, especially of the oxygen molecules at the cathode. A change in the diameter of this arc results from a limitation of the oxygen diffusion. This may be the

case at high current densities when the mass flow of the oxygen is not ensured anymore because of insufficient air flow, blocking by other gases like nitrogen or high flow resistances due to dense gas diffusion layers. This also means that high stoichiometry at the cathode will decrease the low frequency impedance, e. g. when the fuel cell is operated at high volume flows or with pure oxygen [91] [93]. From a components' perspective, changing the thickness, the material itself or the porosity of the electrode will also influence the diffusion of the species. Hence, EIS measurements of different fuel cell setups will result in different values of the Warburg impedance.

Analysis of EIS spectra may be complex. Usually, the results are not as clear as in the example model above. The evaluation, quantification and interpretation of specific arcs of a Nyquist diagram are crucial in understanding drawbacks of certain electrode configurations or operation parameters. This is why software tools were developed which are able to simulate different circuit models and help to match single parameters like the charge transfer resistance with the measurement results. In this thesis, Zplot® (Scribner Inc.) was used to analyze EIS data.

#### 4.4 Electrochemical atomic force microscopy (EC-AFM)

As explained before, PFSA consists of hydrophobic polymer backbones and hydrophilic sulphuric acid groups which form proton conducting channels. These channels are distributed statistically and their position, their relative amount per area as well as their level of hydration are of great importance for proton conduction and fuel cell performance. An interesting method for characterizing the nano-separated region is electrochemical atomic force microscopy (EC-AFM), also referred to as local conductivity (LC-)AFM. This measurement technique offers the possibility to observe morphological

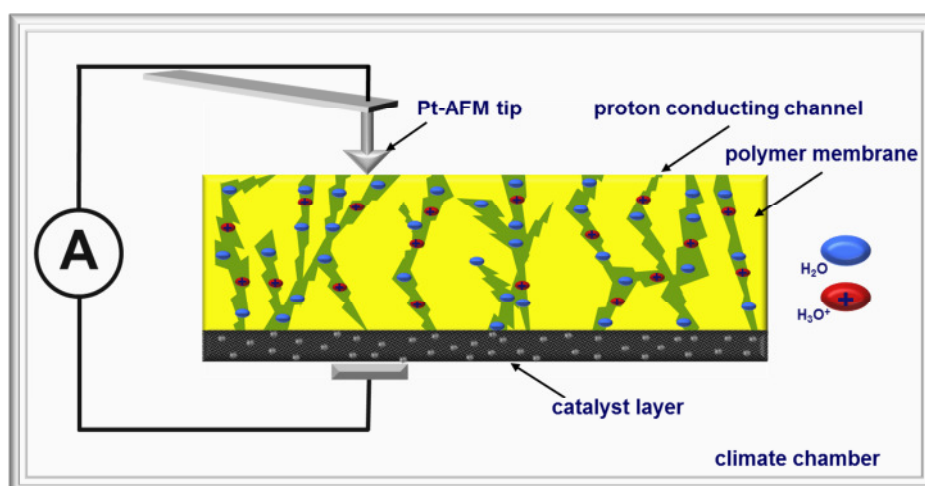
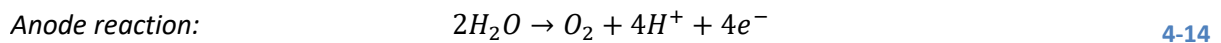
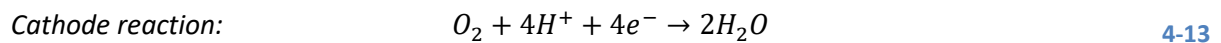


Figure 31: Principle drawing of the measurement setup for electrochemical atomic force microscopy; the sample is placed into a climate chamber and a Pt-based AFM tip works as connecting electrode for position specific reaction

and electrochemical information at the same time. The principle of the measurement setup can be seen in Figure 31. An atomic force microscope (AFM) is integrated into a climate chamber in order to control temperature and relative humidity during the experiment. The tip of the AFM is coated with Pt which provides catalytic activity and electric contact, forming the counter electrode (point electrode). Next, the tip is brought into contact with the membrane sample and a current is induced. The membrane itself has a catalyst layer on the side opposite to the AFM tip which is also connected to the voltage source to close the electric circuit. By applying a current through the membrane, a hydrolysis reaction is initiated at electrodes [94]:



Hence, the current at the conductive AFM-tip is a direct measure of the amount of protons that are transported through the membrane at the position of measurement [95] [96]. By varying the temperature in the range of 25°C up to 100°C, the relative humidity, the tip force or the current important information on the proton transport behavior can be obtained. For characterization of a micro fuel cell that is based on a porous silicon membrane with uniformly distributed micro channels this method can also provide results regarding the dependence of the proton conductivity from the porosity of the silicon membrane, e. g. if the pitch of the micro channels is too small or too large and what the influence of the transversal proton conduction on the membrane surface is.

#### 4.5 Kelvin probe resistance measurements

Modern ohmmeters detect resistances by applying a ratiometric measurement. Two electrodes are used in the basic measurements setup as described in Figure 32. For determination of the resistance of a sample the ratio of a given resistance  $R_g$  and the resistance of the sample  $R_s$  is quantified.  $R_i$  summarizes the internal resistance of the ohmmeter and the cables. By applying a voltage  $U_0$  to the electrical circuit and considering the known value of resistance  $R_g$ , the resistance  $R_s$  can be calculated by determination of the ratio of the dropping potentials  $U_g$  and  $U_s$ :

$$\frac{R_g}{R_s} = \frac{U_g}{U_s} \leftrightarrow R_s = R_g \frac{U_s}{U_g} \quad 4-15$$

The major advantage of the method is that the result is independent from the potential of the source which can vary as a result of declining battery capacity or similar. Unfortunately, measuring electrical resistances with the help of this method can be affected by a lot of sources of errors because all resistances of the electrical circuit are taken into account. Contact resistances and cable resistances distort the results and accurate measurement of the bulk resistance of the sample becomes difficult. This is of great importance in cases where small resistances need to be quantified [97] [98].



This is why 4-probe measurements, so-called Kelvin measurements, are used. The principle of this measurement method is shown in Figure 33. A defined current  $I_0$  is applied by an ammeter to the sample through a pair of electrodes. Additionally, the voltage drop along the sample is detected by another pair of electrodes with the help of a voltmeter. Assuming that the internal resistance of the voltmeter is high compared to the overall contact resistance and the resistances of the cables  $R_w$  and that the resulting measurement current of the voltmeter is small compared to the applied current of the ammeter, the voltage drop across the sample alone is detected [97] [98]. Thus, the resistance of the sample can be determined by Ohm's law because constant current from the Ammeter as well as voltage drop are known values. This method is commonly used for characterization of electrical resistances in fuel cell components, e. g. for bipolar plates, catalyst layers and gas diffusion layers.

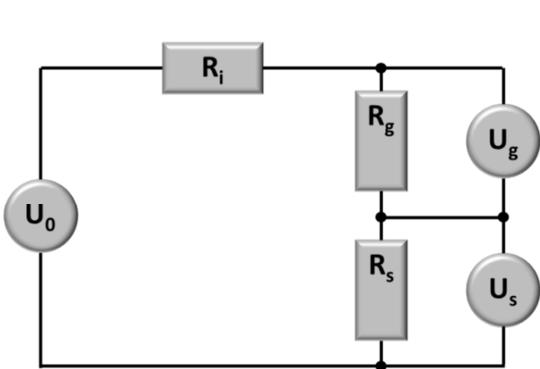


Figure 32: Principle of ratiometric measurement of an Ohmic resistance  $R_s$

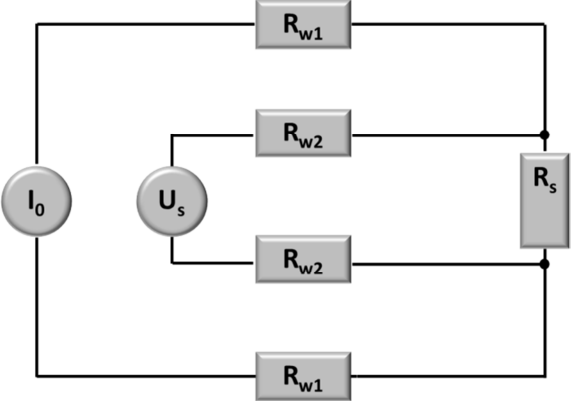


Figure 33: Principle of Kelvin resistance measurements of an Ohmic resistance  $R_s$

## 5 Concept of a micro membrane electrode assembly

In chapter 3.1 the high potential of free-standing micro membranes as micro membrane electrode assemblies was explained in detail. The possibility to integrate all major components (proton conductor, catalyst layer and current collector) allows for the fabrication of micro fuel cells with outstanding small volume. However, some drawbacks regarding thickness, structure size, integration of the electrolyte and fabrication of the current collector/catalyst layer were identified as well. Therefore, a major goal of this thesis is to overcome those issues by improving existing design features or identifying alternative designs and manufacturing procedures.

### 5.1 Design

The aim of this work is to realize a concept for a micro patterned silicon-based membrane electrode assembly that offers the following advantages:

- Thickness of  $\mu$ MEA of less than 30  $\mu\text{m}$
- High porosity of the silicon membrane with minimized pattern sizes of 1  $\mu\text{m}$
- Integrated, sputter deposited metal layer that acts as combined current collector/catalyst layer
- Mass fabrication compatible process for integrating a proton conducting electrolyte

The basic idea of the new concept is to integrate a buried  $\text{SiO}_2$ -layer in the middle of the membrane with a thickness of 100 nm for electric insulation of the electrodes.  $\text{SiO}_2$  differs significantly in wet etching behavior compared to silicon. It can be etched isotropically at significantly higher etching rates compared to silicon. As a consequence, an isotropic etching of the  $\text{SiO}_2$  layer will result in an under-etching which will give a “cave-like” structure (cf. Figure 34). This way, several challenges can be solved.

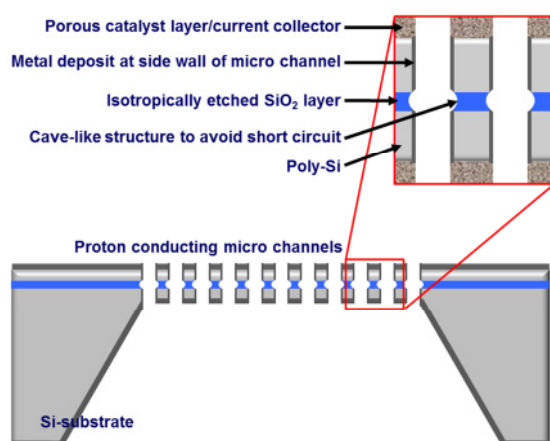


Figure 34: Basic drawing of the new  $\mu$ MEA concept.

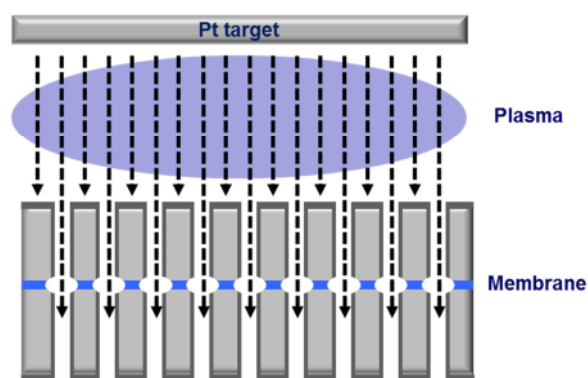


Figure 35: Sputter deposition of catalyst layer/current collector.

First, the catalyst layer/current collector can be sputter deposited after the patterning of the micro channels, because the coating molecules have a strongly directed flow throughout the deposition process (cf. Figure 35). Hence, they do not settle on the under-etched regions during sputter deposition. As a consequence, there is no need for etching the noble metals anymore which leads to a massive simplification of the following fabrication steps as no fences appear.

Second, the membrane can be fabricated extremely thin because possible short circuits do no longer depend on the membrane thickness. The small distance between the electrodes will correlate directly to the Ohmic resistances of the membrane and lead to higher absolute proton conductivity.

Third, it is possible to create a porous, sputter deposited metal layer with adequate thickness that serves as current collector as well as catalyst layer and can be fabricated by MEMS-compatible processes only. Hence, the  $\mu$ MEA can be fabricated within a MEMS production line which will help to

reduce costs and enable mass fabrication. Such a metal thin layer should give high catalytic activity if the sputter parameters are optimized regarding high specific and electrochemical active surface. With increasing thickness it should also exhibit low electric resistances for electron transfer.

## 5.2 Fabrication process

The fabrication process of the silicon-based micro membrane was developed in cooperation with the Institute for Microelectronics Stuttgart (IMS Chips). Figure 36 shows the process flow with the single fabrication steps. As etching of the membrane is the last step before post-processing and all structuring processes are done on a 700  $\mu\text{m}$  thick wafer substrate this is a so called wafer flow process. Obviously, the advantage of this method is the easy handling of the robust substrate in contrast to etching and structuring the free-standing membrane at the beginning which can only be realized with specific equipment.

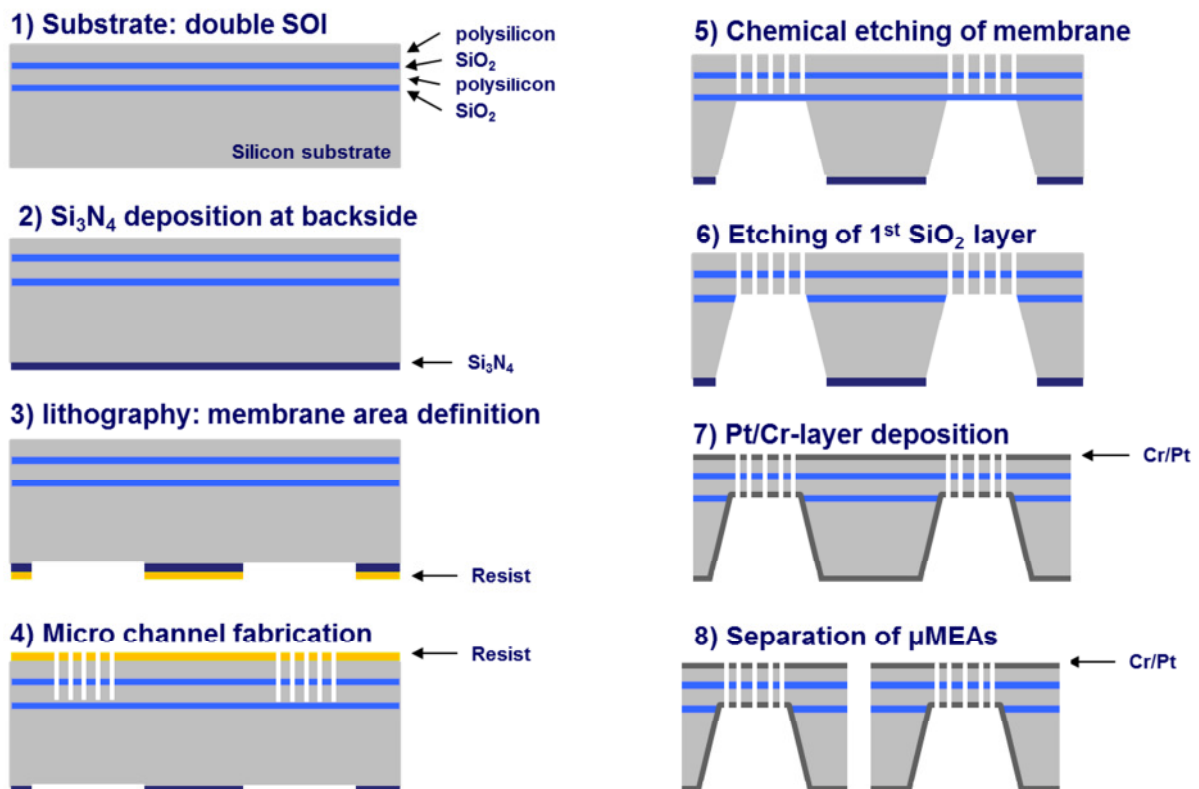


Figure 36: Fabrication process of the micro membrane: a double SOI substrate is prepared by layer deposition processes (1) followed by a  $\text{Si}_3\text{N}_4$  deposition at the backside of the substrate (2); for definition of the backside membrane etching, lithography and etching of the  $\text{Si}_3\text{N}_4$  are processed (3). After that, micro channel fabrication is realized by MEMS etching processes (Bosch process). The first  $\text{SiO}_2$  layer acts as an etch stop. (4); the substrate is wet etched from the backside to create thin membranes and the first  $\text{SiO}_2$  layer is used as an etch stop again (5); micro channels are completed by isotropic wet-etching of the first  $\text{SiO}_2$  layer; finally, Cr/Pt-layer is coated by sputter deposition (7) and single micro membranes are separated (8)

The first step of the fabrication process is to grow alternating layers of silicon dioxide ( $\text{SiO}_2$ ) and amorphous polysilicon (cf. step 1). This so-called double silicon on insulator (SOI) forms the final

membrane. The thickness of the polysilicon layer defines the thickness of the membrane and can be varied in a range between 5  $\mu\text{m}$  and 30  $\mu\text{m}$ . At first, the substrate, a 150 mm diameter, p-type, [100] oriented wafer is oxidized at high temperatures. Next, a thin polysilicon layer is deposited by chemical vapor deposition (CVD) and thickened by an epitaxy process. After levelling the surface by combined chemical/physical polishing the whole process is repeated until the required thickness is reached.

The polysilicon layer plays an important role regarding the control of the intrinsic mechanical stress. If the layer is fabricated in a way that results in compressive stress the membrane will bend undefined after etching which will complicate the following post processes like sputter deposition and integration of the electrolyte. Contrary, if the layer exhibits moderate tensile stress the membrane will be flat after etching but at a certain magnitude the stress will cause the polysilicon to crack.

In order to define the dimensions of the membrane, a silicon nitride ( $\text{Si}_3\text{N}_4$ ) layer is deposited at the backside of the substrate (cf. step 2). This is followed by a combined lithography and etching process (cf. step 3) in order to open windows where the anisotropic wet etching can access the single crystal silicon (cf. Figure 37). Membrane areas from  $5 \times 5 \text{ mm}^2$  up to  $20 \times 20 \text{ mm}^2$  were realized successfully.

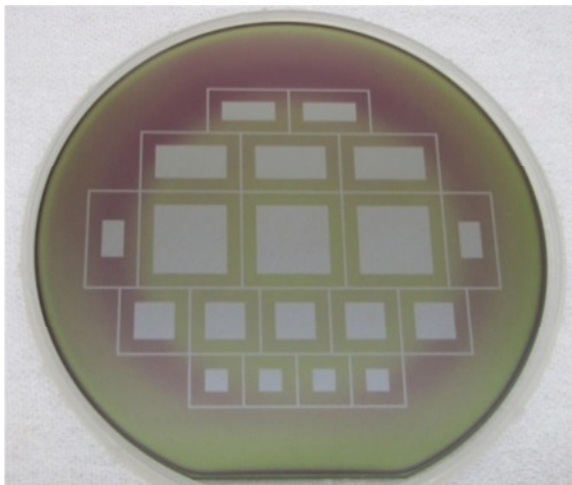


**Figure 37:** Back side of the substrate after defining the membrane areas inside the  $\text{Si}_3\text{N}_4$

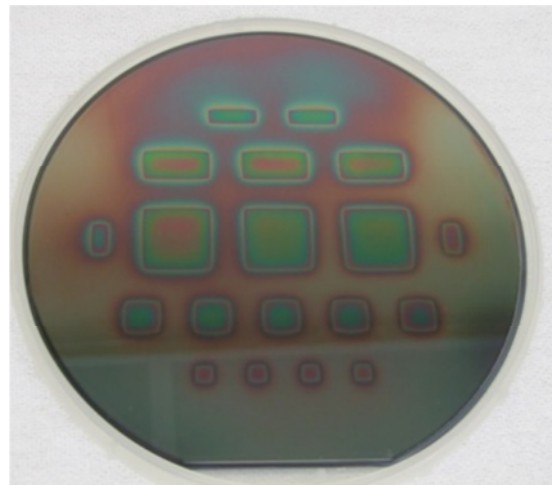


**Figure 38:** Front side of the substrate after structuring of the micro channels

Step 4 involves the definition of the micro channels. Their dimensions (diameter, pitch) are defined by a lithography process. For cost reduction a stepper mask is used. This means that individual fields of  $5 \times 5 \text{ mm}^2$  are exposed next to each other in order to realize the desired dimensions (cf. Figure 38). After that a dry etching process is executed: By alternating etching and passivation processes – the so-called Bosch-process – channels with high aspect ratios can be excavated into the polysilicon. The aspect ratio is defined as the ratio between the lateral and horizontal dimensions of a structure. In this case it is the ratio between the channel diameter and the channel length. As a first result, the

final channel diameter was determined at 1  $\mu\text{m}$  and the channel length at 10  $\mu\text{m}$  (according to the membrane thickness) which correlates to an aspect ratio of 10. For etching  $\text{SF}_6$  and for passivation  $\text{C}_4\text{F}_8$  were used.

The buried  $\text{SiO}_2$  layer between the two polysilicon layers is wet-etched isotropically in HF. The isotropic etching results in the desired cave-like structure that is described above. Figure 39 shows a SEM-image of a cross-section of the etched upper polysilicon layer before etching of the  $\text{SiO}_2$  layer. Figure 40 represents a close-up of the etched  $\text{SiO}_2$ -layer and the resulting undercut. Finally, another anisotropic Bosch process etches the lower polysilicon layer (cf. Figure 41).

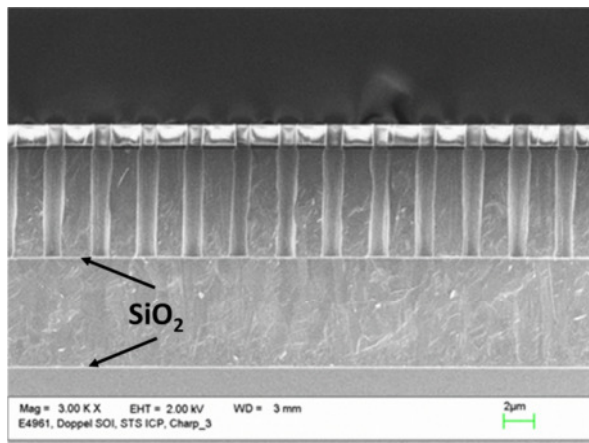


**Figure 39:** SEM image of the double SOI wafer etched anisotropically down to the buried  $\text{SiO}_2$  layer.

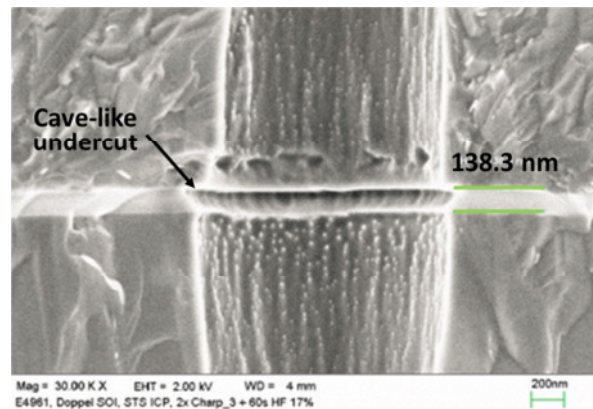


**Figure 40:** SEM image of isotropically etched  $\text{SiO}_2$  layer for creating undercut structure.

Etching of the membrane area is done by an anisotropic wet etching from the backside (cf. step 5). Therefore, the  $\text{SiO}_2$ -layer between monocrystalline silicon substrate and first polysilicon layer serves as an etch stop layer. As the single crystal silicon of the substrate is etched with the help of KOH the etching rate of  $\text{SiO}_2$  is significantly lower (10-50 nm/min at 80°C, 44 % KOH) than the etching rate of single crystal silicon (ca. 1  $\mu\text{m}/\text{min}$  at 80 °C, 44 % KOH). This way, the desired membrane thickness can be realized precisely. In order to achieve the final membrane design the  $\text{SiO}_2$  etch stop layer is completely removed with an isotropic wet etching in HF (cf. step 6).

Before the membranes are separated the bifunctional Cr-/Pt-layer is fabricated by PVD (cf. steps 7 & 8). Figure 42 shows an image of a final silicon micro membrane with a microstructured area of 10 x 20  $\text{mm}^2$ . For further characterization, this size was used for all samples in this thesis to ensure comparability. Separation is realized by breaking the wafer along trenches that were also etched in step 5.

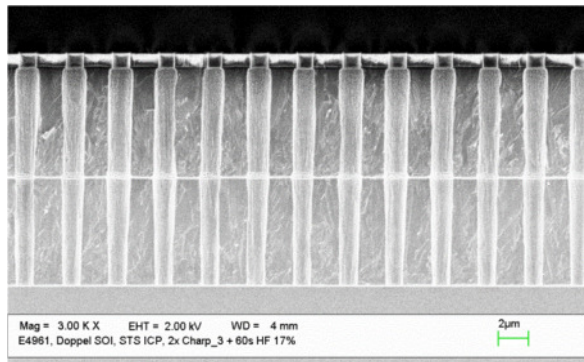


**Figure 41: SEM image of resulting micro channels with buried undercut structure**

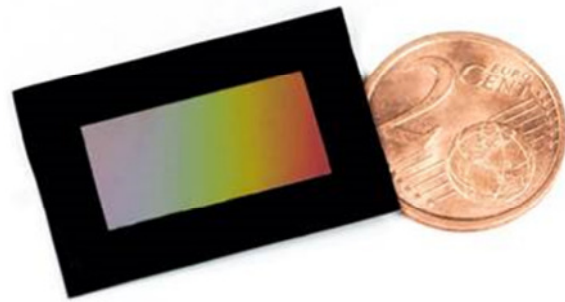


**Figure 42: Image of a 10x20 mm<sup>2</sup> micro membrane with 5 mm solid edge**

### 5.3 Integration of polymer electrolyte

In chapter 3.1 it was emphasized that the integration of the polymer electrolyte into the micro channels of the membrane is crucial for succeeding in the development of an effective  $\mu$ MEA and may be the most difficult process step. Unfilled micro channels lead to leakages that allow fuel gases to reach the other side of the membrane. As a consequence, mixed potentials occur that result in high overpotentials (cf. chapter 2.2). Because of the difficulties of integrating “dry” particles into silicon micro channels, mostly originating from electrostatic charges of the material, it is necessary to apply a sol-gel process. Thus, a suitable dispersion has to be identified which is hydrophobic to the silicon surface of the membrane and the micro channels and – at the same time – contains an adequate amount of ionomer particles that are small enough to fit into the micro. Furthermore, the fabrication method has to provide reproducible results and exhibit short process times as well as low costs.

#### 5.3.1 Identification of suitable electrolyte dispersion

PFSA ionomers can be dispersed in different solvents which differ in surface tension and viscosity affecting the size of the PFSA particles. All dispersions used in this work were delivered by fumatech GmbH, Germany which distribute PFSA under the brand name fumion®. Table 2 gives an overview of the different ionomer dispersions that were tested and their characteristics.

The use of hydrophilic capillary forces for integration of the electrolyte is a promising method as no external forces need to be applied and all micro channels can be filled at once.

When Dimethylacetamide (DMAC) is used as solvent (FLD 910), it contains ionomer particles (500 nm) which are in the range of the size of micro channels (1  $\mu$ m). This makes it unsuitable for the integration process. Partly filled channels would be expected, especially if the channel diameter needs to be reduced further. The remaining dispersions were tested regarding surface tension



interacting with the Pt-coated membrane. Therefore, a droplet of the dispersion was placed onto the surface and the contact angle  $\theta$  was determined with the help of a goniometer. Figure 43 – Figure 46 show the resulting droplets of the dispersions formed when in contact with the Pt-surface.

Labeling	Solvent	Particle size (nm)	Polymer content (wt%)	Acid capacity (H+, meq/g)
FLA 910	Water	ca. 200	10	1,1
FLN 910	N-Propanol	< 100	10	1,1
FLD 910	Dimethylacetamide	ca. 500	10	1,1
FLNA 910	Water/N-Propanol	ca. 120	10	1,1

Table 2: Overview of PFSA dispersions tested for applicability in silicon-based micro MEA.

Water was also tested as a reference. It can be seen that N-propanol is essential for decreasing the contact angle in order to reach hydrophilic behavior of the dispersion ( $\theta < 90^\circ$ ). Fumion® FLA dispersions exhibit strong hydrophobic characteristics ( $\theta > 90^\circ$ ) and are not applicable. So, Fumion® FLNA and Fumion® FLN dispersions were chosen for further characterization.

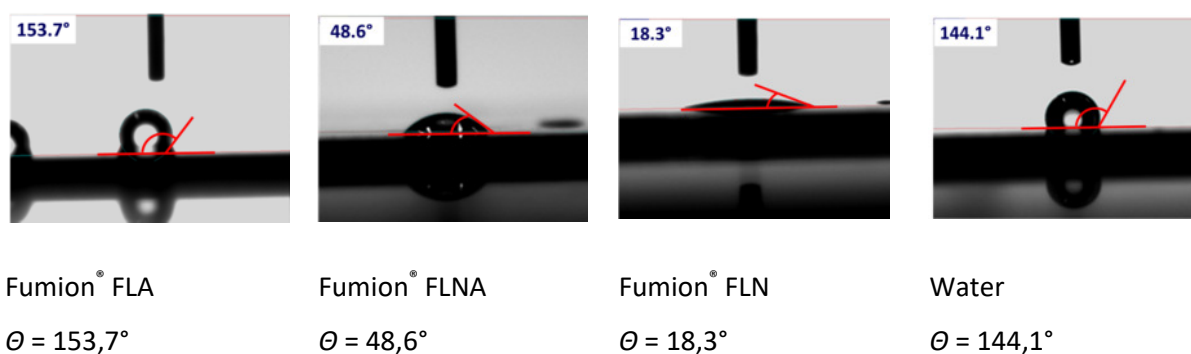


Figure 43: Fumion® FLA on membrane surface.

Figure 44: Fumion® FLNA on membrane surface.

Figure 45: Fumion® FLN on membrane surface.

Figure 46: Water on membrane surface as reference measurement.

Therefore, 0.01 ml Fumion® FLNA 910 dispersion was dropped onto a membrane and dried in a vacuum chamber for 5 min. By applying a vacuum instead of using a hotplate a chemical reaction of the ionomer due to induction of thermal energy and the formation of gas traps from volatilizing solvents were avoided. Figure 47 is a SEM image showing the cross section of the membrane. The PFSA has entered the micro channels and a complete filling could be achieved after drying the solvent. So, the dispersion solvents are suitable for integration of the polymer electrolyte. But two major drawbacks of this method can be identified: The first one is the so-called “coffee-ring effect”. When a droplet of solvent filled with particles evaporates the contact line of the fluid is pinned to the

underlying surface. This leads to a changing contact angle throughout evaporation of the solvent. Hence, a capillary flow of the particles from the center of the droplet to the edges is generated which results in an increased particle concentration and layer thickness of the final polymer layer at the outer region (cf. Figure 48) [99] [100] [101] [102] [103].

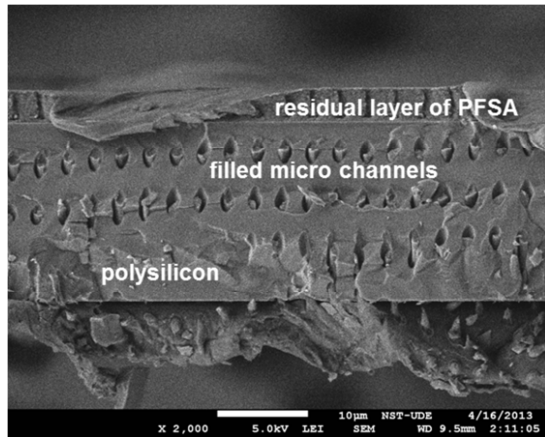


Figure 47: SEM image of PFSA polymer integrated into micro membrane by drop coating process.

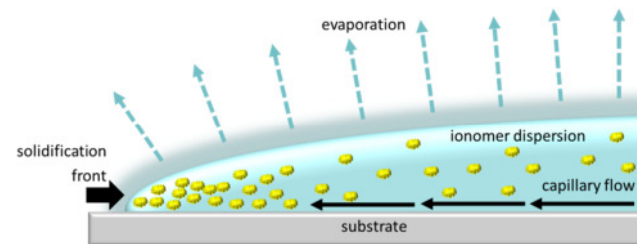


Figure 48: Sketch of the principle emergence of the coffee-ring effect which leads to inhomogeneous distribution of polymer particles.

This phenomenon can also be observed with PFSA dispersions. Figure 49 and Figure 50 show samples of Fumion® FLNA droplets dried on a silicon surface, one by applying a temperature of 50°C on a hotplate and one by evaporation of the solvent in a vacuum chamber. The thickness of the layer was determined with the help of a confocal microscope (Nanofocus µsurf costum). Both samples exhibit typical morphology of the coffee-ring effect. The edges of the polymer layer are significantly thicker than the polymer layer in the middle. Furthermore, the layer thickness is not constant and inhomogeneous. This makes it challenging to achieve a complete filling of the micro channels with a minimized residual layer on the surface which is the second disadvantage of this method. Such a residual layer would hinder the fuel gases to reach the catalyst layer and lead to increased

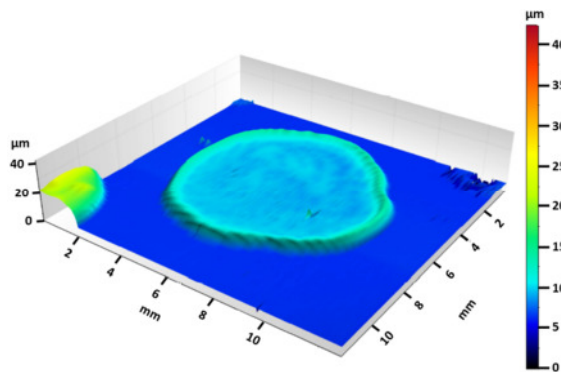


Figure 49: PFSA dispersion (Fumion® FLNA) dried in a vacuum chamber.

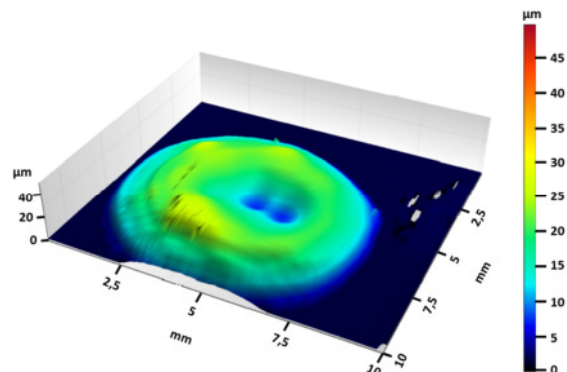


Figure 50: PFSA dispersion (Fumion® FLNA) dried on a hotplate at 50°C.



overpotentials. As can be seen in Figure 47 the residual layer has a thickness of almost 5  $\mu\text{m}$  which is too much for the hydrogen and oxygen molecules to diffuse to the Cr-/Pt- layer.

All in all it has to be constituted that the examined fumion<sup>®</sup>-dispersions are suitable for the integration of a polymer electrolyte into the micro channels. However, the method of simply dropping the PFSA dispersion onto the surface is not appropriate, especially considering the aspects of reproducibility, mass fabrication and performance of the micro MEA.

### 5.3.2 Dip Coating process for integration of electrolyte

In the previous chapter, it became clear that drop coating of the PFSA dispersion leads to inhomogeneous surfaces and large residual film thicknesses. Hence, a process with an in-situ evaporation of the solvent is likely to be advantageous. Furthermore, this process needs to have the potential to fill all micro channels with polymer and result in small residual film thicknesses on the membrane surface. This is a challenging task, especially if it is considered that a membrane as described above with an area of  $10 \times 20 \text{ mm}^2$ , a channel diameter of  $1 \mu\text{m}$  and a channel pitch of  $2 \mu\text{m}$  exhibits no less than  $50 \times 10^6$  micro channels. All micro channels which are not filled completely lead to impermeabilities within the membrane and thereby cause a decrease in voltage and performance of the fuel cell (cf. chapter 2.2).

An interesting alternative to drop coating methods like spray coating is a dip coating process. Being a simple and cheap sol-gel process, dip coating is widely used in industry applications, e. g. for deposition of anti-reflex coatings on windows.

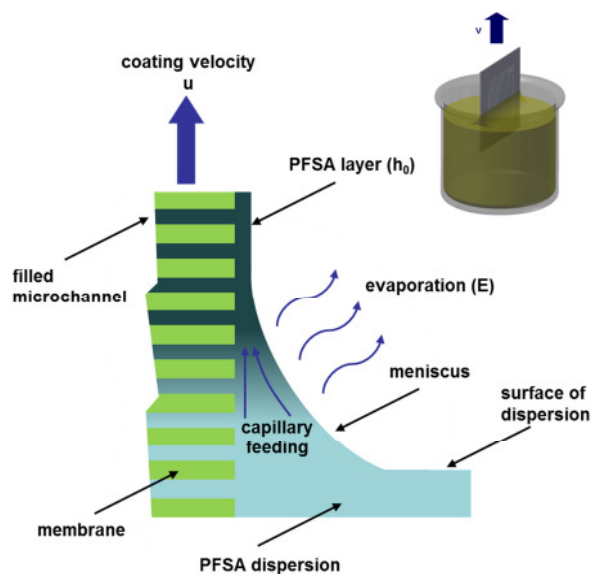


Figure 51: Principle drawing of the dip-coating process for a porous membrane.

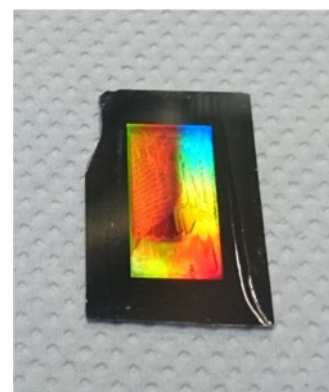


Figure 52: Photo of a membrane where the PFSA was integrated by dip-coating process. Interference pattern indicates residual layer thickness in the range of  $< 1 \mu\text{m}$ .

The basic principle of the dip coating process is shown in Figure 51. It is based on the approach to withdraw a substrate vertically from a dispersion containing the coating particles (sol). By carefully adjusting the withdrawal speed and the evaporation conditions of the solvent a coating of defined thickness and high homogeneity can be obtained. Moreover, it is possible to tailor the microstructure of the coating [104] [105]. Figure 52 shows an image of a micro membrane that was used to test the dip coating process. The interference structure of the active area indicates a residual layer thickness of less than 1  $\mu\text{m}$ .

In order to understand the physical and mechanical correlations that occur throughout dip coating, the balance of forces needs to be considered. The force due to acceleration of gravity  $g$  is directed opposite to the direction of withdrawal and causes the fluid to flow downwards. In contrast to that, the surface tension  $\gamma_{LV}$  of the liquid-vapor interface and the viscosity  $\eta$  define the shape of a steady-state meniscus and by that the flowing behavior of the fluid (cf. Figure 51). When the coating velocity  $u$  is hold at a constant value, a steady-state process is established and the thickness  $h_L$  can be calculated as [104] [106]:

$$h_L = c \frac{(\eta u)^{2/3}}{\gamma_{LV}^{1/6} (\rho g)^{1/2}} \quad 5-1$$

For Newtonian fluids  $c$  is 0.94 and  $\rho$  represents the density of the sol. This is the so-called Landau-Levich equation. It is only valid if the withdrawal speed  $u$  is the dominant factor and evaporation rate can be neglected. In this case, the film thickness increases with higher withdrawal speed.

When the withdrawal speed becomes very slow the evaporation rate  $E$  has a significant influence on the coating film thickness. In this case, a continuous capillary feeding of the sol is established to the upper end of the meniscus, leading to increasing concentrations. Thus, the Landau-Levich equation has to be extended [107] [108]:

$$h_L = \frac{c_i M_i E}{\alpha_i \rho L u} + c \frac{(\eta u)^{2/3}}{\gamma_{LV}^{1/6} (\rho g)^{1/2}} \quad 5-2$$

Within this correlation,  $c_i$  is the inorganic molar concentration of the solution and  $\alpha_i$  the volume fraction of the dispersion particles, while  $M_i$  represents the molar mass and  $L$  the width of the coating sample.

As can be seen from this equation, there are two additive terms, one dominant at very low withdrawal velocities and one dominant at higher withdrawal velocities. The first is defined as capillary regime and the second one as the draining regime [108]. As both regimes exhibit a velocity-dependent film thickness but opposed slopes, a characteristic minimum at intermedium withdrawal velocities can be identified. For the generation of thicker films at constant withdrawal velocities the

evaporation rate has to be increased, e. g. through heating of the solvent or establishing a moderate vacuum.

Besides its ability of generating thin films with high homogeneity, dip coating processes have also proven their ability for the integration of sols onto microstructures and into porous substrates [109] [110] [111] [112] [113]. Grosso *et al.* postulates that dip coating is well suitable for the infiltration of networks of nanopores due to the unidirectional progression of the linear meniscus which ensures the displacement of gases inside the pores. Moreover, the osmophoresis diffusion of a sol into the pores is driven by the increase of concentration throughout evaporation of the solvent. The pore size determines the liquid/vapour interface and, by that, a strongly curved meniscus from the top to the bottom of the porous sample occurs. Hence, the dispersion particles are coated onto the entire pore surface [111]. It was also found by Darhuber *et al.* that parameters like geometry, pattern size and angular orientation have a significant impact on the impregnation result and the thickness of the residual layer [112].

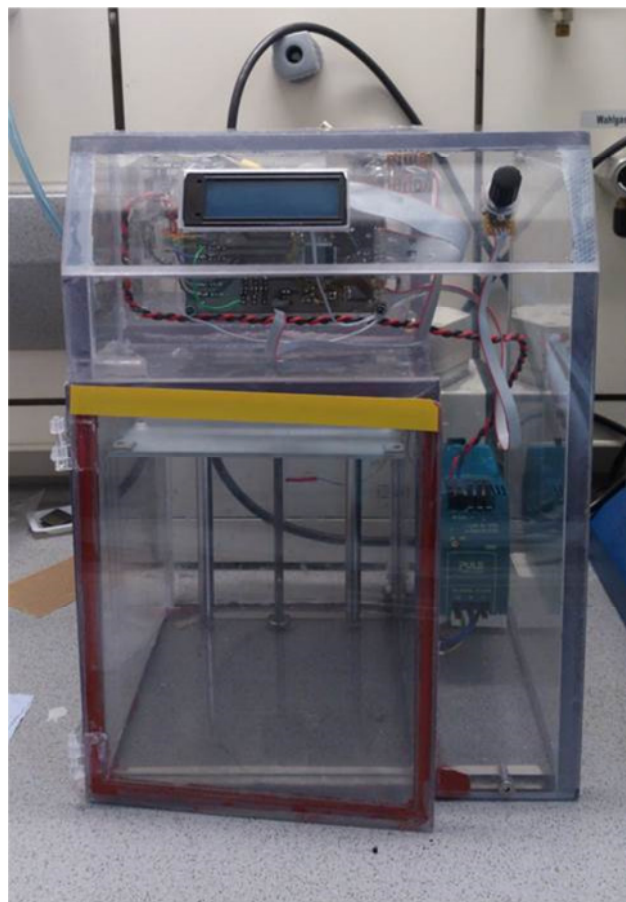


**Figure 53: Photo of the final dip coater which was designed and assembled at ZBT; withdrawal length of 100 mm can be realized and withdrawal speed can be adjusted between 0.1 mm/min and 30 mm/min**

In order to realize a dip coating process for integration of ionomers into porous silicon membranes, a dip coater was designed and assembled. In contrast to most approaches found in literature, the

control of the evaporation rate was not realized by heating the solvent but by applying a negative pressure in a sealed chamber. This way, it was assured that the polymer is not affected by higher temperatures and, moreover, voids inside the micro channels can be avoided. The housing of the dip coater was made out of 10 mm thick PMMA in order to have optical access during the coating process. The samples are clamped into a mounting which is usually used for tensile tests. This way, it can be assured that the sample is kept vertically throughout the whole coating process. With the help of a belt drive and additional gearing mechanisms withdrawal velocities of 0.1 mm/min up to 30 mm/min are achieved. Sensors for pressure, temperature and position monitoring were integrated in order to keep track of the coating parameters. A simple control unit was developed which allows defining start position, end position and withdrawal speed. Figure 53 shows an image of the final dip coater.

For characterization of the dip coating process, silicon substrates with  $15 \times 15 \text{ mm}^2$  were dip coated at varying withdrawal velocities and with different ionomer dispersions. The coating was done at room temperature and at 350 mbar. For each tested velocity, the film thickness of the sample was measured at 5 different spots via confocal microscopy (nanofocus  $\mu\text{surf}$  costum) by detecting the surfaces of the substrate and the transparent PFSA layer. The average of the 5 spots was determined, defining the film thickness. Two ionomer dispersions were investigated, Fumion® FLNA 910 and Fumion® FLN 910 as these two were identified to be the most promising. Figure 54 shows the result of the measurements. Both dispersions exhibit the typical characteristics of a dip coating process. A minimum of the film thickness can be found at withdrawal velocities between 5 mm/min to 10 mm/min. For FLN 910 the film thickness at these velocities could not be detected any more due to limits of the optical measurement method, while a minimum film thickness of  $0.5 \mu\text{m}$  was determined for FLNA 910. At withdrawal velocities below 5 mm/min the film thickness increases significantly, representing the capillary regime, while above 10 mm/min the film thickness is increasing again corresponding to the draining regime of the Landau-Levich equation. For Fumion® FLNA 910 dispersions a maximum thickness of  $2.5 \mu\text{m}$  could be achieved at a withdrawal velocity of 0.1 mm/min and  $1 \mu\text{m}$  thickness at 30 mm/min. For Fumion® FLN 910 dispersions, the obtained thickness at 0.1 mm/min was  $1.8 \mu\text{m}$  and at 30 mm/min a thickness of  $0.2 \mu\text{m}$  was measured.

Thus, if the two ionomers are compared, it can be constituted that Fumion® FLNA 910 results in significantly thicker coatings than Fumion® FLN 910. The reason for that is the lower viscosity of the N-propanol compared to water (cf. eq. 5-2). However, the volume of the micro channels cannot be filled by the amount of polymer that is deposited with Fumion® FLN 910 dispersions. Hence, Fumion® FLNA 910 dispersions were chosen for dip coating of the membrane.

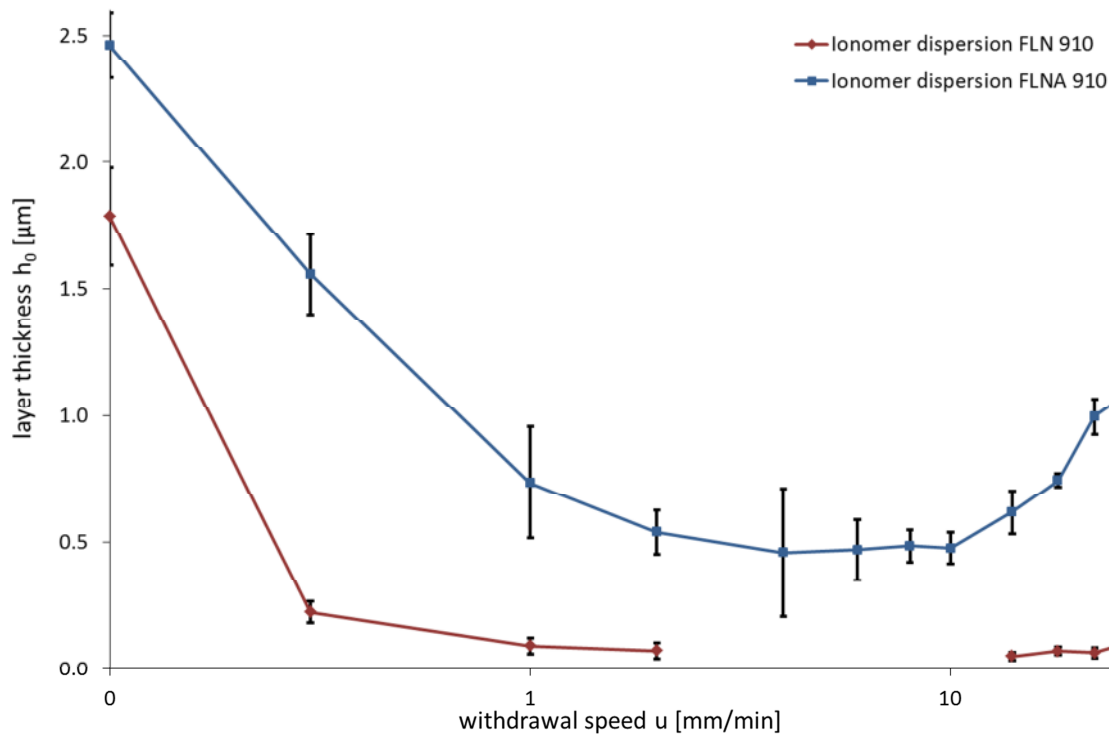


Figure 54: Film thickness as a function of withdrawal speed for two different PFSA dispersions; a clear minimum of film thickness can be identified.

The optimal coating velocity for dip coating of the membrane can be calculated by considering the pore volume compared to the coating volume at different velocities which was determined with the experiment described above. As the membrane thickness is  $5 \mu\text{m}$  and the micro channels exhibit a diameter of  $1 \mu\text{m}$ , the volume of a single channel is  $4 \mu\text{m}^3$ . Considering the pitch of  $2 \mu\text{m}$  the pore volume per  $\text{cm}^2$  can be calculated to  $0.1 \text{ mm}^3/\text{cm}^2$ . This correlates to a film thickness of  $1 \mu\text{m}$  obtained in the experiment above. As it is highly unlikely that all ionomer particles will be deposited into the channels, a withdrawal speed corresponding to  $1.5 \mu\text{m}$  film thickness seems to be a good estimate. This would mean that the optimum of the coating velocity should be  $0.4 \text{ mm/min}$ .

## 6 Characterization of MEMS-based $\mu\text{MEAs}$

In this chapter, the MEMS-based design of a  $\mu\text{MEA}$  was tested regarding its electrochemical performance. This includes basic fuel cell operation, but also detailed electrochemical measurements in order to understand the specific reaction kinetics of different electrode configurations.

As was shown in chapter 5.3, fumion® FLNA 910 was identified to be the best choice for polymer integration into the micro channels. So, for all experiments this ionomer dispersion was used. The gas volume flows in all fuel cell operation tests were set to  $2 \text{ ml/min}$  for  $\text{H}_2$  supply and  $4 \text{ ml/min}$  for air supply corresponding to the minimum gas flows adjustable.

## 6.1 Sputter coated bifunctional Cr-/Pt-layer

This electrode configuration follows the fabrication process described in chapter 5.2. A Cr-/Pt-layer is sputter coated onto the microstructured membrane before a ionomer is integrated into the micro channels. This Cr-/Pt-layer is supposed to serve as current collector for all generated electrons, but also as the catalyst layer that drives the fuel cell reaction. Hence, the first step is to adjust the sputter conditions in order to optimize Pt-utilization and to evaluate the fuel cell performance of such an electrode afterwards.

### 6.1.1 Evaluation of the sputter parameters for optimized electrode performance

As was described in chapter 2.3.2 and chapter 3.2, high specific surface area results in effective Pt-utilization. The Thornton model given in chapter 3.2 gives information about how certain sputter parameters affect the specific surface. This includes variation of temperature, sputter power and pressure of the sputter chamber. At specific combinations of those three parameters, porous structures with high specific surface can be achieved. Due to invariability of the first two parameters within the available sputter equipment, the focus of the experiments was to find optimal sputter pressure conditions and examine the influence of the film thickness.

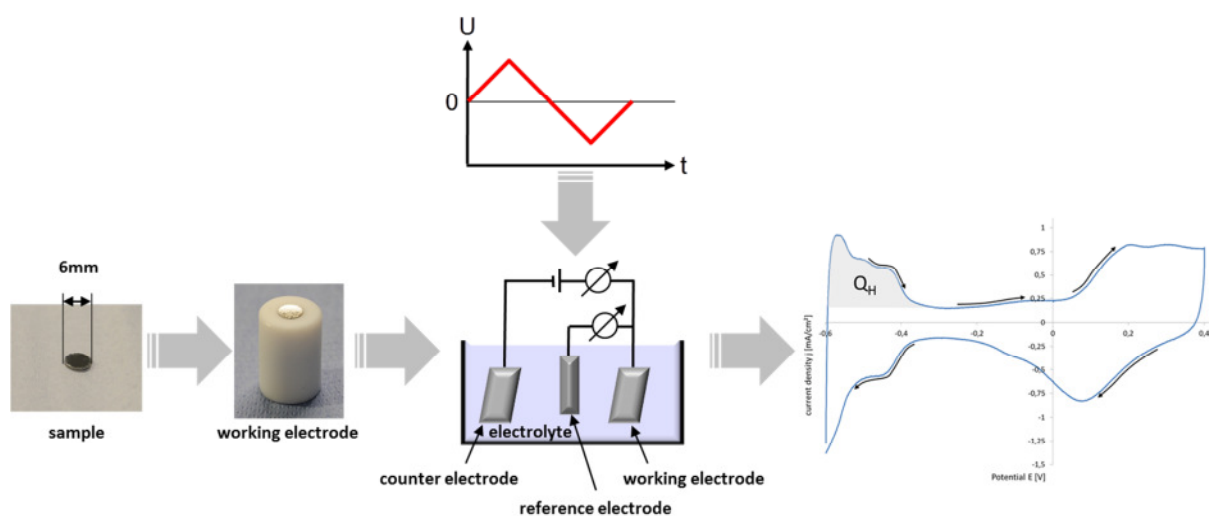
Therefore, samples of silicon with a diameter of 6 mm (28 mm<sup>2</sup> geometrical area) were cut with a solid state laser and sputter coated on both sides and the sidewalls with an 80 nm thick Cr-layer which served as adhesion layer and electric contact for the potentiometer. Afterwards, Pt-layers of varying sputter pressure and thickness were coated on one side of the samples and characterized by cyclic voltammetry. Table 3 gives information about the different sputter conditions that were applied.

Coating material	Film thickness (based on sputter time) [nm]	Sputter voltage [V]	Sputter current [A]	Sputter power [W]	Sputter pressure [mbar]	Resulting Pt loading [mg <sub>Pt</sub> /cm <sup>2</sup> ]
Pt	50	386	3,35	1293.1	4,3x10 <sup>-3</sup>	0.1
Pt	50	434	2,98	1293.3	1,8x10 <sup>-1</sup>	0.1
Pt	50	484	2,67	1292.3	1,9x10 <sup>1</sup>	0.1
Pt	10	485	2,67	1295.0	1,9x10 <sup>1</sup>	0.02
Pt	100	485	2,67	1295.0	1,9x10 <sup>1</sup>	0.2

Table 3: Overview of applied sputter conditions for deposition of Cr-/Pt-layer

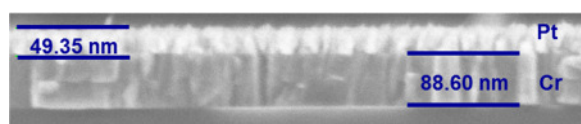
All parameters were fabricated twice in order to back the results. Pt loadings between  $0.02 \text{ mg}_{\text{Pt}}/\text{cm}^2$  and  $0.2 \text{ mg}_{\text{Pt}}/\text{cm}^2$  were realized.

Figure 55 shows the measurement setup for the characterization of the sputtered thin films. The sputter coated silicon samples were integrated into PTFE holders, put into a three electrodes setup and characterized with a Biologic SP-150 potentiometer. As reference electrode  $\text{Hg}/\text{Hg}_2\text{SO}_4$  in saturated  $\text{K}_2\text{SO}_4$  was used. The electrolyte was  $0.05 \text{ M H}_2\text{SO}_4$  while the scan rate was set to  $100 \text{ mV/s}$ . At least 100 cycles were executed prior to the measurement in order to stabilize the current answer. The results were analyzed numerically and ECAS as well as roughness factors according to equation 4-2 respectively 4-3 were compared with results from literature.



**Figure 55: Sketch of the measurement setup for characterization of the sputter deposited Pt-layers.**

Figure 56 and Figure 57 show two scanning electron microscopy (SEM) images of samples sputter coated at different chamber pressures. The first one shows a Pt-layer deposited at  $4.3 \times 10^{-3} \text{ mbar}$  while the second one was fabricated at  $1.9 \times 10^1 \text{ mbar}$ . Both samples underwent the same sputtering time, so the same amount of Pt was deposited onto the surface. It becomes clear that a higher sputter pressure leads to more porous layers as the Thornton model predicts.



**Figure 56: SEM image of a Pt-layer sputter coated at  $4.3 \times 10^{-3} \text{ mbar}$ . Due to the low pressure the Pt-layer is dense and has the expected thickness of 50 nm.**

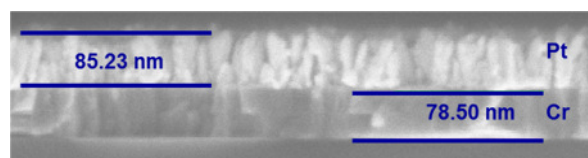


**Figure 57: SEM image of a Pt-layer sputter coated at  $1.9 \times 10^1 \text{ mbar}$ . As pressure was increased significantly, the porosity of the Pt-layer has increased as well. Hence the same sputter time (same amount of Pt) leads to increased thickness of the layer.**



ECAS and RfA of different sputter pressures were determined by cyclic voltammetry. In Figure 58 the final voltammograms are illustrated. They are in good agreement with results obtained from the SEM images. As expected, higher sputter pressures lead to increasing ECAS. Table 4 gives an overview of the resulting roughness factors determined from the voltammograms. A maximum of 9.35 for samples with 50 nm thickness and fabricated at  $1.9 \times 10^1$  mbar was identified. Compared to the findings of Slavcheva *et al.* this is significantly lower as she and her colleagues obtained RfA's up to 15.82 for 50 nm thick layers. One important aspect to be noted is that the applied sputter power of about 1290 W is quite high. Within this experiment it was not possible to vary the sputter power as this parameter of the sputter unit needed to stay fixed for quality assurance purposes in mass production of other applications. However, Slavcheva *et al.* found that low sputter power gives reasonably better porosity and by that higher ECAS [71].

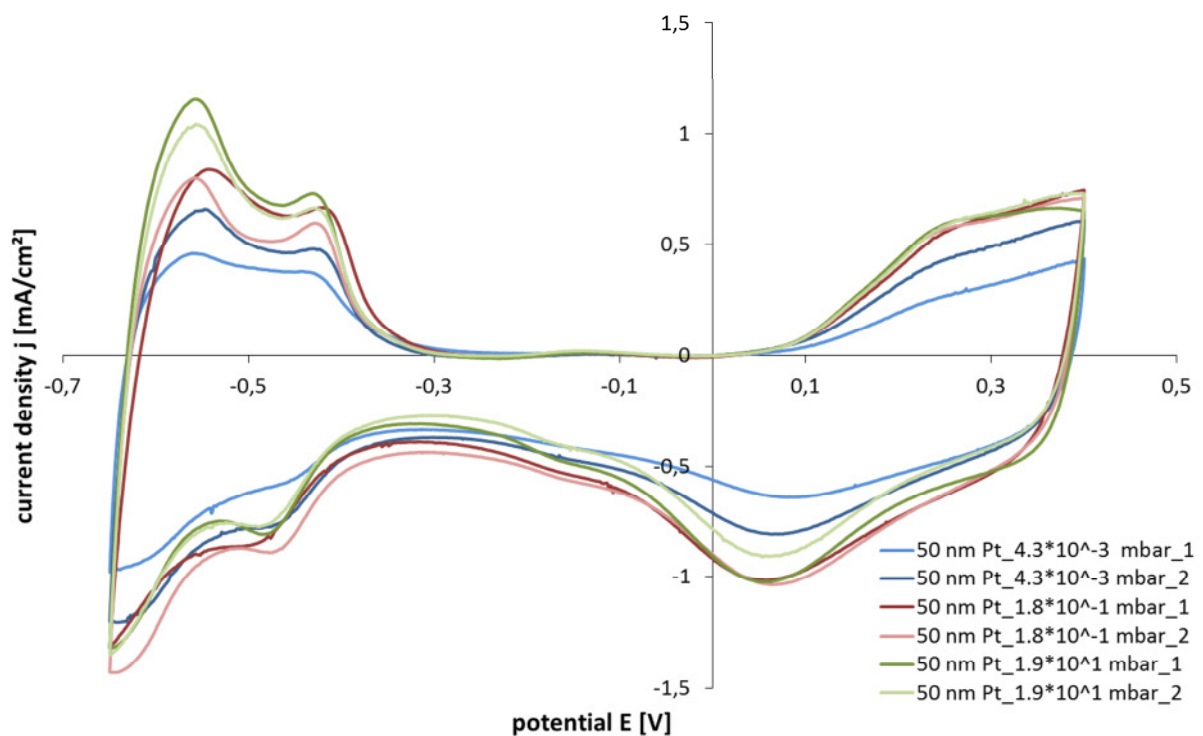


Figure 58: Cyclic voltammograms of 6 layers with 3 varying sputter pressures and layer thickness of 50 nm; scan rate was set to 100 mV/s at 0 rpm; as electrolyte 0.05 M  $\text{H}_2\text{SO}_4$  and as reference electrode  $\text{Hg}/\text{Hg}_2\text{SO}_4$  in saturated  $\text{K}_2\text{SO}_4$  were used; the diagrams were leveled to the x-axis in order to subtract the capacitive currents for determination of the hydrogen desorption.

As optimization of the sputter pressure results in relatively small values for ECAS and RfA, the influence of varying layer thickness needed to be examined as well. Therefore, samples with 10 nm, 50 nm and 100 nm Pt were fabricated. Resulting voltammograms demonstrate that there is a rapid increase of the hydrogen adsorption peaks from 10 nm to 50 nm layer thickness (cf. Figure 59).



Due to the low thickness of 10 nm Pt it is most likely that no dense coating was formed during sputter deposition and that Pt clusters formed instead. Surprisingly, there is no significant increase of ECAS and RFA if the layer thickness is doubled to 100 nm (cf. Table 4). The explanation of this effect is that the porosity does not suffice to maintain a pillar-like structure at higher layer thickness. Instead, Pt settles at the walls of the pillars forming a dense, compact metal film at the bottom of the layer. In contrast to that, Slavcheva *et al.* obtained significant enhancements even for 600 nm thick films which exhibited RFA's up to 93.62 [71], originating from the high porosity of the Pt-layers with more suitable sputter parameters.

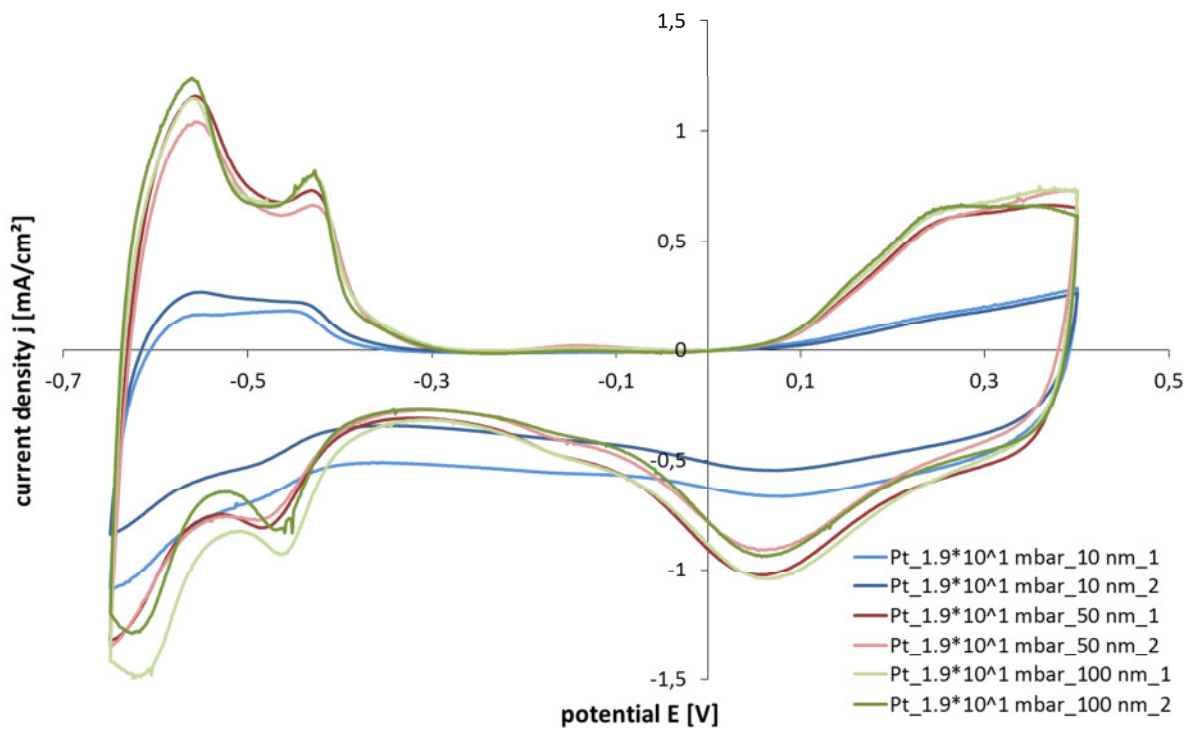


Figure 59: Cyclic voltammograms of 6 layers with 3 varying thicknesses, deposited at  $1.9 \times 10^1$  mbar; scan rate was set to 100 mV/s at 0 rpm; as electrolyte 0.05 M  $H_2SO_4$  and as reference electrode  $Hg/Hg_2SO_4$  in saturated  $K_2SO_4$  were used; the diagrams were leveled to the x-axis in order to subtract the capacitive currents for determination of the hydrogen desorption.

For the given equipment, the best parameters identified by voltammetry experiments are a sputter pressure of  $1.9 \times 10^1$  mbar and a layer thickness of 50 nm. It must be stated that performance of the micro MEA is expected to be low compared to conventional fuel cell concepts as power densities strongly depend on Pt utilization and ECAS of the catalyst layer.

Layer thickness [nm]	Sputter pressure [mbar]	Roughness factor (RFa)	ECAS [mm <sup>2</sup> ]
50	4.3x10 <sup>-3</sup>	6.03	168.84
50	4.3x10 <sup>-3</sup>	7.44	208.32
50	1,8x10 <sup>-1</sup>	8.71	243.88
50	1,8x10 <sup>-1</sup>	8.87	248.36
50	1.9x10 <sup>1</sup>	9.07	253.96
50	1.9x10 <sup>1</sup>	9.35	261.80
10	1.9x10 <sup>1</sup>	2.96	82.88
10	1.9x10 <sup>1</sup>	4.64	129.92
100	1.9x10 <sup>1</sup>	12.37	346.36
100	1.9x10 <sup>1</sup>	12.04	337.12

**Table 4: Overview of the resulting roughness factors and ECAS depending on layer thickness and sputter pressure.**

### 6.1.2 Fuel Cell operation

In order to evaluate the performance of the sputter coated Cr-/Pt-layer and the effect of different methods for integration of ionomer into the micro channels, polarization curves were measured for different setups of the  $\mu$ MEA. First, a  $\mu$ MEA with sputter coated Cr-/Pt-layer and drop-coated ionomer as described in chapter 5.3.2 was characterized with the help of the setup described in chapter 4.2.1. The result is shown in Figure 60. The open circuit voltage (OCV) was determined to be 0.7 V, which is rather low compared to conventional fuel cells which exhibit OCVs of > 0.9 V. A first possible explanation might be permeability due to an incomplete filling of the micro channels. This can be caused by the inhomogeneous distribution of the electrolyte due to the coffee ring effect (cf. chapter 5.3). The resulting crossover of hydrogen and oxygen through the membrane lead to mixed potentials at the electrodes and, by that, generates a voltage drop. A second reason might be the covering of the porous sputter deposited Pt by the residual PFSA layer of the electrolyte which acts as an upstream resistance for the diffusion of the reactants. This has a significant effect on the charge transfer current  $i_0$  (cf. chapter 2.2 and 2.3.3).

It can also be seen that the potential drops very fast with increasing current density. This occurs from high Ohmic resistances within the membrane and the electrodes. It is most likely that the membrane suffers from the dry operating parameters that are caused by the absence of active humidification respectively the high stoichiometry, resulting in limited proton conductivity. Moreover, the high stoichiometry leads to the absence of the mass transfer overpotentials as charge transfer

overpotentials and Ohmic resistances are dominant over the entire measurement. Calculating the power density of the  $\mu$ MEA, a maximum of 1.8 mW/cm<sup>2</sup> was realized with this sample.

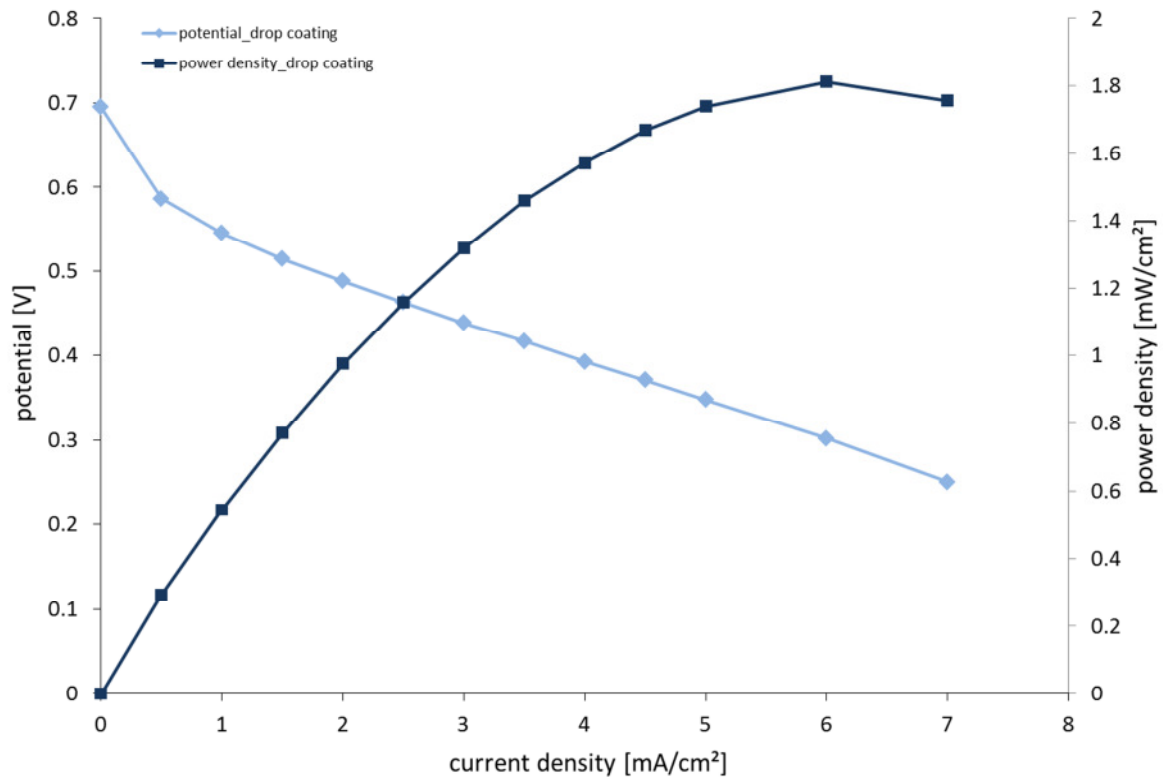


**Figure 60:** Polarization curve of a  $\mu$ MEA that was fabricated by drop coating the PFSA electrolyte onto the porous silicon membrane; a sputter coated Cr-/Pt-layer was used as catalyst and current collector; the gas supply was set to minimum values possible ( $H_2$ : 2 ml/min, air: 4 ml/min); hence, stoichiometries reach values of 20 (cathode) respectively 24 (anode) at the maximum power point (MPP, 6 mA/cm<sup>2</sup>); measurement was done under ambient conditions (1 bar, 20°C) and without humidification.

In comparison to the drop-coated  $\mu$ MEA, a  $\mu$ MEA with the same Cr-/Pt-layer was prepared by dip coating in order to achieve better homogeneity of the pore filling and to minimize the residual PFSA layer on top of the Cr-/Pt-layer. A silicon membrane, which was processed within the same batch as the membrane before, was used as substrate for polymer integration. The dip coating velocity was 0.4 mm/min and the applied pressure was 350 mbar. The operating parameters were the same as for the  $\mu$ MEA tested before. Still, the OCV is in the range of 0.7 V. As the dip coating velocity was optimized for getting a thin residual PFSA layer, unwanted permeability still might be present. Nevertheless, the voltage drop at higher current densities is significantly smaller which can be related to a better Ohmic behavior of the  $\mu$ MEA, better distribution of the 3-phase boundaries and better accessibility of the catalyst layer due to minimized residual PFSA on the surface of the membrane. The power density was more than doubled, reaching a maximum value of 4 mW/cm<sup>2</sup>. Hence, the dip coating process proves to be a more suitable method for integration of the electrolyte into the micro channels. Still, stoichiometries remain very high which is why no mass transfer overpotentials could

be observed although it has to be noted that the potential drops so fast that mass transfer overpotentials and ohmic overpotentials might not be distinguishable from each other.

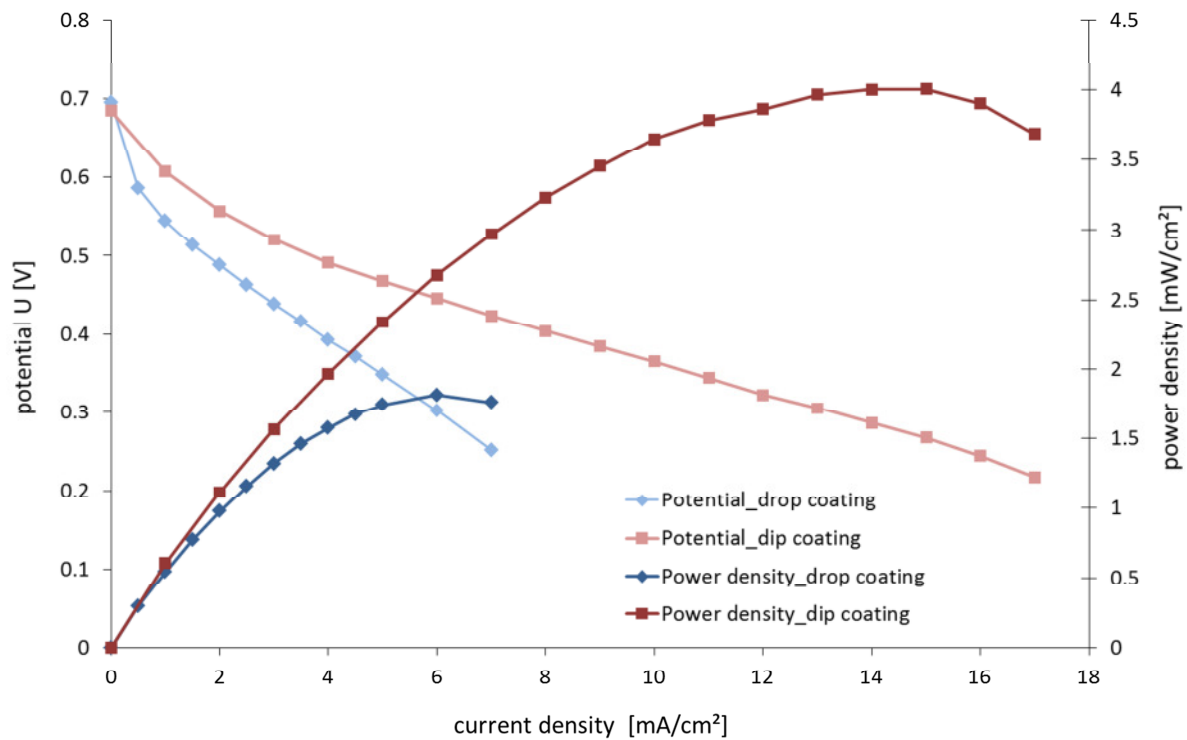


Figure 61: Polarization curve of a  $\mu$ MEA that was fabricated by dip coating in comparison to the  $\mu$ MEA presented in Figure 60; a sputter coated Cr-/Pt-layer was used as catalyst and current collector; the gas supply was set to minimum values possible ( $H_2$ : 2 ml/min, air: 4 ml/min); stoichiometries reach values of 8 (cathode) respectively 9.5 (anode) at the MPP (15 mA/cm<sup>2</sup>); the measurement was done under ambient conditions (1 bar, 20°C) and without humidification.

From the observations above, two important conclusions can be drawn:

1. Dip coating is the superior method of integrating the ionomer compared to drop coating. It is more repeatable, creates a more homogeneous polymer distribution, is suitable for mass production and the fabricated  $\mu$ MEA exhibits more than twice the power density compared to  $\mu$ MEAs prepared by drop coating.
2. The open circuit voltage is rather small. As the Cr-/Pt-layer is deposited onto the surface of the silicon membrane, there is a need to minimize the residual ionomer layer on the surface of the  $\mu$ MEA. Otherwise, the residual layer covers the Cr-/Pt-layer and the reaction gases are unable to reach the Pt-catalyst. But minimizing the thickness of the residual layer, for example by increasing the withdrawal velocity of the dip coating process, makes it difficult to realize a complete filling of all micro channels and eventually leads to impermeabilities that cause a voltage drop.

For a deeper understanding of the reaction kinetics of the  $\mu$ MEA, especially the interaction between the Cr-/Pt-layer and the residual ionomer layer, potentiostatic EIS measurements were conducted during fuel cell operation. As described in chapter 4.3, the resulting Nyquist diagram consists of different elements, representing specific components of the equivalent electric circuit. In general, the diameter of single arcs and their position on the x-axis give information about the individual parameters of the equivalent electric components: At high frequencies, the charge transfer resistances at the anode will be represented by an arc inside the Nyquist diagram with its diameter depending on the values of the resistances. With reduced frequencies the charge transfer resistances at the cathode will appear accordingly, exhibiting significantly higher arc diameters as the reaction kinetics are slower. In case the charge transfer resistances at the cathode become the dominant factor of the reaction, the charge transfer resistances at the anode may not be detectable at all during the EIS measurement. At even lower frequencies the mass transfer resistances of the fuel cell can be characterized, described by a Generalized Finite Warburg element and its corresponding representation inside the Nyquist diagram. At this stage of operation, the gas supply is hindered inside the electrode or diffusion may become too slow to supply the electrode with reaction species at high conversion rates. The results of the EIS measurements depend on the components of the fuel cell electrode as well as on the operation parameters, especially the current density [79] [90]. Usually, the charge transfer resistances are expected to be dominant at low current densities, because only low masses need to be transported to the electrodes. In contrast to that, high current densities will lead to high mass transfer resistances, resulting in Nyquist diagrams dominated by the low frequency arc. The transition from high charge transfer resistances to high mass transfer resistances can be correlated to the polarization curve of the fuel cell. However, this transition is blurry which may result in distorted arcs and difficult allocation at moderate current densities.

For EIS measurements of the  $\mu$ MEA reaction parameters were kept identical to the ones used to record the polarization curves, so that a direct comparison was possible. The measurements were realized with a Zahner potentiostat, setting the frequency range from 1 MHz to 500 mHz with an AC amplitude of 100 mV. According to the measurements of the polarization curves, a dip-coated  $\mu$ MEA with a 50 nm Cr and 80 nm Pt layer was characterized. After that, all results were analyzed with the help of ZView<sup>®</sup> in order to identify and quantify single components of the equivalent electric circle and to draw conclusions regarding the electrochemical behavior of the electrode.

Figure 62 shows impedance spectra for different applied current densities and their simulated fit according to the results obtained in ZView<sup>®</sup>. The applied model of the equivalent electric circuit and the parameters of the simulation for each point of measurement are according to the description in chapter 4.3 and summarized in Table 5.

Charge transfer processes in absence of diffusion limitations are observed for the spectra obtained at OCV and 3.5 mA/cm<sup>2</sup>. The resulting equivalent circuit model consists of a single resistor  $R_{ohm}$  which represents all ohmic proton resistances of the MEA, mostly membrane proton transport resistance. The wires inductance of the test setup is represented by  $L$ . The cathode reaction (ORR) is described by charge transfer resistances  $R_{CT/C}$  in parallel with the impedance of the Constant Phase Element  $Z_{CPE/C1}$  (kinetic arc) which is used to quantify the distortion of the capacitance due to the electrode porous structure. For the result at OCV, a second Constant Phase Element ( $Z_{CPE/C2}$ ) is accounting for the polarization of the cathode at low frequencies. This effect may occur in galvanostatic fuel cell measurements with constant given current density at each point of the polarization curve, when the electrochemical reaction has not reached a steady state. Hence, longer waiting times prior to each of the following measurements were introduced.

At higher current densities, charge transfer resistances decrease, resulting in lower values for  $R_{CT/C}$  and a smaller diameter of the kinetic arc. At 9 mA/cm<sup>2</sup> and 12.5 mA/cm<sup>2</sup> mass transport limitations across the diffusion layer become relevant and in the low frequency region fitting with the previous model is unsatisfactory. Hence, a Generalized Finite-length Warburg element  $W$  accounting the finite-length oxygen diffusion with transmissive boundary [114] is added to the cathode equivalent circuit [115]. At 12.5 mA/cm<sup>2</sup>, mass transport limitations become dominant, causing the low frequency arc to increase to a very high diameter which makes it difficult to keep a good fit together with the other parameters of the simulation.

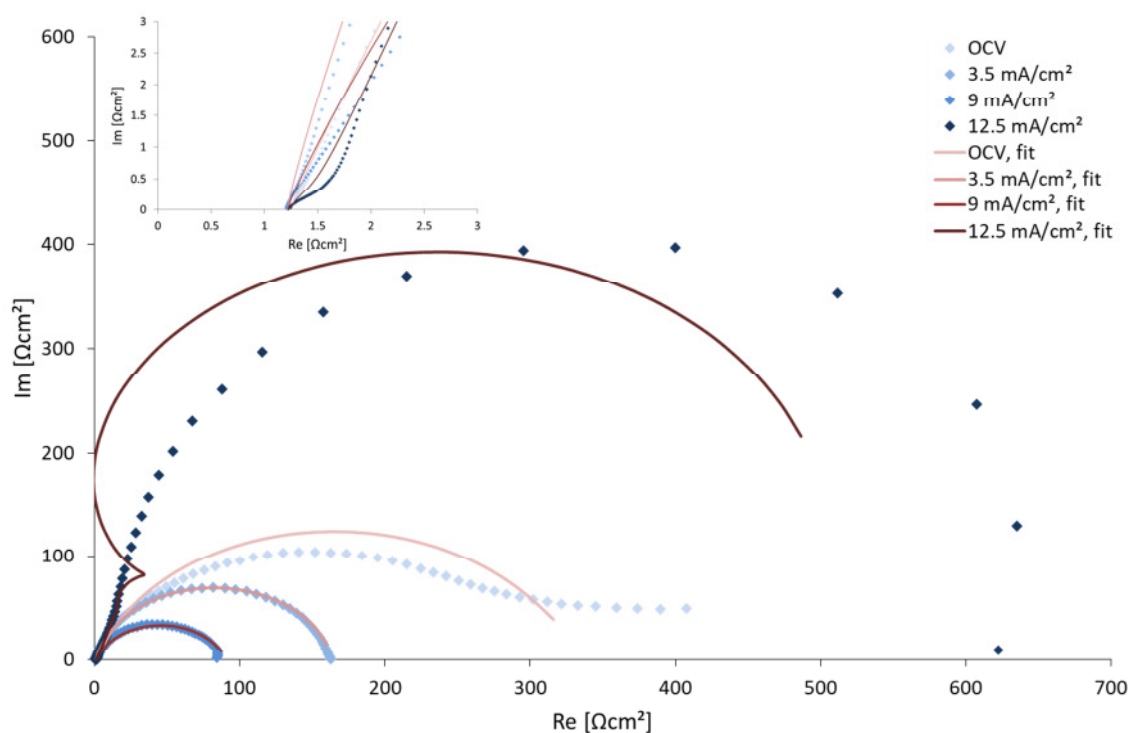


Figure 62: EIS spectra and simulated fits of dip-coated  $\mu$ MEA at different current densities; frequency range was set from 1 MHz to 500 mHz with an amplitude of 100 mV.

The results show that charge transfer resistances are significantly higher compared to conventional fuel cells, leading to high values of  $R_{CT/C}$ . Also, diffusion of the reactants is strongly inhibited, resulting in high values of the Warburg element, especially at 12.5 mA/cm<sup>2</sup>. This correlates well with the results of the cyclic voltammetry which clearly showed poor porosity of the Cr-/Pt-layer. Hence, the effectivity of the catalyst material on the one hand as well as the mass transport along the catalyst layer, on the other hand, is limited, leading to the low performance of the  $\mu$ MEA. Another explanation may be that the residual ionomer layer on the surface is covering the platinum of the Cr-/Pt-layer, preventing the oxygen to reach the catalyst, similar to a thick GDL as described in chapter 2.3.2. This assumption remains to be verified in further tests.

Current density	L	R <sub>ohm</sub>	CPE1-Q	CPE1-n	R <sub>CT/C</sub>	CPE2-Q	CPE2-n	Y <sub>o</sub>	$\delta^2/D$	P
OCV	1.10E-6	1.21	3.7E-4	0.83	326.3	0.66	0.02	-	-	-
(error)	1.63E-8	13.12	8.4E-6	4.6E-3	3.63	5.54	0.22	-	-	-
3.5 mA/cm <sup>2</sup>	1.08E-6	1.20	1.9E-4	0.90	162.8	-	-	-	-	-
(error)	8.45E-9	6.3E-3	2.9E-6	2.2E-3	1.20	-	-	-	-	-
9 mA/cm <sup>2</sup>	1.08E-6	1.19	5.1E-4	0.82	86.4	-	-	3.15	3.4E-3	0.99
(error)	1.06E-8	8.0E-3	1.1E-5	3.1E-3	2.42	-	-	2.24	9.7E-6	7.1E-4
12.5 mA/cm <sup>2</sup>	1.06E-6	1.23	4.5E-4	0.91	0.69	-	-	506.4	0.66	0.79
(error)	2.2E-8	0.02	6.8E-5	0.03	0.21	-	-	25.54	0.02	9.6E-3

**Table 5: Parameters of the equivalent circuits in ZView for each result of the EIS measurement; Three different models need to be applied in order to explain the results: (1) a second CPE is added to take polarization of the cathode at low frequencies into consideration; (2) reaction has reached a constant stage no polarization of the cathode appears, so the second CPE can be deleted from the model; (3) at low voltages, mass transport limitations occur and a Finite Warburg Element has to be added to the model;**

Ohmic resistances of the membrane are represented by the values of  $R_{ohm}$  and the starting point of the Nyquist diagram at high frequencies (cf. chapter 4.3). For all applied current densities they are about 1.2  $\Omega$ cm<sup>2</sup> which can be correlated to the thin membrane and a homogenous filling of the microstructure. Still, the values are significantly higher than in conventional MEAs which exhibit



values of less than  $0.5 \Omega\text{cm}^2$ . A possible explanation for this can be found in the high stoichiometry of the operation parameters which lead to a drying of the polymer membrane.

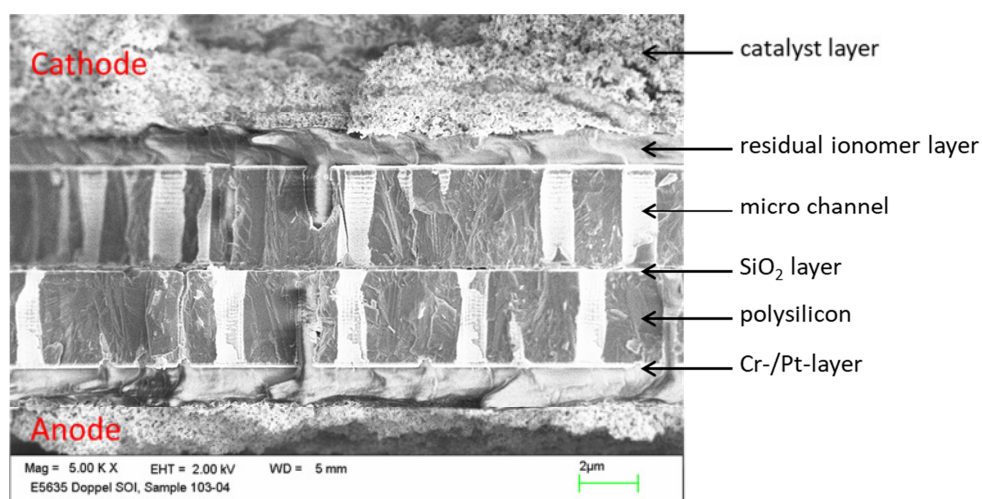
## 6.2 Additional spray coated, porous catalyst layer

Based on the findings above, a possible strategy to enhance the performance of the  $\mu\text{MEA}$  is to deposit a porous catalyst layer on both sides of the membrane. This way, an increase in catalytic activity should be obtained. Based on a dip-coated membrane as described above, a catalyst layer was applied with the help of an ultrasonic spray coater. It was composed of a 20 ml water-based dispersion with a 40 wt% Pt/C catalyst. The exact composition can be seen from Table 6.

Catalyst (Pt/C)	H <sub>2</sub> O	Isopropanol	Ionomer 5wt% in H <sub>2</sub> O
0.4 g	13.6 g	1.19 g	4.91 g

**Table 6: Composition of the spray coated catalyst layer.**

At the anode, 2  $\mu\text{m}$  of catalyst layer were deposit while at the cathode 4  $\mu\text{m}$  were spray coated. The thicker catalyst layer on the cathode side was applied with respect to the dominant overpotentials during the electrochemical reaction. Hence, the anode exhibits a Pt-loading of  $0.16 \text{ mg/cm}^2$  whereas the cathode side exhibits a Pt-loading of  $0.32 \text{ mg/cm}^2$  additional to the Pt loading resulting from the 80 nm Pt layer on top of the membrane surfaces.



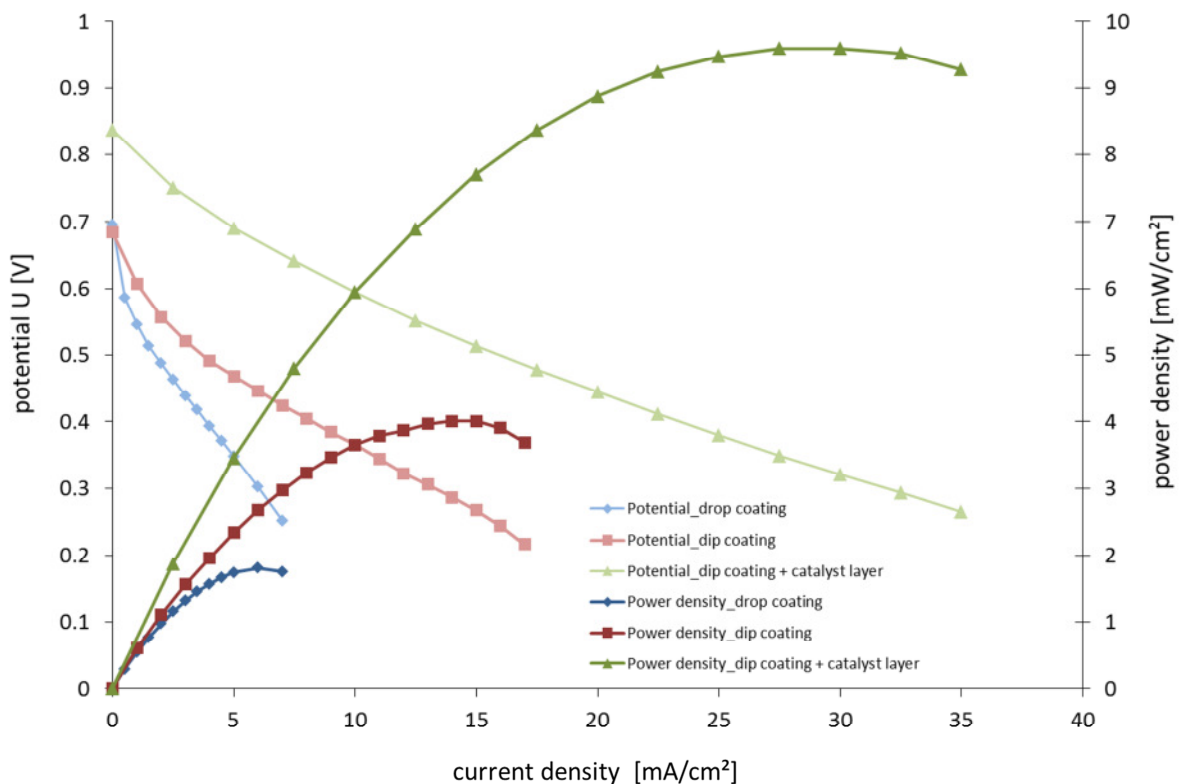
**Figure 63: SEM-image of the  $\mu\text{MEA}$  with porous catalyst layer, the electrolyte integrated into the micro channels and the microstructured silicon membrane; at the anode side, the spray coated catalyst exhibits a thickness of 2  $\mu\text{m}$  on average while at the cathode side, the catalyst layer exhibits a thickness of 4  $\mu\text{m}$  on average; it has to be noted that some micro channels can only be seen partly on the SEM image. This is due to the unsteady breakage of the cross section. As the image does not show the third dimension, steps and chamfers cannot be detected.**

Figure 63 shows a SEM-image of the final  $\mu\text{MEA}$ . All important components can be identified easily. The polysilicon membrane with its buried  $\text{SiO}_2$  layer exhibits a thickness of 5  $\mu\text{m}$ . The micro channels are 1  $\mu\text{m}$  in diameter and are placed within a distance of 2  $\mu\text{m}$ . The filling of the micro channels with



proton conducting polymer was successful. On the surface of the membrane the thin Cr-/Pt layer for current collection is visible. This metal layer is covered with a residual polymer layer of approx. 1  $\mu\text{m}$ , remaining from the dip-coating process. It has to be considered that this is a significantly lower thickness than other research groups achieved with different processes, e. g. by evaporation based polymer integration [49]. On top of the residual layer the porous catalyst layer can be found. It is obvious that the formation of an effective triple phase boundary is limited by the residual layer located between catalyst layer and Cr-/Pt-layer which acts as current collector.

The polarization curve of this  $\mu\text{MEA}$  can be seen in Figure 64. Compared to the  $\mu\text{MEAs}$  that were characterized before, this one shows the best performance. The potential at OCV exhibits a value of 0.83 V which is significantly higher than the results achieved without additional catalyst layer. The maximum achieved power density is 9.7  $\text{mW}/\text{cm}^2$ . The polarization curves discussed before are integrated into the diagram in order to demonstrate the improvements of the single development steps.



**Figure 64:** Effect of adding a porous catalyst layer onto the surfaces of the  $\mu\text{MEA}$ ; the gas supply was set to minimum values possible ( $\text{H}_2$ : 2  $\text{ml}/\text{min}$ , air: 4  $\text{ml}/\text{min}$ ); stoichiometries reach values of 4 (cathode) respectively 4.8 (anode) at the MPP (30  $\text{mA}/\text{cm}^2$ ); the measurement was done under ambient conditions (1 bar, 20°C) and without humidification.

Figure 65 shows the results of the corresponding EIS measurements at different points of operation along the polarization curve. The results were analyzed using ZView® again and parameters of the

simulation results are summarized in Table 7. For this electrode setup, the results are consistent and one equivalent circuit model can be applied. Due to significant overall decrease of impedances, the anode reaction (HOR) can be evidenced on the spectra with the small arc at high frequencies. It is described by charge transfer resistances in parallel with a constant phase element  $Z_{CPE/A}$ . As HOR is not a dominant component and has only minor effects on the simulation result,  $CPE/A-n$  was set to 1, turning the constant phase element into a true capacitor which led to more accurate results on the overall simulation. No mass transport limitation can be observed, so no Warburg element was added to the model.

Results suggest that the Ohmic resistances are comparable to the measurements of a  $\mu$ MEA without a spray coated catalyst layer, with constant values around  $1.4 \Omega\text{cm}^2$ . This is not surprising as the microstructured silicon membrane with dip-coated ionomer and the current collecting Cr-/Pt-layer remain the same compared to the electrode setup before.

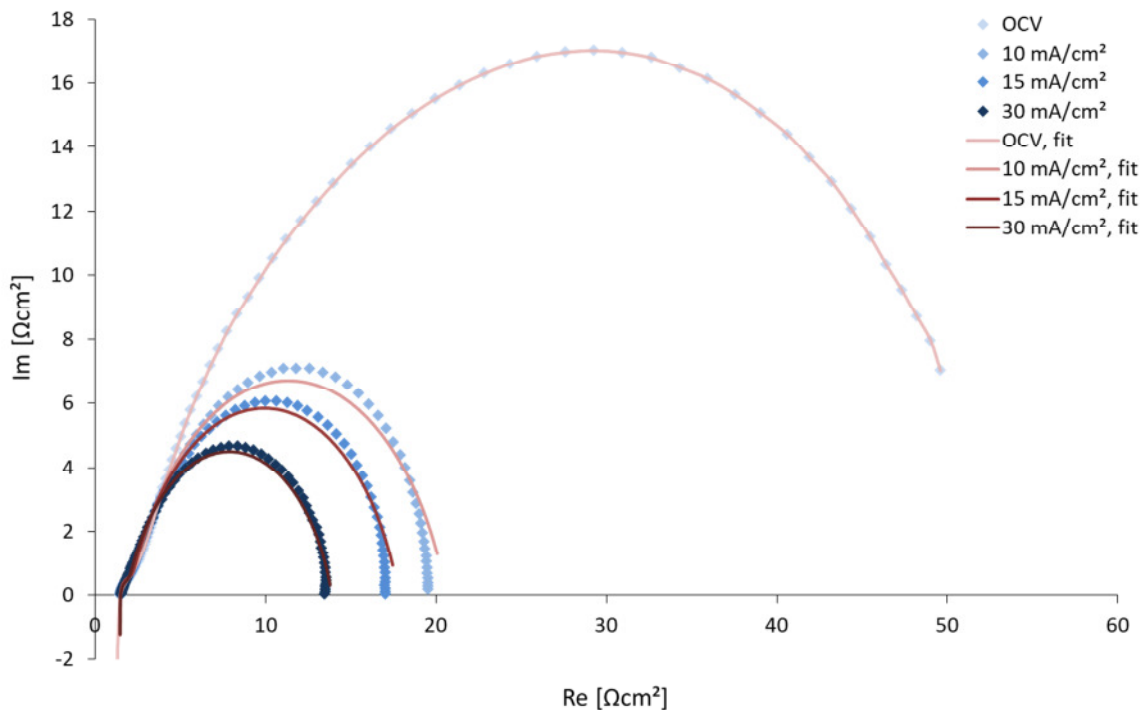


**Figure 65: EIS spectra and simulated fits of a  $\mu$ MEA with a spray coated catalyst layer; frequency range was set from 1 MHz to 500 mHz with an amplitude of 100 mV.**

However, the spray coated catalyst layer has a significant effect on the charge transfer resistance of the cathode reaction. At OCV,  $R_{CT/C}$  is  $54.1 \Omega$  which is already lower than any value measured on the previous electrode setup. With higher current density, the value decreases further until it reaches  $11.99 \Omega$  at  $30 \text{ mA/cm}^2$ . As mentioned above, no mass transport limitation can be observed which is in good correlation with the polarization curve where no voltage drop due to mass transfer overpotentials can be observed. Together, these two results clearly proof that adding a spray coated catalyst layer with high porosity enhances performance of the fuel cell reaction significantly as it

improves diffusion of the reaction species at both electrodes. On the other hand, it corroborates the hypothesis that the accessibility of the Pt layer is inhibited by the residual polymer layer and leads to a limited diffusion of the oxygen to the Pt layer when no additional spray coated catalyst layer is applied. Still, all resistances are significantly higher compared to conventional MEAs. This questions the concept of the bifunctional Cr-/Pt-layer in general. EIS measurements clearly show that the residual PFSA layer and the low porosity of the sputter coated platinum seem to be limiting factors in performance of the electrodes. Hence, further electrochemical investigation on the influence of individual components on the electrochemical reaction need to be done.

Current density	L	R <sub>ohm</sub>	CPE/A-Q	CPE/A-n	R <sub>CT/A</sub>	CPE/C-Q	CPE/C-n	R <sub>CT/C</sub>
<b>OCV</b>	<b>8.7E-7</b>	<b>1.44</b>	<b>1.0E-4</b>	<b>1</b>	<b>0.58</b>	<b>4.2E-3</b>	<b>0.72</b>	<b>54.1</b>
(error)	6.6E-9	7.0E-3	5.1E-6	-	0.02	7.1E-5	3.8E-3	0.60
<b>10 mA/cm<sup>2</sup></b>	<b>8.1E-7</b>	<b>1.46</b>	<b>9.8E-5</b>	<b>1</b>	<b>0.61</b>	<b>2.0E-3</b>	<b>0.80</b>	<b>18.53</b>
(error)	1.36E-8	7.5E-3	4.7E-6	-	0.02	6.0E-5	5.8E-3	0.16
<b>15 mA/cm<sup>2</sup></b>	<b>8.1E-7</b>	<b>1.47</b>	<b>9.7E-5</b>	<b>1</b>	<b>0.59</b>	<b>1.6E-3</b>	<b>0.81</b>	<b>15.75</b>
(error)	1.25E-8	7.0E-3	4.5E-6	-	0.02	5.0E-5	5.7E-3	0.12
<b>30 mA/cm<sup>2</sup></b>	<b>8.0E-7</b>	<b>1.47</b>	<b>6.5E-5</b>	<b>1</b>	<b>0.42</b>	<b>8.9E-4</b>	<b>0.82</b>	<b>11.99</b>
(error)	1.2E-8	7.4E-3	4.0E-6	-	0.02	3.1E-5	5.8E-3	0.08

**Table 7: Parameters of the equivalent circuits in ZView for each result of the EIS measurements: a constant model containing anode and cathode equivalent circuit can be applied.**

### 6.3 Evaluation of the $\mu$ MEA via EC-AFM

In order to evaluate the dependence of electrochemical performance of the  $\mu$ MEA on the residual PFSA which originates from the dip coating process, measurements with EC-AFM were executed. This includes measurements to investigate the effect of depositing an additional, spray coated catalyst layer on top of the PFSA layer.

A  $\mu$ MEA was prepared as follows: A porous silicon membrane was manufactured and sputter coated with the bifunctional Cr-/Pt-layer at one side only by IMS CHIPS. After that, PFSA polymer was integrated into the membrane by dip coating it at 350 mbar with a speed of 0.5 mm/min, followed by a 2 h bake at 70°C. By choosing a coating velocity slightly higher than the optimal parameter, the pores of the membrane were filled with PFSA polymer, giving areas where the residual layer was of continuous and homogenous thickness but also where it exhibited indentations or was not existent.

Moreover, half of the active area of the  $\mu$ MEA was coated with an additional catalyst layer ( $0.8 \text{ mg}_{\text{Pt}}/\text{cm}^2$ ) on the same side of the sputter deposited Cr-/Pt-layer by ultrasonic spray coating. A sketch of the prepared sample is shown in Figure 66.

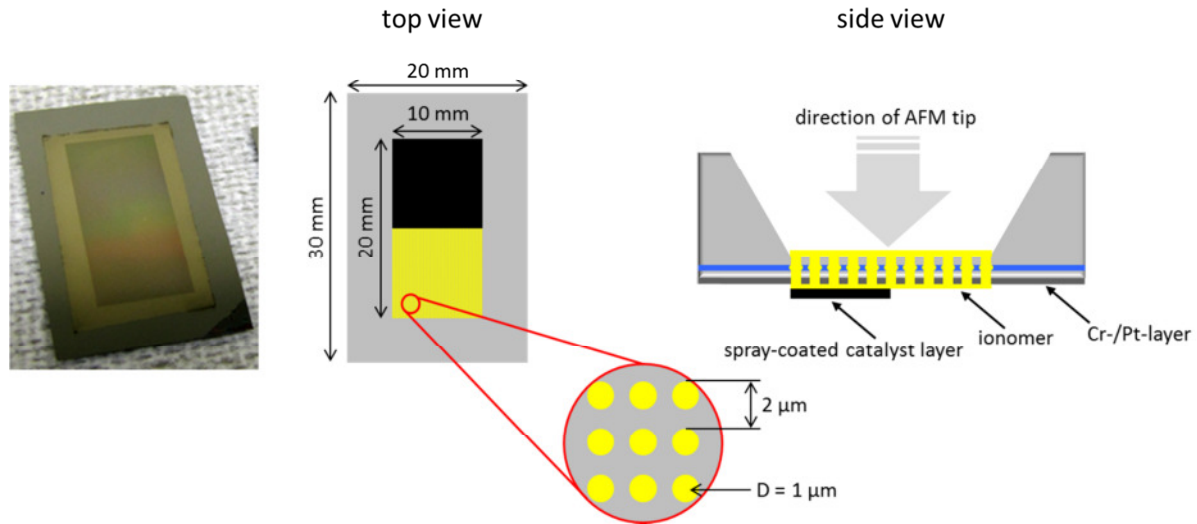


**Figure 66: Sketch of prepared sample for EC-AFM.**

The sample was sent to Esslingen University of Applied Sciences where they were characterized by Prof. Renate Hiesgen and colleagues by EC-AFM. Before measurement, the sample was cut into two pieces, one with the additional catalyst layer and one without. The first one was deposited onto a porous sample holder while the latter one was bonded to an electro-conductive tape. For activation, the samples were placed between two Platinum-meshes and immersed into  $0.05 \text{ M H}_2\text{SO}_4$  electrolyte where a constant potential of  $3 \text{ V}$  was applied for  $3 \text{ h}$ . All measurements were executed under  $60 \text{ \% RH}$ . This way, repeatable acidification and humidification were achieved.

The measurements were conducted as described in chapter 4.4. The proton conductivity of each electrode sample was determined by the value of the DC current resulting from the hydrolysis reaction that was induced by the potential through the Pt tip of the AFM (cf. equation 4-14). Samples with higher proton conductivity exhibit a higher reaction rate and, thus, a higher current can be measured.

The results for the sample without an additional spray coated catalyst layer were very poor. No ion conductive network could be recognized, although Platinum was present at the backside within the sputter coated layer which should act as a catalyst for the hydrolysis reaction. Also, the pores beneath the PFSA residual layer were not detectable in both topography and current measurements

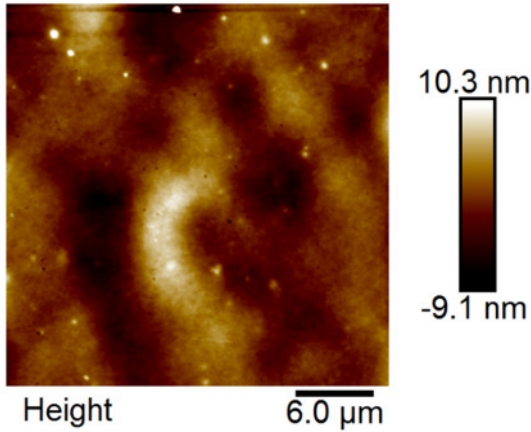


Figure 67: AFM image of surface topography of  $\mu$ MEA (source: Esslingen University of Applied Science).

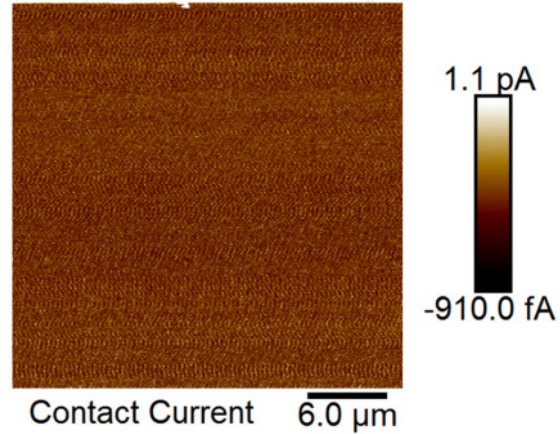


Figure 68: Measured proton current of  $\mu$ MEA on area with no spray coated additional catalyst layer (source: Esslingen University of Applied Science).

(cf. Figure 67 and Figure 68). Hence, there was no influence from the Cr-/Pt-layer on the measured current. The current originates from the AC-component of the tapping AFM-tip, which provokes a movement of charge carriers within the material. This leads to the conclusion that the Cr-/Pt-layer is not – or at least almost not – contributing to the hydrolysis reaction as it is blocked by the residual PFSA layer. After drying out of the sample, no current could be registered at all.

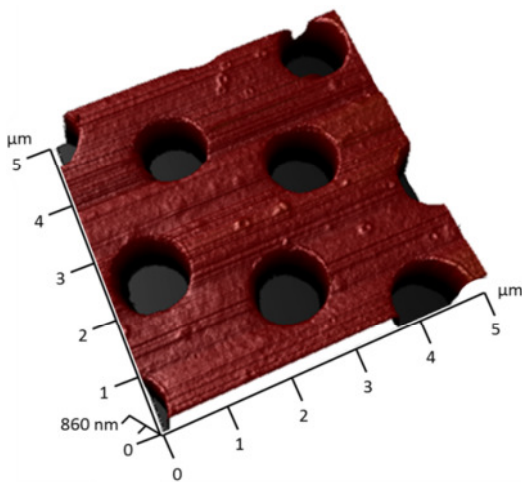


Figure 69: Geometrical information of silicon membrane front side from the EC-AFM measurements on area with no residual PFSA layer (source: Esslingen University of Applied Science).

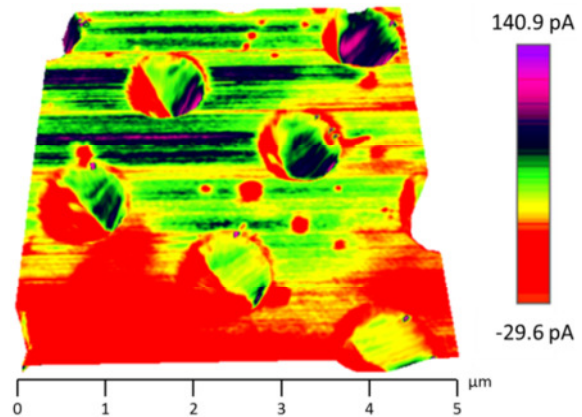
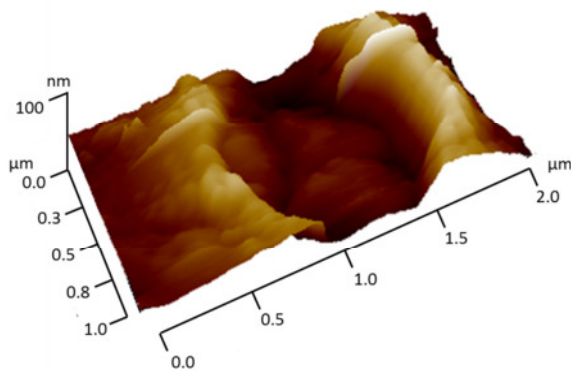


Figure 70: Corresponding measurements of proton current on surface of  $\mu$ MEA; results show no proton current on bare silicon surface but significant proton currents inside the micro pores (source: Esslingen University of Applied Science).

With the additional catalyst layer on the backside of the membrane, the results of the AFM measurements change significantly. First, an area with no residual PFSA layer at the front side was identified and examined (cf. Figure 69). As the pores are filled with PFSA to some level, a proton current could be observed inside the pores, especially at the walls (cf. Figure 70). The space between

the pores offered no proton conducting material. Hence, no proton current was detected. However, this shows that a certain amount of PFSA is needed between the pores in order to realize sufficient in-plane proton conductivity across the microstructured membrane and, by that, maximize the active area of the  $\mu$ MEA.

This result is supported by detailed measurements of a single pore. Figure 71 shows the EC-AFM result of a pore which is completely filled with PFSA while the surrounding exhibits no proton conducting material but just the silicon of the membrane. It can be seen that the proton current on the surface of the pore reaches up to 27.6 pA while it drops to zero outside the pore (cf. Figure 72).



**Figure 71: AFM measurement result of topography on a single micro channel with almost no residual layer on surface of  $\mu$ MEA (source: Esslingen University of Applied Science).**

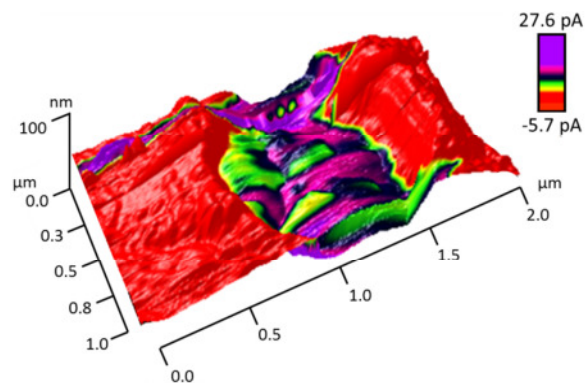


**Figure 72: Combined EC-AFM measurement result of topography and proton current on a single micro channel with almost no residual layer on surface of  $\mu$ MEA; proton current is only detected in micro channel (source: Esslingen University of Applied Science).**

When PFSA can be found also between the pores, a proton current was detected across the whole area of the  $\mu$ MEA. Figure 73 shows the geometrical properties of an area where the pores are filled completely and where PFSA can also be found between the pores but where indentations remain from the fluid flow throughout the dip coating process. Proton current could be determined inside the pores, but also across the surrounding surface between the pores. A maximum was measured at the edge of the pores (cf. Figure 74). Moreover, it was possible to identify the pores just by mapping the proton current without taking the geometrical information into account. In spaces between the pores the proton current decreases significantly with increasing distance from the pores which leads to the conclusion that the residual PFSA layer is not thick enough to offer enough proton conductivity in horizontal direction.



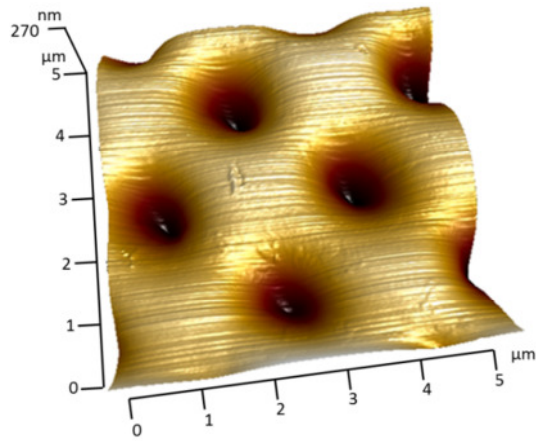


**Figure 73:** AFM measurement result of topography on membrane surface with relatively low residual layer thickness (source: Esslingen University of Applied Science).

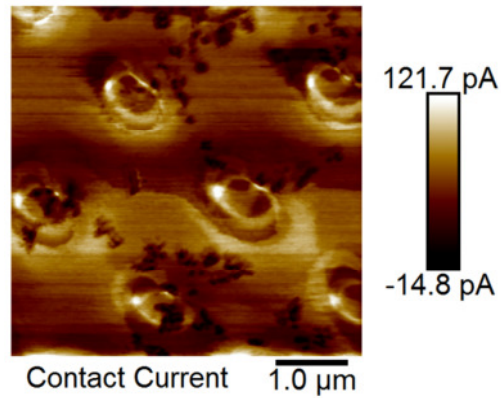


**Figure 74:** Measurement result of proton current on membrane surface with relatively low residual layer thickness (source: Esslingen University of Applied Science).

If the geometrical information and the results of the proton current are combined to only one diagram (cf. Figure 75), the correlation between the indentations and the proton current becomes even more obvious. A detailed view on one single pore can be seen in Figure 76. As the backside of the pore is coated with an additional catalyst layer, the protons can evolve everywhere on the surface. Hence, the highest proton current can be measured in the middle and at the edge of the pore. It is highly likely that the protons which are produced between the pores of the backside, find their way to the front side along the walls of the pores which explains the maximum of the proton current at the edges of the pores.

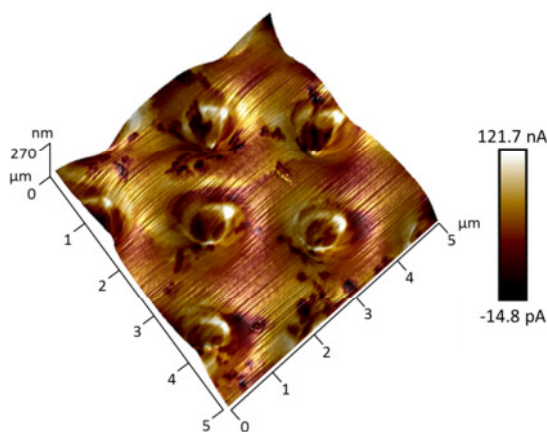


**Figure 75:** Combined EC-AFM image showing topography and proton current of  $\mu$ MEA; residual layer is relatively thin which leads to noches at the micro channels (source: Esslingen University of Applied Science).

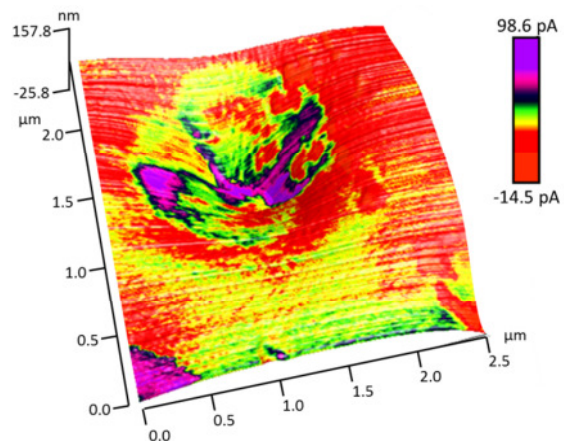


**Figure 76:** Combined EC-AFM image of topography and proton current, magnification of a single micro channel; proton conduction mainly takes place at the edge of the micro channel (source: Esslingen University of Applied Science).

When the thickness of the residual PFSA layer is increased the pores are filled and the whole surface of the membrane is covered with ion conducting polymer homogeneously. In this case, the location of the micro channels cannot be identified with the geometrical AFM measurements anymore (cf.

Figure 77 and Figure 78). When the proton current was measured no maximum regarding to the pores was obtained. However, the distribution of the proton current seems to be random and not depending on the geometry of the membrane. Interestingly, the values of the proton currents were higher compared to the measurements before as they reach up to 268.4 pA. This value is comparable to measurement results of conventional MEAs at the same ambient parameters [94]. So, it can be concluded that the whole geometrical area is electrochemically active as proton current between backside and frontside can be detected by the Pt-tip across the whole surface. This is also important for evaluation of the porosity of the silicon membrane, because the diameter and the spacing of the pores are adequate to provide sufficient proton conductivity over the whole surface.

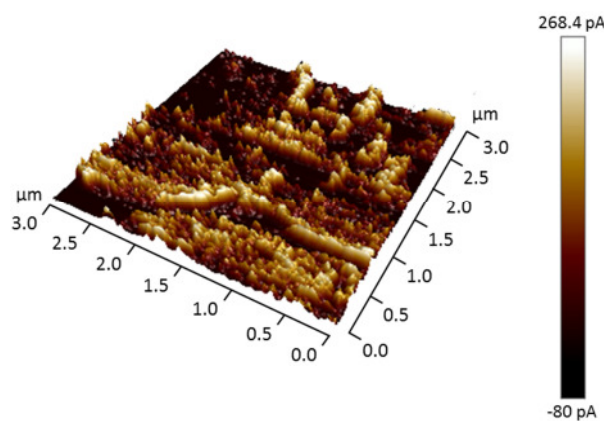


**Figure 77: EC-AFM image of proton current on surface of  $\mu$ MEA with significant residual layer (source: Esslingen University of Applied Science).**

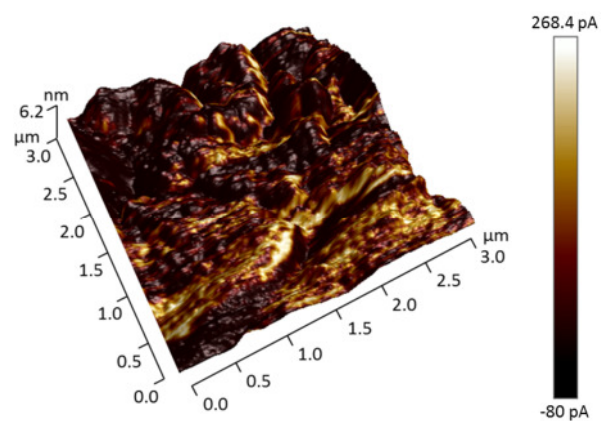


**Figure 78: Combined EC-AFM image of topography and proton current on surface of  $\mu$ MEA with significant residual layer (source: Esslingen University of Applied Science).**

Summarizing the EC-AFM experiments, three important conclusions can be drawn:

1. The residual PFSA layer is necessary; at a certain thickness it offers enough horizontal proton conductivity so that the whole membrane area can be used as active area for the fuel cell reaction.
2. The porosity of the silicon membrane is sufficient to realize good mobility of the protons.
3. The bifunctional Cr-/Pt-layer cannot be deposited onto the surface of the porous silicon membrane.

These conclusions confirm the results obtained from the polarization curves and EIS measurements. As a residual PFSA layer is needed to ensure in-plane proton conductivity, a sputter deposited catalyst layer on the surface of the silicon membrane will be blocked by the polymer. Hence, the hydrogen as well as the oxygen molecules cannot reach the platinum layer which inhibits the fuel cell reaction. This is proved by the EC-AFM measurements where no additional catalyst layer was used. When such a catalyst layer is spray coated onto the surface – and thereby onto the residual PFSA



layer – the fuel cell reaction can take place at this layer. But this leads to a limitation of the electron conduction, because the residual PFSA layer is located between the catalyst layer and the Cr-/Pt-layer which also acts as a current collector. So, the position of the current collector should be changed in order to bring it closer to the catalyst layer. This is an important result regarding the concept of a MEMS-based  $\mu$ MEA. The original approach of just having a bifunctional Cr-/Pt-layer seems to be inefficient and alternative options will be presented in the following sections.

#### 6.4 Electrically conductive catalyst layer

Previous results have shown that a sputter coated thin metal layer exhibits significant disadvantages, especially when it is covered by a thin ionomer layer. This layer, originating from the dip coating process, inhibits the electronic current from the catalyst layer to the current collecting Cr-/Pt-layer. Hence, a change of the electrode design becomes necessary. Primarily, this affects the current collecting layer as it needs to be positioned adjacent to the catalyst layer.

Deposition of a current collector on top of the catalyst layer seems to be a proper method. This solution would be similar to conventional fuel cell electrodes where gas diffusion layers made from carbon cloth are pressed onto the MEA and used for better current collection and improved gas distribution. As stated before, a carbon cloth layer is not suitable for this type of  $\mu$ MEA, because it does not comply with the small tolerances of semiconductor technology and would damage the thin polysilicon membrane. Thus, coating of a conductive layer on top of the catalyst layer seems to be a good option. Furthermore, development of a catalyst layer with a significant electrical conductivity could combine the two components, leading to lower fabrication costs and reduced thickness of the  $\mu$ MEA. By including electrically conductive particles into the catalyst ink, the final catalyst layer can exhibit a significant electric conductivity and an extra current collector becomes obsolete. For evaluation of such an electrode-concept, experiments on the electrical conductivity depending on the amount of conductive particles have been done and are described in this chapter.

Catalyst layers in conventional fuel cells exhibit poor electrical conductivity. In literature, different values of electrical conductivity of the catalyst layer can be identified. Depending on the ionomer content values vary between 5 S/cm and 1.6 S/cm [116] [117] [118]. This is sufficient to enable electrons to find their way through-plain to the GDL. However, it is not enough to use the catalyst layer as current collector with sufficient in-plain conductivity. Usually, the GDL works as the current collector. The electrons migrate in vertical direction through the catalyst layer to the carbon filaments of the GDL. Therefore, no high specific electrical conductivity is necessary inside the thin catalyst layer. However, in silicon-based micro fuel cells no GDL is used which means that electrons need to be conducted in horizontal direction through the catalyst layer in order to reach the current collector at the edge of the MEA. Hence, the catalyst layer itself needs to exhibit low Ohmic

resistances for sufficient electronic conduction. Because of that, the horizontal or in-plane electric conductivity has to be increased and characterized. This can be achieved by integration of conductive particles into the catalyst layer and thereby increase the electrical conductivity significantly. Measurement of the in-plane electric conductivity is realized by Kelvin probe resistance measurements as described in chapter 4.5. Figure 79 and Figure 80 show the theoretical pathway of an electron at the anode side in both, conventional MEAs with gas diffusion layer and silicon based micro MEAs without gas diffusion layer.

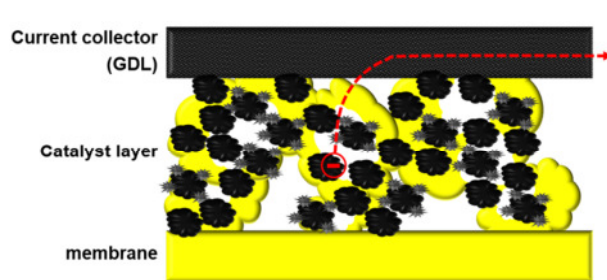


Figure 79: Theoretical pathway of an electron at the anode of a conventional MEA using an electronically highly conductive gas diffusion layer; the thicknesses are not drawn at scale, the distance for the electron in horizontal direction is much longer than in vertical direction.



Figure 80: Theoretical pathway of an electron at the anode of a silicon-based  $\mu$ MEA. As no gas diffusion layer is used, electrons have to be conducted through the catalyst layer in horizontal direction.

#### 6.4.1 Percolation theory

The change in conductivity resulting from the integration of electrically conductive filler particles into isolators or materials with poor electronic conductivity can be described by the so-called percolation theory. It specifies the abrupt increase in electrical conductivity at a certain value of particle concentration. Above this percolation threshold the compound material shows electric conductivity as the distance of the filler particles is small enough to form conductive pathways. When the filler concentration is increased further, the electric conductivity shows declining increase which means that at high concentrations only a moderate gain in conductivity can be observed.

Identification of the percolation threshold may be challenging because it depends on many parameters. In general, the aspect ratio of the added particles plays an important role. Particles with high aspect ratios lead to small percolation thresholds in comparison to spherical particles. Moreover, the size of the particles has a strong effect. As the size of the particles decreases, the ratio of the specific surface to volume increases. This leads to an increased probability of conductive contacts between the particles and thereby a decrease of the percolation threshold.

For mathematical description several models have been developed. A valid model used for electrical percolation in polymer compounds was described by Flory and Stockmayer [119] [120]. They stated

that an infinite lattice exhibits a random amount  $p$  of occupied lattice sites. Hence, the relative amount of unoccupied lattice sites can be described with  $q = 1-p$ . This concept is suitable to specify the electric properties of a lattice filled with conductive particles, for example in isolating polymer matrices. In this case, the lattice would be defined by the polymer matrix and the occupation probability by the concentration of the conductive filler. Thus, a low concentration of filler particles would mean that only a small amount of lattice sites is occupied and the compound material acts as an isolator. With increasing concentration of the conductive filler neighboring lattice points get occupied and form clusters. Within these clusters an electron transport is possible. At a certain value  $p_c$  which defines the percolation threshold a percolation cluster is generated that forms a continuous connection of one end of the lattice to the opposite end. This enables macroscopic electronic conduction and the compound transforms into a conductive material. Then, the electrical conductivity  $\sigma$  above the percolation threshold can be described as a function of the filler concentration [121]:

$$\sigma \propto (p - p_c)^\beta, p > p_c \quad 6-1$$

The value of  $\beta$  depends on the dimension of the microstructure, respectively if the examined lattice is a 2D or 3D material [122] [123].

It is also important to take the geometry of the filler particles into account. This comprises size, aspect ratio and morphology of the specific particles. Figure 81 illustrates the effect of different particle geometries on formation of percolation clusters. Typical components of catalyst layers are specified, for example catalyst support, ionomer particles, catalyst nanoparticles and conductive particles (Figure 81 a). These particles form a matrix, the catalyst layer (Figure 81 b). Large, spherical particles require a relatively large volume which means that the maximal loading of the matrix is reached with fewer amounts of particles (Figure 81 c). When particles of different size are used the loading can be higher and more percolation paths are formed (Figure 81 c). Hence, a better electrical conductivity can be realized.

The aspect ratio of certain filler particles is another important parameter. Non-spherical particles, for example cylindrical geometries, enable low percolation thresholds as the conductive network can be generated with low amounts of particles (Figure 81 d). However, specific parameters throughout fabrication have to be considered as well, because they affect, among others, the orientation and the position of the particles [124].

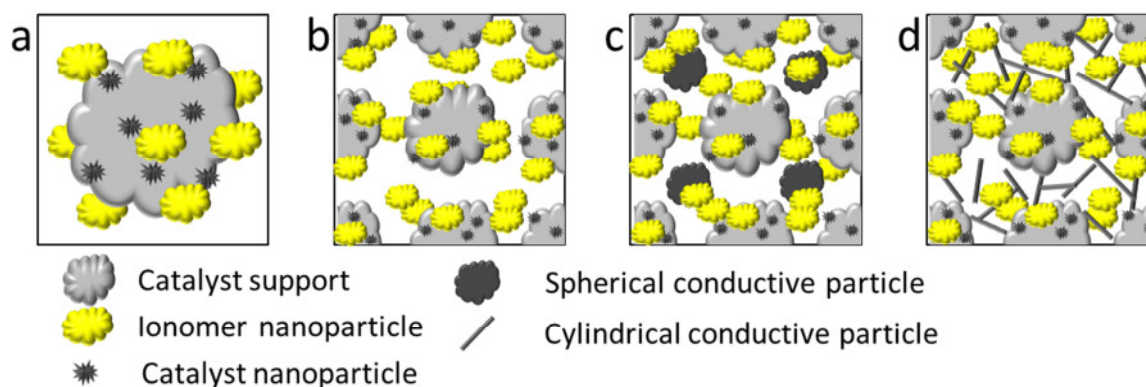


Figure 81: Schematic influence of filler particles in catalyst layers on electric conductivity (according to [124]); a: single catalyst particle, b: matrix of catalyst particles, c: spherical particles integrated into catalyst layer, d: cylindrical particles integrated into catalyst layer.

#### 6.4.2 Enhancing electrical conductivity of the catalyst layer with Carbon Nano Tubes

In chapter 2.3.2 it was described how thickness and porosity influence the effectiveness of the catalyst layer. If electrical conductivity shall be increased, it is of great importance to consider these two aspects as well in order to ensure good electrochemical properties.

As operating conditions in fuel cells are highly corrosive, usually carbon-based materials or precious metals are applied for realizing electrical conductivity. One example is the application of carbon black (CB) as catalyst support. These filler particles offer high specific surface, chemical stability and moderate electric conductivity at relatively low costs. In general, they consist of spherical particles with diameters of less than 50 nm and their agglomerates.

In contrast to that, graphene nano sheets (GNS) are two dimensional particles which consist of several graphene layers. They exhibit higher specific conductivities than CB with higher aspect ratio. A major disadvantage, however, are their high costs [125].

Carbon Nano Tubes (CNT) are well examined filler particles in electrically conductive composites and in electrochemical devices, e. g. as catalyst support in catalyst layers for fuel cells and as electrode material for ionic-polymer metal composites [126] [127]. As they exhibit a 2D structure that is “rolled” to a cylindrical shape they combine high aspect ratio with good electrical conductivity in the range of semiconductors and metals [128] [129]. CNTs can be divided into single-walled carbon nanotubes (SWCNT) and multi-walled carbon nanotubes (MWCNT) which consist of several SWCNTs interleaved to one cylindrical structure. It was shown that CNT-based composites with ionomers reached percolation threshold at concentration of less than 0.5 wt%. Sangeeth *et al.* studied the specific electrical conductivities of ionomer (Nafion®) CNTs compounds. They achieved 0.005 S/cm for 1 wt% MWCNT and 3.2 S/cm for 10 wt% MWCNT compounds [130]. It was also shown that the

choice of CNT and the way of processing have a significant effect on the resulting specific electrical conductivity [128].

Taking into account the specific advantages and disadvantages of different carbon-based filler particles, CNTs were chosen for enhancing the electrical conductivity of the catalyst layer in this thesis. Especially the high specific conductivity of the particle itself, the low theoretical percolation threshold and their good availability on the market make them advantageous in comparison to CB and GNS. For all experiments, NC 7000™ MWCNTs (Nanocyl®) were used.

mass [g]	1 wt% CNT	3 wt% CNT	5 wt% CNT	10 wt% CNT	15 wt% CNT
$m_{\text{Kat}}$	0.1	0.1	0.1	0.1	0.1
$m_{\text{FLNA}}$	0.4286	0.4286	0.4286	0.4286	0.4286
$m_{\text{H}_2\text{O}}$	13.9	13.9	13.9	13.9	13.9
$m_{\text{IPO}}$	5.5714	5.5714	5.5714	5.5714	5.5714
$m_{\text{CNT}}$	0.0014	0.0044	0.0075	0.0159	0.0252

**Table 8: Composition of manufactured catalyst layers with varying amount of CNT.**

In order to gain information about the dependency of the electrical conductivity on the concentration of filler particles, dispersions with different weight percentages were fabricated. Additionally, catalyst particles (Pt/C, 40 wt%<sub>Pt</sub>), ionomer dispersion (FLNA, 10 wt%), isopropanol and deionized water were mixed with the CNTs. Table 3 gives information about the specific compositions of all fabricated samples.

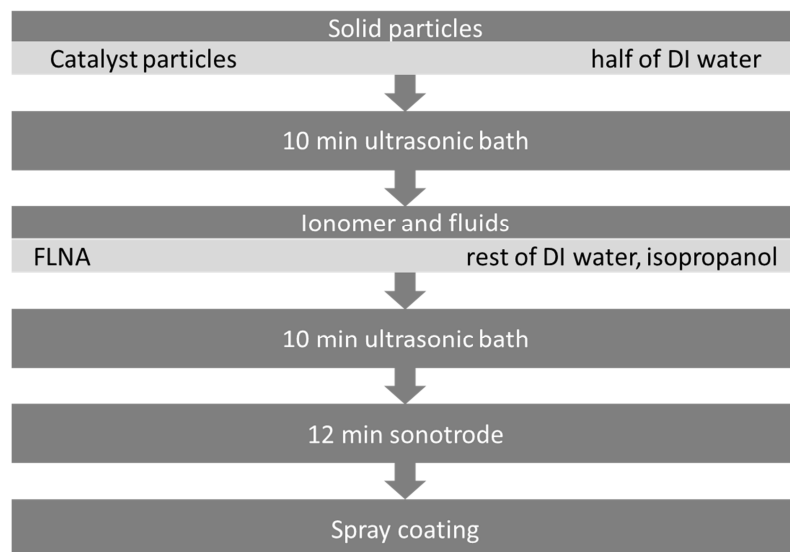


**Figure 82: Fabrication process of catalyst layers with CNT add-ins.**

Figure 82 shows a diagram of the dispersion processing procedure. For homogeneous distribution of the particles, ultrasonic and sonotrode treatment were applied. As isopropanol is oxidized on Pt which may lead to adsorption of CO reactants or even the isopropanol catching fire, half of the DI-water was added before. Finally, the dispersion was spray coated onto a silicon substrate with an oxide layer on top for electrical insulation.

The thickness of the resulting layers was measured by confocal microscopy. Depending on the amount of CNTs, thicknesses between 8.5  $\mu\text{m}$  and 12.5  $\mu\text{m}$  were obtained for layers with a 15 fold spray coating process. Optical microscopy showed that higher concentration of CNTs has a positive effect on homogeneity of the layers. Figure 83 presents images of the layers at 20 fold magnification.

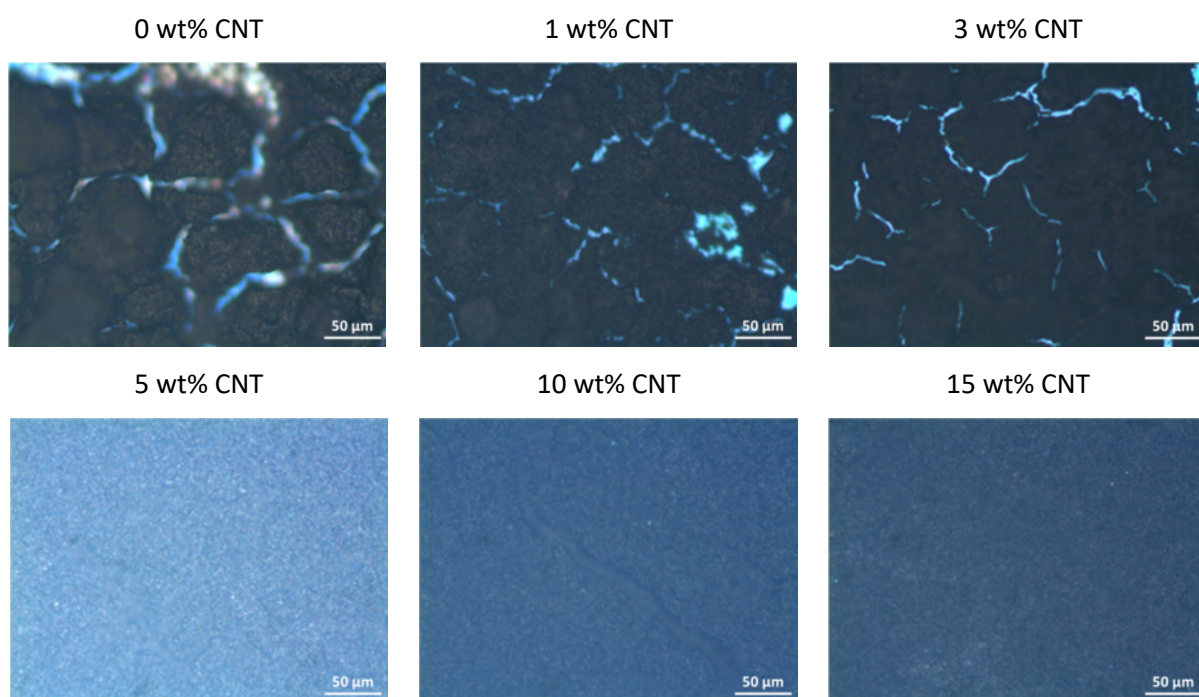
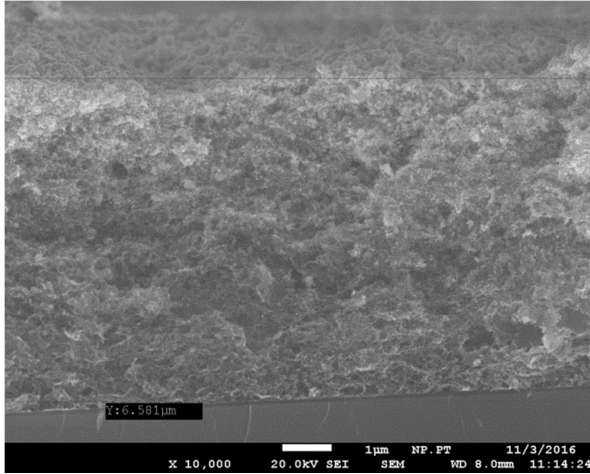


**Figure 83: Microscopy images of the catalyst samples with 15 spray coated single layers each and varying amounts of CNT at 20-fold magnification.**

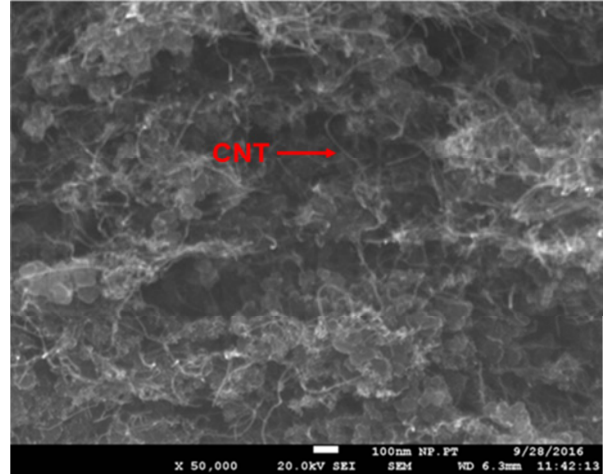
It can be seen that at concentrations below 5 wt% CNT, the layers exhibit cracks and blanks due to agglomeration of the dispersion during drying process. Layers with 5 wt% and above show good homogeneity. This leads to the conclusion that addition of CNTs also has a positive effect on wettability and surface tension.

Figure 84 and Figure 85 show SEM images of a catalyst layer with 15 wt% CNT and a thickness of 6.6  $\mu\text{m}$  resulting from a 10 fold spray coating process. Good porosity of the layer can be observed which is important considering good accessibility of the reactant gases to the Pt particles inside the layer. The distribution of the CNTs is homogeneous and does not show any preferred direction.





**Figure 84:** SEM-image of spray coated catalyst layer (10,000 fold magnification) with 10 wt% CNT exhibiting a thickness of 6.5 μm (according to 10 single coating steps).



**Figure 85:** Detailed view of catalyst layer at 50,000 fold magnification; homogeneous CNT distribution can be observed.

For detection of the electrical conductivity, Kelvin resistance measurements were executed. By applying a constant current of 0.5 mA at the outer electrodes and measuring the voltage drop at the inner electrodes, the electrical resistances of the samples were determined. Taking into account the thickness of the layers, the specific electrical resistance  $\rho_{el}$  can be determined:

$$\rho_{el} = R_{el} \frac{A_{el}}{l_{el}} \quad 6-2$$

The specific electronic resistance is a function of the measured electrical resistance  $R_{el}$ , the cross section  $A_{el}$  perpendicular to the flow of electrons and the distance between the electrodes  $l_{el}$ . As the goal for these experiments was to improve the horizontal electric conductivity of the catalyst layer, the in-plane resistances were determined.

Compounds of PFSA-based ionomers and CNTs show strong dependency on humidity. As thin ionomer films tend to swell up to 48 % at 96 % RH compared to dry state [131] this strongly affects the distance between the CNTs within the matrix and thereby the percolation network. Percolation paths that would be existent at low relative humidity disappear and the specific electrical conductivity decreases. Hence, the conductivity strongly depends on the ambient relative humidity [132]. In order to preserve comparability between single measurements, all samples were tested in DI-water in order to ensure a constant hydration state of the ionomer. This way, the minimal electrical conductivity at maximum level of humidification could be identified which is important considering the application in a fuel cell.

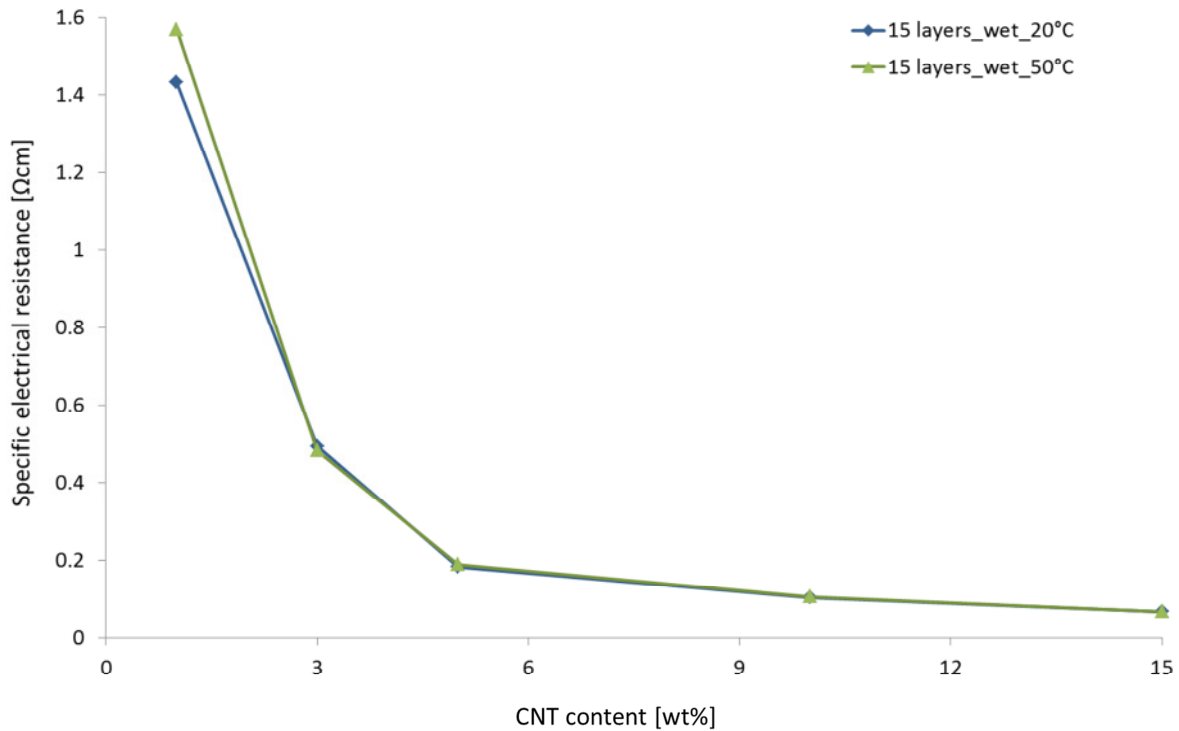


**Figure 86: Specific electrical resistivity in  $\Omega\text{cm}$  correlating to CNT content.**

Figure 86 shows the results of the conductivity measurements. Typical percolation behavior can be obtained. At low percentages of weight (1 wt%) the specific electrical resistance has a value of 1.4  $\Omega\text{cm}$ . With increasing concentration of CNTs the resistances decrease strongly. At 5 wt% the specific electrical resistance can be reduced to 0.18  $\Omega\text{cm}$ . This is in good correlation to the results found in literature. The high aspect ratio leads to low percolation threshold and thereby significant generation of percolation paths with low amount of filler particles. Further addition of CNTs results in moderate decrease of electrical resistance down to 0.07  $\Omega\text{cm}$ . The reason for that is the low growth rate of new percolation paths which leads to a saturation and a final value in specific electrical resistance. As specific electrical conductivity is nothing but the reciprocal value of the specific resistance, the best conductivity at 15 wt% is 15.5 S/cm. This is in good agreement and even slightly higher compared to the values found from literature. Unfortunately, it is still significantly lower than the specific electrical conductivity of bulk carbon (1250 S/cm) which is used for fabrication of the GDL.

A change in temperature does not have a significant effect. Raising the water temperature up to 50°C the measured specific electrical resistances are in accordance with the samples measured at room temperature. Only at a content of 1 wt% CNT, the specific electrical resistance is slightly higher at 50°C. As the CNT concentration is near the percolation threshold, even slight changes in the distance of the filler particles will have a measurable effect on the specific resistances. Thus, the expansion of



the polymer due to the higher temperature can be detected by the slight change in specific conductivity.

In order to characterize the repeatability of the spray coated layers, 10 samples with 15 wt% CNT were fabricated and the specific resistivity was measured. Table 9 shows the results of these measurements:

Sample No.	Specific electrical resistance [ $\Omega\text{cm}$ ]	Sample No.	Specific electrical resistance [ $\Omega\text{cm}$ ]
1	8,03E-02	6	7,87E-02
2	8,09E-02	7	7,51E-02
3	8,11E-02	8	7,82E-02
4	7,12E-02	9	7,35E-02
5	7,48E-02	10	7,29E-02

**Table 9: Overview of specific electrical resistivity of 10 sample which were fabricated identically.**

From these measurements an average electric resistance of  $7.66\text{E-}02 \text{ }\Omega\text{cm}$  was calculated. The standard deviation is  $0.0034 \text{ }\Omega\text{cm}$ , which corresponds to 4.5 % of the average specific resistance, indicating a good repeatability of the spray coating process.

In addition to the specific electrical conductivity, the electrochemical active surface needs to be verified. The integration of an additional component to the catalyst layer can influence the catalyst particles in two ways. First of all, the concentration of catalyst particles contained inside the dispersion decreases when another component is added. Moreover, the CNTs may cover the Pt surface and thereby inhibit the electrochemical reaction. Because of that, the change in electrochemical active surface was determined by cyclic voltammetry.  $3 \mu\text{l}$  of the catalyst dispersion were dropped onto a glassy carbon electrode and dried at room temperature. The layers were measured in  $0.1 \text{ M HClO}_4$  electrolyte under nitrogen saturation at 2000 rpm of the electrode. The feed of the potential was  $20 \text{ mV/s}$  and temperature was set to  $25^\circ\text{C}$ . Figure 87 shows the results for a catalyst layer without CNTs and with 15 wt% CNTs. Analysis of the hydrogen adsorption peak according to chapter 4.1 gives values of  $24.9 \text{ m}^2/\text{g}_{\text{Pt}}$  for the sample without any CNTs and  $21.4 \text{ m}^2/\text{g}_{\text{Pt}}$  for the sample with 15 wt% CNTs. Hence, a significant decrease in electrochemical active surface of 13.6 % can be observed. As this will also affect the electrochemical reaction at the fuel cell electrodes, further increase of the weight percentage of CNTs is not recommendable.

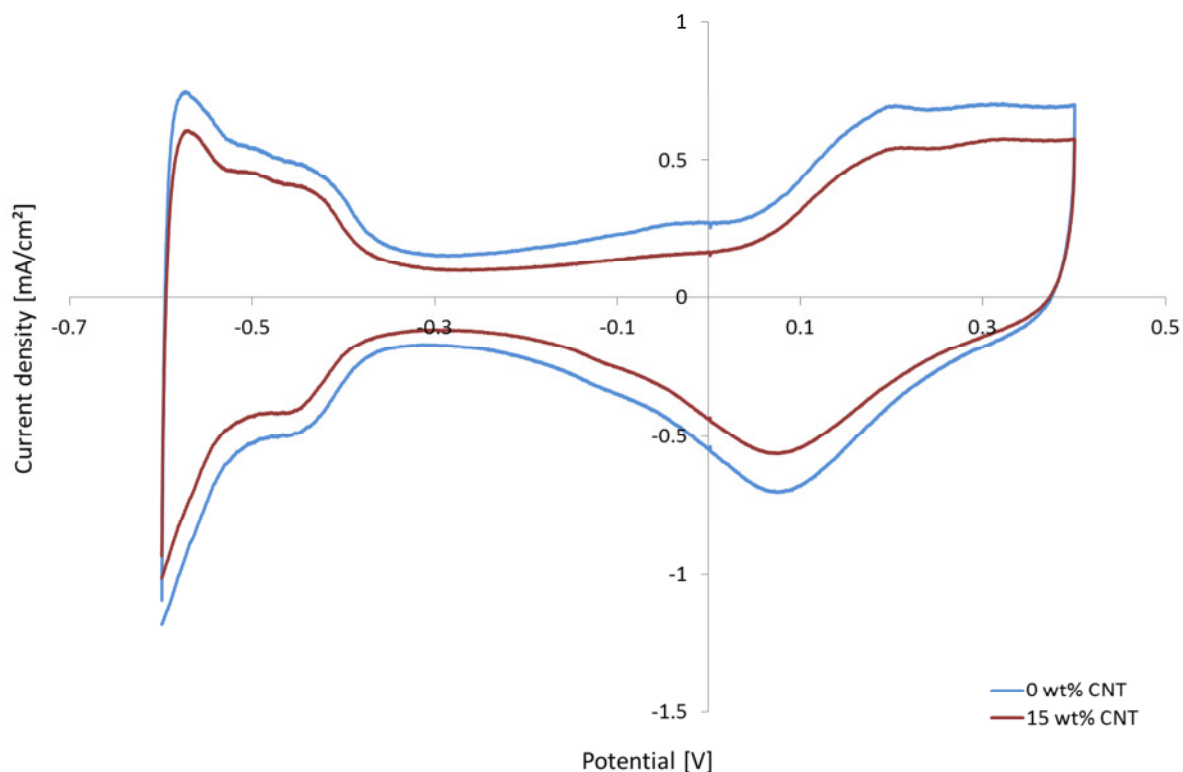


Figure 87: Cyclic voltammogram of catalyst layers without CNT and with 15 wt% CNT; electrolyte was 0.1 M HClO<sub>4</sub> with Hg/Hg<sub>2</sub>SO<sub>4</sub> reference electrode at a scan rate of 20 mV/s; significant decrease in ECAS can be measured for high amount of CNT filler.

#### 6.4.3 Characterization of electrically conductive catalyst layers in $\mu$ MEAs

In order to characterize the electrochemical performance of the above described layers a  $\mu$ MEA was assembled and polarization curves were measured. For that, a 5  $\mu$ m thick silicon membrane with 1  $\mu$ m micro channels was filled with ionomer with the help of a dip coating process as discussed in chapter 5.3.2. In contrast to the  $\mu$ MEAs described so far, the membrane did not have a sputter coated Cr-/Pt-layer on any of its surfaces. Hence, current collection was completely realized by the intrinsic electrical conductivity of the catalyst layer. For comparability of the electrochemical characterization to the  $\mu$ MEAs described in chapters 6.1 and 6.2, test setup and test parameters were kept the same. Figure 88 shows the results of the polarization curves measured at room temperature and with 2 ml/min H<sub>2</sub> and 4 ml/min air for a sample with a catalyst layer with 10 wt% CNTs and a catalyst layer with 15 wt% CNTs. For these two samples opposing effects appear. The increased electrical conductivity of 15 wt% CNT (cf. Figure 86) is accompanied by a decreased ECAS (Figure 87). As observed before, the OCV for spray coated catalyst layer is significantly higher (0.88 V) than for sputter coated Cr-/Pt-layer (0.7 V). Interestingly, the maximum measured power density is higher for the 10 wt% CNT sample (4.2 mW/cm<sup>2</sup>) compared to the 15 wt% CNT sample (3.5 mW/cm<sup>2</sup>). Thus, the decrease in electrochemical ECAS seems to be more dominant than the slight increase in specific electrical conductivity. In comparison to  $\mu$ MEAs with sputter coated

Cr-/Pt-layer, it has to be constituted, that the maximum power density is in the range of the  $\mu$ MEA with a 50 nm Cr layer and 80 nm Pt layer ( $4.0 \text{ mW/cm}^2$ ). Hence, the relatively poor specific electrical conductivity limits the bifunctional use of the catalyst layer as “integrated” current collector and needs further improvement. On the one hand the Ohmic resistances need to be minimized to values comparable to – at least – the same level as solid carbon/graphite while on the other hand a further decrease of the electrochemical active surface area needs to be inhibited.

Nevertheless, power densities similar to sputter coated current collectors could be achieved. This clearly indicates the necessity of replacing the sputter coated metal thin layer and is a promising result for further development. Moreover, the combination of two components (current collector and catalyst layer) has a significant potential in saving costs for manufacturing as the number of production steps decreases and no expensive sputter devices are needed for metal deposition.

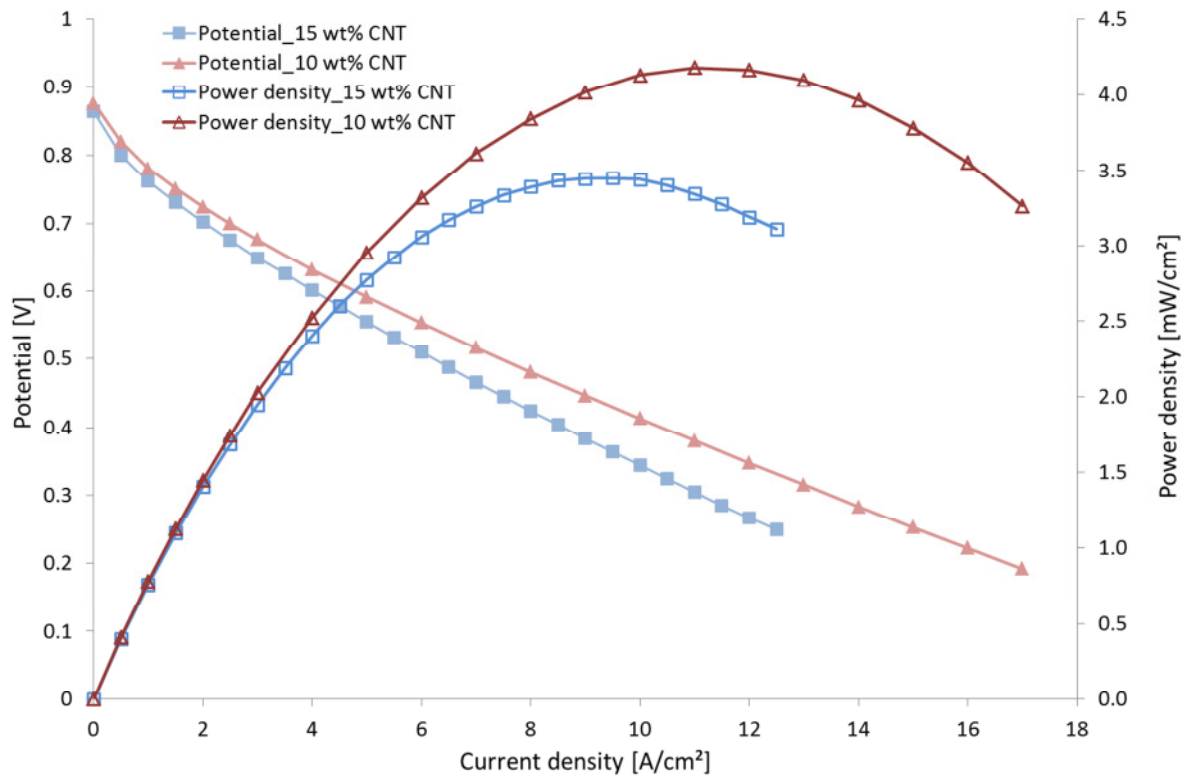


**Figure 88:** Polarization curves of two different  $\mu$ MEAs with different CNT loading; lower CNT loading shows higher power density; the gas supply was set to minimum values possible ( $\text{H}_2$ : 2 ml/min, air: 4 ml/min); for 15 wt% of CNTs stoichiometries reach values of 12.7 (cathode) respectively 15.1 (anode) at the MPP ( $9.5 \text{ mA/cm}^2$ ); for 10 wt% of CNTs stoichiometries reach values of 10.9 (cathode) respectively 13 (anode) at the MPP ( $11 \text{ mA/cm}^2$ ); the measurement was conducted under ambient conditions (1 bar,  $20^\circ\text{C}$ ) and without humidification.

#### 6.4.4 Electrodeposition of Pt inside the catalyst layer

The previous chapter has shown that doping of catalyst layer with conductive nanoparticles can enable fuel cell reaction without usage of additional current collector like a sputter coated Cr-/Pt-layer. Specific electrical conductivity can be increased by a factor of 20 while electrochemical

active surface decreases by 13.6 %. However, the power density of 4.2 mW/cm<sup>2</sup> is lower compared to  $\mu$ MEAs containing a metal current collector and an additional spray coated catalyst layer. This can be related to the low absolute electric conductivity of the electron conducting layer and the lower catalytic activity. Hence, the goal for optimization should be the enhancement of both, electric conductivity and catalytic activity.

In literature, electrodeposition of catalytic Pt particles is described as a promising method for this. Pt was successfully deposited on carbon particles inside fuel cell electrodes and improvement of catalytic activity was observed [133] [134]. Moreover, electrodeposition of Pt inside fuel cell electrodes resulted in significant improvement of electrical performance for current conducting electrodes [135]. Thus, electrodeposition of Pt on the conductive CNT particles inside the catalyst layer should add percolation paths and, at the same time, increase the electrochemical active surface area. As the spray coated catalyst layer consists of conductive particles throughout the entire thickness of the layer, Pt should be deposited homogeneously across the thickness of the layer. The resulting combination of increased amount of electrochemical active Pt particles and electrical conductive percolation paths together with ion conductive PFSA particles of the catalyst layer should result in a high amount of 3 phase boundaries.

Therefore, an experimental setup was developed which makes electrodeposition of Pt inside the spray coated catalyst layer possible for silicon-based  $\mu$ MEAs. A sketch of the final setup is shown in Figure 89. A Galvatron Pt electrolyte with 2.5 g<sub>Pt</sub>/l was used. The glass with electrolyte was dipped into a water bath with controlled temperature between 50 °C – 60 °C and stirred with a magnetic stir bar. A platinized titanium metal grid was used as anode. The current of the electrodeposition was induced by a Keithley source meter.

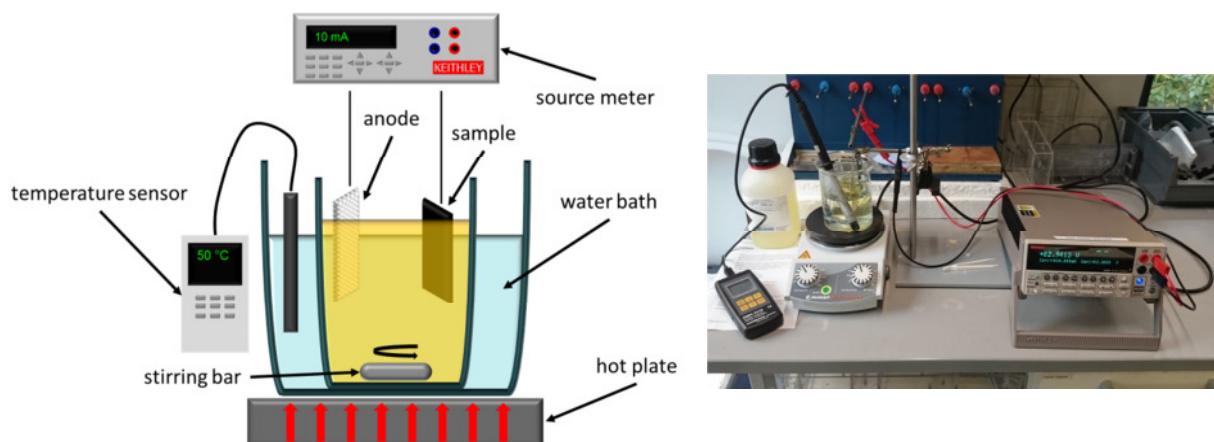


**Figure 89: Sketch of principle setup for galvanic deposition of Pt on catalyst layer and photo of the actual deposition setup.**

The deposition rate  $D_{Pt}$  of the electrolyte was given with 70 mg/Ah from the data sheet. Hence, the mass of the deposited Pt could be calculated by defining constant deposition time  $t$  and current  $I_D$ :

$$m_{Pt} = D_{Pt} I_D t \quad 6-3$$

For first evaluation, a conductive catalyst layer with 15 wt% CNT was spray coated onto a 10 x 30 mm<sup>2</sup> silicon dioxide substrate. Different deposition times and stirring rotation velocities were tested. The relatively low specific electrical conductivity of the catalyst layer induced high voltage loss along the deposition area. This resulted in strong bubble formation as the water of the electrolyte was split into hydrogen and oxygen. Because of this, the deposition current was decreased to 10 mA in order to minimize evolution of hydrogen at the deposition electrode. This way porosity of the Pt layers could be enhanced as well. It was found that stirring velocity of 500 rpm was sufficient for removal of remaining hydrogen gas bubbles without evolution of turbulences of the fluid and for improved supply of Pt at the reaction sites. Specific electric conductivity was measured with the help of Kelvin resistance measurements. For deposition times of 600 s a specific electrical conductivity of 142.6 S/cm and for 1200 s a specific electric conductivity of 540.9 S/cm could be determined. This is a significant improvement compared to conductive catalyst layers without electrodeposited Pt (15 S/cm, cf. chapter 6.4.3).

SEM images were taken for evaluation of the layer (cf. Figure 90). Instead of being deposited homogeneously across the entire thickness of the conductive catalyst layer, Pt was mainly found on the surface as a persistent layer of Pt was formed as was shown by additional EDX measurements (cf. Figure 91) while the amount of Pt decreases gradually with depth of the catalyst layer. A deeper look into the layer at 50,000 fold magnification shows that the Pt on the surface is not a continuous layer but has formed islands that build a porous structure as it was intended to be (cf. Figure 92). This result can be explained with the much higher flow resistance inside the porous catalyst layer compared to the surface. This flow resistance increases with the thickness of the layer, reaching its maximum at the border between porous catalyst layer and membrane. The weaker flow of deposition fluid through the pores leads to a lack of Pt particles whereas the surface is provided with Pt-rich electrolyte during deposition. Hence, the deposition rate on the surface is higher, resulting in more Pt deposited on the surface. This might be beneficial for creating a good electric conductivity, but also reduces porosity near the surface and decreases utilization of the deposited Pt.

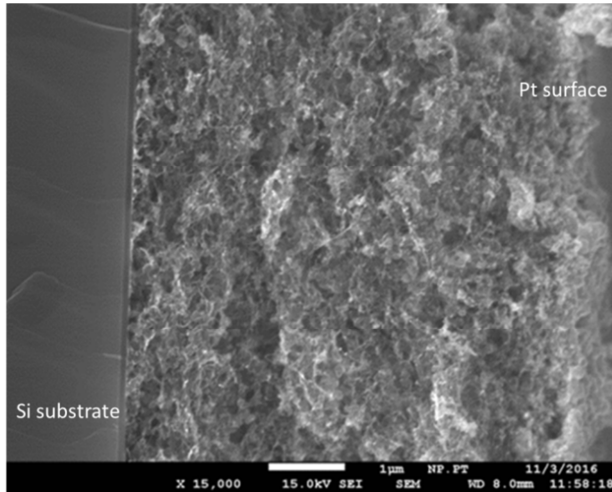


Figure 90: SEM image of the catalyst layer after galvanic deposition of Pt.

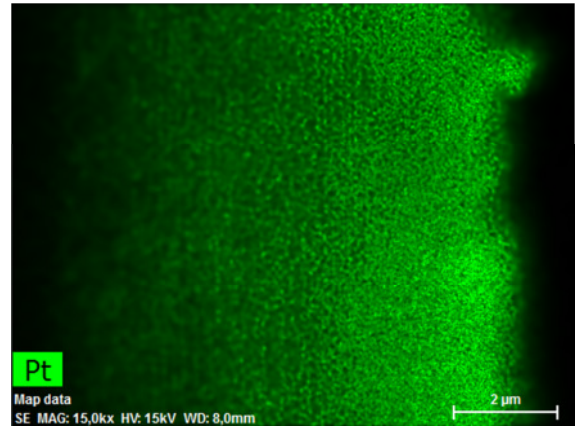


Figure 91: EDX measurement of the catalyst layer showing the distribution of the deposited Pt.

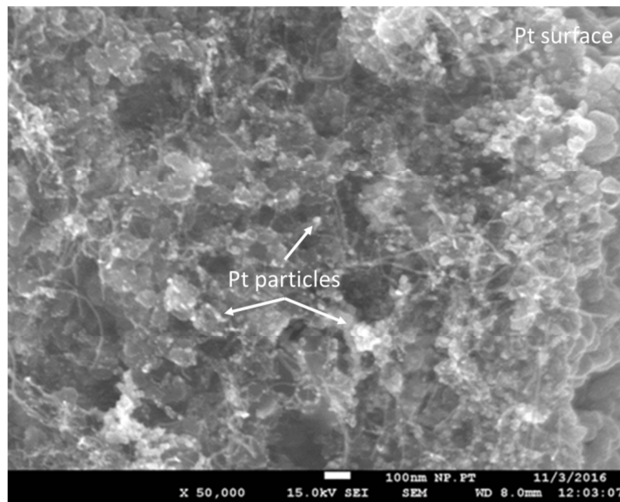


Figure 92: Detailed image of the catalyst layer near surface at 50,000 fold magnification; creation of a continuous Pt-layer at the surface can be observed.

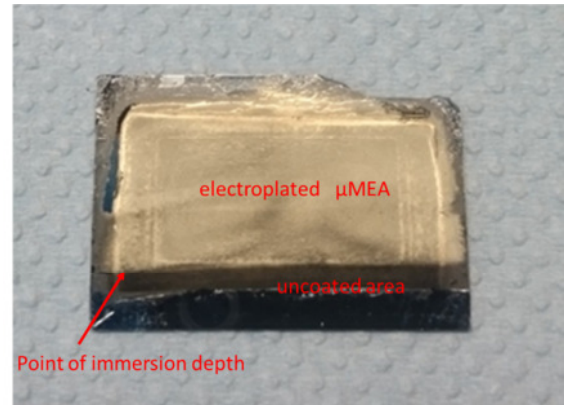


Figure 93: Photo of a  $\mu$ MEA after galvanic deposition of Pt for 840 s at 30 mA.

Based on the finding above, a  $\mu$ MEA was prepared for evaluation of the efficiency of electrodeposited Pt. Therefore, a microstructured silicon membrane was dip-coated with 0.4 mm/min in PFSA ionomer and spray coated with conductive catalyst layer on both sides. The conductive catalyst layer contained 15 wt% CNT and exhibited a thickness of 12.5  $\mu$ m which correlates to 0.36  $\text{mg}_{\text{Pt}}/\text{cm}^2$  at each electrode. After that, the  $\mu$ MEA was electrodeposited with Pt. Stirring velocity was set to 500 rpm and temperature was hold at a constant value of 50  $^{\circ}\text{C}$ . Owing to the fact that the  $\mu$ MEA has a surface area three times larger compared to the samples used for evaluation of the electrodeposition process, the deposition current was set to 30 mA. Deposition time was set to 840 s. According to equation 6-3 this leads to a final Pt loading of 0.245  $\text{mg}_{\text{Pt}}/\text{cm}^2$ . Adding this to the original 0.36  $\text{mg}_{\text{Pt}}/\text{cm}^2$ , the resulting overall Pt loading was 0.605  $\text{mg}_{\text{Pt}}/\text{cm}^2$  at each



electrode. A photo of the final  $\mu$ MEA is shown in Figure 93. The area of electroplated Pt can be identified as color has changed from black to grey.

Polarization curves were taken under ambient temperature and humidity. Gas supply was set to minimum of 2 ml/min  $H_2$  and 4 ml/min air. Power density of the  $\mu$ MEA shows significant increase to 6 mW/cm<sup>2</sup> while OCV shows nearly no change compared to conductive catalyst layers without electrodeposited Pt.

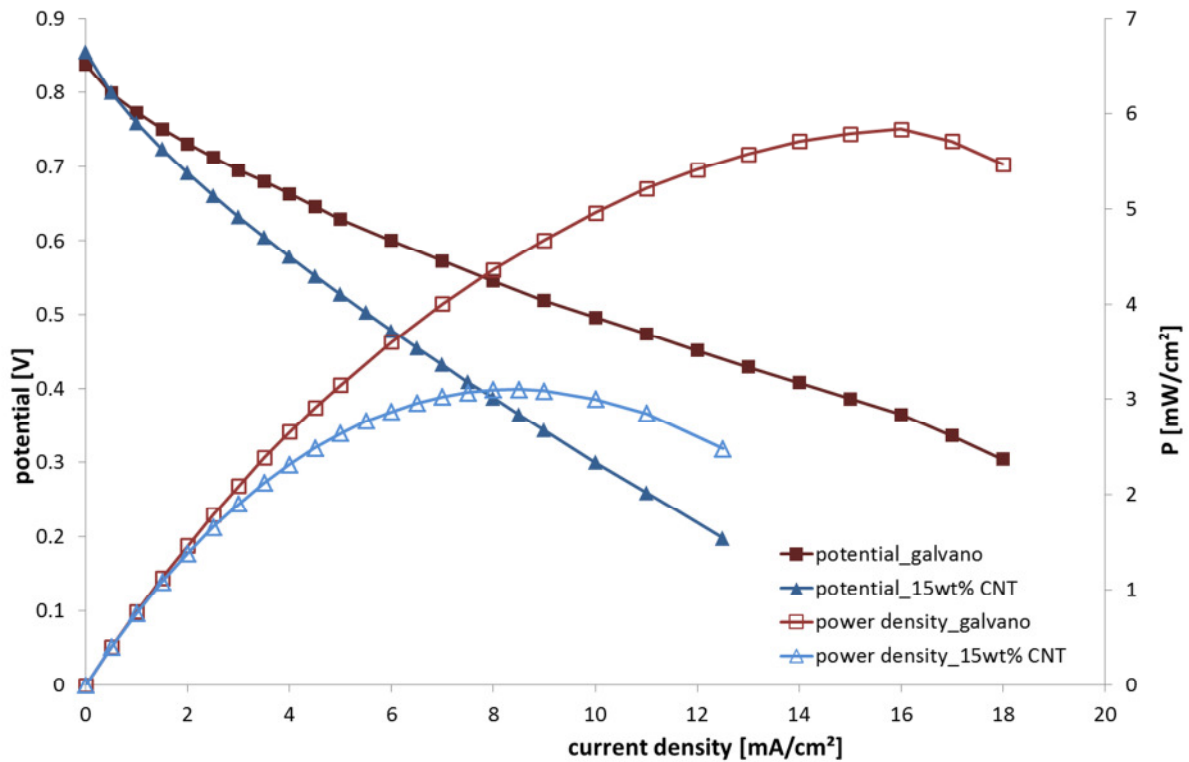


**Figure 94: Electrochemical performance of the  $\mu$ MEA with electrodeposited Pt compared to bare catalyst layer with CNTs only; the gas supply was set to minimum values possible ( $H_2$ : 2 ml/min, air: 4 ml/min); for 15 wt% of CNTs stoichiometries reach values of 12.7 (cathode) respectively 15.1 (anode) at the MPP (9.5 mA/cm<sup>2</sup>); for  $\mu$ MEA with electrodeposited Pt stoichiometries reach values of 7.5 (cathode) respectively 9 (anode) at the MPP (16 mA/cm<sup>2</sup>); the measurement was done under ambient conditions (1 bar, 20°C) and without humidification.**

In order to understand the electrochemical behavior of the  $\mu$ MEA, EIS measurements were conducted. EIS spectra were taken at OCV, 5 mA/cm<sup>2</sup>, 10 mA/cm<sup>2</sup> and 20 mA/cm<sup>2</sup>. Frequencies ranged from 500 kHz to 200 mHz and amplitude was set to 20 mV. Resulting spectra are shown in Figure 95. The results were analyzed using ZView® and calculated simulation parameters are summarized in Table 10. One equivalent circuit model was used for all four EIS spectra. A second constant phase element had to be added as galvanostatic fuel cell operation did not reach a steady state. In order to take diffusion limitation into account, a Generalized Finite Warburg Element was added to the cathode circuit.

Overall Ohmic resistances  $R_{ohm}$  resulting from proton conduction and intrinsic electric resistances like the current collector are reaching  $2.4 \Omega$  which is about two times higher compared to electrode setup that contains sputter coated Cr-/Pt-layers (cf. chapter 6.2). On the one hand, this is not surprising as sputter coated solid metal layers offer higher electric conductivity than polymer layers with conductive particles. On the other hand, the ohmic resistances are low enough to sustain the fuel cell reaction which is a good result.

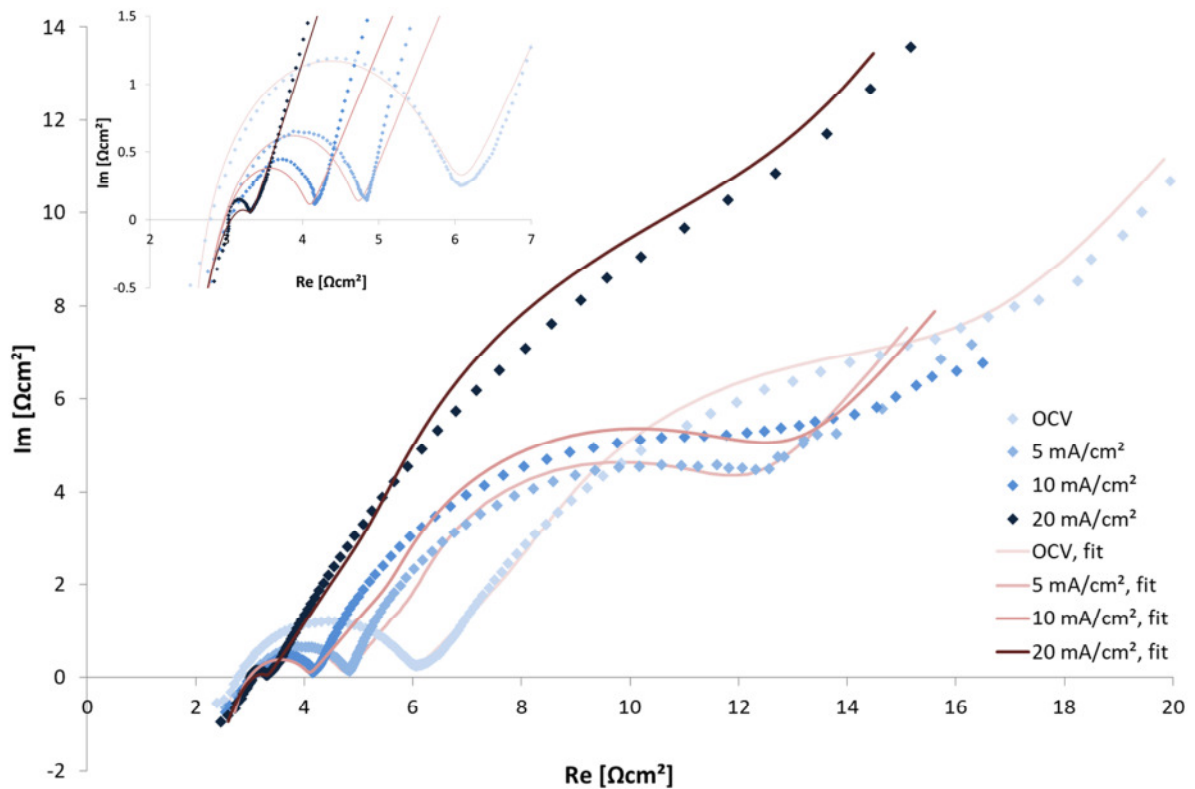
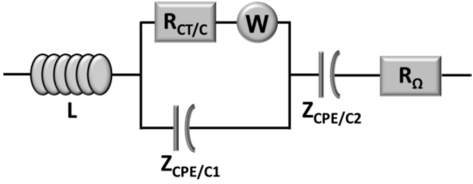


**Figure 95: Electrochemical characterization of operating  $\mu$ MEA with electrodeposited Pt through EIS and corresponding simulation fits; spectra were taken at OCV, 5 mA/cm<sup>2</sup>, 10 mA/cm<sup>2</sup>, 15 mA/cm<sup>2</sup> and 20 mA/cm<sup>2</sup>; frequencies ranged from 500 kHz to 200 mHz; amplitude was set to 20 mV; the inset shows magnification of high frequency arcs.**

Charge transfer resistances could be decreased significantly to values below  $4 \Omega$ . As the amount of platinum was increased massively by electrodeposition compared to previous spray coated catalyst layers this results clearly shows the dependence of the fuel cell performance on available catalyst material.

It also has to be stated that conductive filler particles (CNT) and electrodeposition of platinum have led to reasonable diffusion limitations as can be seen from the simulation results. Both, filler particles as well as electroplated platinum decrease porosity inside the catalyst layer, resulting in inhibited mass transport and diffusion. All these factors together lead to an inferior fuel cell performance compared to the electrode setup described in chapter 6.2.





Current density	L1	R <sub>ohm</sub>	CPE1-Q	CPE1-n	R <sub>CT/C</sub>	CPE2-Q	CPE2-n	Y <sub>o</sub>	δ <sup>2</sup> /D	P
<b>OCV</b>	<b>3.5E-7</b>	<b>2.32</b>	<b>1.8E-5</b>	<b>0.76</b>	<b>3.70</b>	<b>0.06</b>	<b>0.62</b>	<b>6.65</b>	<b>0.21</b>	<b>0.55</b>
(error)	9.4E-9	0.04	2.1E-6	0.01	0.05	3.0E-3	0.05	1.17	0.02	0.02
<b>5 mA/cm<sup>2</sup></b>	<b>3.8E-7</b>	<b>2.28</b>	<b>7.1E-6</b>	<b>0.80</b>	<b>2.42</b>	<b>0.11</b>	<b>0.62</b>	<b>5.33</b>	<b>0.16</b>	<b>0.59</b>
(error)	2.1E-8	0.12	1.8E-6	0.03	0.12	4.1E-3	0.04	0.50	7.6E-3	0.02
<b>10 mA/cm<sup>2</sup></b>	<b>3.7E-7</b>	<b>2.44</b>	<b>1.0E-5</b>	<b>0.80</b>	<b>1.63</b>	<b>0.12</b>	<b>0.62</b>	<b>6.40</b>	<b>0.25</b>	<b>0.58</b>
(error)	2.2E-8	0.11	4.0E-6	0.04	0.12	7.7E-3	0.05	0.72	0.01	0.02
<b>20 mA/cm<sup>2</sup></b>	<b>4.8E-7</b>	<b>1.08</b>	<b>1.43E-5</b>	<b>0.65</b>	<b>2.24</b>	<b>0.06</b>	<b>0.71</b>	<b>5.49</b>	<b>0.66</b>	<b>0.59</b>
(error)	6.6E-8	1.64	1.4E-5	0.06	1.65	4.3E-3	0.04	1.39	0.06	0.03

**Table 10: Parameters of the equivalent circuits in ZView for each result of the EIS measurements: a second CPE is added to take polarization of the cathode at low frequencies into consideration; strong mass transport limitations occur and a Finite Warburg Element has to be added to the equivalent circuit.**

Taking all results into account, the addition of electrically conductive filler particles into conventional catalyst layers seems to be a promising way to replace dense metal layers for current collection in micro fuel cells. By using CNTs with high aspect ratio, reasonable specific electrical conductivity was achieved. Nevertheless, the total electrical resistances remain higher compared to sputter coated metal layers because porosity and ionomer content inside the catalyst layer need to be maintained. Enriching the electrically conductive catalyst layer with Pt by galvanic deposition leads to significant increase in electric conductivity and reduction of charge transfer resistances. Hence, higher power density can be measured in fuel cell operation compared to catalyst layers without electro-deposited platinum while still performing worse than  $\mu$ MEAs with sputter coated Cr-/Pt-layers. That is why further development of this approach is necessary. Porosity, electrical resistance and catalytic activity need to be optimized. Therefore, better distribution of Pt particles within the catalyst layer deposited by galvanic processes seems to be a reasonable starting point.

## 6.5 Summarizing considerations on MEMS-based $\mu$ MEAs

In chapter 6, three different electrode setups were characterized. The first one uses a sputter coated bifunctional Cr-/Pt-layer as both, catalyst layer and current collector. Being the simplest setup which is most adaptive to mass production in semiconductor and MEMS technology, this approach has significant disadvantages. The sputter coated platinum does not offer enough porosity to ensure high catalyst effectivity. Also, a thin residual ionomer layer, resulting from the dip-coating process to

integrate the ionomer into the microstructure of the silicon membrane, covers the platinum, leading to even higher mass transport limitations of the reactants.

Adding a spray coated catalyst layer with high porosity on top of the electrodes decreases charge transfer resistances and mass transport limitations significantly. Still, the residual ionomer layer between sputter coated Cr-/Pt-layer which still serves as current collector and the spray coated catalyst layer remains an issue. On the other hand, EC-AFM measurements have shown that the residual ionomer layer is necessary to ensure good proton conductivity on the areas between the micro channels.

Replacing the sputter coated Cr-/Pt-layer with a conductive catalyst layer solves this issue. Unfortunately, adding conductive filler particles to the spray coated catalyst layer results in decreased overall electric conductivity and lower porosity which correlates to increased diffusion limitations. This leads to decreased fuel cell performance compared to the second electrode setup.

All in all, it was shown successfully that a  $\mu$ MEA can be designed and manufactured and operated with the help of MEMS technology. Using the results of the in depth electrochemical characterization of the electrode setups, it will be possible to adjust individual components for achieving reasonable power densities in the near future.

## 7 Combining micro fuel cells with high throughput methods for catalyst development

### 7.1 Combinatorial methods in materials development

Today, global markets are pressurized by fast innovation cycles. The time-to-market needs to be short in order to reduce development costs and create competitive advantages. Especially in sectors that depend on innovation in materials this might be challenging. Representative examples are the pharmaceutical and the catalyst industry. Often, the development of new materials is more empirical rather than based on calculations or physical and chemical models. The reason for is the multidimensional parameter space which influences the performance of the material. For example, in catalyst development the activity of a catalyst may be determined by the alloy (ternary, quaternary, etc.), the morphology (size, structure, porosity), the fabrication process (purity, defects) or the catalyst support (specific surface). This is why the physical and chemical behavior of certain catalyst alloys remains hard to predict.

Because of that, the optimization of empirical development processes has created the field of combinatorial materials development. By using statistical approaches the variation of samples is reduced and time, material and workforce can be saved. Combinatorial methods include the synthesis as well as the screening of high amounts of different samples within one work step. This does not mean that any combination of material shall be tested but that libraries of samples are fabricated on the basis of statistical principles. Hence, factors of success for combinatorial materials development are parallelization, miniaturization and automation.

Figure 96 shows the basic approach of combinatorial methods. First, a validation of the general physical properties is executed. This so-called primary screening is used for identification of interesting candidates from a vast number of material combinations. Mostly, a primary screening is a relative comparison between the materials and does not give information about the absolute efficiency. Next, the identified candidates are characterized further by a secondary screening which allows detailed conclusions on the total performance of the materials. If the results indicate a substantial improvement, the most effective materials are transferred to an application-near functional model where they can be tested under operating conditions. Successful characterization will lead to a prototype and finally to a product applying the new material [136].

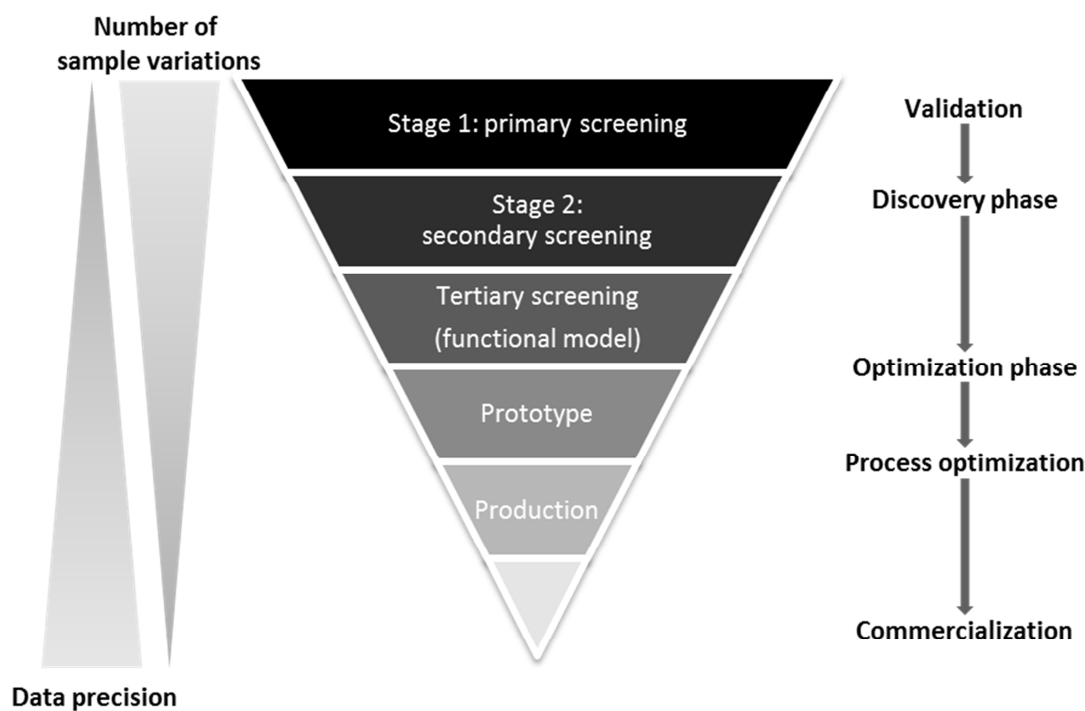


**Figure 96: Process flow of a high-throughput catalyst optimization from validation to commercialization (according to [136]); as the number of tested samples decreases the precision of the characterization method increases.**

Combinatorial methods have widely been used to develop new components for fuel cells. Especially the search for effective and cheap catalysts has been the focus of research. This includes the application of combinatorial methods for fabrication as well as for characterization. For example, sputter technology has been used to manufacture material libraries with high amount of material combinations and scanning electrochemical microscopy was developed for evaluation of those libraries [137].

However, high-throughput screening of fuel cells remains an issue as it is challenging to characterize high numbers of assembled fuel cell MEAs in parallel. Some attempts have been made using fuel cell arrays with different materials and components [138] [139]. However, the amount of individual samples was limited, which questions the effectivity of these experiments.

## 7.2 Infrared thermography for high-throughput screening

As described above, the duration of the development cycle in combinatorial development depends not only on the possibility to synthesize a high number of sample variations but also on the speed of the characterization method. Hence, the definition of high-throughput screening (HTS) is based on parallel measuring techniques that enable fast and reliable identification of superior materials. In case of catalyst development this would be the search for more electroactive candidates.

A HTS method that is well established in catalyst development is infrared (IR-) thermography. IR-thermography can also be found in many other applications such as aviation, electronics, medical science or quality control. By utilizing the exothermic or endothermic nature of catalytic reactions, this technique allows evaluating the dissipation of heat of a surface without contacting or destroying the sample. This is done by detection of the intensity of the thermal radiation through a focal-plane array detector. Detection of the temperature and emissivity distribution leads to high resolution 2 dimensional images where different colors indicate the intensity of the photons generated by heat. Usually, radiation with a wavelength in the range of 800 nm to 1 mm is measured. In order to minimize the influence of the atmosphere the use of wavelengths between 8  $\mu\text{m}$  and 14  $\mu\text{m}$  are common. Within this range there is almost no absorption by the atmosphere.

### 7.2.1 Physical principles of IR-thermography

All bodies with a temperature above 0 K emit infrared radiation whose intensity depends on its temperature  $T$ , the wavelength of the radiation  $\lambda_R$  and its emissivity  $\varphi$ . If a heat flow  $\Phi$  hits a body, it is divided into a reflected part  $\Phi_R$ , an adsorbed part  $\Phi_A$  and a transmitted part  $\Phi_T$  (cf. Figure 97).

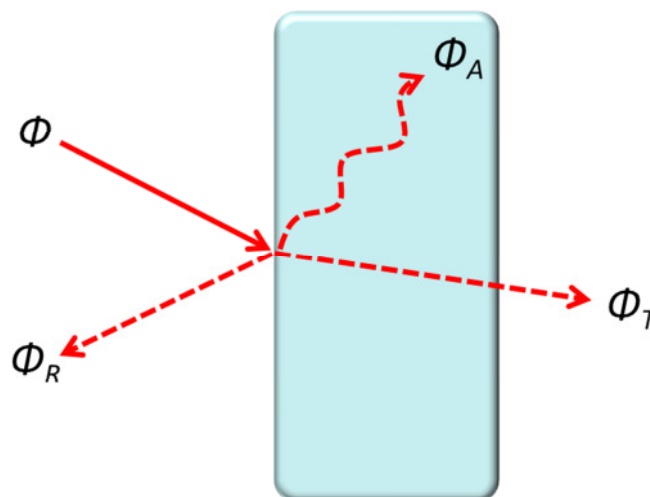


Figure 97: Distribution of heat flow in an arbitrary body.

Hence, a reflection coefficient  $C_R$ , an adsorption coefficient  $C_A$  and a transmission coefficient  $C_T$  can be defined:

$$C_R = \frac{\Phi_R}{\Phi}, C_A = \frac{\Phi_A}{\Phi}, C_T = \frac{\Phi_T}{\Phi} \quad 7-1$$

The sum of all three coefficients is always 1 which is known as Kirchhoff's law [140]:

$$C_R + C_A + C_T = 1 \quad 7-2$$

It is suitable for spectra of light as well as for monochromatic radiation.  $C_R$ ,  $C_A$  and  $C_T$  depend on the material, its surface morphology and its temperature. Within a so-called black body, all light is adsorbed, which leads to:  $C_A = 1$ ,  $C_T = 0$  and  $C_R = 0$ . Hence, the emitted spectrum of the black body

itself only depends on its temperature. This is why the radiation of black bodies can be used as a reference for the determination of a sample's temperature by IR-thermography. In reality, there is no ideal black body which is why it can only be described in a theoretical model, e. g. by assuming infinite reflection of a light beam within the body.

The distribution of the intensity of a spectrum can be determined with the help of Planck's law:

$$M_b(\lambda_R, T) = \frac{1}{\lambda_R^5} \cdot \frac{2\pi hc^2}{\exp\left(\frac{hc}{\lambda_R k_b T}\right) - 1} \quad \lambda_{Max} = \frac{2897.8 \mu\text{m} \cdot \text{K}}{T} \quad 7-3$$

$M_b(\lambda, T)$  is called the emittance and depends on the wavelength  $\lambda_R$ , the speed of light  $c$  ( $3 \times 10^8$  m/s), the Planck's constant  $h$  ( $6.626 \times 10^{-34}$  m<sup>2</sup> kg/s) and the Boltzmann constant  $k_B$  ( $1.38 \times 10^{-23}$  m<sup>2</sup> kg s<sup>-2</sup> K<sup>-1</sup>) [140]. By calculating spectra for different temperatures the correlation becomes clear. Figure 98 shows the emittance for different temperatures depending on the wavelength. The relevant range for IR thermography is highlighted in red color.

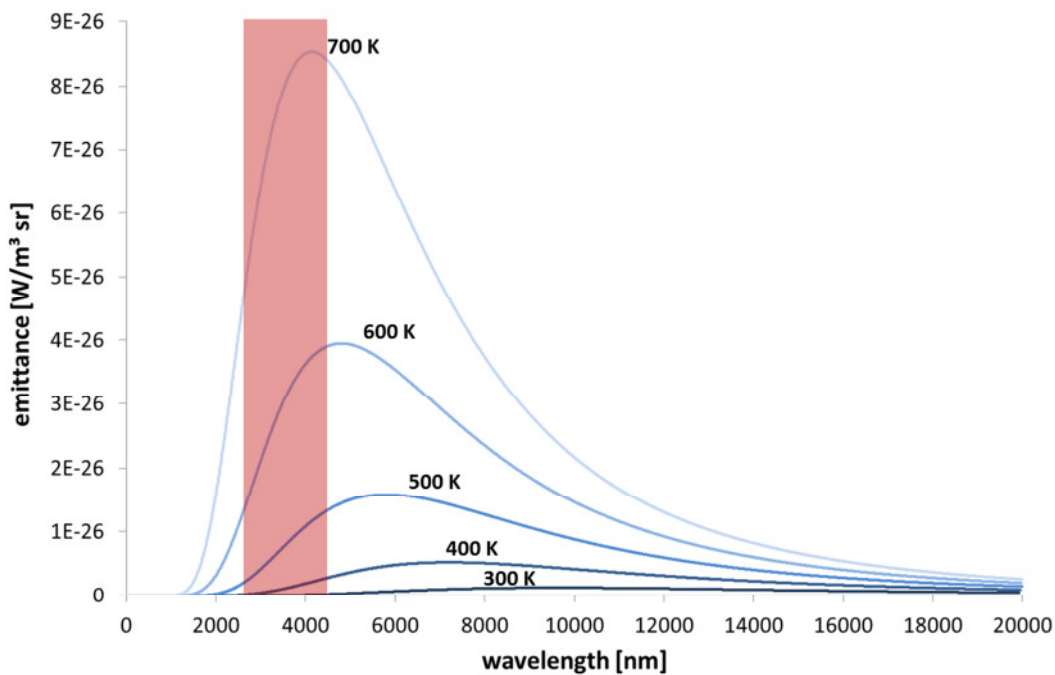


Figure 98: Emittance vs. wavelength for different temperatures calculated with the help of Planck's law.

By integration of the emittance over all wavelengths, the total radiation power  $P_r$  can be correlated to the temperature  $T$  and the intensity of the radiator over a given area  $A_{geom}$ . This is called the Stefan-Boltzmann law. A constant  $\sigma$  is introduced which is the Stefan Boltzmann constant ( $5.67 \times 10^{-8}$  W/m). In its general form, it takes the temperature dependent emissivity  $\varepsilon(T)$  of the body into account. This is defined as the ratio of the possible and the real radiation power and becomes a significant factor for detection of temperature difference in the range of a few Kelvin.

A black body would exhibit an emissivity of 1 whereas so-called grey bodies exhibit emissivity between 0 and 1 [140]:

$$P_r = \varepsilon(T) \cdot \sigma \cdot A_{geom} \cdot T^4 \quad 7-4$$

The so-called emissivity corrected Infrared Thermography (ecIRT) for material analysis was introduced by Maier *et al.* in 1998 [141]. The emissivity differences need to be taken into consideration by correction of each pixel of the IR image. Therefore, two options can be applied. First, it is possible to calibrate the emissivity by recording several images under controlled and steady state conditions (temperature, no reactions). In this case, the temperature across the whole area of the image should be the same. Emissivity differences can then be detected and calculated for each pixel of the camera chip and compensated by the software. After calibration, a change in IR radiation can be correlated to a change in temperature. The second option defines specific areas of emissivity which are taken from previously determined material parameters at the temperature of interest. For example, all areas made of carbon filament will be assigned to an emissivity factor of 0.53 whereas all areas made of oxidized stainless steel will be assigned to an emissivity factor of 0.83. In this work, the latter method was applied as the software did not provide multiple temperature calibration.

### 7.2.2 IR-thermography for characterization of catalysts and fuel cells

The use of ecIRT for identification of new materials has been established for almost two decades, especially in the field of research for heterogeneous catalyst materials. Most research groups focus on the development of innovative oxidation catalysts. Maier *et al.* have successfully applied ecIRT for characterization of hydrogenation of 1-hexyne and the oxidation of isooctane [141]. Furthermore, they realized a time dependent method to evaluate catalyst deactivation of the oxidation of toluene [142] and identified new catalyst alloys for the oxidation of carbon monoxide (CO) [143].

Yamada *et al.* used ecIRT to identify CO tolerant anode catalysts for PEMFCs. They detected the change in heat for different metal oxides when carbon monoxide (1000 ppm) with and without H<sub>2</sub> was brought into the reaction chamber. For electrochemical characterization they used rotating disc electrode measurements [144].

While these publications focus on combustion reactions the search for new electrocatalysts appears to be a challenging task. According to chapter 2.2 fuel cell reaction exhibits overpotentials that are transferred into heat. Therefore, the effectiveness of an electrochemical reaction may be characterized by the amount of heat that is produced at a certain point of the polarization curve. In this case, the question arises, if the temperature difference that is detected by an IR-camera is expected to be rather small or rather high in order to qualify a fuel cell as more powerful than another. To answer that question, polarization curves of two fuel cells A and B with different

performance behavior need to be compared. When both fuel cells are operated at the same current density  $I_m$ , the amount of hydrogen that is converted is the same (cf. Figure 99). Fuel cell A shows a higher electric power density because less overpotentials are generated during the electrochemical reaction. Thus, the thermal output  $P_{loss/A}$  is smaller compared to that of fuel cell B which provides a smaller electric power density and, hence, converts more chemical energy into thermal energy. In this case, fuel cell B would exhibit a higher temperature increase than fuel cell A which could be detected by the IR camera. However, if the same two fuel cells are operated at a constant potential  $U_m$ , the result changes (cf. Figure 100). As fuel cell A will exhibit a higher current density the electrical power density as well as the heat dissipation will be higher than that of fuel cell B. In this case, the increase in temperature will be higher for fuel cell A although it might have a higher effectiveness.

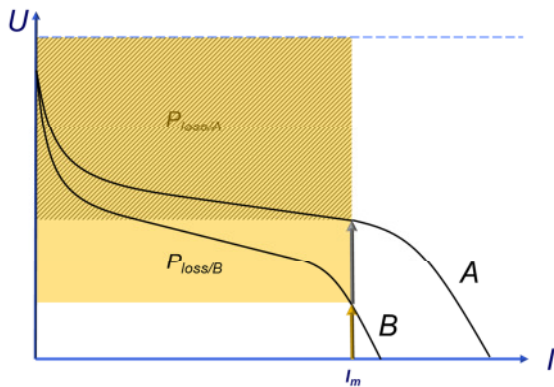


**Figure 99:** Heat dissipation of two different fuel cells at a constant current density  $I_m$ ; the heat output can be calculated by subtraction of the electrical power from the total power; the more effective fuel cell generates less heat.

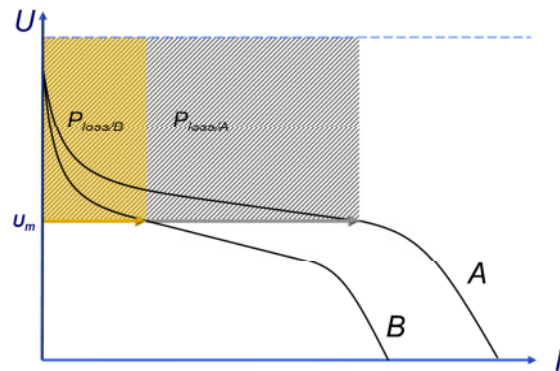


**Figure 100:** Heat dissipation of two different fuel cells at a constant potential  $U_m$ ; the heat output can be calculated by subtraction of the electrical power from the total power; the more effective fuel cell generates more heat.

The temperature rise of a fuel cell will be proportional to the heat dissipation at a certain operating point. Hence, the differences in heat dissipation will be more noticeable at high current densities respectively low operating potentials.

However, the visualization of fuel cell reactions and the triple phase boundary with ecIRT has not been achieved as it turns out to be challenging to realize an optical access to the fuel cell reaction with a high spatial resolution. Gas diffusion layer and bipolar plate of conventional fuel cells are necessary components to maintain fuel cell reaction. This makes it impossible for ecIRT equipment to detect the emitted heat with high speed and high resolution.

### 7.3 Micro fuel cells as basis for high throughput screening

The use of micro fuel cells is not limited to supplying energy for portable electronic devices. They are also used in materials development for fuel cell components, because their small mass offers two



major advantages: On the one hand micro fuel cells need only small amounts of materials for testing and on the other hand the answer of the system to a change of the ambient parameters like temperature or humidity is relatively fast. This allows to characterize complete fuel cells systems with minimal invest and reduces experimental times and development costs. Yet, it is a drawback that for every characterization cycle a whole micro fuel cell needs to be assembled, tested and disassembled for the next experiment. This serial approach increases the overall time of identifying new powerful materials or material systems.

For single fuel cell components like catalysts high-throughput methods have been applied successfully. Ludwig *et al.* developed a combinatorial sputter deposition method for fabrication of so-called material libraries with a high amount of different material combinations. These libraries are produced within one fabrication cycle by applying co-sputtering techniques and moveable shutters. The fabricated alloys can differ in composition as well as thickness and morphology [145].

As a next step, the material libraries can be characterized by automated testing devices in order to identify the most promising samples of the library. By using a scanning electrochemical microscope (SECM), the samples are locally characterized according to their electrochemical behavior one by one and candidates with high catalytic activity are identified [146]. Disadvantages of this method are the consecutive measurement of the samples on the one hand and the fact that only single components but not the whole fuel cell can be tested on the other hand.

The approach that is postulated in this thesis is to use a microstructured silicon membrane that combines all electrode components on one substrate. This allows applying high-throughput methods on the basis of micro fuel cells. Parallel investigation by ecIRT of several micro fuel cells can be realized. As there are no components that inhibit an optical access to the fuel cell reaction zone the dissipation of heat can be detected, localized and quantified at high speed with high spatial resolution. This way, the effectiveness of a  $\mu$ MEA relative to another can be measured. Figure 101 shows the basic approach of such a measurement. An array of micro fuel cells is brought into a reaction chamber where the fuel cell reaction takes place. All samples of the library differ in specific ways, for example, by using a different catalyst for each sample. The dissipated heat, generated by the overpotentials of each specific micro fuel cell can be detected by an IR camber and analyzed regarding their effectiveness.

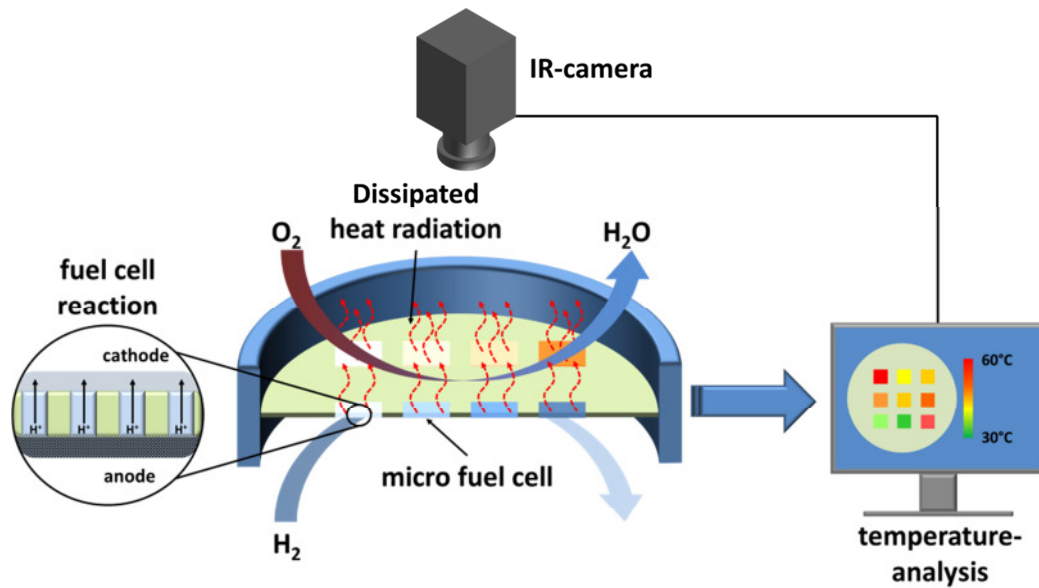


Figure 101: Principle setup of high throughput screening based on micro fuel cells; a micro fuel cell library is brought into a reaction chamber where fuel cell reaction takes place. By analyzing the dissipated heat radiation information about the effectiveness of single micro fuel cell can be obtained.

### 7.3.1 Design of a reaction chamber for micro fuel cell libraries

In order to realize a characterization of a silicon-based  $\mu$ MEA by eIRT, an application specific test chamber was designed. The main specifications of this chamber are:

- Optical access to the  $\mu$ MEA
- Precise control of the temperature inside the chamber
- No gas diffusion between anode and cathode
- No electrical short circuits

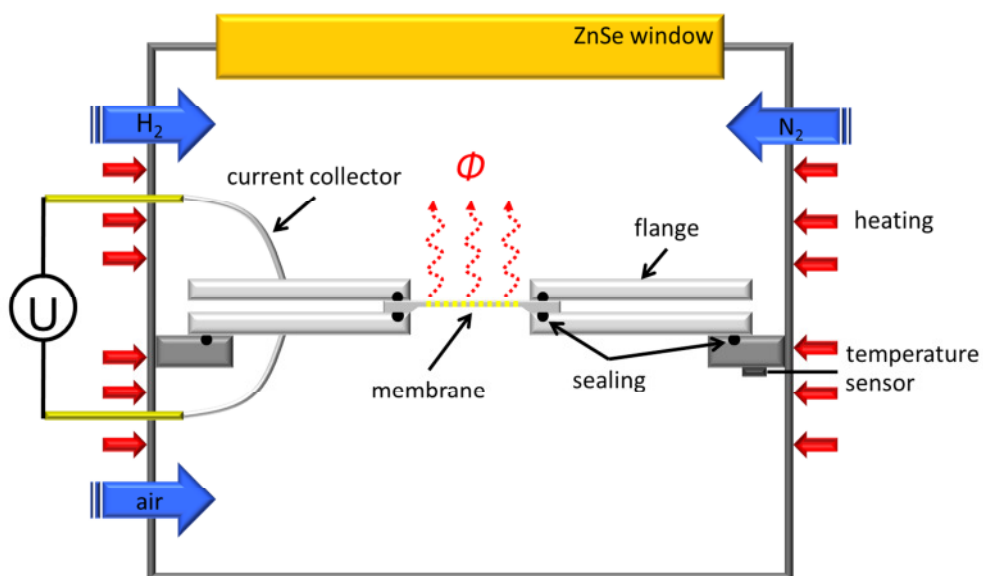
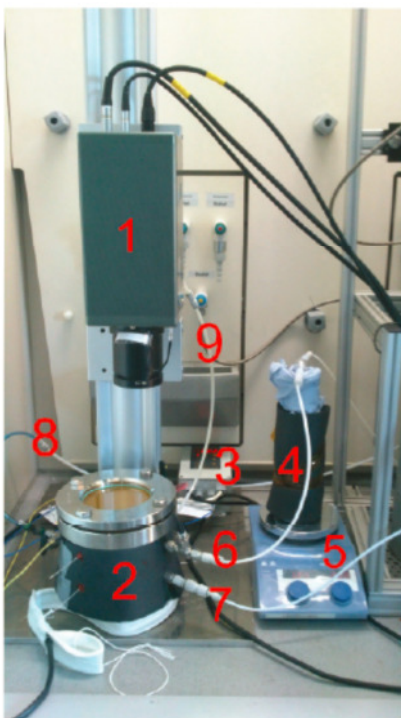


Figure 102: Schematic illustration of the reaction chamber; the micro fuel cell library is placed between two flanges in the middle of the chamber and separates cathode from the anode. A ZnSe window allows optical connection of the IR-camera to the active area of the micro fuel cells.

A detailed sketch of the test chamber is illustrated in Figure 102. It is divided into two reaction chambers, the anode side and the cathode side. In between, the  $\mu$ MEA is placed between two flanges which separate the two chambers. The flanges are made of stainless steel which exhibits sufficient corrosion stability in this case. The electric current of the fuel cell reaction is collected at the flanges and directed to gas-tight bushings which are connected to a source meter. The upper side of the test chamber includes a ZnSe-window so that an optical access can be realized. ZnSe is an IR permeable, cost-effective material. After filling the chambers with the fuel gases, the gas supply is closed and the reaction takes place only by the available oxygen and hydrogen inside the chambers. Because of this “Dead-End” configuration, the volume of the chambers was designed relatively large in order to ensure a sufficient amount of fuel gases during the experiments. The configuration prevents a fluctuation of the IR-signal by flowing gases. Precise temperature control of the test chamber is critical for the accuracy of this test method. Heating the sidewalls of the test chamber avoids that the heat source influenced the IR image. To ensure homogenous heating and continuous temperature distribution the whole test chamber was enclosed with thermal insulation material.



1. IR-camera
2. Test chamber
3. Temperature control
4. Humidifier
5. Hotplate
6. Oxygen supply
7. Hydrogen supply
8. Nitrogen supply
9. Exhaust air

**Figure 103: Photo of the final test setup.**

Figure 103 shows the final setup of the test chamber. Beneath the IR-camera (1, InSb-640, Thermosensorik GmbH) the test chamber (2) was placed. It is connected to a Keithley source meter (not on photo), the temperature control (3) and gas supply with an interjacent humidifier (4) of the cathode air placed on a hotplate (5). Air supply (6), hydrogen supply (7) and nitrogen supply (8) can

be opened and closed by a selector valve. Exhaust air (9) from the cathode can exit to the surrounding.

The distance between the IR-camera and the  $\mu$ MEA is defined by the focal length of the objective lens of the IR-camera. In this case, a lens with 20 cm focal length was used which is a good compromise between a sufficient image section and an adequate resolution in order to get a detailed image of the surface of the  $\mu$ MEA. The humidifier was realized by placing a bubbler on a hotplate where the cathode air passed through before entering the test chamber. By changing the temperature of the hotplate, the humidity of the air could be controlled. For precise control of the temperature of the test chamber, a heating band was used that was wrapped around the outer chamber walls. By this, no IR emission of the heating disturbs the measurements as it would be the case, if the heating would be installed beneath the flanges. The temperature control was realized by a microcontroller based thermostat (Horst GmbH) which uses the temperature information of a Pt-100 temperature sensor by utilizing a PID-element. The accuracy of the microcontroller was specified to 0.1 K by the manufacturer.

After integration of a  $\mu$ MEA into the measurement setup, a typical test procedure starts with heating of the test chamber to the desired temperature. The temperature range may be varied between 20°C and 90°C for ionomer based electrolytes. Hence, it may take up to 3 h until a constant temperature profile is reached, as the test chamber is heated from the outside and the heat conductivity to the middle of the flanges is relatively slow. Next, the anode side of the test chamber is purged for 15 min with nitrogen in order to replace all oxygen (contained in air) inside the chamber. This is followed by a 15 min purge with hydrogen at the anode side and – if needed – with humidified air at the cathode side. After that, the characterization of the  $\mu$ MEA can be started. Therefore, the polarization curve of the  $\mu$ MEA is measured while the relative temperature difference at a certain operating point is detected. This way, a correlation between the electrochemical behavior and the heat dissipation can be identified. The software of the IR-camera provides the option to measure the average temperature of a certain region and to detect the temperature at specific points which are useful tools to distinguish between the overall performance of the  $\mu$ MEA and certain measurement points within a materials library.

#### **7.4 Validation of IR-thermography by characterization of conventional MEAs**

In order to evaluate the eCIRT-based screening method and to identify stable test parameters, a test series with conventional MEAs was executed. For this, standard MEAs from Solvicore with an active area of 2x2 cm<sup>2</sup> were used and integrated into the test chamber. Figure 104 shows a photo of the MEA inside the chamber. As current collection in conventional MEAs is realized by the GDL, which requires a certain contact pressure for good electrical contact, two gold-coated, stainless steel grids

were positioned between the surface of the MEA and the flanges. With this, one of the drawbacks of conventional MEAs for this screening method becomes clear. The metal grid as well as the GDL hinders optical access to the electrochemical reaction. Figure 105 gives an impression of a typical image taken by the IR-camera while the fuel cell reaction takes place at an operating temperature of 70°C. The regions with higher temperature are represented in red, those with lower temperature in blue. From such a picture the average temperature of the whole MEA can be calculated for different operation points. Therefore, the MEA is defined as region of interest (ROI) by the software. Within this ROI the average temperature is measured by the IR-software over time. As temperature changes with variation of the operation point along the polarization curve, a change in temperature  $\Delta T$  can be detected.

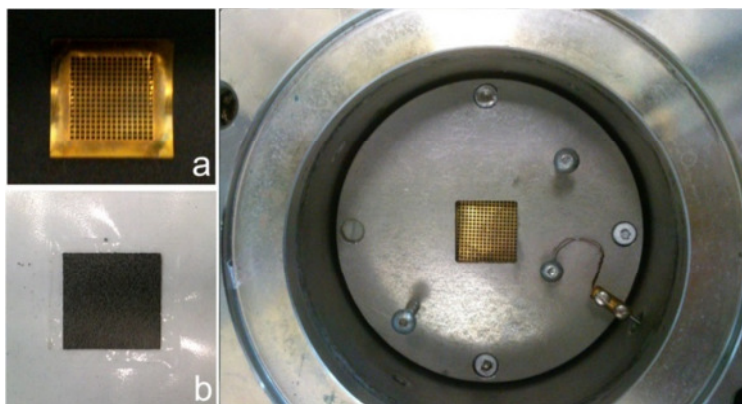


**Figure 104:** Photo of the thin metal grid for current collection (a), the MEA (b) and the two components integrated into the measurement chamber.

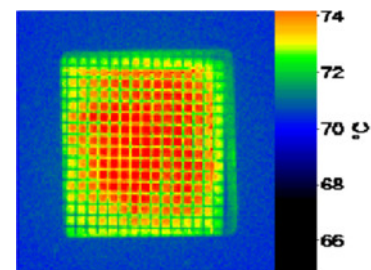


**Figure 105:** Typical image of the IR-camera while the MEA is operating; the metal grid can be identified clearly. Active regions on the MEA exhibit higher heat radiation.

Unlike a materials library, a conventional MEA has a homogenous distribution of the same catalyst on its surface, so no differences between certain measurement points should be expected. This is why a different experiment was conducted: The performance of the MEA was changed by variation of specific parameters. By that, different polarization curves and temperature profiles were recorded and compared among each other. A suitable parameter to achieve different performance was to change the relative humidity inside the measurement chamber. This was realized by purging the chamber with humidified air for 1 h before each measurement. Water temperature inside the humidifier was set to 90°C. By varying the air flow the relative humidity changes as dwell time of the gas bubbles inside the humidifier decreases with increasing flow rate. By that, relative humidity decreases as well. This affects the performance of the MEA and thus leads to variation of the heat loss. Another parameter that was changed is the chamber temperature. This also influences performance of the MEA as relative humidity and catalyst depend on temperature.

In Figure 106, a typical polarization curve of the MEA can be seen. The diagram was measured at 76°C chamber temperature and a relative humidity of 90 %. As the chamber represents a dead-end fuel cell, the stoichiometry is at a constant value of 1 for both anode and cathode. Because of that and due to the poor electrical contact from the metal grid, the maximum power point was reached at 16 mW/cm<sup>2</sup>. The concentration losses become dominant at comparably low current densities. Moreover, water condensed at the surface of the optical window acting as a heat sink. This leads to poor measurement results because the irradiated heat cannot be detected by the camera anymore (cf. Figure 107). This is why further measurements needed to be conducted at significantly lower humidity levels. It was also noticed that it is advantageous to measure the temperature profile from high current densities to low current densities. As the production of water decreases with lowering the current density, more reproducible results can be achieved as the effect of condensation can be minimized.

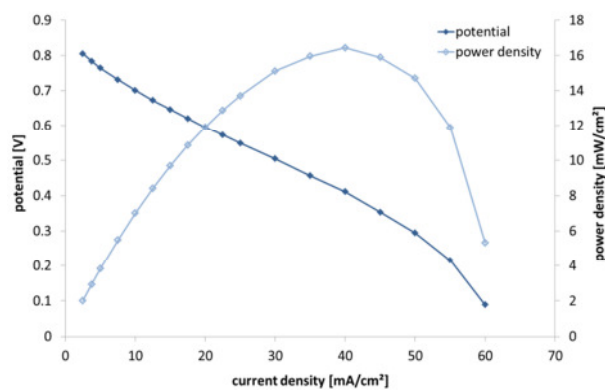


**Figure 106: Polarization curve of the conventional MEA for 76°C and 90 % RH; as the reaction chamber is closed before measurements the stoichiometry is defined as 1 for both anode and cathode.**

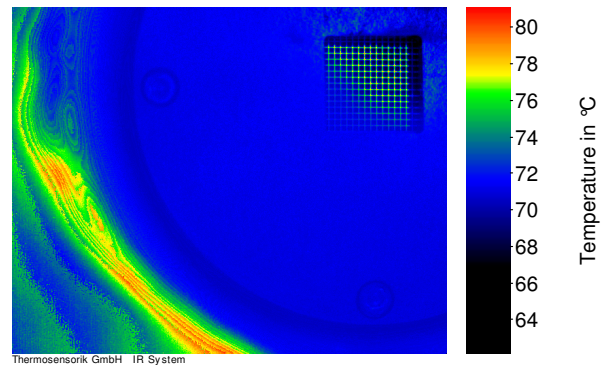


**Figure 107: IR image of the reaction chamber with condensed water on the ZnSe window; the temperature is not detected correctly anymore.**

Figure 108 shows polarization curves for 3 different humidity levels at a constant chamber temperature of 81°C. They were realized by applying different air flows through the bubbler humidifier for 1 h before each measurement was started. As expected, the polarization curve with the smallest flow rate shows the best performance. Compared to this, Figure 109 shows two different polarization curves which were recorded at a constant air flow through the humidifier, but at different temperatures, 76°C and 86°C. Due to dryer conditions at higher temperatures, the performance of the MEA is more effective at 76°C. Looking at the corresponding heat profiles in Figure 110, Figure 111, Figure 112 and Figure 113 it can be seen that the temperature increase of the MEA correlates to the theoretical assumptions made above. In Figure 110 and Figure 111 the relative temperature increase is shown on the basis of the applied current density. In both cases (constant operating temperature and constant humidity) an increase in current density leads to higher relative increase in temperature change  $\Delta T$  which can be determined by the IR camera.



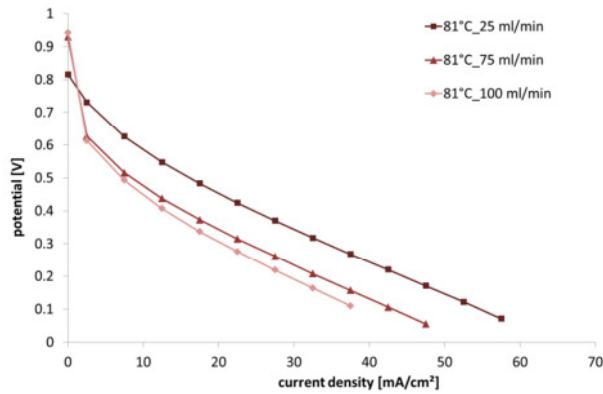


Figure 108: Polarization curves of the MEA at 81°C for different levels of humidification; the camber was operated “dead-end” which results in stoichiometry of 1 for both, anode and cathode.

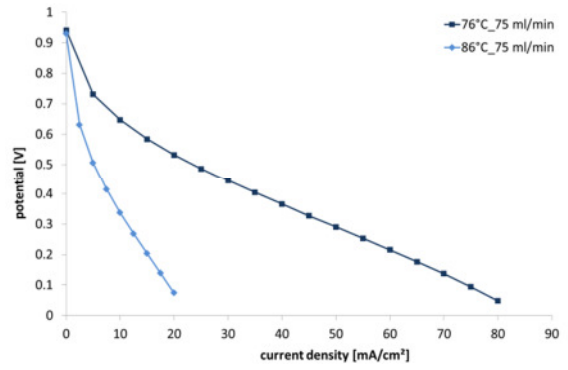


Figure 109: Polarization curves of the MEA with 75 ml/min humidification process (1 h) for 2 different temperatures; the camber was operated “dead-end” which results in stoichiometry of 1 for both, anode and cathode.

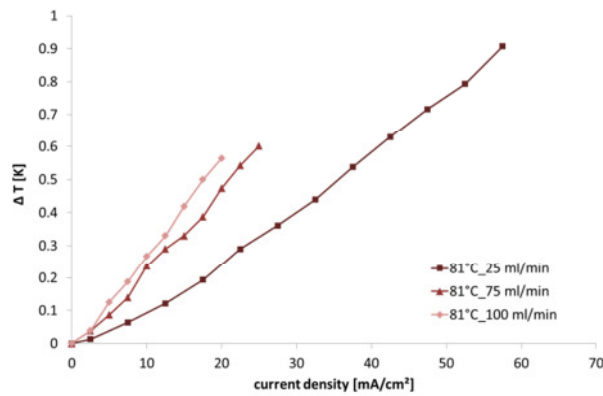


Figure 110: Increase in temperature of the MEA depending on the applied current density for different levels of humidification according to polarization curves shown in Figure 108.

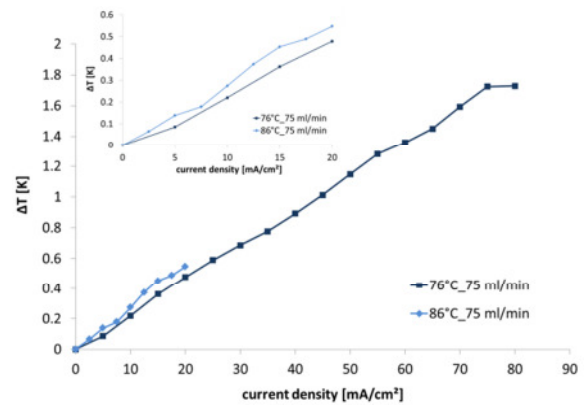


Figure 111: Relative increase in temperature of the MEA depending on the applied current density for different operating temperatures of the chamber according to polarization curves shown in Figure 109.

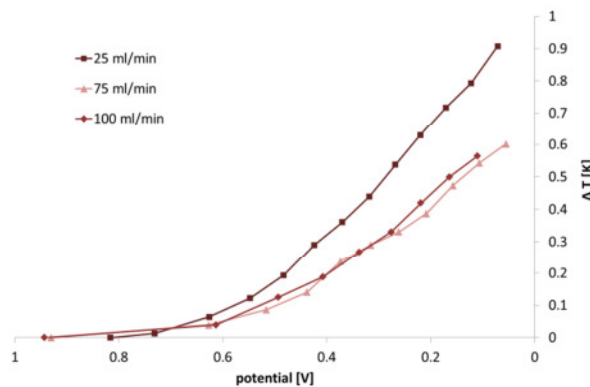


Figure 112: Increase in temperature of the MEA depending on the applied potential for different levels of humidification according to polarization curves shown in Figure 108.

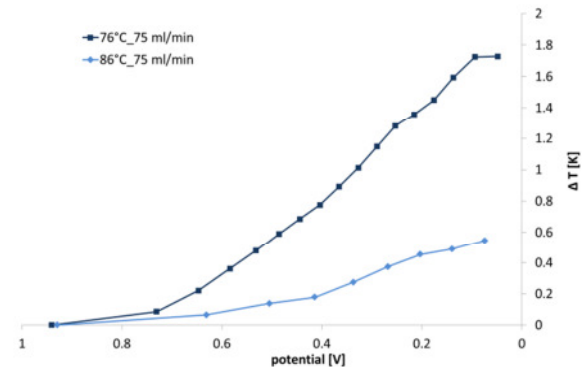


Figure 113: Increase in temperature of the MEA depending on the applied potential for different temperatures of the chamber according to polarization curves shown in Figure 109.

Temperature differences are in the range of 1 K. Furthermore, the slope of the rise in temperature is smaller for more effective polarization curves, but the maximum relative increase in temperature is higher. That means that at the same current density the temperature of the more effective MEA exhibits a smaller relative increase in temperature compared to the less effective MEA. In contrast to that the relative increase in temperature at a specific potential is higher for a more effective MEA compared to the inferior one which can be seen from Figure 112 and Figure 113. Hence, the interpretation of the result needs to be done considering the basis of analysis: temperature increase vs. applied current density, respectively temperature increase vs. applied potential.

As a first result, the characterization of fuel cell MEAs by IR thermography proves to be a valid method for determination of the performance of the fuel cell reaction and thereby for the components and materials used. The next step in evaluation of the eCI RT high-throughput method is to include different materials which are operated at the same conditions in order to be able to identify more effective material combinations. This will be realized in two steps: First, a  $\mu$ MEA with two different catalyst specifications will be characterized. The specifications of the catalyst layers will be chosen in a way that it is clear which material combination will lead to better results. Second, a materials library with well-defined active areas and different catalyst specifications will be built and analyzed.

## 7.5 Characterization of $\mu$ MEA through IR-thermography

As the measurements described above were conducted with a conventional MEA and changes in performance were realized by change of operating conditions (humidity, temperature), the next step of validating the IR-screening method is to evaluate a silicon-based  $\mu$ MEA with different material combinations. For those, no gas diffusion layers and metal grid current collectors are needed compared to conventional MEAs. Hence, a direct optical access to the fuel cell reaction can be realized which leads to a significant enhancement of the measurement.

In chapter 6.4.4 it was shown that electrodeposition of Pt leads to enhanced power density of the  $\mu$ MEA. This finding was verified by the new eCI RT-screening method and will be described in detail in the next section. A  $\mu$ MEA with a conductive catalyst layer was prepared. At first, a microstructured silicon membrane was dip-coated with PFSA ionomer as described in chapter 5.3.2. Then, a conductive catalyst layer containing 15 wt% CNTs and exhibiting a thickness of 12.5  $\mu$ m was spray coated onto each side of the silicon membrane. The  $\mu$ MEA was coated with Pt by electrodeposition as described in chapter 6.4.4, except that only half of the active area of the  $\mu$ MEA was dipped into the electrolyte and only half of the deposition time was used (420 s). This way, one half of the  $\mu$ MEA exhibited electro-deposited Pt, the other half did not. Finally, the  $\mu$ MEA was integrated into the measurement chamber of the IR-screening apparatus. As can be seen in Figure 114, the grey areas on



the black surface originate from the electro-deposited Pt. The  $\mu$ MEA was dipped into different depths of the electrolyte during electrodeposition which leads to a line shaped appearance of the deposited Pt. The correlating IR-image at ambient conditions (20 °C) without the fuel cell reaction taking place can be seen in Figure 115. As the temperature is distributed evenly across the measurement chamber, all components show almost the same color. The areas with Pt can be identified easily (highlighted in red square) which proves the first advantage in comparison to conventional MEAs where a GDL would inhibit the identification of interesting areas.

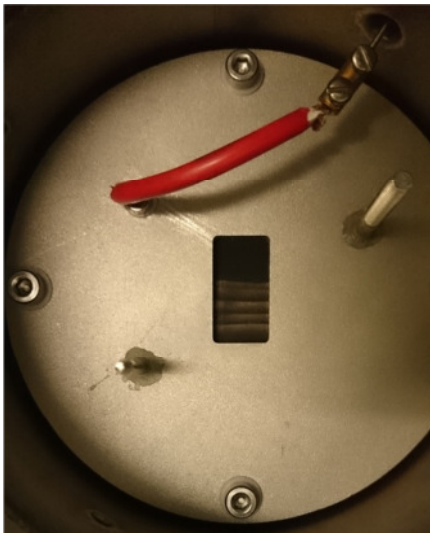


Figure 114: Photo of the  $\mu$ MEA inserted into the measurement chamber; the area of galvanic Pt deposition can be identified easily.

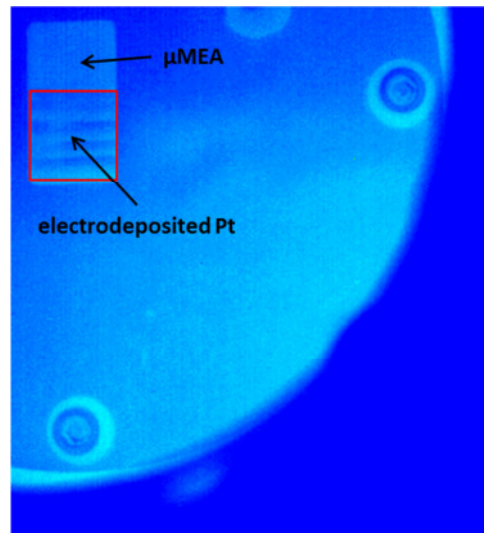


Figure 115: IR image of the inserted  $\mu$ MEA; still, the area of galvanic Pt deposition can be identified.

For measurements, the chamber was closed and the anode side was purged with nitrogen for 30 min. At the same time, the chamber was heated to 25°C, according to the temperature sensor placed at the edge of the flange. The whole  $\mu$ MEA was defined as ROI. Moreover, ten observation points were defined. Four of them (A-D) were located in areas without electro-deposited Pt, four were situated in areas with electro-deposited Pt (E-H). The other two observation points (I,J) were placed onto the flange in order to serve as reference points where no electrochemical reaction takes place and which could be used to subtract temperature variations occurring from the heating. As one reference point was located near the edge of the flange and one near to the membrane, temperature calibration could be realized. The temperature given by the temperature sensor was taken into account: It provides the temperature at the edge of the flange. As the flange is made of stainless steel ( $\epsilon = 0.83$ ) and exhibits the same emissivity over the whole surface, the temperature in the middle of the flange can be detected as well. This is where the flange and the  $\mu$ MEA share the same temperature. Thus, the temperature of the membrane is also known and the emissivity of the membrane can be calibrated.

After purging, hydrogen was filled into the chamber and all valves were closed. Figure 116 shows an IR-image of the  $\mu$ MEA operated at 25°C with all measurements points and regions. The red area indicates the active surface of the membrane. Six measurement points were induced by the source meter: The current was set from 15 mA to open circuit voltage in intervals of 3 mA. As measurement was found to be more stable when going from higher currents to lower currents, this way of measurement was preferred. The reason is the production of water at high currents which leads to humidification of the ionomer and thereby improved performance of the  $\mu$ MEA. Figure 117 shows a typical diagram resulting from a measurement. It can be seen clearly that switching over to lower currents decreases temperature significantly. A steady temperature decrease was detected which may occur from the continuous drying of the  $\mu$ MEA when switching to lower electrical currents. As the diagram only sums up the temperature of the ROI, it cannot be used for evaluation of the different areas on the  $\mu$ MEA. Nevertheless, it clearly indicates that even small changes in current of only 3 mA can be detected by the IR camera.

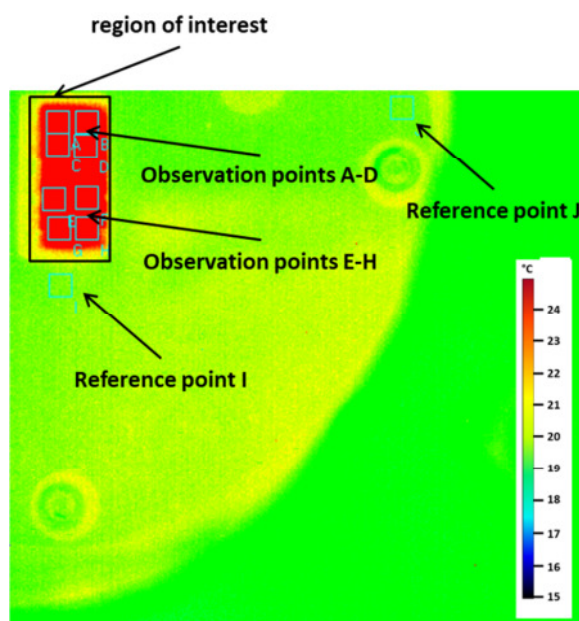


Figure 116: IR image of the measurement chamber including the observation points and the ROI.

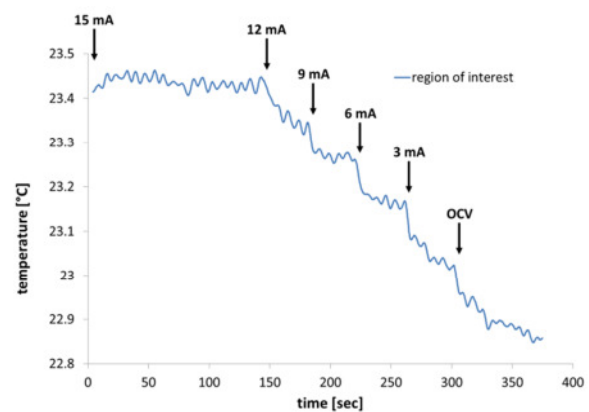


Figure 117: Absolute temperature averaged over ROI over time; the points of change in current can be observed clearly.

The analysis of the single observation and reference points yields more detailed results. Figure 118 shows the temperature difference from start of the measurement to its end depending on the current that was applied. It is obvious that observation points A-D exhibit higher temperature differences compared to observation points E-H. This result is in good correlation with the hypothesis that less effective region should show higher heat loss at constant currents. As reference point J shows negligible temperature increase, the origin of the temperature differences must be the electrochemical reaction of the  $\mu$ MEA. In Figure 119, the temperature increase detected at reference

point J was subtracted from the observation points. This represents the final result of the measurement. Hence, the result from chapter 6.4.4 of electroplated Pt having a positive effect on the  $\mu$ MEA is confirmed by this eCIRT-screening. At the same time, the capability of the measurement method was validated for silicon-based  $\mu$ MEAs.

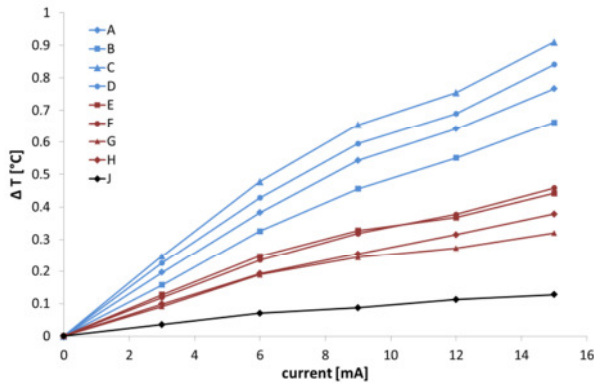


Figure 118: Relative change in temperature of the observation points depending on the applied current.

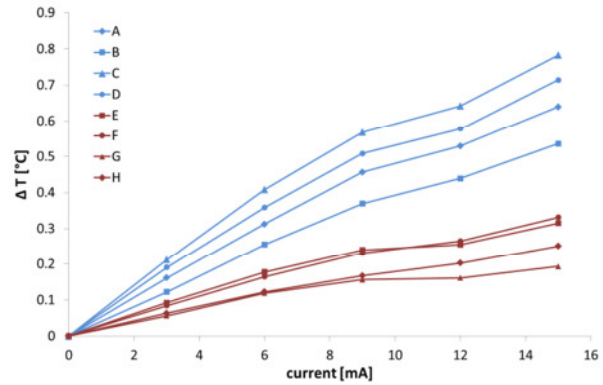


Figure 119: Relative change in temperature of the observation points depending on the applied current including the subtraction of the relative temperature increase of the flange (reference point J).

## 7.6 Characterization of Pt/Cu alloy micro fuel cell library

In chapter 6.1.1 the electrochemical active surface of sputter coated Pt layers was characterized. It was shown that the specific Pt surface is depending on the sputter parameters. As the highest roughness factor obtained was only 12.37 this was not enough for effective fuel cell reaction. Another way to enhance the specific surface is to co-sputter Pt alloys with non-noble metals such as Cu and to etch the non-noble component in a second step.

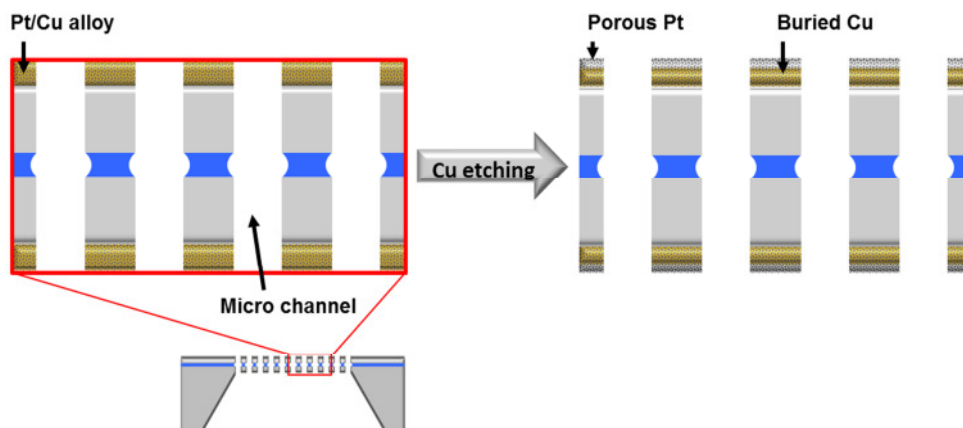


Figure 120: Schematic illustration of the fabrication process for porous alloy catalyst layer: etching of the non-noble metal (Cu) leads to porous Pt surface with buried Pt-/Cu alloy.

This way, a porous frame of Pt can be realized. In greater depths where the etchant cannot reach the non-noble Cu the originally co-sputtered metal alloy remains (cf. Figure 120). Copper is an interesting

candidate for being used as non-noble metal component. Its properties for utilization in low temperature PEM fuel cells were investigated intensively. Besides the possibility to etch Cu relatively easy by wet etching or electrochemical etching processes, it was shown that PtCu alloys exhibit higher catalytic reactivity, especially for the oxygen reduction reaction. The reasons for this are so-called strain and ligand effects that are induced in PtCu. They arise from deformation of the electronic band structure caused by Cu atoms located next to Pt atoms, resulting in electronic charge transfer and from deformation of the metal lattice provoked by induced surface strain [147] [148] [149] [150].

Therefore, fabrication of a PtCu catalyst layer would result in a porous Pt surface resulting from the etching of the Cu and a higher catalytic activity induced by buried Cu that is located beneath continuous Pt surfaces where the etchant cannot reach the non-noble component. Besides that, Pt as well as Cu exhibit face-centered cubic crystals which allows a complete miscibility and thereby a broad variation of the composition. This makes PtCu alloys an ideal candidate for combinatorial experiments and validation of the new characterization method based on ecIRT.

As a first step, validation of materials library by an established screening method was performed. For this, a materials library with varying Cu concentration and layer thickness was fabricated by combinatorial sputter deposition. This was done in cooperation with the Chair for MEMS materials at the Ruhr-University Bochum (Prof. Ludwig). The materials library was fabricated by using a shadow mask with 69 rectangular openings which covered the silicon substrate during the sputter process. By

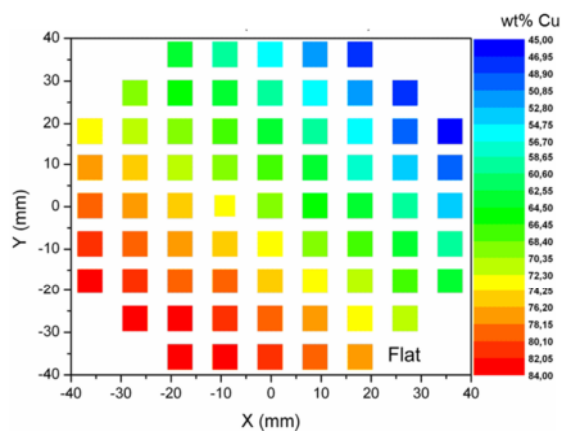


Figure 121: Result of EDX measurement of materials library; the image is showing the weight percentage of Cu for each sample (source: chair of MEMS materials, Ruhr-University Bochum).

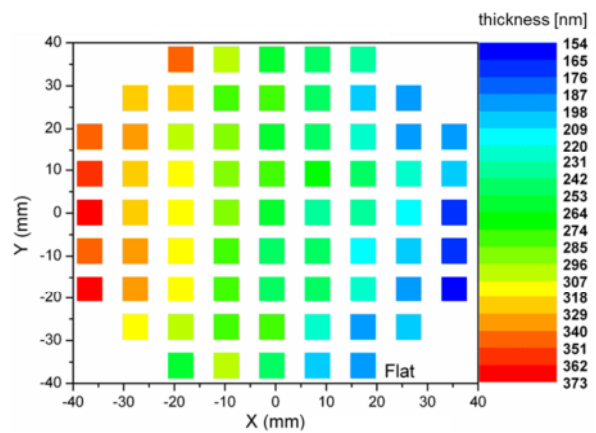
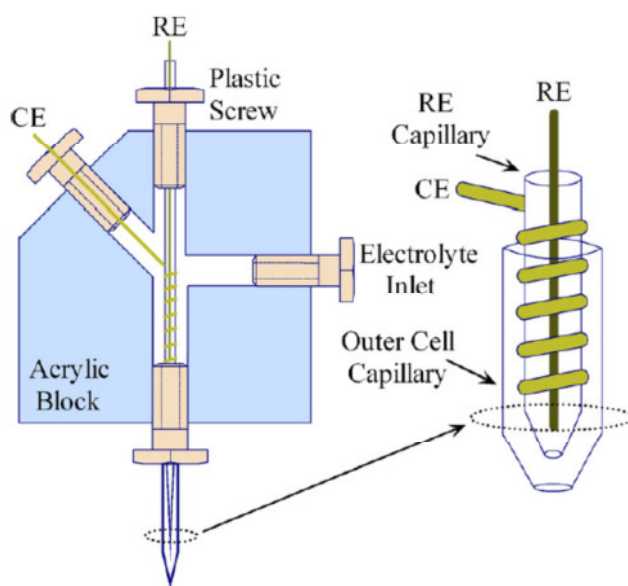


Figure 122: Result of EDX thickness measurements of the materials library (source: chair of MEMS materials, Ruhr-University Bochum).

using a co-sputtering process and movable shutters near the substrate surface, gradually varying samples could be realized. Sputter pressure was set to 1 mTorr (0.0013 mbar). Figure 121 and Figure 122 show EDX-measurements of the library and give information about the composition and the layer thickness of the specific samples.

For evaluation, the samples were tested by Scanning Droplet Cell (SDC) measurements at the Center for Electrochemical Science, Bochum (Prof. Schuhmann). SDC is an established high throughput screening method for evaluation of heterogeneous catalysts for electrochemical applications. A sketch of such a SDC is shown in Figure 123. Using a miniaturized SDC it is possible to conduct cyclic voltammetry at defined positions of a materials library. The area of the sample surface is defined by the diameter of the glass capillary and the resulting droplet that gets into contact with the sample surface. Inside the capillary, counter electrode and reference electrode are integrated. By using an automatic x-y-stage material libraries can be scanned automatically.



**Figure 123: Illustration of the SDC as used for electrochemical characterization of the materials library [151].**

For SDC measurements, 1 M  $\text{H}_2\text{SO}_4$  electrolyte and a miniaturized Ag/AgCl (3 M KCl) reference electrode were used. A Pt wire served as counter electrode. Scan rate was set to 20 mV/s.

In order to create a porous Pt-layer, a stripping of the surface Cu was realized by repeating 200 CV cycles. Figure 124 shows the voltammograms of the first cycle. The numbers indicate the amount of Cu, starting from low to high amounts. Dominant oxidation peaks can be observed at approximately 150 mV and 350 mV – 750 mV. The peak value decreases with decreasing amount of Cu. Hence, it is most likely that they originate from Cu oxidation.

This assumption can be confirmed by looking at the results of the 200<sup>th</sup> scan of each sample of the materials library (cf. Figure 125). The oxidation peaks have decreased significantly, still depending on the amount of Cu inside the sample. Unfortunately, it was not possible to obtain pure Pt voltammograms for samples with less than 37 wt% Pt, because the amount of coherent Pt decreases with increasing amount of Cu, resulting in unstable and mechanically weak layers. In fact, the porosity of the remaining Pt layer is too high. This is impaired by the appearance of cracks

throughout the layer originating from intrinsic stresses, resulting in ongoing etching of more Cu without reaching a stable state. Thus, such samples are not applicable for fuel cells as exposed Cu would poison the fuel cell.

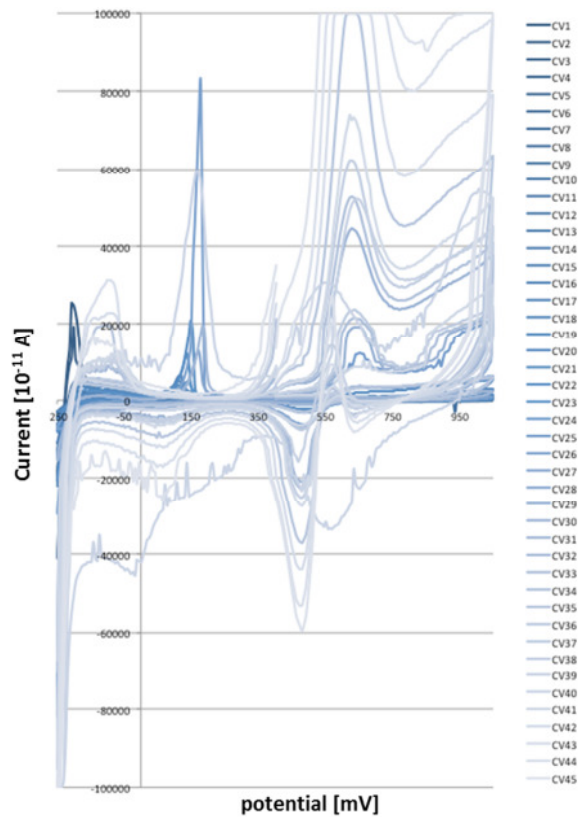


Figure 124: Results of the 1<sup>st</sup> CV scan of each sample of the materials library; sweep rate was set to 20 mV/s, electrolyte was 1 M H<sub>2</sub>SO<sub>4</sub>, reference electrode was Ag/AgCl (3 M KCl) and counter electrode was Pt wire (source: Centre for Electrochemical Science, Bochum).

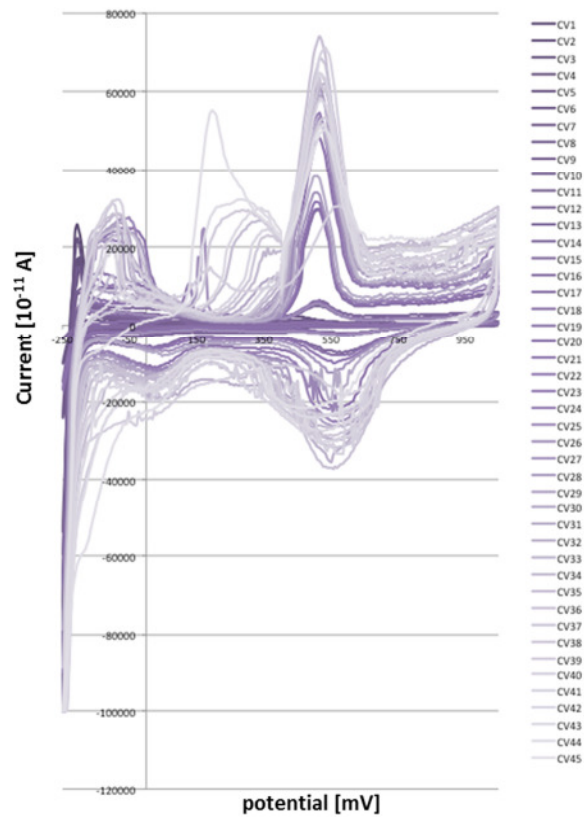


Figure 125: Results of the 200<sup>th</sup> CV scan of each sample of the materials library; sweep rate was set to 20 mV/s, electrolyte was 1 M H<sub>2</sub>SO<sub>4</sub>, reference electrode was Ag/AgCl (3 M KCl) and counter electrode was Pt wire (source: Centre for Electrochemical Science, Bochum).

For those voltammograms with less than 63 at% Cu, stable cyclic voltammograms with significant Pt signals were achieved (cf. Figure 126). Hydrogen adsorption and oxygen peaks can be identified. The results show that the integration of Cu does not necessarily lead to an enhancement of the absolute ECAS. Considering Pt content (cf. Figure 121) and layer thickness (cf. Figure 122) of the measured samples (cf. Figure 127), layer samples with almost the same thickness were measured with stable electrochemical behavior: Samples with 55 wt% Pt (sample 9\_7 in Figure 127), exhibiting a layer thickness of 242 nm could be compared with samples of only 37 wt% (sample 5\_7 in Figure 127), exhibiting a layer thickness of 220 nm. As the thickness is kept constant the higher Pt concentration leads to a higher total amount of Pt. The effect of adding Cu does not show significant improvement of the hydrogen adsorption. In this case, a direct correlation between Pt content and catalyst performance was measured. A reason might be found in the fabrication process as only the last layer of Pt will benefit from the underlying Cu whereas the porous Pt above will not be affected by Cu at



all. Hence, sputter coated PtCu layers with a constant layer thickness but higher amounts of Pt result in improved catalytic activity and thereby in better fuel cell performance. This will be proved by eCIRT screening in the next step.

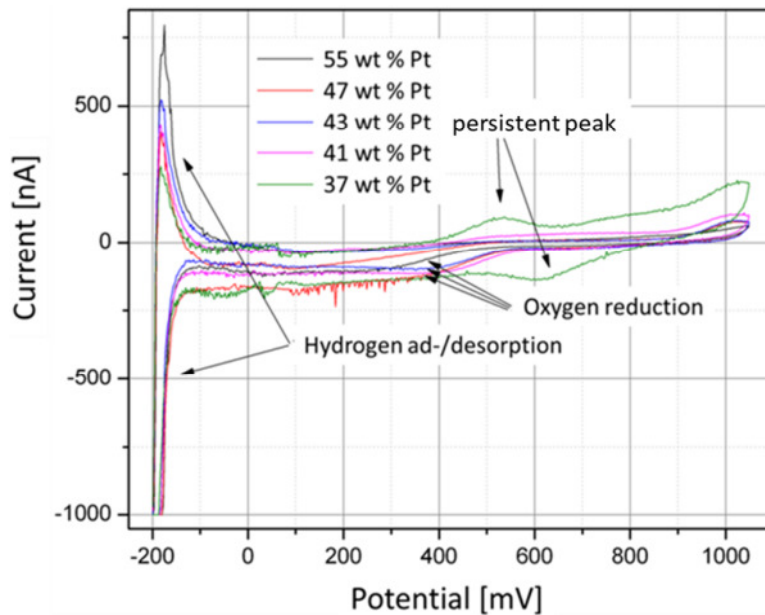


Figure 126: Diagram showing only the results of the CV scans with stable Pt signal (source: Centre for Electrochemical Science, Bochum).

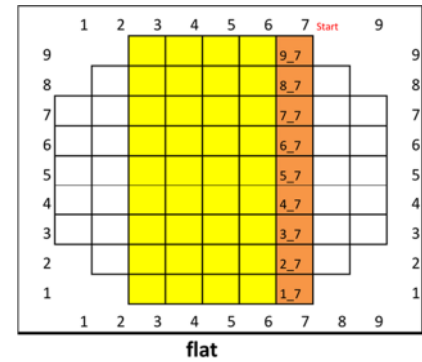
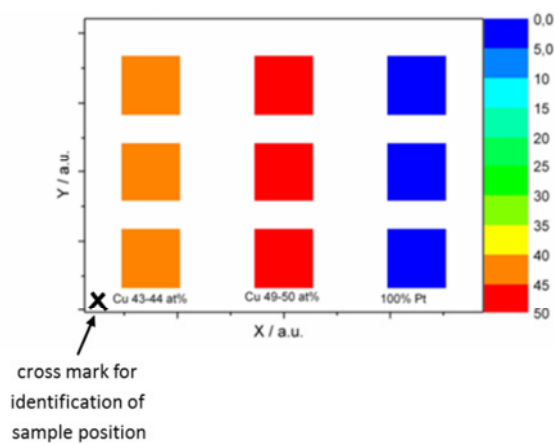


Figure 127: Position of the samples on the materials library; sample 9\_7 correlates to 55 wt% Pt, sample 5\_7 correlates to 37 wt% Pt (source: Centre for Electrochemical Science, Bochum).

Based on the results of the SDC measurements, a silicon-based  $\mu$ MEA was fabricated. The goal was to realize a “system library” of independent micro fuel cells on one common device that differ just in the composition of their anode catalyst. Thus, a 20 x 20 mm<sup>2</sup> silicon membrane was sputter coated with an adhesive Cr layer (50 nm) which also served as a shared current collector. In the next step, a shadow mask was placed onto the surface of the membrane that contains 9 quadratic openings with a side length of 6 mm. Through these openings different compositions of Pt and PtCu were deposited onto the membrane. As illustrated in Figure 128, three different compositions were realized: 43-44 at% Cu, 49-50 at% Cu and pure Pt. In order to check reproducibility each composition was deposited three times. At the backside a 50 nm Cr layer and a 50 nm Pt layer for current collection were deposited onto the surface. After integration of FLNA ionomer into the micro channels, a standard catalyst layer for cathode reaction was spray coated onto the backside. This way, the cathode side of the system library exhibits the same catalyst for all samples. Figure 129 shows a photograph of the final system library. The different colors of the quadratic samples indicate the varying composition of the anode catalyst layer. Additionally, a cross in one of the corners was used for orientation. On the

right side of Figure 129, a photograph of the system library integrated into the eCIRT characterization chamber is shown. The system library is placed in the middle of the chamber.



**Figure 128: Result of EDX measurement of the micro fuel cell library; three different catalyst compositions were fabricated.**

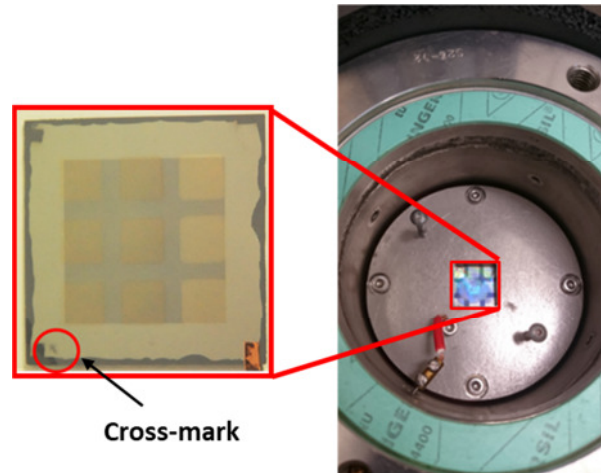


**Figure 129: Photo of the final micro fuel cell library (left) and integration of the library into the measurement chamber (right).**

After heating the characterization chamber to 45 °C for 3 h, the temperature stability was within 1°C. In order to prevent oxyhydrogen reaction at the anode catalyst of the materials library from oxygen contained in air, the anode chamber was purged with nitrogen for 30 min. Oxyhydrogen reaction can have devastating effects on the measurement results as it is highly exothermic and may damage the Pt catalyst. After replacing the air in the chamber with nitrogen, the anode side was purged with hydrogen for 30 min. Gas supply was finally stopped in order to realize dead-end operation during the measurements. The electrodes were connected to a Keithley source meter and the resulting potential as a function of applied current was measured. As all 9 samples share a common cathode, the current answer at a certain potential is the sum of all produced electrons across those samples, because they represent a parallel circuit. Hence, the measured polarization curve does not give information about the differences in performance between the single micro fuel cells of the materials library.

Dead-end operation results in limited convection of the gases and thereby in poor mass transportation. Thus, the overall power density of the system library is rather low. Only 1.2 mW/cm<sup>2</sup> were achieved (cf. Figure 130). More interestingly, the signal of the temperature increase of the whole membrane can be correlated to the single operation points very clearly. Figure 131 shows the summarized temperature (by defining a ROI) of the membrane over time. The arrows indicate when the operation point was changed by setting a new current. For current densities lower than 1.7 mA/cm<sup>2</sup>, the heat losses of different operation points are not distinguishable from each other. But at higher current densities, a sharp increase in temperature of at least 0.05 K can be detected.



This is a strong prove for the sensitivity of this characterization method as the difference between two operation points is only  $0.9 \text{ mA/cm}^2$ . When the current density is set to  $0 \text{ mA/cm}^2$  again, the temperature decreases abruptly by  $0.2 \text{ K}$ . Additionally, the overall temperature before and after the measurement shows linear increase of  $0.2 \text{ K}$  which can be attributed to changes of the chamber temperature caused by the microcontroller. This overall change has to be subtracted from the results of the single micro fuel cells. Hence, it can be constituted that even slight changes in current density of only  $0.9 \text{ mA/cm}^2$  can be detected through the change of heat losses by the IR camera.

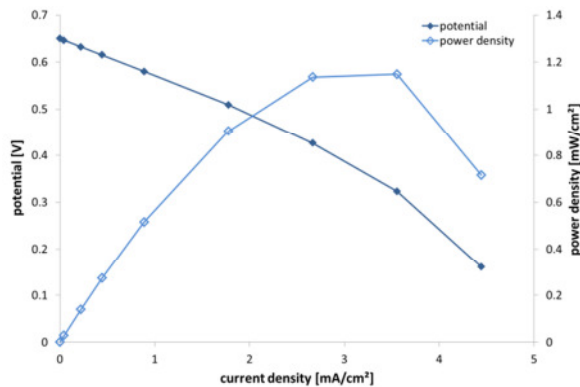


**Figure 130: Polarization curve of the micro fuel cell library; the result includes all micro fuel cells as these are connected in parallel.**

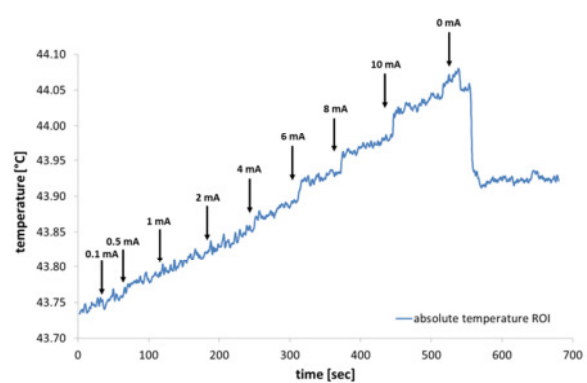


**Figure 131: Absolute temperature of the micro fuel cell library over time; points of change in applied current and drift in temperature can be observed.**

Observation points were used to detect the temperature at the catalyst samples for each micro fuel cell. From an observation point on the mounting of the system library the changes of the temperature of the measurement chamber were detected and subtracted from the measured temperature of the micro fuel cells. Figure 132 shows the resulting differences in temperature depending on the applied current density. Similar to the results of the eCI RT-measurements of the electroplated  $\mu\text{MEA}$ , the highest change in temperature can be identified at high current densities. The temperature differences of the CuPt alloy samples are not distinguishable from each other because of the slight difference in the amount of Cu that was used. In contrast to that, the pure Pt samples show a significantly different result. All three samples exhibit the lowest increase of temperature from all measured samples. This is in good correlation with the results gained from the CV-measurements which predicted the pure Pt catalyst layers to be the most effective. As explained above, more effective catalysts will result in lower increase of the temperature when they are operated at the same current density. It has to be noted that this result gives information about the effectiveness of the fuel cell but not the effectiveness of the catalyst. As pointed out earlier, the total amount of Pt for a catalyst consisting only of pure Pt is higher compared to PtCu alloys when the same layer thickness is used. Hence, the amount of Pt relating to the power density ( $\text{mW/mg}_{\text{Pt}}$ ) cannot be extracted from the eCI RT measurement. It may well be that the PtCu alloys are more effective than pure Pt layers as less Pt was used in these. In order to prove this assumption a system

library with different layer thicknesses but constant Pt amount would be necessary, but could not be realized within this thesis.

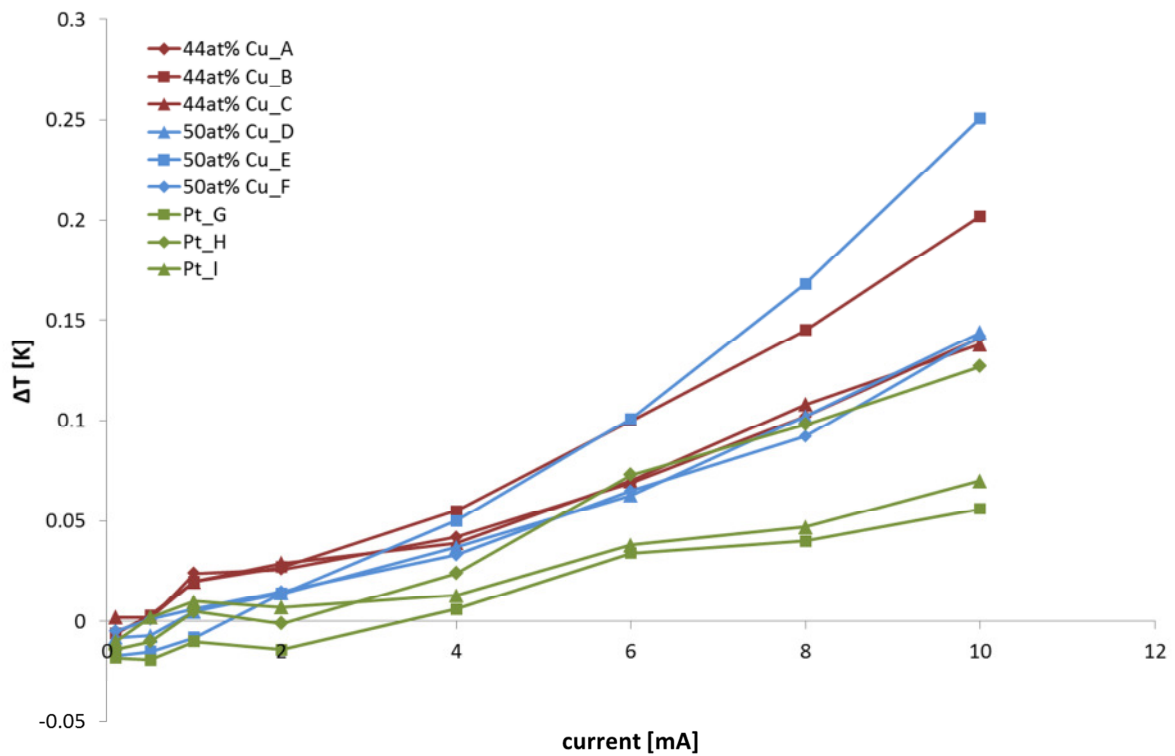


**Figure 132: Relative changes in temperature of the single micro fuel cells; relative change of reference point was subtracted which leads to negative results at low currents.**

In summary, the development of a new high throughput screening method can be stated as a success. It was possible to prove theoretical aspects of heat loss inside fuel cells with the help of eClRT measurements. Moreover, the characterization of silicon-based  $\mu$ MEAs by eClRT was possible with high accuracy and reproducibility. Finally, the fabrication of a system library with varying catalyst alloys was demonstrated successfully. Measurements of  $\mu$ MEAs as well as the system library could be approved with the help of established characterization methods, namely polarization curves and SDC measurements. However, improvement of temperature and humidity control is necessary in order to enhance accuracy of the measurement results.

## 8 Summary and outlook

The goal of this thesis was to develop concepts and fabrication technologies for a micro membrane electrode assembly that can be manufactured within MEMS and semiconductor production lines. The major application for this technology is expected to be power supply for portable devices like smartphones and devices within the internet of things. Furthermore, a new high-throughput screening method based on parallel IR-thermographic characterization of multiple micro fuel cells was developed and evaluated.

A detailed literature research showed that semiconductor based micro fuel cells can be divided into three categories. The first category describes the adaption of conventional MEA concepts to microsystem processes and their miniaturization through the application of high precision processes like lithography, wet and dry etching or thin film technologies. As these micro fuel cells are based on the same concept as macro fuel cells which are used, for example, in automotive industry they offer high power densities and long lifetimes. However, the use of conventional components like ionomer membranes, gas diffusion layers and bipolar plates brings miniaturization to certain limits as tolerances of the components, especially carbon cloth and ionomer membrane do not match with semiconductor industry standards. The other two categories make use of free standing silicon membranes that combine several features of a MEA: gas supply, electrochemical processing of the reactants, proton conduction and current collection. The major difference between the two categories was identified to be the use of either porous or microstructured membranes which exhibit specific advantages and disadvantages. On the one hand porous membranes make it possible to fabricate very small pores in the nanometer range similar to ionomer membranes which results in good hydrogen impermeability. On the other hand, microstructured silicon membranes show homogenous porosity and good mechanical stability.

Based on the results of the literature research, the proposed concept of this thesis was based on microstructured silicon membranes with a pore diameter of 1  $\mu\text{m}$  and a pitch of 2  $\mu\text{m}$  distributed over an active area of 10 x 20  $\text{mm}^2$ . The membranes were fabricated with MEMS processes, including lithography and anisotropic deep reactive ion etching which made them suitable for mass production. By integration of a buried  $\text{SiO}_2$  layer short circuits between anode and cathode could be avoided successfully and a minimum membrane thicknesses of 5  $\mu\text{m}$  was achieved. A 80 nm thick Pt-layer with an underlying 50 nm thick Cr adhesion layer was sputter coated onto the surfaces of the membrane and used as bifunctional catalyst layer and current collector. The sputter parameters were optimized regarding porosity and thickness in order to enable optimal use of the Pt. The micro channels were filled with a PFSA ionomer by application of a newly developed dip-coating process that resulted in good homogeneity and low residual ionomer layer on the surface.

First measurements of polarization curves revealed low power densities of less than  $5 \text{ mW/cm}^2$  at room temperature and without humidification. It was found that the bifunctional Cr-/Pt-layer is not able to promote effective electrochemical reaction. Hence, the electrode setup of the  $\mu\text{MEA}$  was extended by spray coating additional porous catalyst layers onto the anode and the cathode. Consequently, power density could be doubled to nearly  $10 \text{ mW/cm}^2$ , which is comparable to achieved power densities found in literature. However, measurements with electrochemical atomic force microscopy and electrochemical impedance spectroscopy revealed that there is a strong correlation between the residual ionomer layer, the current collector and the catalyst layer. On the one hand, the residual ionomer layer, which separates the bifunctional Cr-/Pt-layer from the reaction gases and the additional spray coated catalyst layer, improves in-plane proton conduction between the individual micro channels. On the other hand, it hinders electrons to reach the Cr-Pt-layer which also serves as the current collector inside the  $\mu\text{MEA}$ , resulting in high ohmic overpotentials. The spray coated catalyst layer increases the power density by decreasing charge transfer and mass transfer overpotentials significantly, especially for the ORR which could be shown by detailed EIS measurements and corresponding curve fitting. Hence, electrode layer, residual ionomer and current collecting metal layer have a major influence on the performance of the  $\mu\text{MEA}$ . Within this thesis it became clear that identification of optimized electrode setup remains the major challenge in designing a  $\mu\text{MEA}$ .

Based on the findings above, the bifunctional Cr-/Pt-layer and the spray coated catalyst layer were replaced by one single electrically conductive compound in order to optimize the triple phase boundary. The use of such a compound represented a third electrode setup and aimed to eliminate the influence of the residual ionomer layer on current collection. It contained electrically conductive CNTs which were integrated into a conventional porous catalyst layer. This way, the initial specific electrical conductivity of the compound was increased by a factor of 20 to  $15.5 \text{ S/cm}$ . The electrochemical performance of the compound was characterized by cyclic voltammetry and application within silicon based  $\mu\text{MEAs}$ . For those, power densities of  $3 \text{ mW/cm}^2$  were realized. In order to increase electrical conductivity and electrochemical effectivity further, an electroplating process was developed. It was shown that Pt particles can be coated along the conductive pathways inside the porous layer. Conductivities of  $540.9 \text{ S/cm}$  were achieved, while Pt loading remained below  $1 \text{ mg/cm}^2$ . The resulting power density was  $6 \text{ mW/cm}^2$ .

However, some challenges remain and need to be addressed in the future. First, power density is still below the necessary values that would be capable of powering electronic devices. For example, a smartphone would require a fuel cell power density of at least  $80 \text{ mW/cm}^2$  based on the power needed and the active area that could be integrated into the housing of the phone. Optimization of

the current collector and the catalyst layer are crucial factors for achieving this goal as was shown in this thesis. One possibility might be adding conductive particles with higher specific conductivity to the catalyst layer in order to improve current collection. Another aspect that has to be considered in the future is the optimization of the fabrication costs. This includes the use of precious metals and the cost effects of mass production which define the total costs of a  $\mu$ MEA.

Besides the intended application of micro fuel cells in portable electronic devices, a new high throughput screening concept was developed which allows the use of  $\mu$ MEA-libraries in materials development. Therefore, a new test procedure was realized where eClRT measurements can be used to realize parallel screening of several  $\mu$ MEAs. Because of the innovative design of the  $\mu$ MEA, a direct optical access to the fuel cell reaction is possible which allows direct measurements by the IR-camera. The principle was successfully applied to microstructured  $\mu$ MEAs and showed great potential to be used in material science as temperature differences below 0.1 K could be detected which resulted from changing the operation current in the range of  $< 0.1 \text{ mA/cm}^2$ . The results were compared to established electrochemical high throughput screening methods and were in good agreement.

For optimization of eClRT based high throughput screening method, improvement of temperature and humidity control will be crucial. Temperature fluctuations of the measurement setup are still in the range of the measured temperature differences. Moreover, the use of improved software that allows multiple temperature calibration will enhance results significantly.

In conclusion, the development of silicon-based micro fuel cell was demonstrated to be a promising technology for power supply in portable devices. They can be manufactured with established mass fabrication processes and exhibit a small volumetric footprint which is essential in consumer electronics like smartphones or tablet PCs. Moreover, micro fuel cells are a renewable option for portable power supply. The concept of MEMS-based micro fuel cells has the potential to be manufactured in high quantities at reasonable costs. The developed concepts and fabrication methods presented in this thesis are a promising starting point for future innovations. Silicon-based  $\mu$ MEAs cannot only serve for providing a current in low power applications, but also as basis for system libraries in high throughput screening methods in materials development. The developed methodology makes it possible for the first time to characterize high quantities of  $\mu$ MEAs in parallel while fuel cell reaction takes place. Hence, parallel characterization of fuel cells at the system level becomes possible where all components can be evaluated not only regarding their individual performance, but as part of an operating electrochemical system.

## References

- [1] T. Coughlin, "A Moore's Law for Mobile Energy," *IEEE Consumer Electronics Magazine*, vol. 4, pp. 74-82, 2015.
- [2] S. B. Schaevitz, "Powering the Wireless World with MEMS," *Proceedings of SPIE*, vol. 8248, pp. 824802-1 - 17, 2012.
- [3] L. Shaw, J. Pratt, L. Klebanoff, T. Johnson, M. Arienti and M. Moreno, "Analysis of H<sub>2</sub> storage needs for early market "man-portable" fuel cell applications," *International Journal of Hydrogen Energy*, vol. 38, pp. 2810-2823, 2013.
- [4] A. Perujo, G. Van Grootveld and H. Scholz, "Present and Future Role of Battery Electrical Vehicles in Private and Public Urban Transport," in *New Generation of Electric Vehicles*, 2012.
- [5] E. D. Wachsman and K. T. Lee, "Lowering the Temperature of Solid Oxide Fuel Cells," *Science*, vol. 334, pp. 935-939, 2011.
- [6] S. Curtin and J. Gangi, "2013 Fuel Cell Technologies Market Report," U. S. Department of Energy, 2014.
- [7] W. R. Grove, *Philosophical Magazine*, vol. 14, 1839.
- [8] J. Larminie and A. Dicks, *Fuel Cell Systems Explained*, 2. ed., John Wiley & Sons Ltd, 2003.
- [9] P. Choi, N. Jalani and R. Datta, "Thermodynamics and Proton Transport in Nafion - II. Proton Diffusion Mechanisms and Conductivity," *Journal of The Electrochemical Society*, vol. 152, pp. E123-E130, 2005.
- [10] M. Eikerling, A. A. Kornyshev, A. M. Kuznetsov, J. Ulstrup and S. Walbran, "Mechanisms of Proton Conductance in Polymer Electrolyte Membranes," *The Journal of Physical Chemistry B*, vol. 105, pp. 3646-3662, 2001.
- [11] S. Slade, S. A. Campbell, T. R. Ralph and F. C. Walsh, "Ionic Conductivity of an Extruded Nafion 1100 EW Series of Membranes," *Journal of The Electrochemical Society*, vol. 149, pp. A1556-A1564, 2002.

- [12] Q. Zhao, P. Majsztrik and J. Benziger, "Diffusion and Interfacial Transport of Water in Nafion," *The Journal of Physical Chemistry B*, vol. 115, p. 2717–2727, 2011.
- [13] M. Eikerling and A. A. Kornyshev, "Modelling the performance of the cathode catalyst layer of polymer electrolyte fuel cells," *Journal of Electroanalytical Chemistry*, vol. 453, pp. 89-106, 1998.
- [14] M. Eikerling, A. S. Ioselevich and A. A. Kornyshev, "How good are the Electrodes we use in PEMFCs?," vol. 4, pp. 131-140, 2004.
- [15] P. Quaino, F. Juarez, E. Santos and W. Schmickler, "Volcano plots in hydrogen electrocatalysis – uses and abuses," *Beilstein Journal of Nanotechnology*, vol. 5, p. 846–854, 2014.
- [16] A. Rabis, P. Rodriguez and T. J. Schmidt, "Electrocatalysis for Polymer Electrolyte Fuel Cells: Recent Achievements and Future Challenges," *ACS Catalysis*, vol. 2, pp. 864-890, 2012.
- [17] H. A. Gasteiger, S. S. Kocha, B. Sompalli and F. T. Wagner, "Activity benchmarks and requirements for Pt, Pt-alloy, and non-Pt oxygen reduction catalysts for PEMFCs," *Applied Catalysis B: Environmental*, vol. 56, pp. 9-35, 2005.
- [18] A. Marinkas, F. Arena, J. Mitzel, G. M. Prinz, A. Heinzl, V. Peinecke and H. Natter, "Graphene as catalyst support: The influences of carbon additives and catalyst preparation methods on the performance of PEM fuel cells," *Carbon*, vol. 58, pp. 139-150, 2013.
- [19] X. Leimin, L. Shijun and L. Zhenxing, "Investigation of a Novel Catalyst Coated Membrane Method to Prepare Low-Platinum-Loading Membrane Electrode Assemblies for PEMFCs," *Fuel Cells*, vol. 9, pp. 101-105, 2009.
- [20] K. Kim, K. Lee, H. Kim, E. Cho, S. Lee, T. Lim, S. Yoon, I. Hwang and J. Jang, "The effects of Nafion ionomer content in PEMFC MEAs prepared by a catalyst-coated membrane (CCM) spraying method," *International Journal of Hydrogen Energy*, vol. 35, pp. 2119-2126, 2010.

- [21] T. Suzuki, S. Tsushima and S. Hirai, "Effects of Nafion ionomer and carbon particles on structure formation in a proton-exchange membrane fuel cell catalyst layer fabricated by the decal-transfer method," *International Journal of Hydrogen Energy*, vol. 36, pp. 12361-12369, 2011.
- [22] A. Suzuki, U. Sen, T. Hattori, R. Miura, R. Nagumo, H. Tsuboi, N. Hatakeyama, A. Endou, H. Takaba, M. C. Williams and A. Miyamoto, "Ionomer content in the catalyst layer of polymer electrolyte membrane fuel cell (PEMFC): Effects on diffusion and performance," *International Journal of Hydrogen Energy*, vol. 36, pp. 2221-2229, 2011.
- [23] D. Song, Q. Wang, Z. Liu, T. Navessin, M. Eikerling and S. Holdcroft, "Numerical optimization study of the catalyst layer of PEM fuel cell cathode," *Journal of Power Sources*, vol. 126, pp. 104-111, 2004.
- [24] M. Lee, M. Uchida, D. A. Tryk, H. Uchida and M. Watanabe, "The effectiveness of platinum/carbon electrocatalysts: Dependence on catalyst layer thickness and Pt alloy catalytic effects," vol. 56, p. 4783-4790, 2011.
- [25] K. T. Jeng, S. F. Lee, G. F. Tsai and C. H. Wang, "Oxygen mass transfer in PEM fuel cell gas diffusion layers," *Journal of Power Sources*, vol. 138, pp. 41-50, 2004.
- [26] T. Zhou and H. Liu, "Effects of the electrical resistances of the GDL in a PEM fuel cell," *Journal of Power Sources*, vol. 161, pp. 444-453, 2006.
- [27] I. Nitta, O. Himanen and M. Mikkola, "Contact resistance between gas diffusion layer and catalyst layer of PEM fuel cells," *Electrochemistry Communications*, vol. 10, pp. 47-51, 2008.
- [28] A. Hakenjos, H. Muentner and U. Wittstadt, "A PEM fuel cell for combined measurement of current and temperature distribution, and flow field flooding," *Journal of Power Sources*, vol. 131, pp. 213-216, 2004.
- [29] A. Heinzl, C. Hebling, M. Müller, M. Zedda and C. Müller, "Fuel cells for low power applications," *Journal of Power Sources*, vol. 105, pp. 250-255, 2002.



- [30] S. C. Kelley, G. A. Deluga and W. H. Smyrl, "Miniature Fuel Cells Fabricated on Silicon Substrates," *AIChE Journal*, pp. 1071-1082, 2002.
- [31] J. Cao, Z. Zou, Q. Huang, T. Yuan, Z. Li, B. Xia and H. Yang, "Planar air-breathing micro-direct methanol fuel cell stacks based on micro-electronic–mechanical-system technology," *Journal of Power Sources*, vol. 185, pp. 433-438, 2008.
- [32] Q. Zhang, X. Wang, L. Zhong, Y. Zhou, X. Qiu and L. Liu, "A Silicon-Based Micro Direct Methanol Fuel Cell With Microblocks in Anode Structure," in *MEMS-Conference*, Tuscon, Arizona, USA, 2008.
- [33] R. W. Verjullo, J. Santander, N. Sabate, J. P. Esquivel, N. Torres-Herrero, A. Habrioux and N. Alonso-Vante, "Fabrication and evaluation of a passive alkaline membrane micro direct methanol fuel cell," *International Journal of Hydrogen Energy*, vol. 39, pp. 5406-5413, 2014.
- [34] D. Zheng, K. Zhang, Z. F. Guo, B. J. Xia and X. Li, "Optimal-Catalyzed Porous Silicon Electrodes for Self-breathing MEMS Fuel Cells," in *Power-MEMS Conference*, Atlanta, Georgia, USA, 2012.
- [35] M. Kobayashi, T. Suzuki and M. Hayase, "A miniature fuel cell with monolithically fabricated Si electrodes - Reduction of residual porous Si on catalyst layer," *Journal of Power Sources*, vol. 267, pp. 622-628, 2014.
- [36] J. Yeom, G. Z. Mozsgai, B. R. Flachsbar, E. R. Choban, A. Asthana, M. A. Shannon and P. J. A. Kenis, "Microfabrication and characterization of a silicon-based millimeter scale, PEM fuel cell operating with hydrogen, methanol, or formic acid," *Sensors and Actuators B*, vol. 107, p. 882–891, 2005.
- [37] Y. Zhang, J. Lu, S. Shimano, H. Zhou and R. Maeda, "Nanoimprint of Proton Exchange Membrane for MEMS-based Fuel Cell Application," in *Polytronic Conference*, Tokyo, Japan, 2007.
- [38] S. Kouassi, G. Gautier, J. Thery, S. Desplobain, M. Borella, L. Ventura and J.-Y. Laurant, "Proton exchange membrane micro fuel cells on 3D porous silicon gas diffusion layers," *Journal of Power Sources*, vol. 216, pp. 15-21, 2012.
- [39] R. Hahn, S. Wagner, A. Schmitz and H. Reichl, "Development of a planar micro fuel cell with thin film and micro patterning technologies," *Journal of Power Sources*, vol. 131, pp. 73-78, 2004.

- [40] C. Weinmueller, G. Tautschnig, N. Hotz and D. Pouliska, "A flexible direct methanol micro-fuel cell based on a metalized, photosensitive polymer film," *Journal of Power Sources*, vol. 195, p. 3849–3857, 2010.
- [41] S. Moghaddam, E. Pengwang, Y.-B. Jiang, A. R. Garcia, D. J. Burnett, C. J. Brinker, R. I. Masel and M. A. Shannon, "An inorganic–organic proton exchange membrane for fuel cells with a controlled nanoscale pore structure," *Nature Nanotechnology*, vol. 5, pp. 230-236, 2010.
- [42] X. H. Wang, W. J. Wang, Q. Zhang, X. P. Qiu, X. Guo and L. T. Liu, "Silicon-Based Proton Exchange Membrane for Micro Direct Methanol Fuel Cells," in *PowerMEMS Conference*, Freiburg, Germany, 2007.
- [43] N. Torres-Herrero, J. Santander, N. Sabaté, C. Cané, T. Trifonov, A. Rodriguez and R. Alcubilla, "A monolithic micro fuel cell based on a functionalized porous silicon membrane," in *International Conference on Advanced Semiconductor Devices & Microsystems (ASDAM)*, Smolenice, Slovakia, 2010.
- [44] S. Gold, K.-L. Chu, C. Lu, M. A. Shannon and R. I. Masel, "Acid loaded porous silicon as a proton exchange membrane for micro-fuel cells," *Journal of Power Sources*, vol. 135, p. 198–203, 2004.
- [45] M. Wang, X. Wang, S. Wu, Z. Tan and X. Guo, "Nano Porous Silicon Membrane with Channels for Micro Direct Methanol Fuel Cells," in *International Conference on Nano/Micro Engineered and Molecular Systems*, Kaohsiung, Taiwan, 2011.
- [46] K.-L. Chu, S. Gold, V. Subramanian, C. Lu, M. A. Shannon and R. I. Masel, "ANanoporous Silicon Membrane Electrode Assembly for On-Chip Micro Fuel Cell Applications," *Journal of Microelectromechanical Systems*, vol. 15, pp. 671-677, 2006.
- [47] T. Pichonat and B. Gauthier-Manuel, "Development of porous silicon-based miniature fuel cells," *Journal of Micromechanics and Microengineering*, vol. 15, p. 179–184, 2005.
- [48] G. Nagayama, A. Kuromaru, M. Kaneda and T. Tsuruta, "Effects of nano/microstructures on performance of Si-based microfuel cells," *Applied Thermal Engineering*, vol. 72, pp. 298-303, 2014.
- [49] J. V. Larsen, B. T. Dalslet, C. Kallesoe and E. V. Thomsen, "Characterization of Micro Direct Methanol Fuel Cells with Silicon Plate Supported Integrated Ionomer Membranes," in *Transducers Conference*, Barcelona, Spain, 2013.

- [50] J. V. Larsen, B. T. Dalslet, A. C. Johansson, C. Kallesøe and E. V. Thomsen, "Micro direct methanol fuel cell with perforated silicon-plate integrated ionomer membrane," *Journal of Power Sources*, vol. 257, pp. 237-245, 2014.
- [51] J. V. Larsen, B. T. Dalslet, C. Kallesøe, S. Engberg, J. Thomsen and E. V. Thomsen, "Micro Direct Methanol Fuel Cell Utilizing Silicon Supported Ionomer Membrane," in *PowerMEMS Conference*, Seoul, Korea, 2011.
- [52] L. Zhu, K. Y. Lin, R. D. Morgan, V. V. Swaminathana, H. S. Kim, B. Gurau, D. Kim, B. Bae, R. I. Masel and M. A. Shannon, "Integrated micro-power source based on a micro-silicon fuel cell and a micro electromechanical system hydrogen generator," *Journal of Power Sources*, vol. 185, p. 1305–1310, 2008.
- [53] S. Moghaddam, E. Pengwang, K. Y. Lin, R. I. Masel and M. A. Shannon, "Millimeter-Scale Fuel Cell With Onboard Fuel and Passive Control System," *Journal of Microelectromechanical Systems*, vol. 17, pp. 1388-1395, 2008.
- [54] P. A. Köllensperger, W. J. Karl, M. M. Ahmad, W. T. Pike and M. Green, "Patterning of platinum (Pt) thin films by chemical wet etching in Aqua Regia," *Journal of Micromechanics and Microengineering*, vol. 22, pp. 1-6, 2012.
- [55] T. A. Green, "Gold etching for microfabrication," *Gold Bulletin*, vol. 47, pp. 205-216, 2014.
- [56] A. K. T. Yeow, V. Retnasamy, Z. Sauli. and G. S. Chui, "Surface Roughness Analysis on Platinum Deposited Wafer After Reactive Ion Etching Using SF<sub>6</sub>+Argon/CF<sub>4</sub>+Argon Gaseous," in *Regional Symposium on Micro- and Nanoelectronics*, Langkawi, Malaysia, 2013.
- [57] Z. Yao, C. Wang, H.-K. Sung and N.-Y. Kim, "Defined micropatterns of platinum thin films by inductively coupled plasma etching using SF<sub>6</sub>/Ar/O<sub>2</sub> mixture gas," *Materials Science in Semiconductor Processing*, vol. 27, pp. 228-332, 2014.
- [58] T.-S. Choi and D. W. Hess, "Chemical Etching and Patterning of Copper, Silver, and Gold Films at low temperatures," *ECS Journal of Solid State Science and Technology*, vol. 4, pp. N3084-N3093, 2015.
- [59] C. Bretthauer, C. Müller and H. Reinecke, "A precious-metal free micro fuel cell accumulator," *Journal of Power Sources*, vol. 196, p. 4729–4734, 2011.

- [60] G. Nagayama, N. Idera, T. Tsuruta, J. Yu, K. Takahashi and M. Hori, "Porous silicon as a proton exchange membrane for micro fuel cells," *Electrochemistry (Tokyo)*, vol. 73, pp. 939-941, 2005.
- [61] K.-L. Chu, M. A. Shannon and R. I. Masel, "Porous silicon fuel cells for micro power generation," *Journal of Micromechanics and Microengineering*, vol. 17, p. 243–249, 2007.
- [62] J. A. Thornton, "High Rate Thick Film Growth," *Annual Reviews of Materials Science*, vol. 7, pp. 239-260, 1977.
- [63] J. A. Thornton, "Influence of apparatus geometry and deposition conditions on the structure and topography of thick sputtered coatings," *Journal of Vacuum Science & Technology*, vol. 11, pp. 666-670, 1974.
- [64] J. A. Thornton, "The microstructure of sputter-deposited coatings," *Journal of Vacuum Science & Technology*, vol. A4, pp. 3059-3065, 1986.
- [65] J. A. Thornton and D. W. Hoffmann, "Stress-Related Effects In Thin Films," *Thin Solid Films*, vol. 171, pp. 5-31, 1989.
- [66] A. T. Haug, R. E. White, J. W. Weidner, W. Huang, S. Shi, T. Stoner and N. Rana, "Increasing Proton Exchange Membrane Fuel Cell Catalyst Effectiveness Through Sputter Deposition," *Journal of The Electrochemical Society*, vol. 149, pp. A280-A287, 2002.
- [67] M. D. Gasda, R. Teki, T.-M. Lu, N. Koratkar, G. A. Eismann and D. Galla, "Sputter-Deposited Pt PEM Fuel Cell Electrodes: Particles vs Layers," *Journal of The Electrochemical Society*, vol. 156, pp. B614-B619, 2009.
- [68] K.-L. Huang, Y.-C. Lai and C.-H. Tsai, "Effects of sputtering parameters on the performance of electrodes fabricated for polymer electrolyte membrane fuel cells," *Journal of Power Sources*, vol. 156, pp. 224-231, 2006.
- [69] R. O'Hayre, S.-J. Lee, S.-W. Cha and B. P. Fritz, "A sharp peak in the performance of sputtered Platinum fuel cells at ultra low Platinum loading," *Journal of Power Sources*, vol. 109, pp. 483-493, 2002.

- [70] R. O'Hayre, *Microscale Electrochemistry: Application to Fuel Cells*, Stanford University, 2004.
- [71] E. Slavcheva, G. Ganske, G. Topalov, W. Mokwa and U. Schnakenberg, "Effect of sputtering parameters on surface morphology and catalytic efficiency of thin platinum films," *Applied Surface Science*, vol. 255, p. 6479–6486, 2009.
- [72] M. Frank, G. Erdler, H.-P. Frerichs, C. Müller and H. Reinecke, "Chip integrated fuel cell accumulator," *Journal of Power Sources*, vol. 181, p. 371–377, 2008.
- [73] L. Schlapbach and A. Züttel, "Hydrogen storage materials - mobile applications," *Nature*, vol. 414, pp. 353-358, 2001.
- [74] A. Balakrishnan, J. Becker, C. Mueller and H. Reinecke, "Advanced Hydrogen Storage Technique To Improve The Run Time Of The "Chip Integrated Micro PEM Fuel Cell System"," in *PowerMEMS Conference*, Atlanta, USA, 2012.
- [75] J. I. Hur and C.-J. Kim, "Miniature fuel-cell system complete with on-demand fuel and oxidant supply," *Journal of Power Sources*, vol. 274, pp. 916-921, 2015.
- [76] A. Pozio, M. De Francesco, A. Cemmi, F. Cardellini and L. Giorgi, "Comparison of high surface Pt/C catalysts by cyclic voltammetry," *Journal of Power Sources*, vol. 105, pp. 13-19, 2002.
- [77] W. Tang, S. Jayaraman, T. F. Jaramillo, G. D. Stucky and E. W. McFarland, "Electrocatalytic Activity of Gold-Platinum Clusters for Low Temperature Fuel Cell Applications," *Journal of Physical Chemistry C*, vol. 113, p. 5014–5024, 2009.
- [78] J. Shan and P. G. Pickup, "Characterization of polymer supported catalysts by cyclic voltammetry and rotating disk voltammetry," *Electrochimica Acta*, vol. 46, pp. 119-125, 2000.
- [79] J. Wu, X. Z. Yuan, H. Wang, M. Blanco, J. J. Martin and J. Zhang, "Diagnostic tools in PEM fuel cell research: Part I Electrochemical techniques," *International Journal of Hydrogen Energy*, vol. 33, pp. 1735-1746, 2008.

- [80] J.-H. Wee, K.-Y. Lee and S. H. Kim, "Fabrication methods for low-Pt-loading electrocatalysts in proton exchange membrane fuel cell systems," *Journal of Power Sources*, vol. 165, pp. 667-677, 2007.
- [81] T. Biegler, D. A. J. Rand and R. Woods, "Limiting Oxygen Coverage on Platinized Platinum; Relevance to Determination of Real Platinum Area," *Electroanalytical Chemistry and Interfacial Electrochemistry*, vol. 29, pp. 269-277, 1971.
- [82] S. Qu, X. Li, M. Hou, Z. Shao and B. Yi, "The effect of air stoichiometry change on the dynamic behavior of a proton exchange membrane fuel cell," *Journal of Power Sources*, vol. 185, p. 302–310, 2008.
- [83] M. M. Mench, *Fuel Cell Engines*, John Wiley & Sons Inc., 2008.
- [84] A. A. Kulikovskiy, "The effect of stoichiometric ratio  $\lambda$  on the performance of a polymer electrolyte fuel cell," *Electrochimica Acta*, vol. 49, p. 617–625, 2004.
- [85] G. J. Brug, A. L. G. van den Eeden, M. Sluyters-Rehbach and J. H. Sluyters, "The Analysis of Electrode Impedances Complicated by the Presence of a Constant Phase Element," *J. Electroanal. Chem.*, vol. 176, pp. 275-295, 1984.
- [86] R. de Levie, "Electrochemical response of porous and rough electrodes," *Adv. Electrochem. Eng.*, vol. 6, pp. 329-397, 1967.
- [87] S. D. Mikhailenko, M. D. Guiver and S. Kaliaguine, "Measurements of PEM conductivity by impedance spectroscopy," *Solid State Ionics*, vol. 179, p. 619–624, 2008.
- [88] T. Soboleva, Z. Xie, Z. Shi, E. Tsang, T. Navessin and S. Holdcroft, "Investigation of the through-plane impedance technique for evaluation of anisotropy of proton conducting polymer membranes," *Journal of Electroanalytical Chemistry*, vol. 622, p. 145–152, 2008.
- [89] G. Dotelli, R. Ferrero, P. G. Stampino and S. Latorrata, "Analysis and Compensation of PEM Fuel Cell Instabilities in Low-Frequency EIS Measurements," *IEEE TRANSACTIONS ON INSTRUMENTATION AND MEASUREMENT*, vol. 63, pp. 1693-1700, 2014.
- [90] X. Yuan, J. C. Sun, M. Blanco, H. Wang, J. Zhang and D. P. Wilkinson, "AC impedance diagnosis of a 500W PEM fuel cell stack Part I: Stack impedance," *Journal of Power Sources*, vol. 161, p. 920–928, 2006.

- [91] M. Ciureanu and R. Roberge, "Electrochemical Impedance Study of PEM Fuel Cells. Experimental Diagnostics and Modeling of Air Cathodes," *J. Phys. Chem. B*, vol. 105, pp. 3531-3539, 2001.
- [92] M. Pérez-Page and V. Pérez-Herranz, "Study of the electrochemical behaviour of a 300 W PEM fuel cell stack by Electrochemical Impedance Spectroscopy," *International Journal of Hydrogen Energy*, vol. 39, pp. 4009-4015, 2014.
- [93] X. Yuan, H. Wang, J. C. Sun and J. Zhang, "AC impedance technique in PEM fuel cell diagnosis—A review," *International Journal of Hydrogen Energy*, vol. 32, p. 4365 – 4380, 2007.
- [94] R. Hiesgen, I. Wehl, E. Aleksandrova, E. Roduner, A. Bauder and K. A. Friedrich, "Nanoscale properties of polymer fuel cell materials—A selected review," *International Journal of Polymer Research*, vol. 34, pp. 1223-1238, 2010.
- [95] E. Aleksandrova, S. Hink, R. Hiesgen and E. Roduner, "Spatial distribution and dynamics of proton conductivity in fuel cell membranes: potential and limitations of electrochemical atomic force microscopy measurements," *Journal of Physics: Condensed Matter*, vol. 23, pp. 1-10, 2011.
- [96] S. Hink, N. Wagner, W. G. Bessler and E. Roduner, "Impedance Spectroscopic Investigation of Proton Conductivity in Nafion Using Transient Electrochemical Atomic Force Microscopy (AFM)," *Membranes*, vol. 2, pp. 237-252, 2012.
- [97] A. R. Blythe, "Electrical Resistivity Measurements of Polymer Materials," *Polymer Testing*, vol. 4, pp. 195-209, 1984.
- [98] Y. Long, J. Duvail, M. Li, C. Gu, Z. Liu and S. P. Ringer, "Electrical Conductivity Studies on Individual Conjugated Polymer Nanowires: Two-Probe and Four-Probe Results," *Nanoscale Research Letters*, vol. 5, p. 237–242, 2010.
- [99] G. L. Brown, "Formation of Films from Polymer Dispersions," *Journal of Polymer Science*, vol. 22, pp. 423-434, 1956.
- [100] L. Cui, J. Zhang, X. Zhang, L. Huang, T. Wang and B. Yang, "Suppression of the Coffee Ring Effect by Hydrosoluble Polymer Additives," *Applied Materials and Interfaces*, vol. 4, p. 2775–2780, 2012.

- [101] X. Shen, C.-M. Ho and T.-S. Wong, "Minimal Size of Coffee Ring Structure," *Journal of Physical Chemistry B.*, vol. 114, p. 5269–5274, 2010.
- [102] B.-J. de Gans and U. S. Schubert, "Inkjet Printing of Well-Defined Polymer Dots and Arrays," *Langmuir*, vol. 20, pp. 7789-7793, 2004.
- [103] P. J. Yunker, T. Stil, M. A. Lohr and A. G. Yodh, "Suppression of the coffee-ring effect by shape-dependent capillary interactions," *Nature*, vol. 476, pp. 308-311, 2011.
- [104] C. J. Brinker, G. C. Frye, A. J. Hurd and C. S. Ashley, "Fundamentals of Sol-Gel Dip Coating," *Thin Solid Films*, vol. 201, pp. 97-108, 1991.
- [105] D. Grosso, C. Boissière, B. Smarsly, T. Brezesinski, N. Pinna, P. A. Albouy, H. Amenitsch, M. Antonietti and C. Sanchez, "Periodically ordered nanoscale islands and mesoporous films composed of nanocrystalline multimetallic oxides," *Nature Materials*, vol. 4, pp. 787-792, 2004.
- [106] G. Berteloot, A. Daerra, F. Lequeux and L. Limat, "Dip coating with colloids and evaporation," *Chemical Engineering and Processing*, vol. 68, pp. 69-73, 2013.
- [107] Y. D. Jung and K. H. Ahn, "Prediction of Coating Thickness in the Convective Assembly Process," *Langmuir*, vol. 29, p. 15762–15769, 2013.
- [108] M. Faustini, B. Louis, P. A. Albouy, M. Kümmel and D. Grosso, "Preparation of Sol-Gel Films by Dip-Coating in Extreme Conditions," *Journal of Physical Chemistry C*, vol. 114, p. 7637–7645, 2010.
- [109] M. Faustini, A. Capobianchi, G. Varvaro and D. Grosso, "Highly Controlled Dip-Coating Deposition of fct FePt Nanoparticles from Layered Salt Precursor into Nanostructured Thin Films: An Easy Way To Tune Magnetic and Optical Properties," *Chemistry of Materials*, vol. 24, p. 1072–1079, 2012.
- [110] S. Lepoutre, J.-H. Småt, C. Laberty, H. Amenitsch, D. Grosso and M. Lindén, "Detailed study of the pore-filling processes during nanocasting of mesoporous films using SnO<sub>2</sub>/SiO<sub>2</sub> as a model system," *Microporous and Mesoporous Materials*, vol. 123, p. 185–192, 2009.
- [111] D. Grosso, "How to exploit the full potential of the dip-coating process to better control film formation," *Journal of Materials Chemistry*, vol. 21, p. 17033–17038, 2011.



- [112] A. A. Darhuber, S. M. Troian, J. M. Davis, S. M. Miller and S. Wagner, "Selective dip-coating of chemically micropatterned surfaces," *Journal of Applied Physics*, vol. 88, pp. 5119-5126, 2000.
- [113] A. Diguët, M. Le Berre, Y. Chen and D. Baigl, "Preparation of Phospholipid Multilayer Patterns of Controlled Size and Thickness by Capillary Assembly on a Microstructured Substrate," *small*, vol. 5, p. 1661–1666, 2009.
- [114] E. Barsoukov and J. R. MacDonald, Impedance spectroscopy theory, experiment and applications, John Wiley & Sons, Inc., 2005, pp. pp. 118-119.
- [115] M. Boillot, C. Bonnet, N. Jatroudakis, P. Carre, S. Didierjean and F. Lopicque, "Effect of gas dilution on PEM fuel cell performance and impedance response," *Fuel Cells*, vol. 6, pp. 7-31, 2006.
- [116] S. Litster and G. McLean, "PEM fuel cell electrodes," *Journal of Power Sources*, vol. 130, p. 61–76.
- [117] A. Havranek and K. Wippermann, "Determination of proton conductivity in anode catalyst layers of the Direct Methanol Fuel Cell (DMFC)," *Journal of Electroanalytical Chemistry*, vol. 567, pp. 305-315.
- [118] S. Obayopo, T. Bello-Ochende and J. P. Meyer, "Three-dimensional optimisation of a fuel gas channel of a proton exchange membrane fuel cell for maximum current density," *International Journal of Energy Research*, vol. 37, p. 228–241, 2013.
- [119] F. Mollaamin and M. Monajjemi, "Fractal Dimension on Carbon Nanotube-Polymer Composite Materials Using Percolation Theory," *Journal of Computational and Theoretical Nanoscience*, vol. 5, pp. 597-601, 2012.
- [120] M. Monajjemi, H. Baheri and F. Mollaamin, "A percolation model for carbon nanotube-polymer composites using the Mandelbrot-Given curve," *Journal of Structural Chemistry*, vol. 52, pp. 54-59, 2011.

- [121] P. G. De Gennes , "On a relation between percolation theory and the elasticity of gels," *Journal de Physique Letters*, vol. 37, pp. 1-2, 1976.
- [122] G. Hu, C. Zhao, S. Zhang, M. Yang and Z. Wang, "Low percolation thresholds of electrical conductivity and rheology in poly(ethylene terephthalate) through the networks of multi-walled carbon nanotubes," vol. 47, p. 480–488, 2006.
- [123] R. Ramasubramaniam and J. Chen, "Homogeneous carbon nanotube/polymer composites for electrical applications," *Applied Physics Letters*, vol. 83, pp. 2928-2930, 2003.
- [124] H. S. Katz and J. V. Milewski, *Handbook of Fillers for Plastics*, New York: Van Nostrand Reinhold Co, 1987.
- [125] S. Stankovich, D. A. Dikin, G. H. B. Dommett, K. M. Kohlhaas and E. J. Zimney, "Graphene-based composite materials," *Nature*, vol. 442, pp. 282-286, 2006.
- [126] S. Liu, Y. Liu, H. Cebeci, R. G. de Villoria, J.-H. Lin, B. L. Wardle and Q. M. Zhang, "High Electromechanical Response of Ionic Polymer Actuators with Controlled-Morphology Aligned Carbon Nanotube/Nafion Nanocomposite Electrodes," *Advanced Functional Materials*, vol. 20, p. 3266–3271.
- [127] D. Y. Lee, I.-S. Park, M.-H. Lee, K. J. Kim and S. Heo, "Ionic polymer–metal composite bending actuator loaded with multi-walled carbon nanotubes," *Sensors and Actuators A: Physical*, vol. 133, p. 117–127, 2007.
- [128] Y. S. Song and J. R. Youn, "Influence of dispersion states of carbon nanotubes on physical properties of epoxy nanocomposites," *Carbon*, vol. 43, p. 1378–1385, 2005.
- [129] N. G. Sahoo, S. Rana, J. W. Cho, L. Li and S. H. Chan, "Polymer nanocomposites based on functionalized carbon nanotubes," *Progress in Polymer Science*, vol. 35, p. 837–867, 2010.
- [130] C. S. Suchand Sangeeth, R. Kannan, V. K. Pillai and R. Menon, "Charge transport in functionalized multi-wall carbon nanotube-Nafion composite," *Journal of Applied Physics*, vol. 112, pp. 053706-1 - 053706-6.
- [131] W. P. Kalisvaart, H. Fritzsche and W. Mérida, "Water Uptake and Swelling Hysteresis in a Nafion Thin Film Measured with Neutron Reflectometry," *Langmuir*, vol. 31, p. 5416–5422, 2015.

- [132] V. Ijori, L. Cappelletto, S. Bianco, M. Tortello and P. Spinelli, "Nafion and carbon nanotube nanocomposites for mixed proton and electron conduction," *Journal of Membrane Science*, vol. 363, p. 265–270, 2010.
- [133] S. D. Thompson, L. R. Jordan and M. Forsyth, "Platinum electrodeposition for polymer electrolyte membrane fuel cells," *Electrochimica Acta*, vol. 46, p. 1657–1663, 2001.
- [134] M. C. Tsai, T.-K. Yeh and C.-H. Tsai, "An improved electrodeposition technique for preparing platinum and platinum–ruthenium nanoparticles on carbon nanotubes directly grown on carbon cloth for methanol oxidation," *Electrochemistry Communications*, vol. 8, p. 1445–1452, 2006.
- [135] M. Shahinpoor and K. J. Kim, "The effect of surface-electrode resistance on the performance of ionic polymer-metal composite (IPMC) artificial muscles," *Smart Materials and Structures*, vol. 9, p. 543–551, 2000.
- [136] B. Jandeleit, D. J. Schaefer, T. S. Powers, H. W. Turner and W. H. Weinberg, "Kombinatorische Materialforschung und Katalyse," *Angewandte Chemie*, vol. 111, pp. 2648 - 2689, 1999.
- [137] D. Schäfer, C. Mardare, A. Savan, M. D. Sanchez, B. Mei, W. Xia, M. Muhler, A. Ludwig and W. Schuhmann, "High-Throughput Characterization of Pt Supported on Thin Film Oxide Material Libraries Applied in the Oxygen Reduction Reaction," *Analytical Chemistry*, vol. 83, p. 1916–1923, 2011.
- [138] E. S. Smotkin, J. Jiang, A. Nayar and R. Liu, "High-throughput screening of fuel cell electrocatalysts," *Applied Surface Science*, vol. 252, p. 2573–2579, 2006.
- [139] R. Liu and E. S. Smotkin, "Array membrane electrode assemblies for high throughput screening of direct methanol fuel cell anode catalysts," *Journal of Electroanalytical Chemistry*, vol. 535, pp. 49-55, 2002.
- [140] G. Gaussorgues and S. Chomet, *Infrared Thermography*, Lavoisier: Chapman & Hall, 1994.

- [141] A. Holzwarth, W. H. Schmidt and W. F. Maier, "Detection of Catalytic Activity in Combinatorial Libraries of Heterogeneous Catalysts by IR Thermography," *Angewandte Chemie*, vol. 37, p. 2644–2647, 1998.
- [142] A. Holzwarth and W. F. Maier, "Catalytic Phenomena in Combinatorial Libraries of Heterogeneous Catalysts," *Platinum Metals Review*, vol. 44, pp. 16-21, 2000.
- [143] J. W. Saalfrank and W. F. Maier, "Edelmetallfreie Katalysatoren für die CO-Oxidation bei Raumtemperatur durch gezielte Evolution," *Angewandte Chemie*, vol. 116, p. 2062–2066, 2004.
- [144] Y. Yamada, A. Ueda, H. Shioyama and T. Kobayashi, "High-throughput screening of PEMFC anode catalysts by IR-thermography," *Applied Surface Science*, vol. 223, pp. 220-223, 2004.
- [145] D. Schäfer, C. Mardare, A. Savan, M. D. Sanchez, B. Mei, W. Xia, M. Muhler, A. Ludwig and W. Schuhmann, "High-Throughput Characterization of Pt Supported on Thin Film Oxide Material Libraries Applied in the Oxygen Reduction Reaction," *Analytical Chemistry*, vol. 83, p. 1916–1923, 2011.
- [146] K. Eckhard and W. Schuhmann, "Localised visualisation of O<sub>2</sub> consumption and H<sub>2</sub>O<sub>2</sub> formation by means of SECM for the characterisation of fuel cell catalyst activity," *Electrochimica Acta*, vol. 53, p. 1164–1169, 2007.
- [147] K. C. Neyerlin, R. Srivastava, C. Yu and P. Strasser, "Electrochemical activity and stability of dealloyed Pt–Cu and Pt–Cu–Co electrocatalysts for the oxygen reduction reaction (ORR)," *Journal of Power Sources*, vol. 186, p. 261–267, 2009.
- [148] P. Strasser, S. Koh, T. Anniyev, J. Greeley, K. More, C. Yu, Z. Liu, S. Kaya, D. Nordlund, H. Ogasawara, M. F. Toney and A. Nilsson, "Lattice-strain control of the activity in dealloyed core–shell fuel cell catalysts," *Nature Chemistry*, vol. 2, pp. 454-460, 2010.
- [149] M. Shao, K. Shoemaker, A. Peles, K. Kaneko and L. Protsailo, "Pt Monolayer on Porous Pd-Cu Alloys as Oxygen Reduction Electrocatalysts," *Journal of the American Chemical Society*, vol. 132, p. 9253–9255, 2010.
- [150] L. Xiong, A. M. Kannan and A. Manthiram, "Pt–M (M¼Fe, Co, Ni and Cu) electrocatalysts synthesized by an aqueous route for proton exchange membrane fuel cells," *Electrochemistry Communications*, vol. 4, p. 898–903, 2002.

- [151] A. I. Mardare, A. D. Wieck and A. W. Hass, "Microelectrochemical lithography: A method for direct writing of surface oxides," *Electrochimica Acta*, vol. 52, p. 7865–7869, 2007.
- [152] M. Jeske, C. Soltmann, C. Ellenberg, M. Wilhelm, D. Koch and G. Grathwohl, "Proton Conducting Membranes for the High Temperature-Polymer Electrolyte Membrane-Fuel Cell (HT-PEM) Based on Functionalized Polysiloxanes," *Fuel Cells*, vol. 7, pp. 40-46, 2007.
- [153] M. Jeske, C. Ellenberg, C. Soltmann, M. Wilhelm, D. Koch and G. Grathwohl, "Synthesis of Polysiloxane Based Proton Conducting Membranes for the HT-PEMFC and Their Use in Membrane-Electrode-Assemblies," *Journal of New Materials for Electrochemical Systems*, vol. 11, pp. 31-36, 2008.
- [154] S. R. Samms, S. Wasmus and R. F. Savinell, "Thermal Stability of Proton Conducting Acid Doped Polybenzimidazole in Simulated Fuel Cell Environments," *Journal of the Electrochemical Society*, vol. 143, pp. 1225-1232, 1996.
- [155] M. Schuster, W. H. Meyer, H. G. Herz, M. Ise, M. Schuster, K. D. Kreuer and J. Maier, "Proton mobility in oligomer-bound proton solvents: imidazole immobilization via flexible spacers," *Solid State Ionics*, vol. 145, pp. 85-92, 2001.
- [156] M. Wilhelm, M. Jeske, R. Marshall, W. L. Cavalcanti, P. Tölle, C. Köhler, D. Koch, T. Frauenheim, G. Grathwohl, J. Caro and M. Wark, "New proton conducting hybrid membranes for HT-PEMFC systems based on polysiloxanes and SO<sub>3</sub>H-functionalized mesoporous Si-MCM-41 particles," *Journal of Membrane Science*, vol. 316, pp. 164-175, 2008.
- [157] S. Bose, T. Kuila, T. X. Ngyuen, N. H. Kim, K. Lau and J. H. Lee, "Polymer membranes for high temperature proton exchange membrane fuel cell: Recent advances and challenges," *Progress in Polymer Science*, vol. 36, pp. 813-843, 2011.
- [158] C. Harms, M. Wilhelm and G. Grathwohl, "Influence of PDMS chain length on proton conductivity in polysiloxane based membranes for HT-PEMFC application," *Journal of Membrane Science*, vol. 383, pp. 135-143, 2011.
- [159] S. F. Flipsen, "Power sources compared: The ultimate truth?," *Journal of Power Sources*, vol. 162, p. 927–934, 2006.
- [160] F. Doumenc and B. Guerrier, "Drying of a Solution in a Meniscus: A Model Coupling the Liquid and the Gas Phases," *Langmuir*, vol. 26, p. 13959–13967, 2010.

- [161] M. R. Wertheimer, "Plasma Processing and Polymers: A Personal Perspective," *Plasma Chemistry and Plasma Polymers*, vol. 34, pp. 363-376, 2014.
- [162] C. Zheng and X. Tan, "Monolithic fabrication of ionic polymer–metal composite actuators capable of complex deformation," *Sensors and Actuators A*, vol. 157, pp. 246-257, 2010.
- [163] C. Tendero, C. Tixier, P. Tristant, J. Desmaison and P. Leprince, "Atmospheric pressure plasmas: A review," *Spectrochimica Acta Part B*, vol. 61, pp. 2-30, 2006.
- [164] G. Selwyn, H. W. Herrmann, J. Park and I. Henins, "Materials Processing Using an Atmospheric Pressure, RF-generated Plasma Source," *Contributions to Plasma Physics*, vol. 6, pp. 610-619, 2001.
- [165] S. Prakash, W. E. Mustain, S.-H. Park and P. A. Kohl, "Phosphorus-doped glass proton exchange membranes for low temperature direct methanol fuel cells," *Journal of Power Sources*, vol. 175, pp. 91-97, 2008.
- [166] H.-J. Lee, J.-H. Kim, J.-H. Won, J.-M. Lim, Y. T. Hong and S.-Y. Lee, "Highly Flexible, Proton-Conductive Silicate Glass Electrolytes for Medium-Temperature/Low-Humidity Proton Exchange Membrane Fuel Cells," *ACS Applied Materials Interfaces*, vol. 5, p. 5034–5043, 2013.
- [167] H. Kim, S. Prakash, W. E. Mustain and P. A. Kohl, "Sol–gel based sulfonic acid-functionalized silica proton conductive membrane," *Journal of Power Sources*, vol. 193, p. 562–569, 2009.
- [168] H. Li, M. Yi and F. Jiang, "Ultra-thin, Free-Standing Proton-Conducting Membrane with Organic/Inorganic Sandwich Structure," *Macromolecular Chemistry and Physics*, vol. 211, p. 863–868, 2010.
- [169] T. Zhao, *Micro Fuel Cells: Principles and Applications*, Academic Press, 2009.
- [170] C. Wang, M. Nogami and Y. Abe, "Protonic Conduction in P2O5-SiO2 Glasses Prepared by Sol-Gel Method," *Journal of Sol-Gel Science and Technology*, vol. 14, p. 273–279, 1999.

- [171] S. C. Deshmukh and E. S. Aydil, "Low-temperature plasma enhanced chemical vapor deposition of SiO<sub>2</sub>," *Applied Physics Letters*, vol. 65, pp. 3185-3187, 1994.
- [172] S.-P. Tung and B.-J. Hwang, "Synthesis and characterization of hydrated phosphor–silicate glass membrane prepared by an accelerated sol–gel process with water/vapor management," *Journal of Materials Chemistry*, vol. 15, pp. 3532-3538, 2005.
- [173] E. Reddington, A. Sapienza, B. Gurau, R. Viswanathan, S. Sarangapani, E. S. Smotkin and T. E. Mallouk, "Combinatorial Electrochemistry: A Highly Parallel, Optical Screening Method for Discovery of Better Electrocatalysts," *Science*, vol. 280, pp. 1735-1737, 1998.
- [174] C. Chang, T. Abe and M. Esashi, "Trench filling characteristics of low stress TEOS/ozone oxide deposited by PECVD and SACVD," *Microsystem Technologies*, vol. 10, pp. 97-102, 2004.
- [175] M. Lisker, S. Marschmeyer, M. Kaynak and I. Tekin, "A Sub-Atmospheric Chemical Vapor Deposition Process for Deposition of Oxide Liner in High Aspect Ratio Through Silicon Vias," *Journal of Nanoscience and Nanotechnology*, vol. 11, p. 8061–8067, 2011.
- [176] I. A. Shareef, G. W. Rubloff, M. Anderle, W. N. Gill, J. Cotte and D. H. Kim, "Subatmospheric chemical vapor deposition ozone/TEOS process for SiO<sub>2</sub> trench filling," *Journal of Vacuum Science Technology B*, vol. 13, pp. 1888-1892, 1995.
- [177] L.-Q. Xia, E. Yieh, P. Gee, F. Campana and B. C. Nguyen, "Process Characteristics for Subatmospheric Chemical Vapor Deposited Borophosphosilicate Glass and Effect of Carrier Gas," *Journal of the Electrochemical Society*, vol. 144, pp. 3208-3212, 1997.
- [178] S. Nguyen, D. Dobuzinsky, D. Harmon, R. Gleason and S. Fridmann, "Reaction Mechanisms of Plasma- and Thermal-Assisted Chemical Vapor Deposition of Tetraethylorthosilicate Oxide Films," *Journal of the Electrochemical Society*, vol. 137, pp. 2209-2215, 1990.

- [179] F. Chen, B. Li, T. D. Sullivan, C. L. Gonzalez, C. D. Muzzy, H. K. Lee, M. D. Levy, M. W. Dashiell and J. Kolodzey, "Influence of underlying interlevel dielectric films on extrusion formation in aluminum interconnects," *Journal of Vacuum Science & Technology B*, vol. 18, pp. 2826-2834, 2000.
- [180] Z. Xie, C. Song, B. Andreaus, T. Navessin, Z. Shi, J. Zhang and S. Holdcroft, "Discrepancies in the Measurement of Ionic Conductivity of PEMs Using Two- and Four-Probe AC Impedance Spectroscopy," *Journal of the Electrochemical Society*, vol. 153, pp. E173-E178, 2006.
- [181] Y. Sone, P. Ekdunge and D. Simonsson, "Proton Conductivity of Nafion 117 as Measured by a Four-Electrode AC Impedance Method," *Journal of the Electrochemical Society*, vol. 143, pp. 1254-1259, 1996.
- [182] W. C. Hsiao, C.-P. Liu and Y.-L. Wang, "Influence of thermal budget on phosphosilicate glass prepared by high-density plasma chemical-vapor deposition," *Journal of Vacuum Science and Technology B*, vol. 23, pp. 2146-2150, 2005.
- [183] J. Stone and G. E. Walrafen, "Overtone vibrations of OH groups in fused silica optical fibers," *The Journal of Chemical Physics*, vol. 76, pp. 1712-1722, 1982.
- [184] C. W. Nam and S. I. Woo, "Characterization of spin-coated silicate and phosphosilicate thin films prepared by the sol-gel method," *Thin Solid Films*, vol. 237, pp. 314-319.
- [185] A. M. Mahajan, L. S. Patil, J. P. Bange and D. K. Gautam, "TEOS-PECVD system for high growth rate deposition of SiO<sub>2</sub> films," *Vacuum*, vol. 79, p. 194-202, 2009.
- [186] K. T. Adjemian, S. J. Lee, S. Srinivasan, J. Benziger and A. B. Bocarsly, "Silicon Oxide Nafion Composite Membranes for Proton-Exchange Membrane Fuel Cell Operation at 80-140°C," vol. 149, pp. A256-A261, 2002.
- [187] N. Sooraj Hussain, M. A. Lopes and J. D. Santos, "A comparative study of CaO-P<sub>2</sub>O<sub>5</sub>-SiO<sub>2</sub> gels prepared by a sol-gel method," *Materials Chemistry and Physics*, vol. 88, pp. 5-8, 2004.



- [188] Y. S. Kim and R. E. Tressler, "Microstructural evolution of sol-gel-derived phosphosilicate gel with heat treatment," *Journal of Materials Science*, vol. 29, pp. 2531-2535, 1994.
- [189] Y. Chakk, S. Altshuler, V. Averkin and A. Sharon, "Novel method for PSG-to-PSG interface integrity improving," in *Proceedings of the 5th International Conference on ASIC*, Beijing, China, 2003.
- [190] B. Stuart, *Infrared Spectroscopy: Fundamentals and Applications*, John Wiley & Sons, Ltd., 2004.
- [191] G. Ramer and B. Lendl, "Attenuated Total Reflection Fourier Transform Infrared Spectroscopy," *Encyclopedia of Analytical Chemistry*, pp. 1-27, 2013.
- [192] K. Kunitatsu, B. Bae, K. Miyatake, H. Uchida and M. Watanabe, "ATR-FTIR Study of Water in Nafion Membrane Combined with Proton Conductivity Measurements during Hydration/Dehydration Cycle," *The Journal of Physical Chemistry B*, vol. 115, p. 4315–4321, 2011.
- [193] B. Navinsek, P. Panjan and I. Milosev, "PVD coatings as an environmentally clean alternative to electroplating and electroless processes," *Surface and Coatings Technology*, Vols. 116-119, p. 476–487, 1999.